UNIVERSITY OF CALIFORNIA

Santa Barbara

The Character, Stability and Consequences of Mn-Ni-Si Precipitates in Irradiated Reactor Pressure Vessel Steels

A dissertation submitted in partial satisfaction of the

requirements for the degree Doctor of Philosophy

in Materials

by

Peter Benjamin Wells

Committee in charge:

Professor G. Robert Odette, Chair

Professor Carlos G. Levi

Professor Glenn E. Lucas

Professor Tresa M. Pollock

March 2016

The dissertation of Peter Benjamin Wells is approved.

_____

Carlos G. Levi

_____

Glenn E. Lucas

_____

Tresa M. Pollock

_____

G. Robert Odette, Committee Chair

November 2015

Acknowledgments

Before acknowledging the many people that have directly contributed to this work, I would like to thank my family, especially my wife, Aislinn. She has been incredibly supportive through this whole process and has helped me through the many stressful times before exams and conferences, while also graciously putting up my many research trips away from Santa Barbara. I also want to thank the rest of my family for their love and encouragement, especially my parents, Pete and Cathy, who instilled the importance of academics in me at a young age.

I thank my advisor, Professor G. Robert Odette, for the opportunity he gave me to work on such a challenging and interesting project. He has worked hard to help me grow as a scientist and for that I am extremely grateful. I would also like to thank my committee, Dr. Carlos Levi, Dr. Tresa Pollock, and Dr. Gene Lucas for their feedback and advice throughout my studies.

The members of the Materials Performance and Reliability Group (MR&PG), both past and present, have also made significant contributions to this work and to my overall experience as a graduate student. Dr. Takuya Yamamoto has been instrumental in obtaining the many irradiated samples that were studied. While we joke that he has put samples in every reactor and particle accelerator around the world, the statement isn't far from the truth. David Gragg, Kirk Fields and Doug Klingensmith were especially helpful not only when it came to testing but also in providing support and humor during stressful periods where things didn't seem to be going well. I would also like to thank the other students in the group, Dr. Nick Cunningham, Tibi Stan, Kevin Cunningham, Nathan Almirall, Tim Milot and Erin

Haney for being available to discuss and critique theories as well as just generally making my graduate student experience more enjoyable. Last, this work would not have been possible without the many contributions of previous graduate students in the MR&PG, most notably Brian Wirth and Erik Mader, whose theses I often referenced during my studies.

Also at UCSB, I would like to thank the staff in the Materials Department, specifically Tom Mates, Mark Cornish and Stephan Krämer for the time they spent training and assisting me with the various instruments used in this research. In addition, a separate collaboration between Stephan and I, most of which is not included in this dissertation, has been especially exciting and rewarding.

I would also like to thank a number of collaborators outside of UCSB. The team at the University of Wisconsin, especially Huibin Ke and Dane Morgan, has been instrumental not only in interpreting our various results, but also in guiding us to design better experiments. In addition, there are a number of questions that we would not have been able to address without the expertise and facilities provided by David Sprouster and Lynne Ecker at Brookhaven National Lab. Oak Ridge National Lab provided access to the Ringhals surveillance specimen, which was very interesting to compare to our much higher flux test reactor irradiated specimens. I also want to acknowledge and thank Kiyohiro Yabuuchi and Akihiko Kimura at Kyoto University and Kenta Murakami at the University of Tokyo for both providing access and completing the ion irradiations at the DuET and HIT facilities, respectively. I want to thank the Nuclear Scientific User Facilities for both completing two large scale irradiations in collaboration with UCSB and providing support for the PIE at the Center for Advanced Energy Studies, whose staff was extremely helpful in providing access to their various instruments.

Curriculum Vitae

Peter Benjamin Wells

EDUCATION

University of California, Santa Barbara (September 2010-present)
Ph.D. in Materials Science
Cumulative GPA: 3.86 (4.0 scale)
Thesis: *The Character, Stability, and Consequences of Mn-Ni-Si Phases in Irradiated Reactor Pressure Vessel Steels*
Advisor: Prof. G. Robert Odette
Expected Graduation: March 2016

University of Idaho (August 2005-May 2010)
Bachelor of Science in Mechanical Engineering (*Cum Laude*)
Cumulative GPA: 3.83 (4.0 scale)

ENGINEERING INTERNSHIP EXPERIENCE

Idaho National Laboratory, Idaho Falls, ID (2006, 2007, 2008, 2009)
Student Summer Internship

TEAM EXPERIENCE

- Student Member of the UC Santa Barbara Radiation Safety Committee (September 2011-Present)
- Student member of the Advanced Test Reactor National Scientific User Organization Executive Committee (June 2012-June 2013)
- Student Member of the Minerals, Metals and Materials Society (March 2012-Present)

HONORS AND AWARDS

- Materials Block Grant Award (Spring 2015)
- Nuclear Energy University Programs Fellow, U.S. DOE (September 2010-September 2013)
- Best Student Poster Award, Symposium of Microstructural Processes in Irradiated Materials, TMS 2013 Annual Meeting (March 2013)
- Alumni Award for Excellence, University of Idaho Alumni Group (December 2009)
- Member of Tau Beta Pi engineering honor society (November 2009-Present)

RELEVANT SKILLS

- Focused Ion Beam
- Cameca LEAP 3000 and 4000x HR
- IVAS (Atom Probe Tomography Reconstruction Software)
- MATLAB
- SolidWorks

PUBLICATIONS

H. Watanabe, S. Arase, T. Yamamoto, P. B. Wells, T. Onishi, G. R. Odette, "Hardening and microstructural evolution of A533b steels irradiated with Fe ions and electrons," *J Nucl Mater*, in press (2016).

D. J. Sprouster, J. Sinsheimer, E. Dooryhee, S. K. Ghose, P. B. Wells, T. Stan, N. Almirall, G. R. Odette, L. E. Ecker, "Structural Characterization of Nanoscale Intermetallic Precipitates in Highly Neutron Irradiated Reactor Pressure Vessel Steels," *Scripta Mater.* **113** (2016) 18-22.

P. B. Wells, T. Yamamoto, B. Miller, T. Milot, J. Cole, Y. Wu, G. R. Odette, "Evolution of manganese-nickel-silicon-dominated phases in highly irradiated reactor pressure vessel steels," *Acta Mater.* **80** (2014) 205.

W. Xiong, H. Ke, R. Krishnamurthy, P. B. Wells, L. Barnard, G. R. Odette, D. Morgen, "Thermodynamic models of low-temperature Mn-Ni-Si precipitation in reactor pressure vessel steels," *MRS Comm.* **4** (2014) 101.

P. B. Wells, G. R. Odette, T. Yamamoto, Y. Wu, N. Almirall, "On Developing a Mechanistic Model and Supporting Database to Predict High Fluence-Low Flux Extended Life RPV Embrittlement," *ANS Trans,* **111** (2014).

D. E. Burkes, N. P. Hallinan, K. L. Shropshire, P. B. Wells, "Effects of applied load on 6061-T6 aluminum joined employing a novel friction bonding process," *Metall Mater Trans A*, 39A (2008) 2852-61.

INVITED TECHNICAL PRESENTATIONS

P. B. Wells, G. R. Odette, T. Yamamoto, N. Almirall, Y. Wu, "The Status of a Low-Flux, High-Fluence Embrittlement Prediction Model for Reactor Pressure Vessel Extended Life," ATR NSUF Semi-Annual Review, Washington D.C., December 9-10, 2014.

P. B. Wells, G. R. Odette, T. Yamamoto, Y. Wu, N. Almirall, "On Developing a Mechanistic Model and Supporting Database to Predict High Fluence-Low Flux Extended Life RPV Embrittlement," ANS 2014 Winter Meeting, Anaheim, CA, November 10-15, 2014.

TECHNICAL PRESENTATIONS

P. B. Wells, S. Krämer, Y. Wu, S. Pal, G. R. Odette, T. Yamamoto, "Nuclear Materials Characterization with 3D Correlative Tomography," TMS 2016 Annual Meeting, Nashville, TN, February 15-18, 2016.

P. B. Wells, N. Almirall, G. R. Odette, T. Yamamoto, D. Gragg, H. Ke, D. Morgan, "Thermal Stability of Hardening Features in Irradiated Reactor Pressure Vessel Steels," TMS 2016 Annual Meeting, Nashville, TN, February 15-18, 2016.

P. B. Wells, S. Krämer, Y. Wu, S. Pal, G. R. Odette, T. Yamamoto, "Characterization of Nuclear Materials using Combined TEM and Atom Probe Tomography," TMS 2015 Annual Meeting, Orlando, FL, March 14-19, 2015.

P. B. Wells, N. Cunningham, G. R. Odette, T. Yamamoto, D. Gragg, "Characterization of Nano-precipitates in Irradiated RPV Steels: A Critical Comparison of SANS and APT Techniques," TMS 2015 Annual Meeting, Orlando, FL, March 14-19, 2015.

P. B. Wells, N. Almirall, G. R. Odette, T. Yamamoto, D. Gragg, H. Ke, D. Morgan, "Thermal Stability of Nanoscale Mn-Ni-Si Precipitates in Irradiated Reactor Pressure Vessel Steels," TMS 2015 Annual Meeting, Orlando, FL, March 14-19, 2015.

P. B. Wells, G. R. Odette, T. Yamamoto, N. Almirall, Y. Wu, H. Watanabe, S. Kondo, A. Kimura, "A Comparison of Precipitates Formed Under Neutron, Ion and Electron Irradiations," International Group of Radiation Damage Mechanisms 18th Semiannual Meeting, Miyazaki, Japan, November 24-28, 2014.

P. B. Wells, G. R. Odette, T. Yamamoto, N. Almirall, Y. Wu, H. Ke, D. Morgan, "Thermal Stability of Hardening Features Formed at Very High Dose," International Group of Radiation Damage Mechanisms 18th Semiannual Meeting, Miyazaki, Japan, November 24-28, 2014.

P. B. Wells, G. R. Odette, T. Yamamoto, N. Almirall, Y. Wu, "Effect of Ni on Precipitates in Highly Irradiated RPV Steels," International Group of Radiation Damage Mechanisms 18th Semiannual Meeting, Miyazaki, Japan, November 24-28, 2014.

P. B. Wells, G. R. Odette, T. Yamamoto, Y. Wu, J. Cole, B. Miller, "Effect of Ni on formation of intermetallic phases in highly irradiated reactor pressure vessel steels," TMS 2014 Annual Meeting, San Diego, CA, February 17-20, 2014.

P. B. Wells, G. R. Odette, T. Yamamoto, Y. Wu, J. Cole, B. Miller, C. Knight, "The Evolution of Late Blooming Phases from High to Very High Fluence," TMS 2013 Annual Meeting, San Antonio, TX, March 3-7, 2013.

P. B. Wells, T. Yamamoto, Y. Wu, N. Cunningham, G. R. Odette, S. Kondo, A. Kimura, "Evolution of Ni-Si-Mn Dominated Phases and Solute Segregation in RPV Steels under Charged Particle Irradiation," International Group of Radiation Damage Mechanisms 17th Semiannual Meeting, Embiez Island, France, May 19-24, 2013.

P. B. Wells, G. R. Odette, T. Yamamoto, Y. Wu, J. Cole, B. Miller, C. Knight, "Late Blooming Phases in RPV Steels at High Fluence and Flux," International Group of Radiation Damage Mechanisms 17th Semiannual Meeting, Embiez Island, France, May 19-24, 2013.

P. B. Wells, N. Cunningham. G. R. Odette, B. Geiser, "Towards Understanding Atom Probe Artifacts: Measuring and Modeling the Effects of Trajectory Aberrations and Variable Field

Evaporation Potentials," International Group of Radiation Damage Mechanisms 17th Semiannual Meeting, Embiez Island, France, May 19-24, 2013.

P. B. Wells, G. R. Odette, Y. Wu, T. Milot, T. Yamamoto, D. Klingensmith, N. Cunningham, J. Cole, "The Search for Late Blooming Phases: Atom Probe Tomography of Irradiated RPV Steels and Model Alloys," MRS Spring Meeting 2012, San Francisco, CA, April 9-13, 2012.

P. B. Wells, G. R. Odette, N. Cunningham, Y. Wu, "APT Characterization of Nanometer Scale Features in RPV Steels and Oxide Dispersion Strengthened Alloys: Insight, Challenges and Opportunities," TMS 2012 Annual Meeting, Orlando, FL, March 12-16, 2012.

P. B. Wells, G. R. Odette, N. Cunningham, E. Stergar, "Atom Probe Observations and Issues," International Group of Radiation Damage Mechanisms 16th Semiannual Meeting, Santa Barbara, CA, December 4-9, 2011.

P. B. Wells, G. R. Odette, D. Klingensmith, "Post Irradiation Annealing of High Flux, High Fluence Irradiated RPV Steels," International Group of Radiation Damage Mechanisms 16th Semiannual Meeting, Santa Barbara, CA, December 4-9, 2011.

Abstract

The Character, Stability and Consequences of Mn-Ni-Si Precipitates in Irradiated Reactor Pressure Vessel Steels

Peter B. Wells

Formation of a high density of Mn-Ni-Si nanoscale precipitates in irradiated reactor pressure vessel steels could lead to severe, unexpected embrittlement, which may limit the lifetimes of our nation's light water reactors. While the existence of these precipitates was hypothesized over 20 years ago, they are currently not included in embrittlement prediction models used by the Nuclear Regulatory Commission. This work aims to investigate the mechanisms and variables that control Mn-Ni-Si precipitate (MNSP) formation as well as correlate their formation with hardening and embrittlement.

A series of RPV model steels with systematic variations in Cu and Ni contents, two variables that have been shown to have a dominant effect on hardening, were irradiated in a series of test reactor and power reactor surveillance irradiations. Atom probe tomography (APT) measurements show that large volume fractions (f_v) of MNSPs form in all the steels irradiated at high fluence, even those containing no added Cu, which were previously believed to have low sensitivity to embrittlement. It is demonstrated that while Cu enhances the rate of MNSP formation, it does not appear to significantly alter their saturation f_v or composition. The high fluence MNSPs have compositions consistent with known intermetallic phases in the Mn-Ni-Si system and have f_v very near those predicted by equilibrium thermodynamic models. In addition, X-ray diffraction experiments by

collaborators shows that these precipitates also have the expected crystal structure of the predicted Mn-Ni-Si phases.

Post irradiation annealing experiments are used to measure the hardness recovery at various temperatures as well as to determine if the large f_v of MNSPs that form under high fluence neutron irradiation are thermodynamically stable phases or non-equilibrium solute clusters, enhanced or induced by irradiation, respectively. Notably, while post irradiation annealing of a Cu-free, high Ni steel at 425°C results in dissolution of most precipitates, a few larger MNSPs appear to remain stable and may begin to coarsen after long times. A cluster dynamics model rationalizes the dissolution and reduction in precipitate number density, since most are less than the critical radius at the annealing temperature and decomposed matrix composition. The stability of larger precipitates suggests that they are an equilibrium phase, consistent with thermodynamic models.

Charged particle irradiations using Fe^{3+} ions are also used to investigate the precipitates which form under irradiation. Two steels irradiated to a dose of 0.2 dpa using both neutrons and ions show precipitates with very similar compositions. The ion irradiation shows a smaller f_v, likely due to the much higher dose rate, which has been previously shown to delay precipitation to higher fluences. While the precipitates in the ion irradiated condition are slightly deficient in Mn and enriched in Ni and Si compared to neutron irradiated condition, the overall similarities between the two conditions suggest that ion irradiations can be a very useful tool to study the susceptibility of a given steel to irradiation embrittlement.

Finally, the large f_v of MNSPs that are shown to form in all steels, including those low in Cu, at high fluence, even those without added Cu, result in large amounts of hardening and embrittlement. A preliminary embrittlement prediction model, which incorporates

MNSPs at high fluence, is presented, along with results from a recent test reactor irradiation to fluences representative of extended lifetimes. This model shows very good agreement with the data.

Table of Contents

List of Figures

List of Tables

Nomenclature

APT	atom probe tomography
ATR	Advanced Test Reactor
BR2	Belgian Reactor 2
CAES	Center for Advanced Energy Studies
CPI	charged particle irradiations
CRP	Cu-rich precipitates
DBTT	ductile to brittle transition temperature
DLD	delay line detector
DuET	Dual Beam for Energy Science and Technology Facility
dpa	displacements per atom
EONY	Eason-Odette-Nanstad-Yamamoto embrittlement prediction model
f_v	precipitate volume fraction
FIB	focused ion beam
HIT	Heavy Fluence Irradiation Facility
IVAR	Irradiation Variables Program
IVAS	CAMECA Integrated Visualization and Analysis Software
LBP	late blooming phases
LEAP	local electrode atom probe
LS	linear sum superposition model
LWR	light water reactor
MCP	microchannel plate
MNS	manganese-nickel-silicon
MNSP	manganese-nickel-silicon precipitates
MRPG	Materials Reliability and Performance Group led by Dr. Odette
m/n	mass-to-charge ratio of an ion
N	number density
NRC	Nuclear Regulatory Commission

PKA	primary knock-on atom
PIA	post irradiation annealing
RB	Russell-Brown hardening model
RPV	reactor pressure vessel
RED	radiation enhanced diffusion
RIS	radiation induced segregation
RSS	root sum square superposition model
SANS	small angle neutron scattering
SIA	self-interstitial atom
SMF	stable matrix feature
SMMS	split melt model steel
<r>	average radius
T_{irr}	irradiation temperature
ΔT	increase in the DBTT due to irradiation
$\Delta\sigma_y$	increase in yield strength due to irradiation
ϕ	neutron flux ($n/cm^2/s$)
ϕt	neutron fluence (n/cm^2)
ϕt_e	effective neutron fluence (n/cm^2)

Chapter 1 Introduction

Nuclear power in the United States generates approximately 20% of all electricity and over 60% of the nation's carbon-free energy [1]. The vast majority of reactors are nearing or surpassing their original operating licenses, set by the US Nuclear Regulatory Commission (NRC) at 40 years. If all reactors are shut down after 40 years of operation, the power generated by nuclear power in the US will drop by 60% by 2025 [1]. Fortunately, the original license term of 40 years was selected not due to engineering limitations, but for economic and antitrust considerations [2]. Furthermore, the NRC determined in the mid-1980s that most aging processes were readily manageable. Thus, the NRC will grant license renewals for up to 20 years of additional operation if plant operators can show they meet a given set of requirements [2].

Over 70 of the 100 reactors in the US have been approved for this 20 year life extension, for a total operating lifetime of 60 years [1]. While these extensions will result in continued operation of our nation's largest carbon-free energy source, unless there is a significant increase in the rate of new plant builds, which is unlikely in part due to high costs and long construction times, the country will be faced with a similar problem by 2030, when the first of these extensions will end [1]. Thus, a primary objective of the Department of Energy is to determine the feasibility of a second license renewal, for a total operational lifetime of 80 years [3].

The reactor pressure vessel (RPV), which is the primary containment structure in the reactor and also one of the only irreplaceable components, becomes embrittled by exposure to the high energy neutrons generated in the reactor core [4]. This embrittlement is manifested by an upwards shift of the ductile-to-brittle transition temperature. Current models of RPV embrittlement, for example the Eason-Odette-Nanstad-Yamamoto (EONY) model used by the NRC for pressurized thermal shock, predict that transition temperature shifts (ΔT) increase with increasing neutron fluence (ϕt), measured in neutrons/cm^2 [4, 5]. Because life extension leads to high RPV fluences, beyond those ever before experienced by in service vessels, the causes of embrittlement must be well understood and modeled.

Surveillance material was included in most US reactors and was designed to be periodically removed and tested. These samples, located within the RPV, are irradiated at a higher neutron flux than the RPV itself. Thus, measurements of surveillance specimens signal the ΔT the RPV will likely experience at a later date. Unfortunately, the surveillance database is somewhat limited, and plant specific surveillance data is often not sufficient to predict ΔT [6]. Thus, a primary way of studying RPV embrittlement is through the use of material test reactors, which can irradiate materials to high fluence in a much shorter time than power reactors due to the high neutron fluxes (ϕ), with typical units of neutrons/cm^2-s. A significant issue with regards to reactor life extension is that the EONY model, which was fit to the low-flux surveillance ΔT database up to medium fluence, under-predicts the ΔT data at high fluences from higher flux test reactor irradiations [7]. Figure 1.1 shows that the ΔT under-prediction increases with increasing neutron fluence [7].

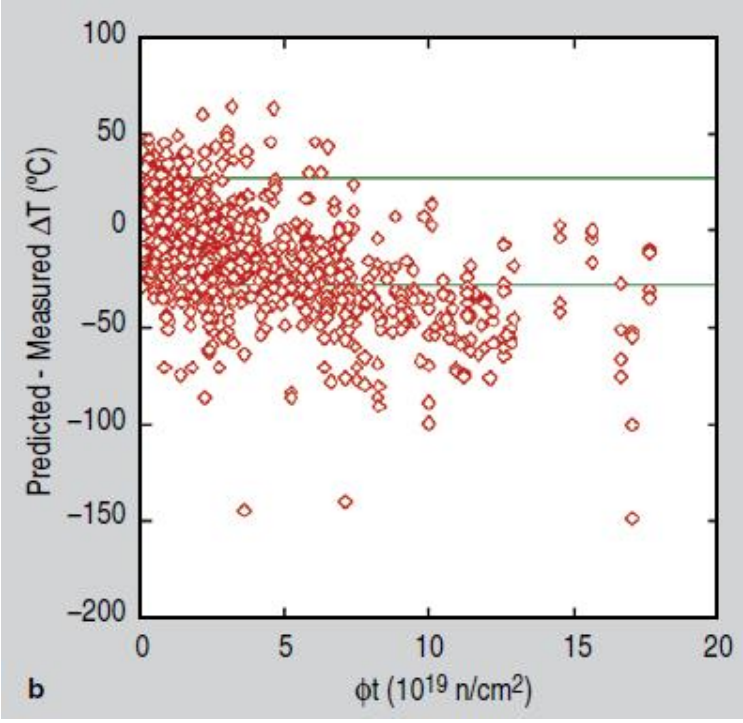

Figure 1.1. Predicted vs measured ΔT as a function of neutron fluence for material irradiated in test reactors, from [7].

This dissertation will show that perhaps the most important reason for the ΔT under-prediction is the formation of Mn-Ni-Si precipitates at high fluences, beyond those reached by the current surveillance database [3, 7]. Acting as barriers to dislocation motion, the precipitates result in hardening and a corresponding ΔT, at a nominal rate of approximately 0.7ºC/MPa [8]. Though long ago predicted [9], the precipitates have only recently been found experimentally found in test reactor irradiations [7, 10, 11] and most notably, in a low Cu, high-Ni surveillance steel [12, 13]. The Mn-Ni-Si precipitates, that have been called "Late-Blooming Phases" due to their slow nucleation and/or growth rates, are unaccounted for in the EONY model [7]. Thus, life extension to 80 years will require a thorough understanding

of these Mn-Ni-Si precipitates and the variables that influence their formation and evolution, such as alloy composition and flux, fluence and temperature. Developing such understanding is the focus of this dissertation.

1.1 Primary Research Objectives

The underlying hypothesis behind this research is that Mn-Ni-Si precipitation must be included within models in order to accurately predict embrittlement at high fluence. This hypothesis will be addressed through a set of primary research objectives, which can be broadly categorized as follows:

1. Characterize the Mn-Ni-Si precipitates (MNSPs) formed under neutron irradiation to determine their size, number density, volume fraction, composition and morphology, and how these characteristics vary with neutron flux, fluence, irradiation temperature, and alloy composition.
2. Carry out post irradiation annealing experiments to probe phase boundaries, to assess the potential role of non-equilibrium radiation induced segregation (RIS), and to discriminate between various hardening features that have different recovery signatures. The annealing studies also permit investigating the individual and combined hardening contributions from the features formed under irradiation.
3. Explore the possibility of using charged particle irradiations to study mechanism of irradiation embrittlement, including precipitation of MNSPs.
4. Correlate the precipitates size and f_v with the changes in mechanical properties, namely hardness and yield strength.

1.2 Significance and Organization

Reactor life extension to 80 years will require a model that can accurately predict ΔT at high fluence and low flux for a wide range of steels, over the range of service temperatures experienced by the nation's fleet of reactors. A particular focus of this model must be the proper treatment of the MNSPs, including what they are (i.e. intermetallic phases or non-equilibrium solute clusters), when (i.e. what fluence) and where (i.e. what steels are most susceptible) they will form, and how they form (i.e. what is the detailed mechanism relating to their formation and how is this affected in high flux test reactor irradiations). This work provides a significant experimental foundation for the development of such models.

This dissertation is organized into 9 chapters. The second chapter provides background regarding the sequence of events leading to RPV embrittlement (ΔT): a) starting with neutron-nuclear interactions producing energetic primary recoil atoms that generate displacement cascades; b) creation of a population of excess vacancies and self-interstitials and small clusters of these defects; c) diffusion of solutes and defects to sinks, including the cited clusters, at enhanced rates (radiation enhanced diffusion, RED); d) hardening by the clusters; and e) elevation of the transition temperature caused by the hardening. Chapter 3 outlines the materials, irradiation conditions and experimental methods used to characterize the mechanical property and microstructure changes that occur under irradiation for a matrix of RPV steels with systematic variations in key alloying elements. Chapter 4 focuses on the reconstruction and analysis methods used in atom probe tomography to characterize the irradiated microstructure. Chapter 5 presents the key results on MNSPs that form in high

fluence neutron irradiations, both from test reactors and a surveillance program. Post irradiation annealing results on the test reactor irradiated materials are presented in Chapter 6 with a focus on the thermal stability of MNSPs. Results from a series of charged particle irradiations (CPI) are presented in Chapter 7 and compared with the results from the neutron irradiations in Chapter 5. The focus here is to determine how to properly use CPI to explore radiation damage mechanisms, including MNS precipitation, and not as an effort to simulate neutron damage. Chapter 8 details the relations between precipitate f_v and $\Delta\sigma_y$ and presents preliminary data from a high fluence test reactor irradiation specifically designed to investigate ΔT at RPV extended lifetimes. Chapter 9 contains a broad summary and discussion of the results, the insight gained from the collective observations and resulting conclusions, and suggested future work.

1.3 References

1. "Integrated Program Plan," Light Water Reactor Sustainability Program, DOE Office of Nuclear Energy, 2014; INL/EXT-11-23452 Rev. 2.
2. "Light Water Reactor Sustainability Research and Development Program Plan Fiscal Year 2009 – 2013," Light Water Reactor Sustainability Program, DOE Office of Nuclear Energy, 2009; INL/MIS-08-14918 Rev. 2
3. "Materials Aging and Degradation Technical Program Plan," Light Water Reactor Sustainability Program, DOE Office of Nuclear Energy, 2015; ORNL/LTR-2012/327 Rev. 3.
4. Eason ED, Odette GR, Nanstad RK and Yamamoto T. "A physically based correlation of irradiation-induced transition temperature shifts for RPV steels," Oak Ridge National Lab, 2007; ORNL/TM-2006/530.
5. Eason ED, Odette GR, Nanstad RK and Yamamoto T. "A physically-based correlation of irradiation-induced transition temperature shifts for RPV steels", *J. Nucl. Mater.* 2013;433:240–254.
6. Odette GR and Lucas GE. "Embrittlement of nuclear reactor pressure vessels", *JOM*

2001;53:18–22.

7. Odette GR and Nanstad RK. "Predictive reactor pressure vessel steel irradiation embrittlement models: Issues and opportunities", *JOM* 2009;61(7):17–23.

8. Odette GR and He MY. "Cleavage toughness master curve model", *J. Nucl. Mater.* 2000;283-287:120–127.

9. Odette GR. "Radiation Induced Microstructural Evolution in Reactor Pressure Vessel Steels", *Mater. Res. Soc. Symp. Proc.* 1995;373:137–148.

10. Miller MK, Chernobaeva AA, Shtrombakh YI, Russell KF, et al. "Evolution of the nanostructure of VVER-1000 RPV materials under neutron irradiation and post irradiation annealing", *J. Nucl. Mater.* 2009;385(3):615–622.

11. Miller MK, Russell KF, Sokolov MA and Nanstad RK. "APT characterization of irradiated high nickel RPV steels", *J. Nucl. Mater.* 2007;361:248–261.

12. Miller MK, Powers KA, Nanstad RK and Efsing P. "Atom probe tomography characterizations of high nickel, low copper surveillance RPV welds irradiated to high fluences", *J. Nucl. Mater.* 2013;437(1-3):107–115.

13. Styman PD, Hyde JM, Parfitt D, Wilford K, et al. "Post-irradiation annealing of Ni–Mn–Si-enriched clusters in a neutron-irradiated RPV steel weld using Atom Probe Tomography", *J. Nucl. Mater.* 2015;459:127–134.

Chapter 2 Background

2.1 Introduction

Light water reactor (LWR) plant life extension to 80 years is needed to sustain the largest US carbon-free energy resource [1]. The major permanent and safety critical LWR component is the massive reactor pressure vessel (RPV). Neutron irradiation of RPV steels results in embrittlement, manifested as an upward shift in the ductile to brittle transition temperature [2]. These transition temperature shifts (ΔT) are primarily caused by the precipitation and defect hardening that occur under irradiation. Life extension will require demonstration of large inherent safety margins for the RPV, including ensuring that the effects of long-term irradiation service on fracture toughness can be predicted and safely managed. The major challenge is to develop robust predictive models of ΔT in neutron flux ($n/cm^2/s$) and fluence (n/cm^2) regimes where data does not currently exist [3]. Here the existence of a new, high fluence, severe embrittlement mechanism is verified and a number of discoveries and related details of the nature and potential impact of the responsible precipitation hardening phases are reported.

The following sections will present the background information necessary to interpret the results in the coming chapters. First, a brief background on light water reactors will be presented including a description of the reactor pressure vessel and its purpose in the reactor. Next, a short overview of radiation damage in materials will be presented. This description

will be very concise with a focus on the aspects of radiation damage that have specific implications to RPV embrittlement, namely the production of point defects and their ultimate fate. Following this, the driving force behind precipitation of secondary phases and the implications of these precipitates will be presented. Next, a brief description of the current model used by the NRC for reactor pressure vessel embrittlement will be discussed along with what is essentially the motivation behind this dissertation, the large under-prediction in ΔT in high fluence test reactor data. A possible explanation for this under-prediction, formation of Mn-Ni-Si phases at high fluence, will be presented, with a brief overview of the understanding of these precipitates and the outstanding questions that remain. Finally, a short description of the effects of varying neutron flux will be presented. While this dissertation does not specifically address the challenges associated with correlating high flux test reactor data to low flux power reactor data, it is important to present some supporting information regarding the effects of flux since the bulk of the data presented comes from high flux test reactors.

2.2 The Reactor Pressure Vessel

The reactor pressure vessel (RPV) is a large steel vessel that surrounds the reactor core. The RPV keeps the coolant water at a high pressure, up to 7 MPa in boiling water reactors and 14 MPa in pressurized water reactors, and acts as the primary containment between the core and the secondary concrete containment structure [4, 1]. Due to the size of the RPV, which for a PWR is typically on the order of 14 m tall, 5 m in diameter, 20-30 cm

thick and weighs several hundred tons, along with the overall design of the reactor, it is one of the only irreplaceable components [5, 4].

RPV's are low-alloy steels that contain C, Cr, Mn, Si, Ni and Mo along with impurity Cu and P [1]. They also typically have a stainless steel inner lining to prevent corrosion from the coolant water [4]. The alloys are tempered and stress relieved following welding, typically at ≈ 625°C for 30 h resulting in a bainitic microstructure [1]. The yield strength for these steels is approximately 475±50 MPa with a starting transition temperature of between -50 and -100°C [3]. It should be noted that no two RPVs are the same. Among the US surveillance database, the plates and forgings have solute contents in the following ranges (wt.%): 0.04-1.26%Ni, 0.58-1.96%Mn, 0.15-0.37%Si, 0.01-0.41%Cu, and 0.003-0.031%P [2]. Thus, understanding and predicting ΔT requires not only understanding the effect of each individual variable, but also of the synergistic interactions among all variables.

2.3 Radiation Damage in Metals

There are currently over 100 operating nuclear reactors in the United States, almost all of which are light water reactors (LWRs) [5]. The basic design of a reactor is to use heat produced through nuclear fission to heat water to steam, which turns a turbine to generate electricity. Nuclear fission occurs when a fissile atom, such as ^{235}U or ^{239}Pu, captures a neutron, becomes unstable, and then splits into two or more other atoms along with emitting more neutrons and heat. The fission reaction for ^{235}U, the fuel source for LWRs, is given by

$$^{235}_{92}U + ^{1}_{0}n \rightarrow ^{236}_{92}U \rightarrow F1 + F2 + X^{1}_{0}n + Y\,MeV \quad (2.1)$$

where F1 and F2 are fission fragment nuclei, X is the number of emitted neutrons, which averages 2.5 per reaction for thermal fission of ^{235}U, and Y is energy, which is typically on the order of 200 MeV [4]. The emitted neutrons have an average of ≈ 2 MeV of energy. The nuclear cross section of ^{235}U is ≈ 10 times larger for thermal neutrons (E < 1eV) than fast neutrons, so the emitted neutrons must be slowed down by a moderator to increase the likelihood of additional fission events, which in the case of LWRs is water, to continue the fission chain reaction. A very small percent of fast neutrons are able to escape the reactor core and reach the reactor pressure vessel, where they cause damage to the RPV lattice.

When an atom is struck by a high energy neutron (E > 1 MeV), it is displaced from its lattice site, while gaining a significant amount of kinetic energy, on the order of several tens of keV [2, 6–8]. This atom, called the primary knock-on atom (PKA), subsequently hits other atoms in the lattice, creating what is termed a displacement cascade, or a chain reaction of atomic collisions resulting in the creation of a large number of vacancies, or empty lattice sites, and self-interstitial atoms (SIAs), or two atoms occupying the same lattice site. The series of atomic collisions continues until the energy transferred to the final atoms is not sufficient to displace them from their lattice sites. Figure 2.1 shows a molecular dynamics simulation of a displacement cascade in α-Fe, from [2]. For clarity, only SIAs (green) and vacancies (red) are shown. While the MD simulation shows a large number of defects created at 0.26 ps, seen in the top right of Figure 2.1, most of these defects recombine very quickly. The defects that remain after ≈ 20 ps, which are highly mobile in the matrix, undergo long range diffusion. While most eventually recombine or are annihilated at sinks, such as

dislocations, free surfaces or grain boundaries, the main consequence is that during irradiation the concentration of defects is higher than at thermal equilibrium. In addition, the defects that are not annihilated form clusters of like defects, sometimes enriched in solutes.

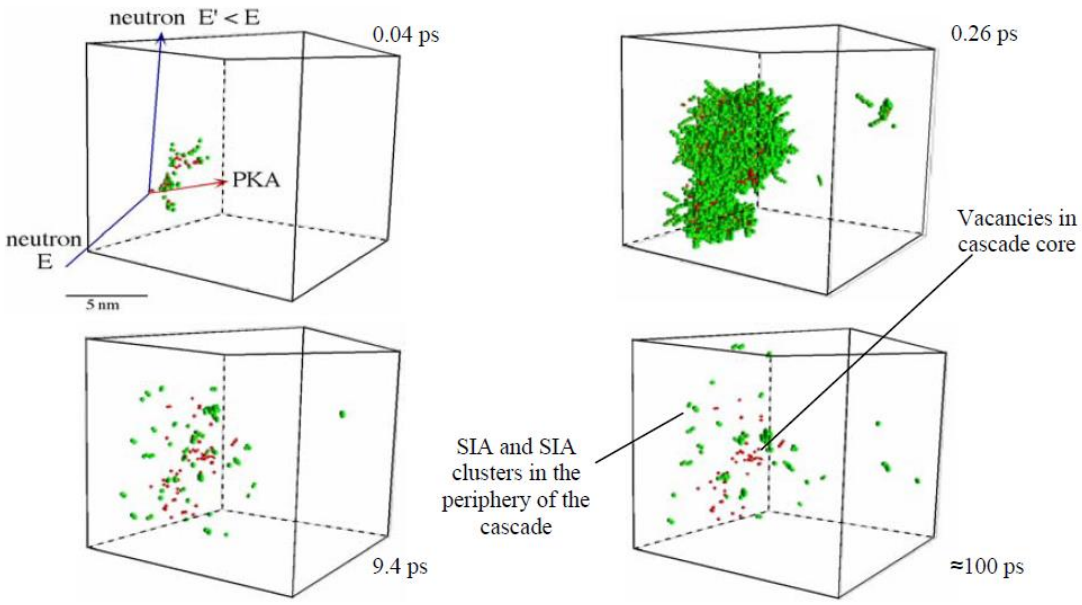

Figure 2.1. The evolution of a displacement cascade from the primary knock-on atom (top left) to the remaining defects in the lattice after the energy has been dissipated (bottom right). Green dots represent self-interstitial atoms and red dots represent vacancies, from [2].

Substitutional solute atoms may only move around the Fe lattice if the neighboring lattice site is vacant. The increased vacancy concentration under irradiation increases the probability that vacancies will be nearby, resulting in increased diffusion rates. Radiation enhanced diffusion (RED) is the source of the significant microstructural changes that occur under irradiation. Thermal diffusion rates in Fe at typical T_{irr} are so low that essentially no microstructural changes can be observed over timescales relevant to reactor operation. Under irradiation, diffusion rates are increased by several orders of magnitude, leading to formation

of secondary phases for elements that are above the solubility limit. For example, the low solubility of Cu in Fe, combined with RED, results in rapid Cu precipitation in alloys with Cu ≈ 0.07 wt.% or above [2]. These precipitates, along with defect or solute-defect clusters, act as barriers to dislocation motion, resulting in hardening and embrittlement of the steel.

2.4 Strengthening Mechanisms in Steels

The yield strength of a material is essentially determined by the stress needed to cause movement of dislocations. Thus, any microstructural feature in the material which acts as a barrier to dislocation motion increases the strength. The total strength of a material can be written by the following

$$\sigma_y = \sigma_f(T, \dot{\varepsilon}) + \sigma_{lrs} + kd_g^{-1/2} + \sigma_{obs} \tag{2.2}$$

where σ_f is the frictional lattice resistance, also known as the Peierls stress, which is dependent on test temperature and strain rate; σ_{lrs} is the strength contribution from features with long range stress fields, such as dislocations; $kd_g^{-1/2}$ is the grain-size (d_g) strengthening contribution; and σ_{obs} is the strength contribution from obstacles such as solid substitutional atoms or precipitates [9]. The main change that occurs under irradiation is the formation of either precipitates or defect clusters, which act as obstacles, so the focus here is on σ_{obs}.

Figure 2.2 shows a schematic of a dislocation (dark line) passing through an array of obstacles (circles). The force, F, exerted on the obstacle is given by [10]

$$F = 2T\cos\left(\frac{\phi}{2}\right) \tag{2.3}$$

where T is the dislocation line tension and ϕ is the bowing angle. Inputting the dislocation line tension as $T \approx Gb^2/2$ and area as A = L*b gives the shear stress, τ, required to move the dislocation through the obstacle as

$$\tau \cong \frac{Gb}{L'} cos \frac{\phi_c}{2} \tag{2.4}$$

where G is the shear modulus of the material, b is the burgers vector for the dislocation, L' is the effective spacing of the obstacles and ϕ_c is the critical bowing angle necessary to move through the obstacle [9]. For very strong obstacles, $\phi_c \approx 0$ and $L' \approx L$, thus eqn. (2.4) reduces to give the maximum strength from an array of obstacles as $\tau_{max} = Gb/L$, also known as the Orowan hardening relationship.

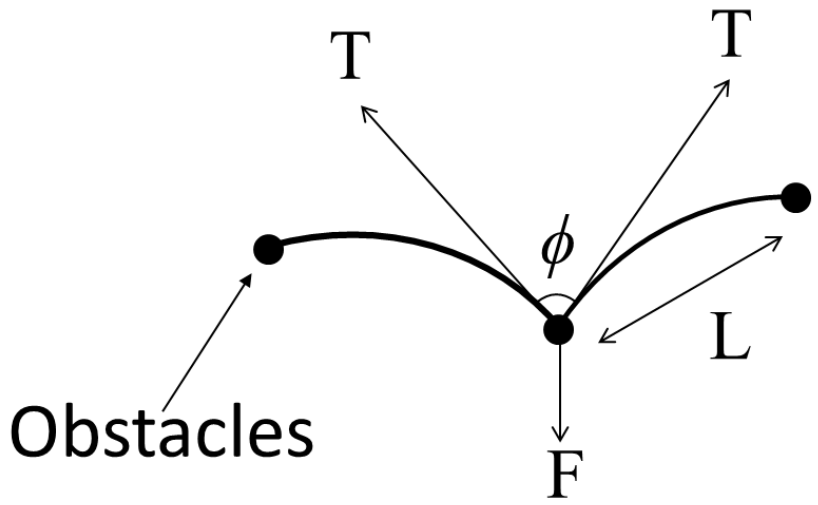

Figure 2.2. Schematic of a dislocation passing through an array of obstacles.

For weaker obstacles, the effective particle spacing, L', is larger than L, eqn. (2.4) can be rewritten as [10, 11]

$$\tau \cong 0.8\frac{Gb}{L}\cos\frac{\phi_c}{2} \qquad \phi_c < 100° \tag{2.5}$$

$$\tau \cong \frac{Gb}{L}\left[\cos\frac{\phi_c}{2}\right]^{3/2} \qquad \phi_c \geq 100° \tag{2.6}$$

Thus, ϕ_c must be known in order to determine the strength of an array of obstacles. Russell and Brown proposed a model for determining ϕ_c for an array of precipitates with a lower shear modulus than the matrix [11], which is the case for Cu-rich precipitates in an Fe matrix. This model proposes that the critical bowing angle when the dislocation is about to break away from the precipitate is given by

$$\phi_c = 2\sin^{-1}\frac{E_1}{E_2} \tag{2.7}$$

where E_1 is the dislocation energy per unit length in the precipitate and E_2 is the dislocation energy per unit length in the matrix. Substituting eqn. (2.7) into eqns. (2.6) and (2.5) gives the following

$$\tau \cong 0.8\frac{Gb}{L}\left[1-\frac{E_1^2}{E_2^2}\right]^{1/2} \qquad \sin^{-1}\frac{E_1}{E_2} < 50° \tag{2.8}$$

$$\tau \cong \frac{Gb}{L}\left[1-\frac{E_1^2}{E_2^2}\right]^{3/4} \qquad \sin^{-1}\frac{E_1}{E_2} \geq 50° \tag{2.9}$$

The interparticle slip plane spacing, L, can be defined in terms of the volume fraction, f_v, and mean precipitate radius, r, as [11]

$$L^{-1} = \frac{\sqrt{f_v}}{1.77r} \tag{2.10}$$

Finally, the critical resolved shear stress can be related to the yield stress in a polycrystal through the Taylor factor

$$\sigma_y = m\tau_c \tag{2.11}$$

Thus, for a polycrystalline material, the increase in yield stress due to obstacles can be written

$$\Delta\sigma_y \cong 0.8\frac{\sqrt{f_v}}{1.77r}mGb\left[1-\frac{E_1^2}{E_2^2}\right]^{1/2} \qquad \sin^{-1}\frac{E_1}{E_2} < 50° \tag{2.12}$$

$$\Delta\sigma_y \cong \frac{\sqrt{f_v}}{1.77r}mGb\left[1-\frac{E_1^2}{E_2^2}\right]^{3/4} \qquad \sin^{-1}\frac{E_1}{E_2} \geq 50° \tag{2.13}$$

Russell and Brown estimated the ratio E_1/E_2 as a function of precipitate radius, r, as [11]

$$\frac{E_1}{E_2} = \frac{E_1^{\infty}\log\frac{r}{r_0}}{E_2^{\infty}\log\frac{R}{r_0}} + \frac{\log\frac{R}{r}}{\log\frac{R}{r_0}} \tag{2.14}$$

where R and r_0 are the outer and inner cutoff radius that determine the energy of the dislocation, respectively, and E^{∞} is the energy per unit length in an infinite particle (E_1^{∞}) and matrix (E_2^{∞}). While Russell and Brown estimated values for m, r_0, R, and $E_1^{\infty}/E_2^{\infty}$, E_1/E_2 was empirically calibrated in this dissertation by using measurements of hardening after irradiation and precipitate f_v.

2.5 Superposition

To determine the total hardening in an alloy from obstacles created under irradiation, the strengths of those obstacles must be combined with the strengths of the features in the unirradiated steel, such as carbides. Foreman and Makin showed that the total yield stress contributions from two different features depend on their relative strengths [10]. For example, features of similar strength must be combined through a root sum square (RSS) law. For a combination of medium and high strength features, the high strength features cause significant dislocation bowing, resulting in the intersection of the dislocation with more medium strength features than would occur if only the latter were present. Thus, the total σ_y for medium and high strength obstacles is larger than would be predicted by a RSS law. For low strength obstacles combined with high strength obstacles, the dislocation shears through the low strength obstacles and does not alter the shape of the dislocation. In this case, the total strength can be calculated through a simple linear sum (LS) of the two features. Thus, the two limiting rules for superposition are RSS or LS depending on the various strengths of the obstacles present.

Computer simulations have been developed to determine the total σ_y from a population of obstacles with different strengths. One study [2, 12] calculated the net σ_y from a population of weak ($\alpha_w < 0.1$), medium ($0.1 < \alpha_m < 0.6$) and strong ($\alpha_s > 0.6$) obstacles as

$$\sigma_y = \sigma_{yw} + (1 - S)\left(\sigma_{ym}{}^2 + \sigma_{ys}{}^2\right)^{\frac{1}{2}} + S(\sigma_{ym} + \sigma_{ys}) \tag{2.15}$$

where σ_y is the total yield strength, σ_{yw}, σ_{ym} and σ_{ys} are the yield strength contributions from weak, medium and strong obstacles, respectively, and S is the superposition factor.

The superposition factor is given by

$$S = \alpha_s - \alpha_m(5 - 3.3\alpha_s) \tag{2.16}$$

Here, the assumption is that the only hardening features are the precipitates that form under irradiation and the pre-existing features, such as carbides, which are strong features (α_s = 0.8). The hardening due to the pre-existing features has been estimated to be ≈ 180 MPa [2].

Thus, the total yield strength can be written

$$\sigma_y(MPa) = (1 - S)\left(\sigma_{yp}{}^2 + 180^2\right)^{\frac{1}{2}} + S(\sigma_{yp} + 180) \tag{2.17}$$

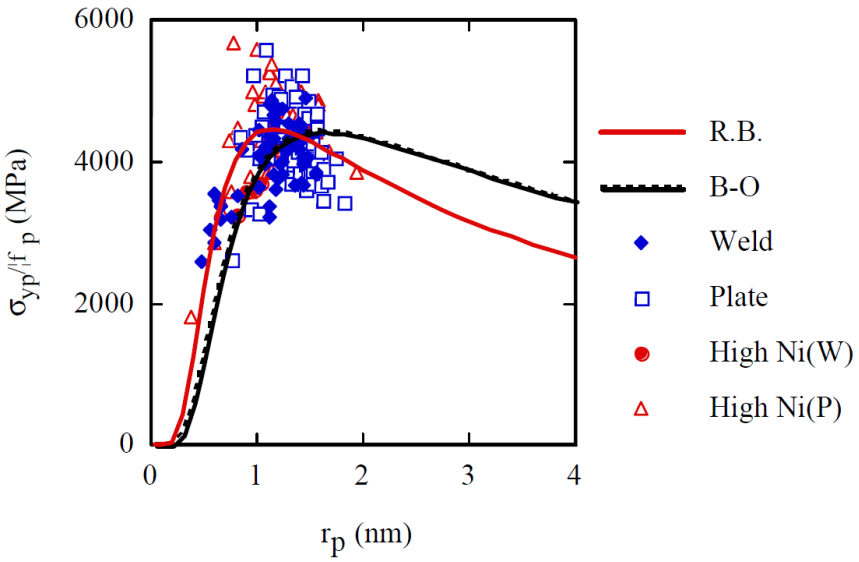

Figure 2.3. Normalized hardening efficiency ($\sigma_{yp}/\sqrt{f_v}$) as a function of r_p for a number of irradiated alloys with two model fits, a Russell-Brown type (RB) and Bacon and Osetsky (BO), from [2].

Thus, the precipitate contribution to the overall hardening, σ_{yp}, can be determined from the total strength of the alloy, σ_y. If both microstructure and mechanical property measurements have been made on an irradiated alloy, then the precipitate hardening

efficiency, given as the amount of hardening (σ_{yp}) caused by a given average precipitate size (<r>) can be determined. An example empirical fit for the normalized precipitate hardening efficiency ($\sigma_{yp}/\sqrt{f_v}$) is given in Figure 2.3 and compared with two models, a fitted Russell-Brown (RB) and Bacon and Osetsky (BO), from [2]. Note that the BO model is not discussed here. These empirical correlations can then be used to predict $\Delta\sigma_y$ from microstructure measurements of f_v and <r>.

2.6 Embrittlement

Cleavage in RPV steels is believed to be caused unstable growth of microcracks nucleated at brittle carbides located on grain boundaries [12, 13]. The local stress required for brittle cleavage, σ^*, is relatively insensitive to test temperature and since it is related to the inverse of the square root of the largest carbide size, it is also unaffected by the much finer precipitates that form under irradiation [12]. While P segregation to grain boundaries, which can occur under irradiation, has been shown to weaken grain boundaries and promote intergranular fracture, western steels contain very low P contents and are not susceptible to this non-hardening embrittlement mechanism [1, 14]. Thus, σ^* is essentially unaffected by irradiation.

From eqn. (2.2), the yield strength of a material is partially dependent on the frictional lattice resistance, or Peierls stress, which is a function of both strain rate and temperature. Increasing temperature increases the thermal energy of atoms making it easier for them to overcome the frictional lattice resistance, and subsequently reducing σ_y. Since σ^* is unaffected by temperature while σ_y increases with temperature, there exists a temperature

at which the failure mode transitions from brittle cleavage, $\sigma^* < \sigma_y$, to ductile tearing, $\sigma^* > \sigma_y$. This temperature is called the ductile-to-brittle-transition temperature (DBTT) and is schematically shown in Figure 2.4.

Under irradiation, the main effect is to increase σ_y. Since σ^* remains constant, this results in an increase in the DBTT, called a transition temperature shift (ΔT), shown schematically in Figure 2.5. The magnitude of ΔT, which is the primary way that embrittlement is quantified in irradiated RPV steels, is measured with Charpy impact tests. In these tests, a notched specimen is mounted on the testing apparatus. A weighted hammer on a nearly frictionless pendulum is dropped from a specified height and impacts the specimen. The impact causes failure of the specimen and a reduction in the height of the hammer swing. The original height of the hammer minus the final height of the hammer swing can then be related to the energy absorbed by the specimen. At low temperatures, where failure is characterized by brittle fracture, little energy is needed to cause failure. On the other hand, at higher temperatures where the failure mode is dominated by ductile tearing, significant energy is absorbed through plastic deformation prior to failure. Thus, tests can be taken at multiple temperatures and the absorbed energy for each test can be plotted against temperature to determine the DBTT. These tests can also be performed on irradiated specimens to measure the increase in DBTT, or ΔT. This is schematically shown in Figure 2.6.

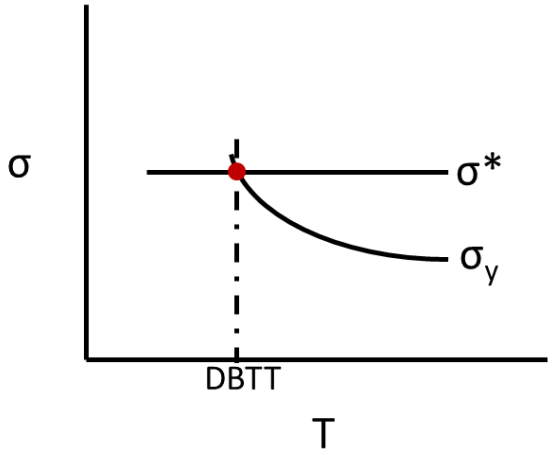

Figure 2.4. Stress needed to cause failure by brittle fracture, σ*, and ductile tearing, σ_y, as a function of temperature.

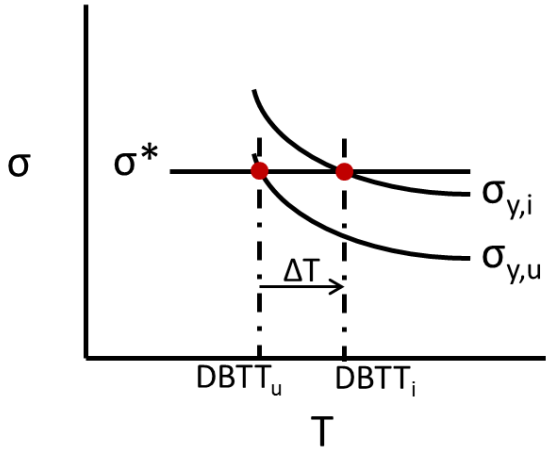

Figure 2.5. Schematic showing a transition temperature shift, ΔT, resulting from an increase in yield strength after irradiation.

Odette et. al. have analyzed CVN test data to show that both σ* and $\Delta\sigma_y$ are independent of temperature [12]. Thus, ΔT is fully controlled by the increase in yield strength after irradiation. ΔT can be determined by finding $DBTT_i$ when $\sigma_{y,u}(DBTT_u) = \sigma_{y,i}(DBTT_i)$. Models have been created based on these concepts that predict $\Delta T = C(USE_u, DBTTu, \Delta\sigma_i)\Delta\sigma_i$, where USE_u is the unirradiated upper shelf energy, $DBTT_u$ is the starting ductile-to-brittle transition temperature, and $\Delta\sigma_i$ is the change in yield strength after irradiation. Predicted values of C have shown to agree well with an empirically determined value of C = 0.68°C/MPa. This means that an alternative method to quantify embrittlement is to measure $\Delta\sigma_y$ and convert it to ΔT through the relation [15]

$$\Delta T(°C) \approx 0.68\Delta\sigma_y(MPa) \tag{2.18}$$

In addition, a correlation has been established to determine Δσy from a change in microhardness, ΔμH [16]

$$\Delta\sigma_y(MPa) \approx 3.3\Delta\mu H(DPH) \tag{2.19}$$

Thus, estimates of ΔT can be made through microhardness measurements.

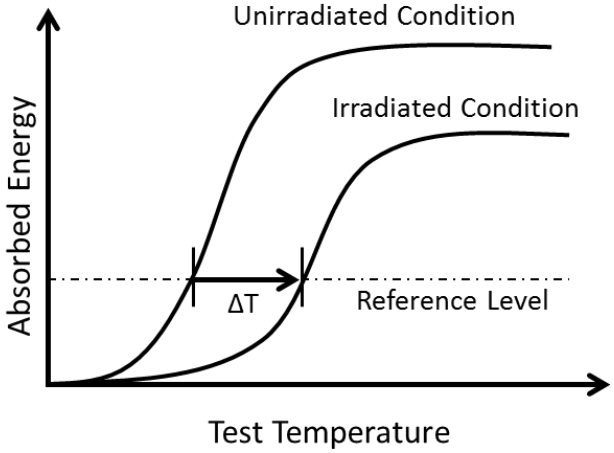

Figure 2.6. Schematic showing the use of Charpy impact testing to determine the ΔT for an irradiated specimen.

2.7 Embrittlement Prediction

The importance of RPV embrittlement was recognized by regulators and manufacturers and led to the creation of RPV surveillance programs. Charpy specimens were placed in capsules within the RPV, meaning that they are irradiated at a higher ϕ than the vessel itself. These specimens are periodically removed and tested and provide an early estimate of the embrittlement of the vessel itself. While the inclusion of these surveillance capsules showed a great deal of early foresight, plant specific surveillance data are often not sufficient to predict ΔT [1]. Instead, ΔT are predicted from a model created by fitting a large

collection of the surveillance data. This physically motivated model, called the Eason-Odette-Nanstad-Yamamoto model (EONY), is a function of ϕ, ϕt, T_{irr}, Cu, Ni, P and product form and is used by the NRC in the case of pressurized thermal shock [1, 2, 17]. While the EONY model was empirically calibrated to the surveillance database, it was motivated by the understanding of the physics leading to RPV embrittlement. Below is a very brief overview of the evolution of the understanding of RPV embrittlement.

It has long been established that the primary variable leading to RPV embrittlement at low to medium ϕt is Cu. The very low Cu solubility in Fe leads to a supersaturation of Cu and, when combined with RED, results in rapid formation of Cu-rich precipitates (CRPs) [18]. It is also well known that Mn and Ni become significantly enriched in the precipitates (CRPs), increasing the total f_v and the corresponding ΔT [6, 19–41]. Small angle neutron scattering and atom probe tomography experiments have shown that typical CRPs have a Cu rich core with a Mn-Ni-(Si) rich shell [28, 34, 39–46]. Lattice Monte Carlo simulations have shown that the formation of the shell driven by the high interfacial energy between the Fe and Cu [43, 47, 48]. While CRPs were correlated with the significant ΔT seen in Cu bearing steels, it was also established that steels containing no Cu harden as well, though at much lower amounts. This small amount of hardening was attributed to so called “stable matrix features” (SMFs), which are thought to be small solute-defect clusters with sizes below the resolution of most characterization techniques [2, 17].

This physical understanding led to the creation of the EONY model, which contains two features, SMFs and CRPs [2, 17]. An example prediction of the two terms from the

EONY model is shown in Figure 2.7 for a high Cu (0.4 wt.%) medium Ni (0.8 wt.%) steel. CRPs, shown in the blue line, are the dominant hardening feature and only occur in steels with > 0.07% Cu. The CRP hardening increases rapidly upon reactor startup, but saturates once the Cu has been depleted from the matrix. It is enhanced by higher alloy Ni and Mn contents because these elements enrich the CRPs resulting in an increase in f_v. The SMF term is included in both Cu-bearing and Cu-free steels and increases linearly with $\sqrt{(\phi t)}$. Thus, after the CRPs have reached saturation, the increase in ΔT with ϕt is predicted to be caused only be SMFs. While EONY ΔT predictions are very accurate at low to medium ϕt, corresponding to 30-50 years of reactor operation, it under-predicts test reactor data at high, extended life ϕt [3]. It has been hypothesized that this under-prediction is caused by formation of Mn-Ni-Si phases at high ϕt, which are not accounted for in the EONY model.

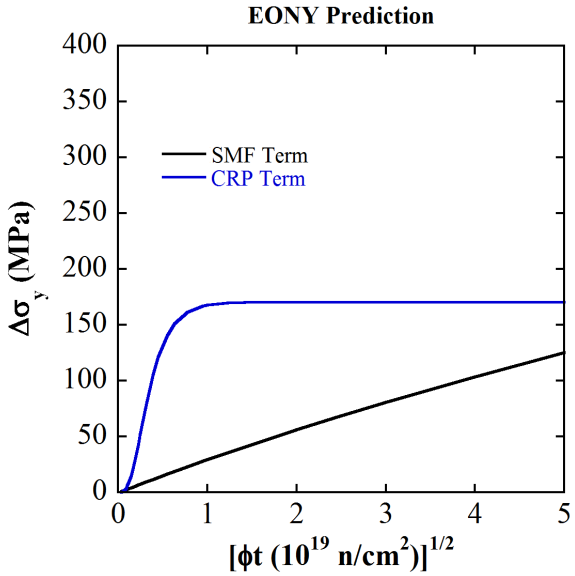

Figure 2.7. EONY prediction of $\Delta\sigma y$ vs $\sqrt{\phi t}$ for Cu-rich precipitates (CRP) and stable matrix features (SMF).

2.8 Late Blooming Phases

It was first predicted in the mid 1990's by Odette that Mn-Ni-(Si) phases could form even in Cu free steels, but that they would have much lower nucleation and/or growth rates than CRPs [19]. Therefore, they would not grow to large f_v, and cause significant amounts of hardening and embrittlement, until the later stages of reactor lifetimes [12, 19, 48]. This led to the name "Late Blooming Phases" (LBPs). There is a large debate in the literature regarding whether or not these Mn-Ni-Si precipitates are in fact "late blooming." A later part of this dissertation will show that these precipitates likely reach saturation at a fluence approximately 10-30 times higher than Cu-rich precipitates, which demonstrates that they do indeed "bloom" later than CRPs. As the focus of this dissertation is on the implications of the precipitates with regards to life extension, and not on what they should be called, they will be referred to as Mn-Ni-Si precipitates (MNSPs) for the rest of this dissertation.

There is now extensive experimental evidence showing the existence MNSPs in dilute Cu alloys from test reactor [3, 20, 37, 44, 49] and surveillance irradiations [29, 50, 51], as well as large MNSPs attached to CRPs in thermal ageing studies [39]. Thus, the existence of MNSPs is no longer in question, but there is substantial debate regarding their detailed character and formation mechanism. For example, a number of groups have argued that MNSPs are not thermodynamically stable phases, but are rather non-equilibrium solute clusters primarily formed by a radiation induced segregation (RIS) mechanism [52–55].

While a large number of papers refer to the clusters as induced by radiation, only a few have actually explored the formation mechanism using models [52–55] or experiments

[49, 56, 57]. One set of simulations suggests, using first principles calculations, that Mn-Ni clusters are not stable in Fe, but that the combination of a high flux of defects traveling toward sinks and a strong binding energy between solutes and defects results in a coupled flux of solutes to sinks [52, 53]. If the solute flux toward the sink is greater than the solute flux away from the sink, a local buildup of solutes will occur. Other simulations find that while small Mn-Ni clusters are not stable, they may be stable as larger clusters at very low temperatures or high solute contents, but likely will not be stable at typical T_{irr} or RPV solute contents [55]. According to a follow-up paper by this group, the presence of dislocation loops, which are caused by radiation damage, may reduce the solubility limit of the Mn and Ni enough to result in precipitation in RPV operating regimes [54].

In contrast, and as will be presented in the rest of this dissertation, recent experiments and models suggest the MNSPs are intermetallic phases, whose formation is accelerated due to RED. Equilibrium thermodynamic models predict large MNSP f_v at the low RPV operating temperatures ≈ 290°C [58]. Notably the predicted equilibrium f_v are in good agreement with data which will be presented in Chapter 5 [44]. Even more recent X-ray diffraction and scattering experiments confirm thermodynamic predictions that the MNSPs have the Γ_2 or G-phase intermetallic crystal structures [59], consistent with atom probe tomography precipitate composition measurements of the same steels [44].

Thus, this dissertation aims to better understand the character of MNSPs and elucidate their formation mechanism. While these details may seem of secondary importance to the overall issue of whether or not MNSPs will result in large ΔT at extended lifetimes,

robust prediction models will require a thorough understanding of the nature of MNSPs so as to better model and predict their formation and evolution with fluence. This dissertation aims to generate this understanding to better inform predictive models.

2.9 Flux Effects

While a detailed study on the effect of ϕ on precipitate formation, and the corresponding ΔT, is beyond the scope of this dissertation, it is important to briefly introduce these effects as almost all data presented in the following chapters come from high ϕ test reactors. Here, the main effect of concern with regards to increasing ϕ is a delay in precipitation and hardening to a higher ϕt. This is illustrated in Figure 2.8 for (a) irradiation hardening, represented by an equivalent change in yield stress ($\Delta\sigma_y$), and (b) precipitate volume fractions (f_v) in a high Cu, medium Ni split melt steel plotted as a function of the square root of fluence (ϕt) for low ϕ irradiations in the previous UCSB Irradiation Variables (IVAR) Program and high ϕ BR2 irradiations [29]. The delay in both precipitation and hardening with increasing ϕ is obvious.

This delay can be rationalized by considering the role ϕ plays with regards to the kinetics of precipitation. The average diffusion distance, d, of a solute atom under radiation is given by $d = \sqrt{(D^*t)}$. Higher ϕ irradiations lead to a higher D*, since more vacancies are created per unit time, but also simultaneously reduce the time is takes to reach a given ϕt. In flux regimes where defects are predominantly annihilated at sinks, an increase in ϕ directly results in an increase in the vacancy concentration and D*. Here, the total diffusion distance of atoms, given by $\sqrt{(D^*t)}$, is constant and there is no effect of increasing ϕ. At very high ϕ,

the steady state concentration of defects is so high that newly created defects quickly recombine with other defects in the matrix. Thus, an asymptotic limit on the vacancy concentration and the corresponding D* is reached. In this regime, called the defect recombination regime, an increase in ϕ with a constant D* results in a decrease in the average diffusion distance of atoms, and consequently the amount of precipitation. While this explanation is overly simplified, it is presented here simply to show that the precipitation hardening in these high ϕt test reactor irradiation conditions would likely occur at much lower ϕt under low ϕ power reactor conditions.

As was shown in Figure 2.8, it is misleading to compare $\Delta\sigma_y$ and f_v for steels irradiated at different ϕ, since higher ϕ irradiations delay precipitation to higher ϕt. Odette has proposed a model for correcting these flux variations to plot data on an equivalent scale by defining an effective fluence, ϕt_e, for a given reference flux, ϕ_r, given by

$$\phi t_e = \phi t \left(\frac{\phi_r}{\phi}\right)^p \tag{2.20}$$

where ϕt is the actual fluence, ϕ is the actual flux, ϕ_r is a reference flux and p is a scaling parameter that varies with ϕ [2, 60].

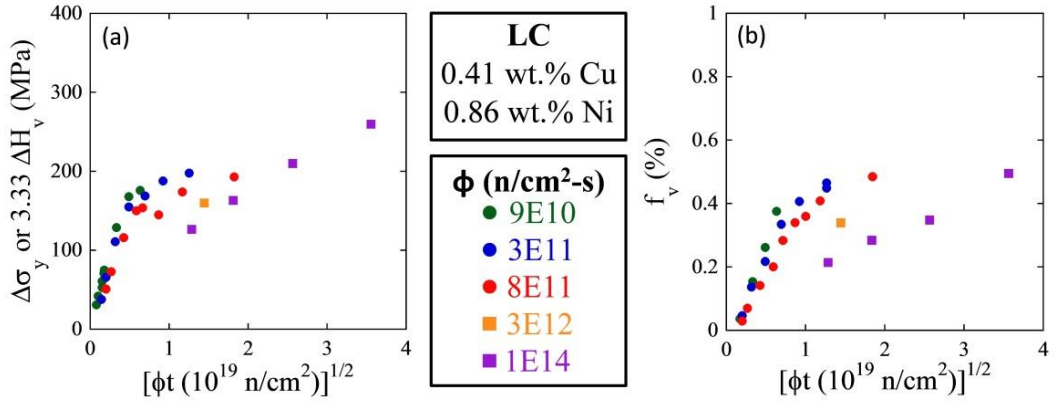

Figure 2.8. (a) $\Delta\sigma_y$ and (b) precipitate f_v for a high Cu, medium Ni steel from a series of test reactor irradiations over a wide range of ϕ.

It should be stressed that while this effective fluence model reduces very complex physics into a simple equation, the scaling parameter, p, varies based on the ϕ regime, such as thermal diffusion dominated, sink dominated or recombination dominated. The best fit p for high flux test irradiations has been found to be ≈ 0.2-0.25 [2]. An example flux correction can be seen in Figure 2.9 for a high Cu, medium Ni steel. The $\Delta\sigma_y$ as a function of ϕt, Figure 2.9a, can be seen to be delayed with increasing ϕ, but shows ≈ consistent trends at all ϕ when plotted in terms of ϕt_e, Figure 2.9b.

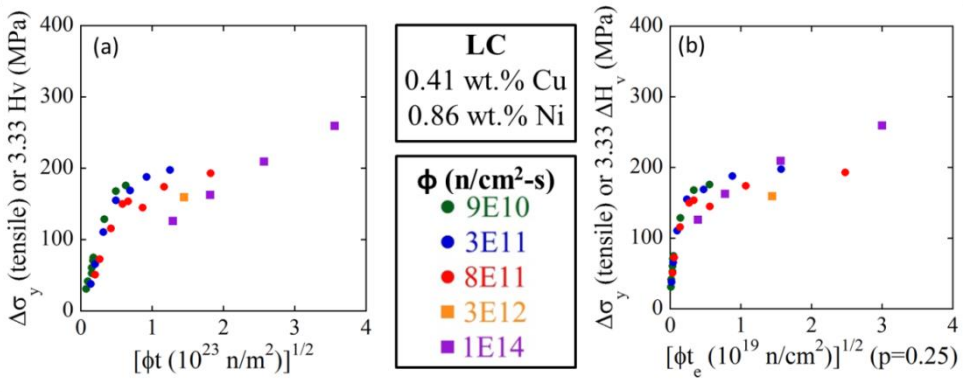

Figure 2.9. $\Delta\sigma_y$ for a high Cu, medium Ni steel as a function of a) ϕt and b) ϕt_e.

2.10 References

1. Odette GR and Lucas GE. "Embrittlement of nuclear reactor pressure vessels", *JOM* 2001;53:18–22.
2. Eason ED, Odette GR, Nanstad RK and Yamamoto T. "A physically based correlation of irradiation-induced transition temperature shifts for RPV steels," Oak Ridge National Lab, 2007; ORNL/TM-2006/530.
3. Odette GR and Nanstad RK. "Predictive reactor pressure vessel steel irradiation embrittlement models: Issues and opportunities", *JOM* 2009;61(7):17–23.
4. Knief RA. "Nuclear Engineering: Theory and Tecnology of Commercial Nuclear Power" American Nuclear Society, Inc., 2008.
5. "Light Water Reactor Sustainability Research and Development Program Plan Fiscal Year 2009 – 2013," Light Water Reactor Sustainability Program, DOE Office of Nuclear Energy, 2009; INL/MIS-08-14918 Rev. 2
6. Mader E. "Kinetics of irradiation embrittlement and the post-irradiation annealing of nuclear reactor pressure vessel steels" [PhD Thesis]. University of California, Santa Barbara, 1995.
7. Stoller RE, Odette GR and Wirth BD. "Primary damage formation in bcc iron", *J. Nucl. Mater.* 1997;251:49–60.
8. Stoller RE. "Molecular Dynamics Simulations of High Energy Cascades in Iron", *Mater. Res. Soc. Symp. Proc.* 1995;373:21–26.
9. Courtney TH. "Mechanical Behavior of Materials" Waveland Press, Inc, 2005.
10. Foreman AJE and Makin MJ. "Dislocation Movement Through Random Arrays of Obstacles", *Can. J. Phys.* 1967;45(2):511–517.
11. Russell KC and Brown L. "A dispersion strengthening model based on differing elastic moduli applied to the iron-copper system", *Acta Metall.* 1972;20(7):969–974.
12. Odette GR and Lucas GE. "Recent Progress in Understanding Reactor Pressure Vessel Steel Embrittlement", *Radiat. Eff. Defects Solids* 1998;144(1-4):189–231.
13. Hahn G. "The influence of microstructure on brittle fracture toughness", *Metall. Mater. Trans. A* 1984;15(June):947–959.
14. Miller MK and Russell KF. "APFIM characterization of a high phosphorus Russian RPV weld", *Appl. Surf. Sci.* 1996;94-95(1996):378–383.
15. Odette GR and He MY. "Cleavage toughness master curve model", *J. Nucl. Mater.* 2000;283-287:120–127.
16. He MY, Odette GR, Yamamoto T and Klingensmith D. "A universal relationship

between indentation hardness and flow stress", *J. Nucl. Mater.* 2007;367-370 A(SPEC. ISS.):556–560.

17. Eason ED, Odette GR, Nanstad RK and Yamamoto T. "A physically-based correlation of irradiation-induced transition temperature shifts for RPV steels", *J. Nucl. Mater.* 2013;433:240–254.

18. Odette GR. "On the dominant mechanism of irradiation embrittlement of reactor pressure vessel steels", *Scr. Metall.* 1983;17(10):1183–1188.

19. Odette GR. "Radiation Induced Microstructural Evolution in Reactor Pressure Vessel Steels", *Mater. Res. Soc. Symp. Proc.* 1995;373:137–148.

20. Miller MK, Chernobaeva AA, Shtrombakh YI, Russell KF, et al. "Evolution of the nanostructure of VVER-1000 RPV materials under neutron irradiation and post irradiation annealing", *J. Nucl. Mater.* 2009;385(3):615–622.

21. Miller MK, Russell KF, Sokolov MA and Nanstad RK. "APT characterization of irradiated high nickel RPV steels", *J. Nucl. Mater.* 2007;361:248–261.

22. Lucas GE, Odette GR and Chen HR. "Recent Advances in Understanding Radiation Hardening and Embrittlement Mechanisms in Pressure Vessel Steels", In: *Proceedings of the 2nd International Symposium on Environmental Degradation of Materials for Nuclear Power Systems-Water Reactors*, ANS; 1986. p. 345.

23. Odette GR and Lucas GE. "The Effect of Nickel on Radiation Hardening of Pressure Vessel Steels", In: *14th International Symposium on the Effects of Irradiation on Materials*, ASTM-STP-1046V2; 1989. p. 323.

24. Miller MK, Hetherington MG and Burke MG. "Atom Probe Field-Ion Microscopy A Technique for Microstructural Characterization of Irradiated Materials on the Atomic Scale", *Metall. Trans. A* 1989;20(A):2651–2661.

25. Miller MK and Burke MG. "An atom probe field ion microscopy study of neutron-irradiated pressure vessel steels", *J. Nucl. Mater.* 1992;195(1-2):68–82.

26. Auger P, Pareige P, Akamatsu M and Van Duysen J-C. "Microstructural characterization of atom clusters in irradiated pressure vessel steels and model alloys", *J. Nucl. Mater.* 1994;211(3):194–201.

27. Buswell JT, Phythian WJ, McElroy RJ, Dumbill S, et al. "Irradiation-induced microstructural changes, and hardening mechanisms, in model PWR reactor pressure vessel steels", *J. Nucl. Mater.* 1995;225:196–214.

28. Pareige P and Miller MK. "Characterization of neutron-induced copper-enriched clusters in pressure vessel steel weld: an APFIM study", *Appl. Surf. Sci.* 1996;94-95(1996):370–377.

29. Pareige P, Russell KF and Miller MK. "APFIM studies of the phase transformations in thermally aged ferritic FeCuNi alloys: comparison with aging under neutron

irradiation", *Appl. Surf. Sci.* 1996;94-95:362–369.

30. Wirth BD. "On the Character of the Nano-Scale Features in Reactor Pressure Vessel Steels" [PhD Thesis]. University of California, Santa Barbara, 1998.

31. Auger P, Pareige P, Welzel S and Van Duysen J-C. "Synthesis of atom probe experiments on irradiation-induced solute segregation in French ferritic pressure vessel steels", *J. Nucl. Mater.* 2000;280(3):331–344.

32. Carter RG, Soneda N, Dohi K, Hyde JM, et al. "Microstructural characterization of irradiation-induced Cu-enriched clusters in reactor pressure vessel steels", *J. Nucl. Mater.* 2001;298(3):211–224.

33. Hyde JM, Ellis D, English CA and Williams TJ. "Microstructural Evolution in High Nickel Submerged Arc Welds", In: *20th ASTM International Symposium on effects of radiation on nuclear materials*, ASTM STP 1405; 2001. p. 262.

34. Miller MK, Wirth BD and Odette GR. "Precipitation in neutron-irradiated Fe–Cu and Fe–Cu–Mn model alloys: a comparison of APT and SANS data", *Mater. Sci. Eng. A* 2003;353(1-2):133–139.

35. Pareige P, Radiguet B, Krummeich-Brangier R, Barbu a., et al. "Atomic-level observation with three-dimensional atom probe of the solute behaviour in neutron-, ion- or electron-irradiated ferritic alloys", *Philos. Mag.* 2005;85(4-7):429–441.

36. Zhang C and Enomoto M. "Study of the influence of alloying elements on Cu precipitation in steel by non-classical nucleation theory", *Acta Mater.* 2006;54(16):4183–4191.

37. Miller MK and Russell KF. "Embrittlement of RPV steels: An atom probe tomography perspective", *J. Nucl. Mater.* 2007;371(1-3):145–160.

38. Dohi K, Nishida K, Nomoto A, Soneda N, et al. "Three Dimensional Atom Probe Observations of Reactor Pressure Vessel Model Alloys Irradiated by Neutrons and Heavy Ions", *J. Japan Inst. Met.* 2010;74(3):191–198.

39. Styman PD, Hyde JM, Wilford K, Morley a., et al. "Precipitation in long term thermally aged high copper, high nickel model RPV steel welds", *Prog. Nucl. Energy* 2012;57:86–92.

40. Styman PD, Hyde JM, Wilford KB and Smith GDW. "Quantitative methods for the APT analysis of thermally aged RPV steels", *Ultramicroscopy* 2013;132:258–264.

41. Miller MK, Pareige P and Burke MG. "Understanding pressure vessel steels: an atom probe perspective", *Mater. Charact.* 2000;44(1-2):235–254.

42. Osamura K, Okuda H, Asano K, Furusaka M, et al. "SANS Study of Phase Decomposition in Fe-Cu Ally with Ni and Mn Addition", *ISIJ Int.* 1994;34(4):346–354.

43. Odette GR, Liu CL and Wirth BD. "On the Composition and Structure of Nanoprecipitates in Irradiated Pressure Vessel Steels", *Mater. Res. Soc. Symp. Proc.* 1997;439:457–469.

44. Wells PB, Yamamoto T, Miller B, Milot T, et al. "Evolution of manganese–nickel–silicon-dominated phases in highly irradiated reactor pressure vessel steels", *Acta Mater.* 2014;80:205–219.

45. Hyde JM, Sha G, Marquis E a., Morley a., et al. "A comparison of the structure of solute clusters formed during thermal ageing and irradiation", *Ultramicroscopy* 2011;111(6):664–671.

46. Styman PD, Hyde JM, Wilford K, Parfitt D, et al. "Characterisation of interfacial segregation to Cu-enriched precipitates in two thermally aged reactor pressure vessel steel welds", *Ultramicroscopy* 2015;No. In Press.

47. Liu CL, Odette GR, Wirth BD and Lucas GE. "A lattice Monte Carlo simulation of nanophase compositions and structures in irradiated pressure vessel Fe-Cu-Ni-Mn-Si steels", *Mater. Sci. Eng. A* 1997;238(1):202–209.

48. Odette GR and Wirth BD. "A computational microscopy study of nanostructural evolution in irradiated pressure vessel steels", *J. Nucl. Mater.* 1997;251:157–171.

49. Meslin E, Radiguet B, Pareige P, Toffolon C, et al. "Irradiation-Induced Solute Clustering in a Low Nickel FeMnNi Ferritic Alloy", *Exp. Mech.* 2011;51(9):1453–1458.

50. Auger P, Pareige P, Akamatsu M and Blavette D. "APFIM Investigation of Clustering in Neutron-Irradiated Fe-Cu Alloys and Pressure Vessel Steels", *J. Nucl. Mater.* 1995;225:225–230.

51. Miller MK, Powers KA, Nanstad RK and Efsing P. "Atom probe tomography characterizations of high nickel, low copper surveillance RPV welds irradiated to high fluences", *J. Nucl. Mater.* 2013;437(1-3):107–115.

52. Ngayam-Happy R, Becquart CS and Domain C. "First principle-based AKMC modelling of the formation and medium-term evolution of point defect and solute-rich clusters in a neutron irradiated complex Fe-CuMnNiSiP alloy representative of reactor pressure vessel steels", *J. Nucl. Mater.* 2013;440(1-3):143–152.

53. Ngayam-Happy R, Becquart CS, Domain C and Malerba L. "Formation and evolution of MnNi clusters in neutron irradiated dilute Fe alloys modelled by a first principle-based AKMC method", *J. Nucl. Mater.* 2012;426(1-3):198–207.

54. Bonny G, Terentyev D, Zhurkin EE and Malerba L. "Monte Carlo study of decorated dislocation loops in FeNiMnCu model alloys", *J. Nucl. Mater.* 2014;452(1-3):486–492.

55. Bonny G, Terentyev D, Bakaev a., Zhurkin EE, et al. "On the thermal stability of late

blooming phases in reactor pressure vessel steels: An atomistic study", *J. Nucl. Mater.* 2013;442(1-3):282–291.

56. Styman PD, Hyde JM, Parfitt D, Wilford K, et al. "Post-irradiation annealing of Ni–Mn–Si-enriched clusters in a neutron-irradiated RPV steel weld using Atom Probe Tomography", *J. Nucl. Mater.* 2015;459:127–134.

57. Meslin E, Radiguet B and Loyer-Prost M. "Radiation-induced precipitation in a ferritic model alloy: An experimental and theoretical study", *Acta Mater.* 2013;61(16):6246–6254.

58. Xiong W, Ke H, Wells PB, Barnard L, et al. "Thermodynamic models of low temperature Mn-Ni-Si precipitation in reactor pressure vessel steels", *MRS Commun.* 2014;4(3):101–105.

59. Sprouster DJ, Sinsheimer J, Dooryhee E, Ghose SK, et al. "Structural Characterization of Nanoscale Intermetallic Precipitates in Highly Neutron Irradiated Reactor Pressure Vessel Steels", *Scr. Mater.* 2016;113:18–22.

60. Odette GR, Yamamoto T and Klingensmith D. "On the effect of dose rate on irradiation hardening of RPV steels", *Philos. Mag.* 2005;85(4-7):779–797.

Chapter 3 Materials and Methods

This chapter describes the various alloys and irradiation conditions studied in later chapters, as well as the methods used to characterize the microstructural and mechanical property changes that occurred after irradiation. First, the compositions, heat treatments, and baseline properties of the model and surveillance steels are presented along with their subsequent irradiation conditions. Following this is a description of the post irradiation annealing experiments. An overview of the theory of atom probe tomography, with a focus on sample preparation and data reconstruction is presented. Finally, details on the microhardness tests, which were the primary method of measuring the mechanical property changes following irradiation, are presented.

3.1 Materials

3.1.1 Model Steels

A previous large scale irradiation, the Irradiation Variables Program (IVAR), performed in collaboration with UCSB in the Ford Nuclear Reactor at the University of Michigan investigated the effects of compositional variations on the embrittlement sensitivity of RPV steels [1]. The IVAR alloy matrix included a number of so-called split melt model steels (SMMS) that have systematic variations in their solute contents. The term split melt comes from the fact that a single melt was used to fabricate a number of alloys by

partitioning the melt and systematically adding certain solute elements to alter the alloy compositions. The use of SMMS was intended to provide precise variations in only the key compositional variables. The baseline composition, fabrication and heat treatments were selected to closely match those of in-service vessels. The resulting microstructure, ranging from tempered bainite to mixed tempered bainite-ferrite, as well as mechanical properties, with σ_y ranging from 400 to 525 MPa, are very similar to those found in typical A533B-type RPV steels [1]. The main difference between the IVAR SMMS matrix and its commercial counterpart is that the IVAR matrix intentionally includes steels with a much wider range of solute contents to better identify the role of different solutes. This SMMS matrix has subsequently been used in a number of other irradiations including those studied in this thesis.

Eight steels were investigated as part of this dissertation including specimens from two different larger matrices, the "Lavals", or L-alloys, and CM alloys. The L-alloys had the following baseline heat treatment: austenitize at 900° for 1 hr, air cool, temper at 664°C for 4 hr, air cool, stress relieve at 600°C fir 49 hr, and air cool. The CMs, of which only CM6 was investigated, had the following heat treatment: austenitize at 900°C for 30 min, salt quench to 450°C and hold for 10 min, temper at 660°C for 4 hr, air cool, stress relieve at 607°C for 24 hr, cool at 8°C/hr to 300°C and air cool. The steel compositions and mechanical properties are summarized in Table 3.1 and Table 3.2, respectively [1].

Table 3.1. Composition (wt.%) of the L and CM model steels.

Alloy	Cu	Ni	Mn	Mo	P	C	Si
LA	0.40	0.00	1.37	0.55	0.005	0.14	0.22
LB	0.40	0.18	1.35	0.55	0.005	0.14	0.22
LC	0.41	0.86	1.44	0.55	0.005	0.14	0.23
LD	0.38	1.25	1.38	0.55	0.005	0.19	0.23
LG	0.01	0.74	1.37	0.55	0.005	0.16	0.22
LH	0.11	0.74	1.39	0.55	0.005	0.16	0.24
LI	0.20	0.74	1.37	0.55	0.005	0.16	0.24
CM6	0.02	1.68	1.50	0.54	0.007	0.15	0.17

Table 3.2. Unirradiated σ_y, UTS and Microhardness for the model steels.

Alloy	σ_y (MPa)	+/-	UTS (MPa)	+/-	DPH	+/-
LA	469	6	583	6	197.9	2.9
LB	483	7	590	4	199.0	2.9
LC	491	4	609	4	209.2	3.6
LD	501	3	633	3	214.5	3.7
LG	493	7	609	6	202.1	3.3
LH	507	4	616	12	209.2	3.3
LI	512	10	628	6	204.8	2.7
CM6	456	10	555	10	201.7	3.4

3.1.2 Surveillance Material

Surveillance material from the Ringhals reactor in Sweden was also investigated. This sample was provided to UCSB by Oak Ridge National Laboratory. The composition of the steel, seen in Table 3.3, has a very similar composition to a UCSB steel, CM6. Comparisons between the irradiated microstructures of these two steels will be shown in subsequent chapters.

Table 3.3. Composition (wt.%) of the Ringhals surveillance steel.

Alloy	Cu	Ni	Mn	Mo	P	C	Si	Cr	Al
Ringhals - N	0.05	1.66	1.35	0.50	0.015	0.068	0.14	0.04	0.024

3.2 Irradiation Conditions

3.2.1 Neutron Irradiations

The UCSB Materials Reliability and Performance Group (MRPG), led by Professor G. Robert Odette, has a rich history of collaborating on large scale neutron irradiations in materials test reactors [1–4]. Data taken by previous students and staff of the MRPG from these various irradiation conditions was used in the model fitting in Chapter 8. The full UCSB irradiation conditions are summarized in appendix A.1. This dissertation built on these previous results by heavily characterizing three additional conditions from test reactors as well as a single surveillance program condition. The irradiation conditions from the test reactor and surveillance program are given in Table 3.4 and Table 3.5, respectively. As was explained in section 2.9, higher ϕ delays precipitation to a higher ϕt, so in order to compare results from different ϕ irradiations, an effective ϕt must be defined. Thus, Table 3.4 also includes ϕt_e for the three high ϕ test reactor irradiation conditions, using $\phi_{ref} = 3x10^{11}$ n/cm^2/s and $p = 0.25$.

Table 3.4. Primary irradiation conditions from materials test reactors.

Condition	Reactor	Neutron ϕ* (n/cm2/s)	Neutron ϕt* (n/cm2)	Neutron ϕt_e* (n/cm2)	Dose Rate (dpa/s)	Dose (dpa)	T_{irr} (°C)
G1	BR2	1.00E+14	1.3E+20	3.0E+19	1.5E-07	0.20	300
TU	BR2	3.00E+13	2.5E+20	7.9E+19	4.5E-08	0.38	290
ATR1	ATR	2.29E+14	1.1E+21	2.1E+20	3.4E-07	1.66	290
ATR2	ATR	3.6E+12	1.2E+20	6.5E+19	5.4E-09	0.18	290

*For neutron energies > 1 MeV

Table 3.5. Surveillance program irradiation conditions.

Condition	Reactor	Neutron Flux* (n/cm2/s)	Neutron Fluence* (n/cm2)	Dose Rate (dpa/s)	Dose (dpa)	T_{irr} (°C)
N	Ringhals	1.49E+11	6.03E+19	2.24E-10	0.09	284

*For neutron energies > 1 MeV

3.2.2 Charge Particle Irradiations

In addition to neutron irradiations, charged particle irradiations (CPI) were performed at two separate ion accelerators in Japan; The Dual-Beam Facility for Energy Science and Technology Facility (DuET) and the Heavy Fluence Irradiation Facility (HIT). While neutron irradiations create uniform damage through the thickness of the specimens, CPI cause damage in a localized region near the surface. An example damage profile for the DuET condition is given in Figure 3.1. To measure the microstructure changes at a constant dose, APT samples were all taken from a depth of ≈ 500 nm. The samples typically only run for 100-150 nm, resulting in a relatively constant dose over the length of the tip. Table 3.6 gives the ion energy, dose, dose rate and irradiation temperature for the various CPI at a depth of 500 nm.

Table 3.6. Summary of CPI conditions at a depth of 500 nm.

Condition	Facility	Particle	Ion Energy (MeV)	Dose Rate (dpa/s)	Dose (dpa)	T_{irr} (°C)
DuET	DuET	Fe^{3+}	6.4 MeV	3.40E-05	0.2	290
TE-6	HIT	Fe^{3+}	2.8 MeV	1.00E-04	2.3	330
TE-8	HIT	Fe^{3+}	2.8 MeV	1.00E-04	2.5	400

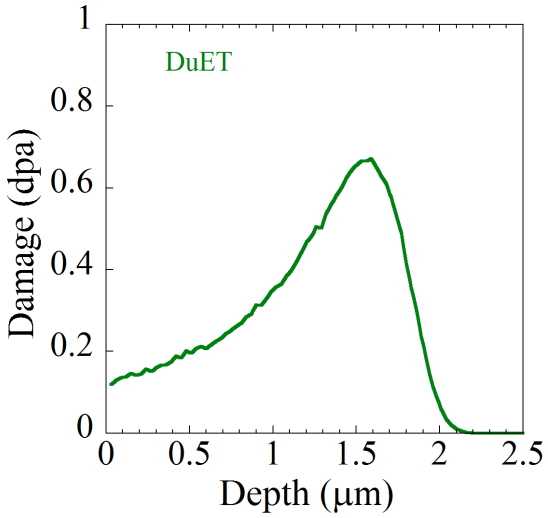

Figure 3.1. Damage profile for the DuET CPI condition.

3.3 Post Irradiation Annealing

Post irradiation annealing experiments were performed on the neutron irradiated steels from the ATR1 irradiation condition. These anneals are split into two types of experiments, long time isothermal anneals and 1-week isochronal anneals. Isothermal anneals were designed to investigate the precipitate dissolution/coarsening for various times at constant temperature. 1 week isochronal anneals were used to measure hardening after a series of sequential anneals at steadily increasing temperatures.

3.3.1 Isothermal Annealing

It should be stressed that steels become activated following neutron irradiation. Thus, while ideally both APT and microhardness measurements would have been made for all conditions, this was not feasible, due to time constraints and the challenges associated with testing radioactive specimens. The isothermal experiments, designed to measure precipitate dissolution/coarsening, used very small 1.5 mm diameter x 0.5 mm thick discs that were punched from the larger irradiated 8 mm discs. These low activities made the sample shipments to the Center for Advanced Energy Studies (CAES) at the Idaho National Lab much easier. Unfortunately, the small size also precluded microhardness measurements from being taken. Since multiple steels at various temperatures were investigated, and because these samples needed to be shipped back and forth numerous times to CAES, the specimens were mounted with a metallic adhesive called Durabond 950. This adhesive is both electrically and thermally conductive. Due to time constraints, only 3 (LD, LG and CM6) of the 8 steels from Table 3.1 were investigated. An example stub is shown in Figure 3.2. After mounting the specimens, they were encapsulated in quartz tube which was then evacuated, backfilled with Argon, and sealed prior to annealing in a tube furnace.

As will be explained in Chapter 6, a relatively low temperature of 425°C was selected to investigate the phase stability of the precipitates which formed under irradiation. One particular challenge with annealing at this temperature is the very slow kinetics. Thus, measuring the precipitate changes at multiple times is necessary to separate kinetic from thermodynamic effects. The selected annealing times, seen in Table 3.7, were arbitrarily

selected as the steels were annealed for as long as possible before scheduled instrument time at CAES, which was sporadically scheduled.

Figure 3.2. Three specimens (LD, LG and CM6) mounted on an SEM stub with Durabond adhesive prior to annealing.

Table 3.7. Isothermal Annealing matrix for the ATR1 materials.

Steels	Temperature (°C)	Annealing Time (khrs)
LD, LG, CM6	425	0.17, 1.17, 2.85, 4.80

3.3.2 Isochronal Annealing

The ATR1 materials were also subjected to a series of sequential 1-week anneals at temperatures from 350-550°C. Vickers microhardness measurements were taken after each annealing temperature. The goal of this experiment was to investigate whether hardening features besides precipitates are present in the irradiated steels and, if so, to determine the

hardening contribution from the various hardening features. 3 mm discs were punched and press fit into a holder that was tightened with screws to prevent the specimens from coming out during the annealing or polishing. The typical hardness of the steels prior to irradiation is on the order of 200 dph. This corresponds to an indent diameter of ≈ 70 μm using a load of 500g. The indents need to be spaced ≥ 3 times the indent diagonal. A pattern, from Mader [3] and shown in Figure 3.3, was used to maximize the number of indents on a 3 mm disc with indents spaced 0.25 mm apart and no closer than 0.5 mm from the edge of the sample, which likely was plastically deformed during punching. Annealing was done for 1 week each at temperatures of 350°C, 375°C, 400°C, 425°C, 450°C and 550°C. The hardness after the 550°C recovery anneal was used as the baseline hardness when calculating the change in hardness due to irradiation.

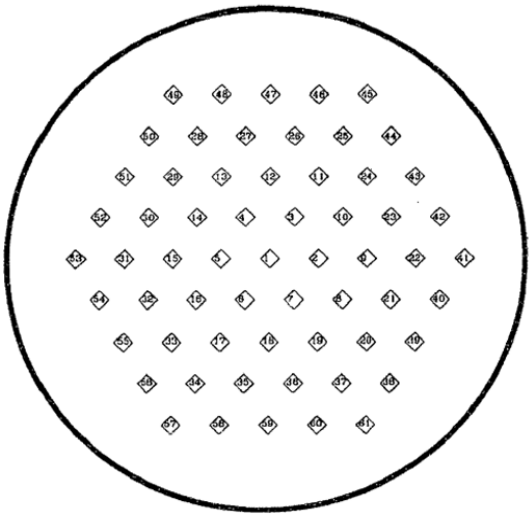

Figure 3.3. Microhardness indent pattern used for 3 mm discs.

3.4 Atom Probe Tomography

Here, the theory behind Atom probe Tomography (APT) will be presented, with a larger discussion on actual testing and data analysis discussed in Chapter 4. APT is a destructive microscopy technique that has the ability to measure compositional fluctuations on the nano-scale. The precipitates that form under irradiation in RPV steels have a radius on the order of 1-3 nm, beyond the resolution of most characterization techniques except APT, which is the primary method used here to measure the precipitate size, number density, volume fraction and composition.

Before testing, the material of interest is either electropolished or ion milled to a very sharp needle on the order of 100 nm in diameter. The tip is then placed inside a local electrode atom probe (LEAP) and subjected to a high voltage, which, due to the small tip radius, induces a high electric field around the specimen. If this electric field is large enough, then atoms will field evaporate from the tip and accelerate through the electric field until they hit a position sensitive detector. The mass-to-charge-state ratio for a given ion, which is used to determine the ions elemental identity, is determined by measuring the time it takes the atom to travel from the tip to the detector. The original tip location of all evaporated ions is reconstructed using an algorithm that incorporates both the ions' hit position on the detector and the sequence of ion evaporations. The resulting dataset gives the location of each atom that was emitted from the tip and its elemental species, which is used to measure the clustering present in the alloy. Each step of the process will now be presented in more detail.

3.4.1 Field Evaporation

If a material is subjected to a high enough electric field, atoms can be removed from the surface through a process called field evaporation. This process is the combination of ionization and desorption of the atom from the sample surface. The high applied electric field polarizes atoms on the tip surface and, at sufficient fields, will remove atoms from the tip surface as an electron from the evaporating atom is concurrently pulled from the atom into the tip. This created ion is then accelerated through the electric field away from the tip surface [5, 6].

Two basic theories, the image hump and charge exchange models, have been presented regarding the sequence of events leading to field evaporation. Both theories are based on the premise that ionic states become more stable than atomic states under an electric field at increasing distances away from a sample surface. Close to the surface, there is an energy barrier (Q), which is reduced with increasing electric field, between the neutral and ionic states that must be overcome by thermal activation in order to cause field evaporation.

At high enough electric field, the energy barrier for field evaporation can be reduced to zero [6]. This electric field is often referred to as the evaporation field and is different for each element and even each charge state for a given element. The evaporation field, F_e, for an element in the nth charge state can be written as

$$F_e = \frac{4\pi\varepsilon_0}{n^3 e^3}\left(\Lambda + \sum_n I_n - n\phi_e\right)^2 \tag{3.1}$$

where ε_0 is the dielectric permittivity of the vacuum, e is the elementary charge, Λ is the sublimation energy, I_n is the nth ionization energy and ϕ_e is the work function of the emitting surface [5, 6]. From this equation, the evaporation field at 0K can be calculated for every elemental charge state. Evaporation fields for typical elements in RPV steels are given in Table 3.8 [5].

Table 3.8. Evaporation field (V/nm) for various charge states of select metals [5].

Metal	F_1	F_2	F_3	F_4
Fe	42	33	54	100
Cr	27	29	51	86
Mo	65	41	51	82
Cu	30	43	77	-
Mn	30	30	60	-
Ni	35	36	65	-
Si	45	33	60	-

3.4.2 Sample Preparation

The electric field around the tip is indirectly related to the tip radius, so a very sharp needle is required before the experiment can begin. Historically, needles were prepared using electropolishing. In the case of this dissertation, electropolishing was very rarely used because it requires the experimenter to be in close proximity to the radioactive samples. In addition, electropolishing results in significant contamination of both the acidic solution and cathode used in the process. An extra consideration for ion irradiated specimens is that the APT needle must be fabricated so that it begins ≈ 500 nm from the sample surface. It would be difficult, if not impossible, to create an electropolished tip that contained the irradiated region in the end of the tip. Thus, all samples presented here were prepared using a focused ion beam.

Focused ion beam (FIB) sample preparation methods allow for a very precise control over the final tip shape as well as the ability to select samples from a specific location, such as a grain boundary. The main drawback with this method is the radiation damage induced in the specimen by the high energy Ga beam. Special care is taken to minimize this damage by coating the sample surface with platinum as well as doing final clean up steps with low energy Ga ions to remove any regions which may be heavily damaged by the higher energy ions used in the initial milling steps.

To fabricate tips, a layer of Pt is deposited on the region of interest, as is seen in Figure 3.4. This Pt layer protects the sample surface from the high energy Ga beam used in the milling. Next, the Ga beam is used to cut trenches on both sides of the Pt layer at angles of 30° with respect to the sample surface. After trenches have been cut on both sides of the Pt, one end is cut off and welded to a probe which is controlled by the FIB instrument. Finally, the other end of the specimen is cut off and the liftout is removed from the material, as seen in Figure 3.5.

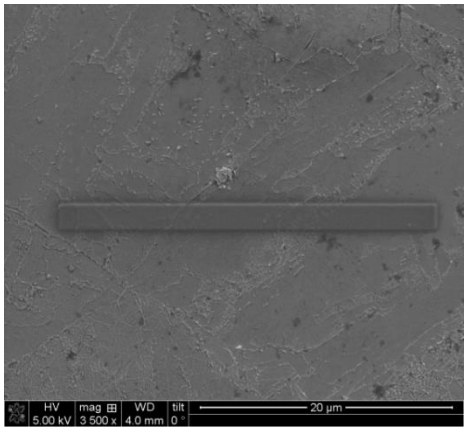

Figure 3.4. Pt weld on surface of specimen.

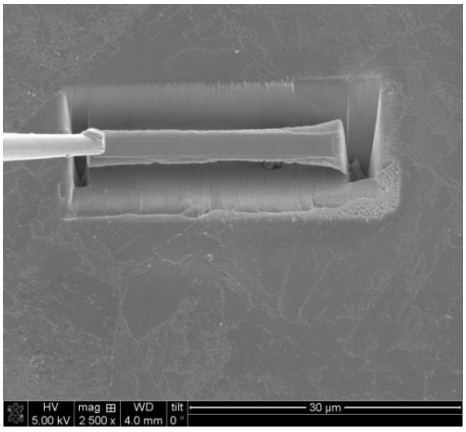

Figure 3.5. Liftout welded to probe.

After the liftout has been made, it is then welded onto a micro-tip coupon containing either 22 or 36 tips. These coupons are provided by CAMECA, the makers of the commercial LEAP instruments, which were used in this dissertation. An image of welded material prior to sharpening is shown in Figure 3.6.

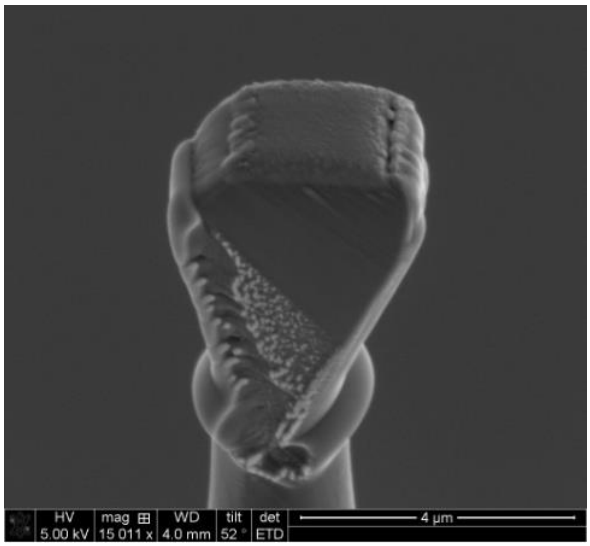

Figure 3.6. Welded material mounted on post prior to sharpening.

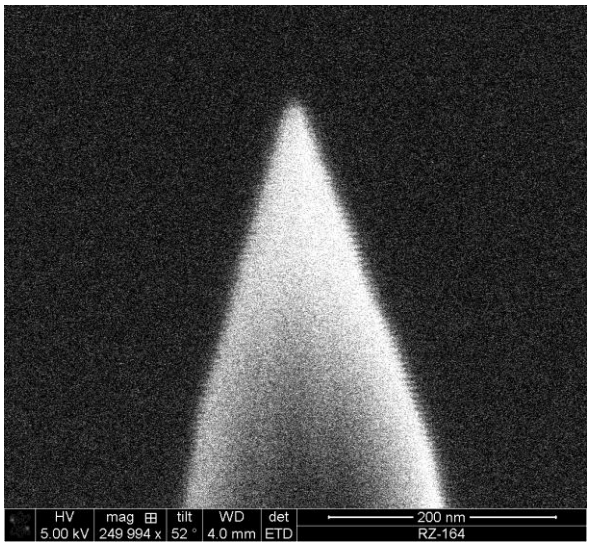

Figure 3.7. Final sharpened APT tip.

Once the material has been welded to the micro-tip, the sample is tilted to 52° to orient the ion beam normal to the sample surface. A circular cutting pattern with an outer diameter larger than the sample and an inner diameter slightly less than the sample width is used to shape the material into a cylinder with the 30 kV ion beam. After the sides of the cylinder have been smoothed, the pattern is stopped and a pattern with smaller inner and outer diameters is used to continue thinning the specimen. These steps are repeated until the diameter of the specimen at the end of the tip is ≈ 200-300 nm. At this point the ion beam voltage is reduced to 5 kV where the clean-up steps are performed. While the tip diameter at

this step is larger than that needed for APT experiments, it typically becomes sharper during the cleaning process. The 5 kV beam is used to mill away ≈ 200-500 nm of material and is stopped once the tip appears to have an end diameter of ≈ 50-100. Following this step, a 2 kV beam is used to mill away ≈ 50-100 nm of additional material. While this step is optional, it was observed to cause a significant reduction in the measured Ga within the tip. If the tip does not appear sharp enough following the 5 kV clean-up, another sharpening step is performed using the 16 kV beam with a pattern with a 1.5 um outer diameter and 100-150 nm inner diameter. This results in a very sharp tip, though if the pattern is run for too long, the probability of tip fracture significantly increases. A final sharpened tip is seen in Figure 3.7.

Tips that are very sharp run at low voltages but are also more prone to fracture because they cannot withstand the stresses induced in the tip by the electric field. On the other hand, while blunt tips can withstand the higher voltages, they require higher voltages for field evaporation. Therefore there is a tradeoff between very sharp tips, which may fracture prematurely, and blunt tips, which may reach the instruments voltage limit before sufficient data has been collected

3.4.3 Instrumentation and Data Collection

The goal of APT is to reconstruct the location of each atom from within a sample and assign the correct element to that atom. While the reconstruction procedure itself will be outlined in section 3.4.5, this section will describe the instrumentation needed to collect the data required to complete a reconstruction, namely the time-of-flight for an ion, the position

it hit on the detector, and the order in which the ions evaporated. Other pieces of information also collected include the total voltage during the time of evaporation and the number of other ions that also came off during that pulse.

After the samples are prepared, they are placed in an ultrahigh vacuum on the order of 5E-11 torr and cooled to cryogenic temperatures (30-60K). A high vacuum is necessary to reduce the probability of residual chamber gas ionization, which increases the background in the mass spectrum. The cryogenic temperatures reduce the diffusion of atoms along the tip, which, if significant, degrades the spatial resolution of the sample.

Field evaporation requires overcoming an energy barrier between the atomic and ionic states of atoms on the specimen surface. This can be accomplished by reducing the energy barrier, i.e. applying a higher electric field, enough that the thermal vibrations of atoms are sufficient to result in field evaporation, or by increasing the energy of atoms enough to overcome the barrier, i.e. increasing the temperature of the specimen. Thus, there are two modes in operating an atom probe; voltage and laser mode.

After the specimen is coarsely aligned with the local electrode using microscopes inside the analysis chamber, the standing voltage is increased until atoms begin evaporating on voltage or laser pulses. The standing voltage should be low enough that no evaporation of atoms takes place between pulses. These concepts are illustrated in Figure 3.8. Here, the base field and temperature result in a condition below the line defining that necessary for field evaporation. Above this line, field evaporation will occur. The magnitude of the voltage pulse is measured as a percentage of the standing voltage and is called the pulse fraction,

which is constant for an experiment. For example, a pulse fraction of 20% would result in pulses of 1000 V when the standing voltage is set at 5000 V. Laser pulses on the other hand are at a constant energy throughout the entire experiment.

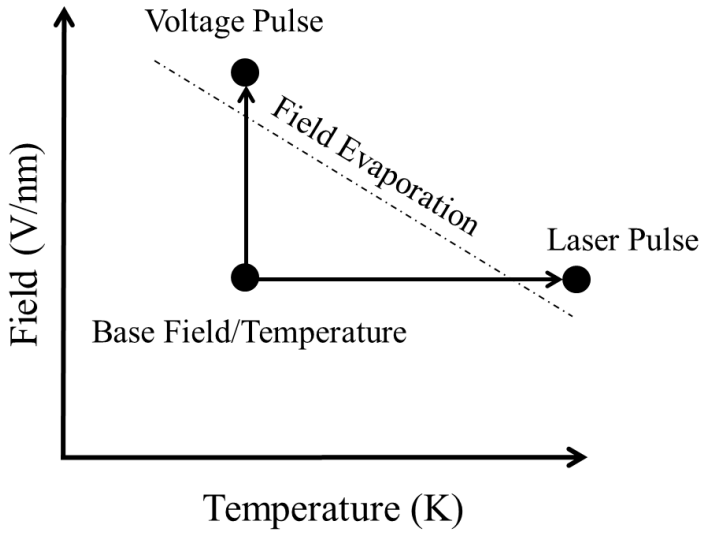

Figure 3.8. Electric field plotted vs temperature showing the required field for evaporation and the two ways to reach this field; voltage or laser pulsing.

Pulsing is a fundamental process in collecting data, because it is the starting point for measuring the time-of-flight (t_{flight}) of an ion. The time is measured between the application of the voltage (or laser) pulse and the ion signal on the detector, meaning that if an ion evaporates in-between pulses, the time-of-flight cannot be accurately measured. In addition, the detector's ability to accurately detect the time and location of a hit degrades with an increasing number of hits from a single voltage pulse. Thus, the goal is to have at most 1 ion evaporate per pulse. The detection rate is the percentage of pulses where an ion is detected. This number is typically set at 1% or less because anything higher than this results in a large

number of pulses with multiple events. Since less than 1% of pulses results in detection of an ion, a high frequency of pulses is used to collect data at a sufficient rate. Typical voltage pulsing frequencies are on the order of 200 kHz, which results in the collection of 3.6 million ions/hr at a detection rate of 0.5%.

A delay line detector (DLD) is used to measure both the time at which at atom hits the detector as well as its location. The detection of a single ion would require extremely sensitive detectors; so instead, the signal of an ion is amplified prior to detection using a micro-channel plate (MCP). When ions collide with the MCP, they generate a cloud of electrons that is more easily detected by the DLD. When the electron cloud hits the detector, a signal is sent to both ends of the three different delay lines. The signal propagates down the wires until it is detected at the end of the lines. The time of impact and X_D and Y_D hit positions on the detector can then be calculated. Once the time of flight, detector hit positions (X_D, Y_D), and sequence of atom hits have been measured, the reconstruction can be performed [6].

3.4.4 Determining the Mass-to-Charge Ratio

After an ion is evaporated from the tip surface, it is accelerated through the applied electric field. The electrical potential energy it acquires through this acceleration can be written as $E_p = neV$ where *ne* is the charge of the ion and V is the voltage applied when the ion is evaporated. Assuming that the ion is accelerated to its final velocity over a very short distance compared to the total distance between the tip surface and detector (L), the velocity

of the atom can be written as $v = \frac{L}{t_{flight}}$. Thus, the kinetic energy of the incoming ion can be written as $E_k = \frac{1}{2}mv^2 = \frac{1}{2}m\left(\frac{L}{t_{flight}}\right)^2$ [6]. The kinetic and potential energy equations can be set equal to each other and rearranged to give the mass-to-charge ratio (m/n) as:

$$\frac{m}{n} = M \approx 2eV\left(\frac{t_{flight}}{L}\right)^2 \tag{3.2}$$

The mass-to-charge ratio is then used to determine the isotope of a given ion. For example, ^{56}Fe evaporating in the +2 charge state will have a mass-to-charge ratio of 28. It should be noted that there are a number of overlapping isotopes and even overlapping m/n of different isotopes, such as $^{14}N_2^{+2}$ and $^{28}Si^{+2}$ which both have an m/n of 14. While it is not possible to know with 100% certainty the true identity of a single ion that falls within overlapping m/n, it is possible to deconvolute these overlaps to determine the average composition. These corrections will be discussed in section 4.2.1.

3.4.5 Reconstructing the Atom Coordinates

The basic premise of an APT reconstruction is to use the location of the hit on the detector to reverse project the ion back into a theoretical tip surface. The magnification, *M*, can be defined as

$$M = \frac{X_D}{x} \tag{3.3}$$

$$M = \frac{Y_D}{y} \tag{3.4}$$

where X_D and Y_D are the positions the ion hit the detector and x and y are the original positions of the ion from the tip [6, 7]. The ion is modeled as traveling linearly to the detector from a projection point within the tip. This projection point is at a distance of ξR from the tip surface, where ξ is known as the image compression factor and R is the tip radius. M can alternatively be defined using ξ, R, and the tip-to-detector distance, L, as [6, 7]

$$M = \frac{L + \xi R}{\xi R} \tag{3.5}$$

These concepts are demonstrated in Figure 3.9. Since the distance ξR is negligible compared to L (i.e. ≈ 50 nm vs ≈ 50 mm), $\xi R + L$ can be approximated as L.

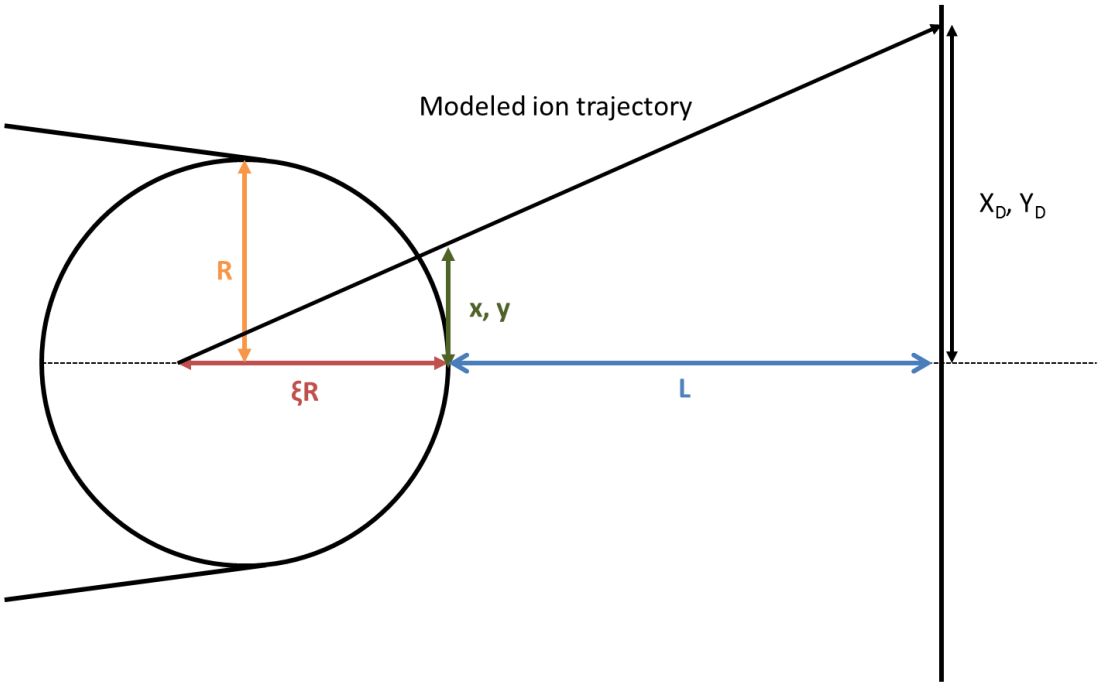

Figure 3.9. Schematic showing the projection of the ion from a point at a distance of ξR from the tip surface.

Setting equation (3.5) equal to equations (3.4) and (3.5) gives the equation used to calculate the *x* and *y* positions of an ion within the tip as

$$x = \frac{X_D \xi R}{L} \tag{3.6}$$

$$y = \frac{Y_D \xi R}{L} \tag{3.7}$$

The z position within the tip is determined through the sequence of ion evaporations and contains two parts *dz* and *dz'* [6, 7]. *dz* is derived from the concept that after N number of ions with an atomic volume Ω have evaporated, a total volume NΩ will have been removed from the tip. The volume of a single atom is divided by the analyzed surface area of the tip, A_s, to give the length, *dz*, of tip that was been evaporated. This length is then subtracted from the theoretical tip surface where a new theoretical tip surface is placed. Because not every single atom is detected, the volume must be corrected for the detection efficiency of the instrument, η, which is ≈ 37% in the case of the reflection equipped LEAPs used in this dissertation. For example, if only 1 of 3 ions is detected, then after 1 ion evaporates, the volume of 3 ions must be incremented. The increment, *dz*, can be written as

$$dz = \frac{\Omega}{\eta A_S} \tag{3.8}$$

To calculate *dz*, A_s must be accurately known. Some atoms evaporate at such large angles that they are outside the APT field of view. This is illustrated in Figure 3.10. Thus, A_s is not the actual surface area of the tip, but the analyzed surface area. The analyzed surface area can be calculated using a reverse projection from the detector to a plane normal to the specimen apex [6, 7].

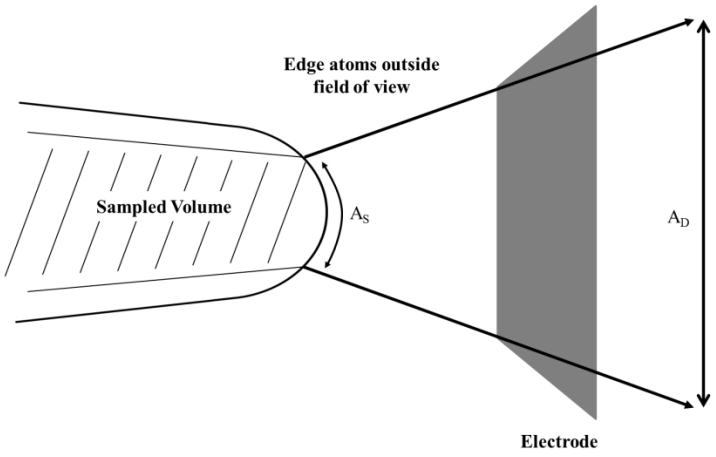

Figure 3.10. Schematic showing that ions on the edge of the APT needle have trajectories such that they do not hit the detector. The center dashed portion of the tip is the sampled region.

The surface area can be rewritten as

$$A_S = \frac{A_D}{M^2} \tag{3.9}$$

where A_D is the surface area of the detector. Substituting the modified version of equation (3.5) in for *M*, and equation (3.9) into equation (3.8) gives [6, 7]

$$dz = \frac{\Omega L^2}{\eta A_D \xi^2 R^2} \tag{3.10}$$

Following the evaporation of each ion, *dz* is subtracted from the theoretical tip surface. A correction is made to the *dz* coordinate using the curvature of the tip. This calculation is done using simple geometry and can be written as

$$dz' = R\left(1 - \sqrt{\frac{x^2 + y^2}{R^2}}\right) \tag{3.11}$$

Thus, the z-coordinate for each ion, schematically shown in Figure 3.11, can be calculated as

$$z = \left(\sum dz\right) + dz' \tag{3.12}$$

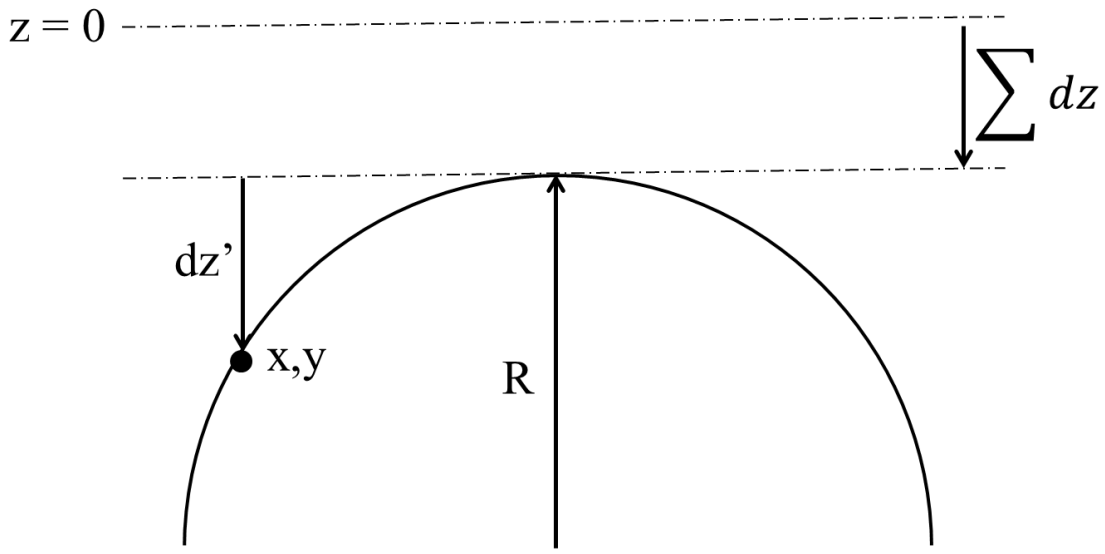

Figure 3.11. Schematic of the calculation of the z ion position.

Thus, a completed APT reconstruction will determine the coordinates and m/n for each evaporated ion.

3.4.6 Atom Probe Artifacts

APT results must be interpreted cautiously in the face of a number of potential artifacts of the technique. While some artifacts can be minimized through the use of carefully selected run conditions, others are difficult to fully quantify and are the subject of intense research interest. Here two main artifacts will be discussed, the preferential evaporation of certain species in between atom pulses, and the variation in location magnification in the

region of the tip near and including precipitates, which results in the incorrect reconstruction of the position of atoms.

3.4.6.1 Preferential Evaporation

Preferential evaporation refers to the evaporation of certain atom species in between either the laser or voltage pulses [6]. As was explained in section 3.4.4, accurately measuring an ions time-of-flight requires knowledge of the moment an ion is evaporated from the sample surface. The only way to accurately know this is to ensure that ions only evaporate during a voltage/laser pulse. If ions evaporate in between pulses, the software still assumes that the detected ion evaporated on the pulse, resulting in an incorrect time-of-flight and corresponding m/n. Thus, ions which evaporate in between pulses appear in the background on the mass spectrum and are not ranged as the proper element.

Because different elements evaporate at different fields, it may be possible that a specific element, and only that element, evaporates in between pulses, resulting in an undercounting of that element. In the case of RPV steels, it has been shown that for simple Fe-Cu model alloys, the apparent Cu in the matrix is reduced with increasing specimen temperature or with reduced voltage pulse fractions [8–11]. This is thought to be caused by preferential evaporation of the Cu, which results in an incorrect time of flight measurement and thus the atom's mass to charge ratio appears in the background. Because the evaporation field for Cu (30 V/nm) is much less than for Fe (33 V/nm), this results in Cu atoms being more easily removed from the surface. If the standing electric field is above that required for field evaporation of Cu, illustrated in Figure 3.12, then it will constantly evaporate. This

preferential evaporation can be mitigated by using low specimen temperatures or large pulse fractions. Hyde et. al. showed that using a specimen temperature of ≤ 50K and a pulse fraction of ≥ 20% prevents the preferential evaporation of Cu [10]. Thus, all APT samples in this thesis were run in voltage mode at 50K and a pulse fraction of 20%.

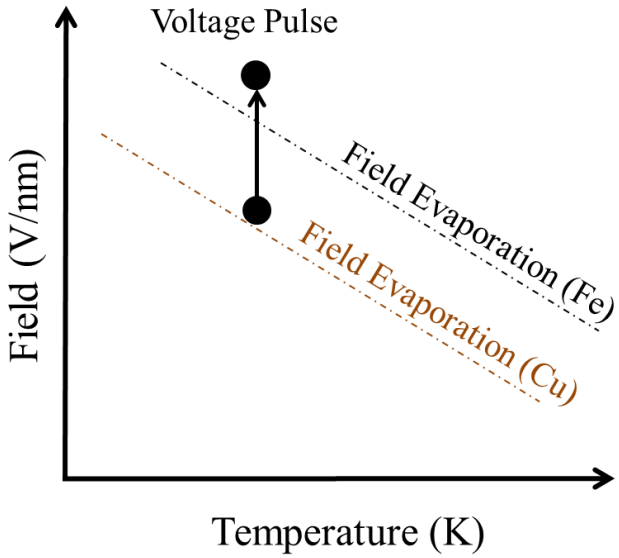

Figure 3.12. Illustration of the concept of preferential evaporation. If the base field/temperature are incorrectly selected, evaporation of certain species, in this case Cu, can occur in between pulses.

3.4.6.2 Local Magnification Effects

The reconstruction procedure, outlined above, uses a set of assumptions about the trajectory of the ions to infer the ion's original position on the tip (x and y) from its measured hit position on the detector (X_D and Y_D). Any deviations from this ideal flight path, or what is essentially a change in the local magnification factor for the ion, result in an incorrect reconstruction of the ion's original coordinates. One such example of local magnification effects can be clearly seen by observing the hit density map of an evaporating tip, as is seen

in Figure 3.13. Here, the number of ions hitting a particular region on the detector is represented through a so called hit density map, where red regions experienced a large number of hits, and blue regions experienced a low density. During evaporation, facets develop on the tip surface, usually around low index poles, caused by the specific work function of various crystallographic directions [6]. The low density region in Figure 3.13 represents the 110 pole. These facets locally change the magnification of the ions during evaporation, resulting in the appearance of a low density region on the detector.

While local magnification effects relating to the crystallography of the tip do not present significant issues, other causes of local magnification changes complicate the interpretation of results. For example, lower evaporation fields, associated with more weakly bound precipitate atoms, result in flattening, or even dimpling, of the region in the vicinity of the feature. This, in turn, produces tip topology-induced ion trajectory aberrations and changes in the local magnification factors. In this case, matrix atoms are focused into the precipitate region of the detector along with solute atoms [12]. Such trajectory aberrations result in errors in the apparent composition of precipitates, and are signaled by higher than physical local atom densities. Coupled with assumptions used in the reconstruction algorithms, in some cases spatially inhomogeneous evaporation sequences may also lead to distortion of the shapes of reconstructed precipitates (flattening or elongation), as well as features with chemically segregated tops and/or bottoms, when there are no physical tops and bottoms along the APT analysis z-direction [12–14].

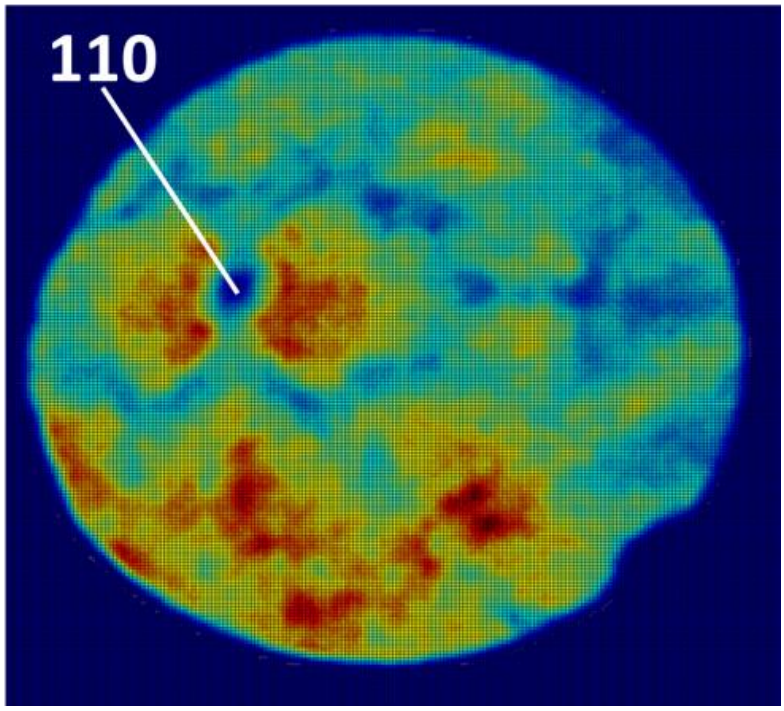

Figure 3.13. Hit map showing low density region that indicates location of the {110} pole.

One such example of the evidence for these trajectory aberrations is given in Figure 3.14 for a Cu-Mn-Ni-Si precipitate evaporating in an Fe matrix. The reconstruction algorithm assumes that ion hits in the same location on the detector come from essentially the same x-y coordinates in the tip. In this case, there are two visible regions showing a high solute hit density, corresponding to the evaporation of a precipitate (Figure 3.14 right). Based on conservation of volume, a region of the tip enriched in solutes must be depleted in Fe. The hit map for Fe not only doesn't show a decrease in the Fe hit density, but in fact shows a higher hit density than the surrounding region (Figure 3.14 left).

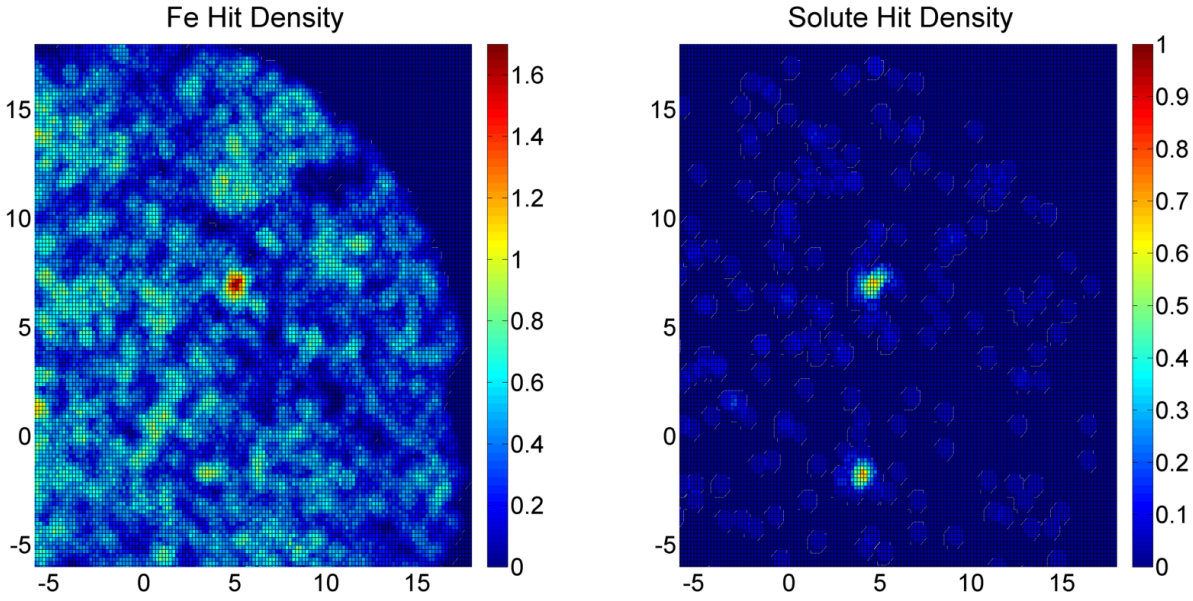

Figure 3.14. Hit map showing hit density of Fe ions (left) and Cu-Mn-Ni-Si ions (right) in irradiated RPV steel.

The result of the high hit densities in the precipitate region on the detector is higher than physical atom densities in the reconstruction. An example line profile is shown in Figure 3.15 where the solute, Fe and total atom densities as a function of distance along a profile are plotted. These issues have long been recognized, but have not yet been resolved. However, they are of current intense interest and recent research is leading to better understanding of APT artifacts, for example, by combining electrostatic simulations of field emission from a tip containing small features with a range of evaporation fields, with experimental observations of spatial-temporal correlations in atom emission sequence [14]. The most relevant conclusion is that excess Fe in precipitates found by the reconstruction software (IVAS) is almost certainly largely an APT artifact, if only because the atom densities in the precipitates are 2-3 times higher than is physical. This conclusion is reinforced by that fact

that high Fe content is inconsistent both with other techniques, such as small angle neutron scattering (SANS), as only one of several examples, as well as with thermodynamic considerations [15, 16]. The high Fe content in the MNS precipitates, which are the focus of this study, is also inconsistent with first principles modeling of the $Mn_6Ni_{16}Si_7$ G-phase. Thus the analysis here assumes the precipitates found in this study do not contain a significant amount of Fe. However, the nominal IVAS Fe contents are included in the tables summarizing the precipitate compositions for those that choose to interpret the data differently.

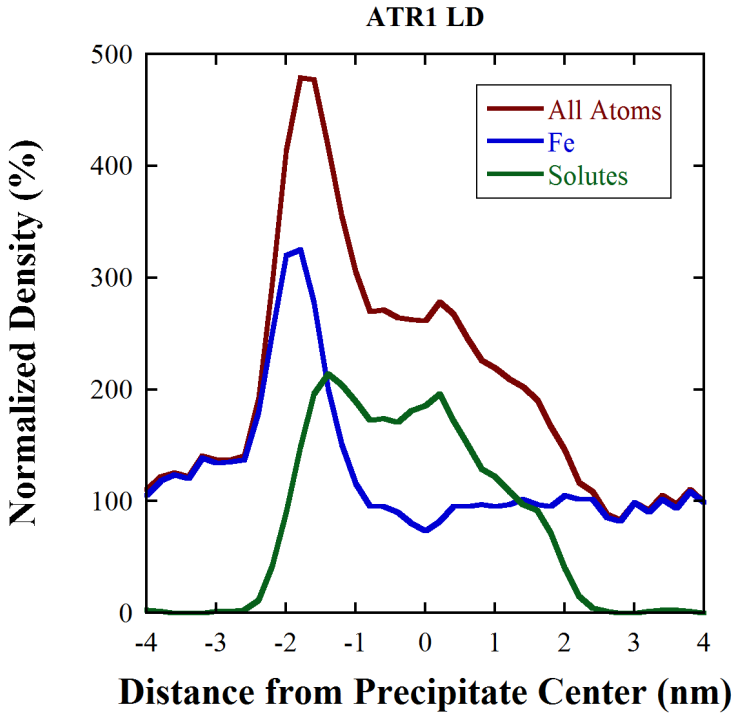

Figure 3.15. 1-D line profile showing atom density through a precipitate along the specimen axis.

3.5 Microhardness Testing

Microhardness tests at UCSB were carried out on a Leco M400 hardness tester with at least 10 indents per sample at a load of 500 grams. The mean and standard error were calculated for the hardness of each alloy in both the baseline and irradiated conditions. For the high flux irradiations, the as irradiated hardness was taken after a mild post irradiation anneal at 350°C for 5 h to remove the thermally unstable damage that is associated only with high flux [3, 4, 17]. The yield stress increase was estimated using the relation $\Delta\sigma_y \approx 3.3\Delta H_v$ [40]. The uncertainty in the $\Delta\sigma_y$ was calculated from the root mean square of the standard errors of the baseline and as irradiated measurements.

3.6 References

1. Eason ED, Odette GR, Nanstad RK and Yamamoto T. "A physically based correlation of irradiation-induced transition temperature shifts for RPV steels," Oak Ridge National Lab, 2007; ORNL/TM-2006/530.
2. Wirth BD. "On the Character of the Nano-Scale Features in Reactor Pressure Vessel Steels" [PhD Thesis]. University of California, Santa Barbara, 1998.
3. Mader E. "Kinetics of irradiation embrittlement and the post-irradiation annealing of nuclear reactor pressure vessel steels" [PhD Thesis]. University of California, Santa Barbara, 1995.
4. Odette GR and Nanstad RK. "Predictive reactor pressure vessel steel irradiation embrittlement models: Issues and opportunities", *JOM* 2009;61(7):17–23.
5. Miller MK and Forbes RG. "Atom-Probe Tomography: The Local Electrode Atom Probe" Springer Science+ Business Media, 2014.
6. Gault B, Moody MP, Cairney JM and Ringer SP. "Atom Probe Microscopy" Springer Science + Business Media, 2012.
7. Gault B, De Geuser F, Stephenson LT, Moody MP, et al. "Estimation of the Reconstruction Parameters for Atom Probe Tomography", *Microsc. Microanal.* 2008;14:296–305.

8. Yamaguchi Y, Takahashi J and Kawakami K. "The study of quantitativeness in atom probe analysis of alloying elements in steel", *Ultramicroscopy* 2009;109(5):541–544.

9. Takahashi J and Kawakami K. "A quantitative model of preferential evaporation and retention for atom probe tomography", *Surf. Interface Anal.* 2014;46(8):535–543.

10. Hyde JM, Burke MG, Gault B, Saxey DW, et al. "Atom probe tomography of reactor pressure vessel steels: An analysis of data integrity", *Ultramicroscopy* 2011;111(6):676–682.

11. Pareige P, Van Duysen JC and Auger P. "An APFIM study of the microstructure of a ferrite alloy after high fluence neutron irradiation", *Appl. Surf. Sci.* 1993;67:342–347.

12. Marquis EA and Hyde JM. "Applications of atom-probe tomography to the characterisation of solute behaviours", *Mater. Sci. Eng. R Reports* 2010;69(4-5):37–62.

13. Marquis EA and Vurpillot F. "Chromatic aberrations in the field evaporation behavior of small precipitates.", *Microsc. Microanal.* 2008;14(6):561–570.

14. Cunningham NJ. "Study of the Structure, Composition, and Stability of Y-Ti-O nm-Scale Features" [PhD Thesis]. University of California, Santa Barbara, 2012.

15. Odette GR and Wirth BD. "A computational microscopy study of nanostructural evolution in irradiated pressure vessel steels", *J. Nucl. Mater.* 1997;251:157–171.

16. Odette GR, Liu CL and Wirth BD. "On the Composition and Structure of Nanoprecipitates in Irradiated Pressure Vessel Steels", *Mater. Res. Soc. Symp. Proc.* 1997;439:457–469.

17. Odette GR, Mader E V., Lucas GE, Phythian WJ, et al. "The Effect of Flux on the Irradiation Hardening of Pressure Vessel Steels", In: *16th International Symposium on the Effects of Radiation on materials*, 1993. p. 373.

Chapter 4 Atom Probe Tomography Analysis

This chapter outlines the procedures used to reconstruct and analyze atom probe data. The methods used to estimate the unknown reconstruction parameters are first presented. This is followed by a discussion on ranging the mass spectrum as well as corrections that must be made to the compositional measurements due to peak overlaps. Next, the methods used to define the precipitates are presented followed by an explanation on the precipitate erosion process used to determine the matrix content far from precipitates. Last, a brief discussion on uncertainty analysis is presented.

4.1 Estimating Reconstruction Parameters

As was explained in the previous chapter, a number of assumptions must be made regarding unknown parameters in order to reconstruct the 3D coordinates of each ion in an APT sample. These assumptions include the tip radius during the evaporation of each ion (R), the tip-to-detector distance (L), the so called image compression factor (ξ), the efficiency of the instrument (η), and the atomic volume of the evaporating ion (Ω). Parameters which are expected to remain constant for all runs on an instrument, such as η and L, are set by the manufacturer and were not varied in this analysis. Since most solutes substitute on the Fe lattice, and the RPV steels are ≈ 98% Fe, the atomic volume is assumed to be that of an Fe

atom. This leaves two main unknown parameters, R and ξ. The following sections will details how these are calibrated.

Historically, the tip radius has been estimated using the simple equation below

$$R = \frac{V}{k_f F_e} \tag{4.1}$$

where V is the standing plus pulsed voltage at the time of evaporation, k_f is a geometric field factor and F_e is the evaporation field for the pure element. k_f is an unknown and varies for different tip geometries. The primary method of estimating k_f is by measuring the plane spacing in low index poles, which in the case of RPV steels are {110} and/or {200} planes [1, 2]. The plane spacing within the poles is measured, and if they are found to deviate from the theoretical plane spacing, k_f is adjusted until they match the theoretical value [2].

While, eqn. (4.1) is commonly used to estimate the radius at a given point in the reconstruction, there are other methods that are arguably more accurate. For example, the software used by almost all APT users and used for this dissertation, the Integrated Visualization and Analysis Software (IVAS), only allows the user to specify a single k_f value for an entire reconstruction. It has been shown that k_f can vary dramatically for a single APT sample, especially if the shank angle is large [3]. Thus, instead of using the k_f factor to estimate the tip radius, a different protocol, which uses an SEM image to estimate the tip radius, was used. The primary unknown in this reconstruction protocol is the initial tip radius, because the first several hundred thousands of ions collected during at APT run are typically discarded since they are collected while the fine alignment of the specimen is taking place. To account for this, the starting tip radius is varied until the correct plane spacing

within the specimen is measured. Ultimately, using either k_f or the tip image to estimate the tip radius uses measurements of the plane spacing to fine tune the parameters. Here, it was found that the use of the tip images resulted in more consistent plane spacing through the entirety of the sample vs using k_f.

The last unknown parameter in the reconstruction procedure is the image compression factor, ξ. The image compression factor is simply defined by the following equation [1, 2]

$$\xi = \frac{\theta_{crys}}{\theta_{obs}} \tag{4.2}$$

where θ_{crys} and θ_{obs} are the theoretical and measured angles between 2 crystallography directions. If ξ=1, then the ions are projected from the exact center of the hemispherical cap of the sample. Due to the electric field lines, the projection point is actually deeper from within the sample at a distance of greater than R. ξ can be calibrated for each run because θ_{obs} can be determined experimentally from the distance between the two poles on the detector (D), the tip-to-detector distance (L) through the relation [2]

$$\theta_{obs} = \arctan\frac{D}{L} \tag{4.3}$$

Calculation of ξ for was performed for several runs during the beginning portion of the thesis, but because the calculated value was always very similar to the default value found in IVAS, and it was a fairly time consuming process, the default value was typically used.

4.2 Data Analysis

4.2.1 Bulk Composition Measurement

The first step in the analysis is determining the bulk composition of the sample from the use of the mass spectrum, a histogram showing the number of ions within each mass-to-charge bin. The user is required to specify the element corresponding to each mass-to-charge range, a process referred to as "ranging". Because more than one element may have an isotope with the same mass-to-charge ratio, measured in units of daltons (Da), knowledge of the expected elements present in the sample, as well as the known isotopes of these elements and their relative abundances, makes the ranging process much easier.

In order to determine whether a peak is likely from a specific element, the peaks around it are often used. If a given element is present in a material, all of its isotopes will be present and, unless specific doping of a given isotope has occurred, the isotopes will be present in relative amounts comparable to their natural abundances on earth. For example, Mo has 7 stable isotopes with atomic masses of 92, 94, 95, 96, 97, 98 and 100. In the +2 charge states, peaks would be seen at 46, 47, 47.5, 48, 48.5, 49 and 50 Da. If a peak is seen at only one of these mass-to-charge ratios but not the other 6, then Mo can be ruled out as the identity of the peak. A typical ranged mass spectrum can be seen in Figure 4.1. After the ranging has been performed, the bulk compositions can be calculated by determining the total number of atoms of a given element and dividing that by the total number of atoms in the sample. This composition then needs to undergo two corrections.

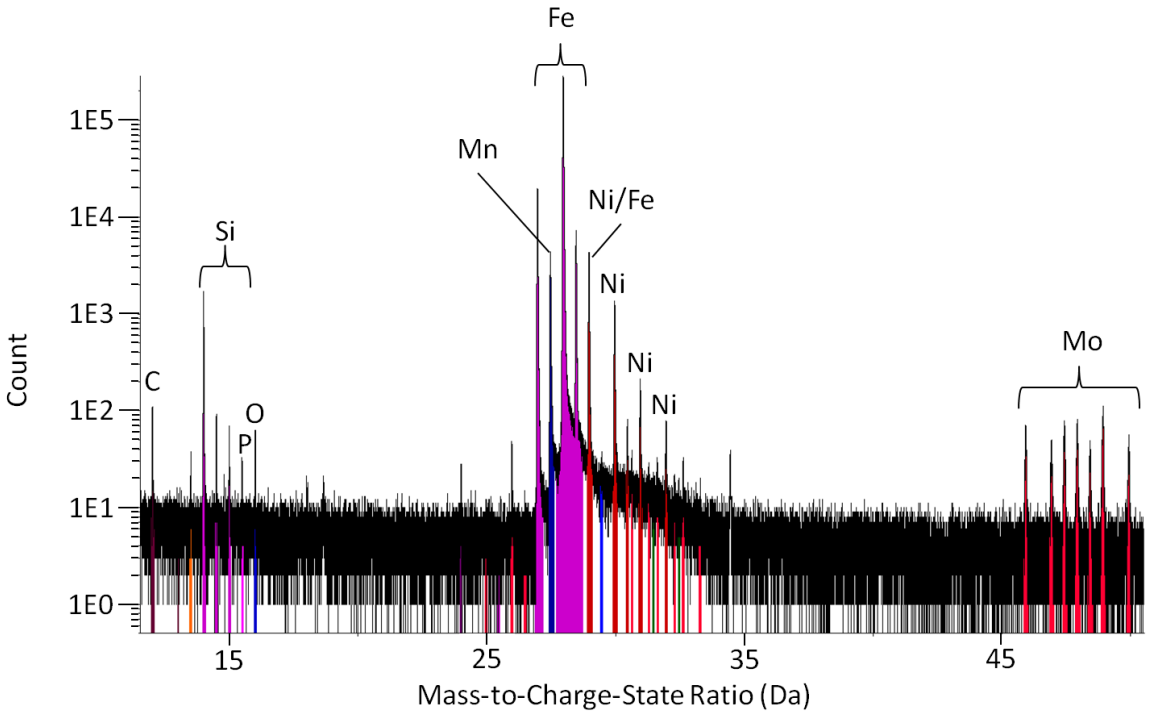

Figure 4.1. Mass spectrum from typical RPV steel with the main elements labelled.

The first correction to the bulk compositions is needed due to the large tail from the $^{56}Fe^{+2}$ peak. Though the instruments used in this thesis, either a LEAP 3000X HR or 4000X HR, have very high mass resolution, there is still some uncertainty in the time-of-flight and in the corresponding mass-to-charge ratio. For example, if ions evaporate just after the voltage pulse, the measured time-of-flight will be slightly longer than the true time-of-flight, resulting in a spread in the measured mass-to-charge ratios for a given element and forming a tail behind the sharp peak. Overall, the percent of ions that fall within this tail is very low, but can still represent a significant number of ions for Fe relative to the other elements since the samples are composed of 96-98% Fe. Figure 4.2 shows the elements that fall within the tail of the $^{56}Fe^{+2}$ peak from an example mass spectrum of an RPV steel. This elevates the

total counts of the elements with ranges in the tail. The element most affected by this tail is Ni, seen in the dark red ranges.

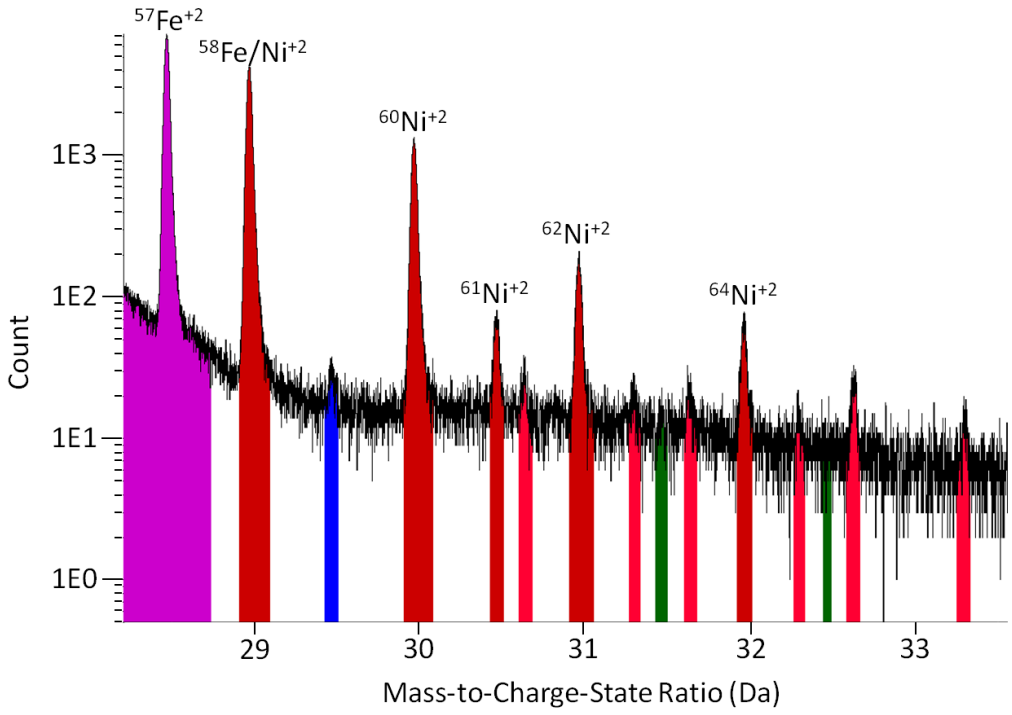

Figure 4.2. Mass spectrum focused on the region immediately after the 56Fe+2 peak at 28 Da showing the tail caused by the Fe atoms.

It has been shown that the tail from a large peak can be fit using an exponential decay function [1]. To correct for this tail, a matlab function was written to fit this tail using a function in the following form

$$C = \frac{B}{(M - M_0)^P} \tag{4.4}$$

where C is the number of counts of a given mass-to-charge ratio bin, M is the mass-to-charge ratio, M_0 is the mass to charge ratio of the peak being fit (29 Da in this case) and B and P are fit parameters. After the tail has been fit, it can be subtracted away from the mass

spectrum. Following this subtraction, the background around the peaks following the $^{56}Fe^{+2}$ peak are at ≈ 0, allowing for a more accurate measurement of the total number of ions in those peaks. The mass spectrum following the Fe peak at 28 Da before and after the tail subtraction is shown in Figure 4.3 and Figure 4.4.

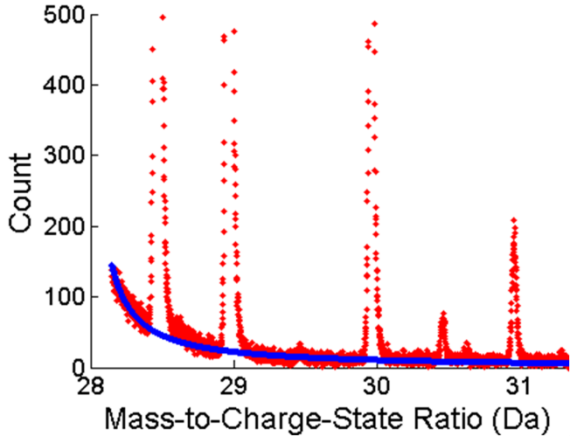

Figure 4.3. Elevation of peaks within $^{56}Fe^{+2}$ tail prior to subtraction.

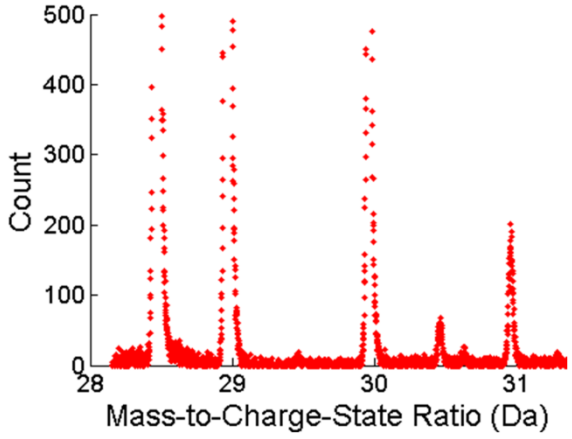

Figure 4.4. Peaks in region of $^{56}Fe^{+2}$ tail following subtraction.

The second correction is a deconvolution of peaks within the mass spectrum that are composed of a mixture of two elements. The largest peak mixture in the case of RPV steels is the peak at 29 Da, which is composed of both $^{58}Fe^{+2}$ and $^{58}Ni^{+2}$. While ^{58}Fe only consists of 0.28% of all naturally occurring Fe, it consists of 68.01% of all Ni. For a typical RPV composition of ≈ 97.5% Fe and 1.0% Ni, this peak would be composed of ≈ 70% Ni and 30% Fe. Thus, this peak is initially ranged as Ni, but corrected using the method described below.

The correction for overlapping peaks uses the relative abundances of the various isotopes of an element and the number of atoms for other isotopes of the element that do not

have overlapping peaks. For example, the expected number of atoms of $^{58}Fe^{+2}$ in the overlapping peak at 29 Da can be estimated from the number of $^{54}Fe^{+2}$ atoms and the respective abundances of the two elements, 0.28% and 5.84%, through the relation

$$^{58}Fe^{+2} = {}^{54}Fe^{+2}\frac{0.28\%}{5.84\%} \tag{4.5}$$

Note that any other Fe isotope could also be used. $^{54}Fe^{+2}$ was selected because it is the second largest Fe isotope and the largest Fe isotope, ^{56}Fe, has a large tail that overlaps a number of other elements, making an accurate count of the atoms for this isotope more difficult. The number of $^{58}Ni^{+2}$ atoms in the overlapping peak at 29 Da can be estimated similarly with the abundances of $^{58}Ni^{+2}$ and $^{60}Ni^{+2}$ using

$$^{58}Ni^{+2} = {}^{60}Ni^{+2}\frac{68.01\%}{26.22\%} \tag{4.6}$$

From these two numbers, the expected number of $^{58}Fe^{+2}$ and $^{58}Ni^{+2}$ atoms within the peak at 29 Da can be estimated.

The combination of both of these corrections results in a significant reduction in the apparent bulk solute content in the alloy, particularly for the Ni content because it is reduced when performing the background subtraction for peaks within the $^{56}Fe^{+2}$ tail and when deconvoluting the Fe-Ni peak overlap at 29 Da. Table 4.1 gives an example of the measured Ni content in a run before any corrections, after the background subtraction of the $^{56}Fe^{+2}$ tail, and after the final deconvolution of the Fe/Ni peak overlap at 28 Da.

Table 4.1. Measured Ni content from an RPV steel (CM6) showing the measured Ni content before and after correction of the mass spectrum.

Condition	Measured Ni Content (at.%)
No Correction	2.02%
Subtraction of Fe tail Only	1.90%
Subtraction of Fe tail and deconvolution of Fe/Ni peak	1.63%

4.2.2 Cluster Analysis

The primary purpose of performing APT on irradiated RPV steels is to look for solute clustering, which is the next step in the analysis. All cluster analysis was performed using a modified version of the maximum separation method, referred to as the density based clustering algorithm [4]. The basic premise of this algorithm is that the atomic density of solute atoms is higher within precipitates than in the matrix. First, the distance (d) between every solute, defined as Cu, Ni, Mn and Si, and its Nth nearest solute neighbor is found, where the Nth atom is defined as the order (K). If d is less than a cutoff distance defined by the user (d_{max}), the solute is considered to be a core atom. After all core atoms have been found, any atom, even those that are not solutes, within d_{max} of a core atom is considered to be within the same cluster. After all clusters have been defined, any clusters that have fewer than N_{min} atoms are excluded from the analysis. Essentially, the selection of d_{max} and K defines a cutoff solute atom density (ρ), where clustering is defined to occur if the following condition is met

$$\rho > \frac{K}{\frac{4}{3}\pi {d_{max}}^3} \tag{4.7}$$

The main challenge in selecting the "optimum" cluster parameters is choosing a large enough d_{max} that all "real" clusters are defined, while making sure not to include random solute fluctuations that are likely to occur even in a solid solution. Styman et. al. and Hyde et. al. found the optimum parameters for RPV steels to be d_{max}=0.5 nm and N_{min}=13-24 atoms [5, 6], though the order parameter used in this case was 1, which results in a higher sensitivity to small clusters. Here the following parameters were used: K=5, d_{max}= 0.50-0.60 nm and N_{min}=15-30. While the d_{max} used here is slightly higher than suggested by Styman and Hyde, because the matrix of the irradiated steels is so dilute in solutes, especially in the ATR1 condition, the larger d_{max} still should not include "background" clusters, or clusters that would be present by chance in a random solid solution, especially considering that a higher order parameter was used.

The precipitate sizes were calculated by determining the spherical radius, r_p, of the volume of total number of solute atoms in a cluster, corrected for the detection efficiency assuming an atomic solute volume that is the same as for Fe, as $r_p = \sqrt[3]{\frac{3N_{sol}\Omega}{4\pi\eta}}$. Here N_{sol} is the number of Cu, Ni, Mn and Si atoms in a given cluster, Ω is the atomic volume of Fe, and η is the efficiency of the LEAP (0.37 in the case of a reflectron equipped instrument). The possible intermetallic phases that exist in these steels have atom densities that vary from those of Fe within ±10%, so the corresponding effect on r_p is less than about ±3%. Given the various artifacts in the APT reconstructions of the precipitates, it is believed that this method of estimating r_p is more physically justified and systematic compared to other common approaches like multi-axis Guiner radius based estimates, especially since the artifacts

discussed above leave the precipitates with distorted shapes, length scales and atomic densities [7–9]. The corresponding cluster mole fraction, f_v, is estimated by dividing the total number of solutes in the precipitates by the total number of atoms in the sample.

Precipitates on the edge of the reconstruction are not used in calculating the size distributions. However, edge precipitates are counted as one half in determining their total number density, N. The N is calculated by dividing the total number of clusters by the total reconstruction volume determined by multiplying the total number of atoms in the reconstruction, corrected for the efficiency, by the atomic volume of Fe.

4.2.3 Matrix Composition

It is difficult to accurately define the interface between precipitates and matrix due to the reduced spatial resolution caused the evaporation of the lower field precipitates and the subsequent changes in local magnification [9–11]. Because of this, instead of observing an atomically sharp interface between precipitates and the matrix, a gradual increase in solute concentration is observed. Attempting to define the cluster interface at the exact point where the solute concentration begins to increase results in also defining random solute fluctuations in the matrix as clusters. Thus, the cluster parameters were selected to slightly err on the side of leaving extra solute atoms near the edges of the precipitates vs erroneously defining random solutes as clustered. The consequence of this decision is that the residual solutes left in the matrix are slightly overestimated. To account for this, the matrix atoms immediately surrounding the clusters were excluded from the matrix composition through an erosion process.

The erosion process starts by defining the center of mass for each cluster. The spatial extent of the clusters in the x, y and z directions (X_e, Y_e, Z_e) is also defined. The volume of atoms, extending a distance of 1.5*(X_e, Y_e, Z_e) on all sides of the mass center is then removed from the reconstruction to define the "matrix". Cross sections of atom maps from an irradiated CM6 sample before and after this erosion are shown in Figure 4.5 and Figure 4.6, respectively. Following the matrix erosion, the matrix composition is determined through the same process outlined for the bulk composition.

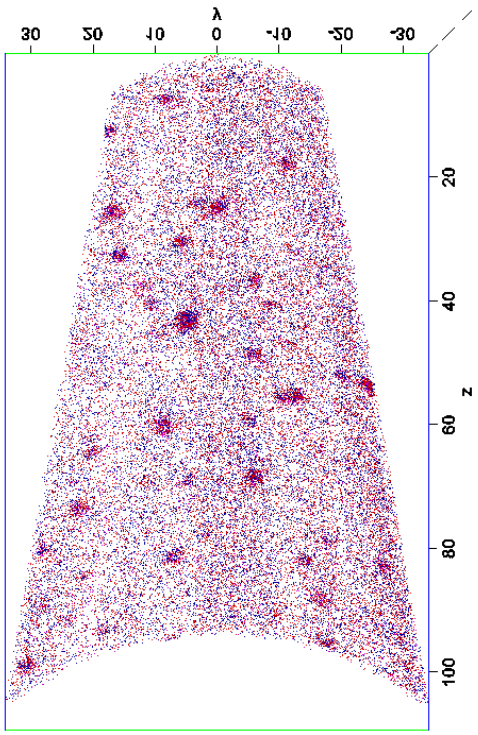

Figure 4.5. 10 nm thick slice of atom map showing location of Mn, Ni and Si atoms from irradiated CM6 prior to matrix erosion.

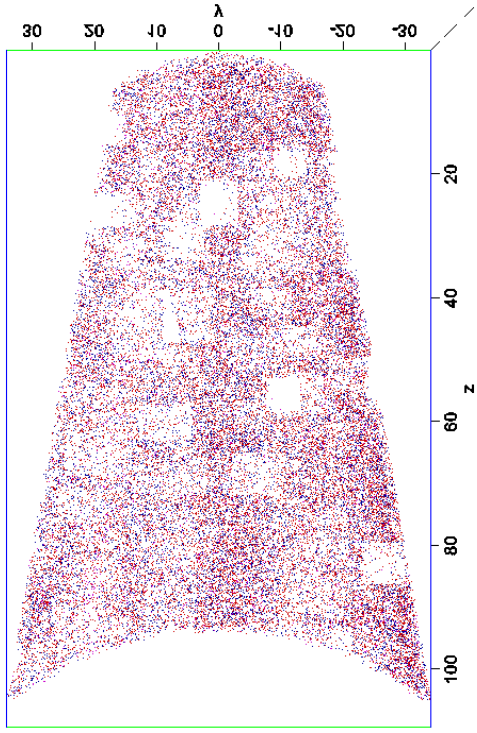

Figure 4.6. 10 nm thick slice of atom map showing the removal of the clustered region to define the "matrix".

4.2.4 Uncertainty Analysis

Multiple APT measurements were carried out on each alloy. The mean bulk, matrix and precipitate compositions, as well as precipitate <r>, N and f_v were calculated for each tip for a given alloy nominal condition. The ion weighted mean and standard deviation were calculated for a given alloy from the means of all runs. The expression for the weighted mean and weighted standard deviation are given by

$$\bar{x} = \frac{\sum_{i=1}^{n} w_i x_i}{\sum_{i=1}^{n} w_i} \tag{4.8}$$

$$S = \sqrt{\frac{n}{(n-1)} * \frac{\sum_{i=1}^{n} w_i (x_i - \bar{x})^2}{\sum_{i=1}^{n} w_i}} \tag{4.9}$$

Here $\bar{x}$ is the mean value for a set of given alloy condition runs, x_i is the calculated value for the i'th run for a single alloy condition, S is the standard deviation of the means for the alloy, w_i is the total number of atoms for the i'th measurement, and n is the total number of measurements on a single alloy condition. The mean value uncertainties were taken as the standard error of a given quantity. The standard error for an alloy condition was calculated by $SE = \frac{S}{\sqrt{n}}$.

The main source of analysis uncertainty in calculating the f_v for a single run is the selection of D_{max} and N_{min}. A parametric study was performed varying D_{max} by ±10%. The corresponding f_v varied by ≈ ±5% of the total and the individual Ni, Mn and Si varied by ≈ ±6%, while the Cu showed very little variation. These uncertainties in f_v for single tips were used in the scatter plots of f_v vs bulk composition for individual runs.

Finally, a major general limitation of APT is the very small volumes of material that are probed, typically on the order of 10^{-16} cm^3. This is a critical issue for heterogeneously distributed features, especially if their number densities are low. However, in this study, involving high number densities of relatively uniformly distributed precipitates, compositional heterogeneities turned out to be an advantage. Specifically, tip-to-tip variations in the overall local bulk solute compositions, which were significant in some cases, can be directly correlated with the corresponding compositions and f_v of the precipitates on a nearly one-to-one basis. It is shown that the tip-to-tip variations for the same alloy conditions are generally consistent with larger alloy-to-alloy compositional variations with respect to their effects on the precipitate parameters. Consequently, all of the APT bulk compositions that follow are the actual measured values in at.% for a given tip, or the average measured value for a given alloy condition.

4.3 References

1. Gault B, Moody MP, Cairney JM and Ringer SP. "Atom Probe Microscopy" Springer Science + Business Media, 2012.
2. Gault B, De Geuser F, Stephenson LT, Moody MP, et al. "Estimation of the Reconstruction Parameters for Atom Probe Tomography", *Microsc. Microanal.* 2008;14:296–305.
3. Gault B, Loi ST, Araullo-Peters VJ, Stephenson LT, et al. "Dynamic reconstruction for atom probe tomography", *Ultramicroscopy* 2011;111(11):1619–1624.
4. Stephenson LT, Moody MP, Liddicoat P V. and Ringer SP. "New techniques for the analysis of fine-scaled clustering phenomena within atom probe tomography (APT) data.", *Microsc. Microanal.* 2007;13(6):448–463.
5. Styman PD, Hyde JM, Wilford KB and Smith GDW. "Quantitative methods for the APT analysis of thermally aged RPV steels", *Ultramicroscopy* 2013;132:258–264.
6. Hyde JM, Marquis EA, Wilford KB and Williams TJ. "A sensitivity analysis of the

maximum separation method for the characterisation of solute clusters", *Ultramicroscopy* 2011;111(6):440–447.

7. Hyde JM, Sha G, Marquis E a., Morley a., et al. "A comparison of the structure of solute clusters formed during thermal ageing and irradiation", *Ultramicroscopy* 2011;111(6):664–671.
8. Marquis EA and Hyde JM. "Applications of atom-probe tomography to the characterisation of solute behaviours", *Mater. Sci. Eng. R Reports* 2010;69(4-5):37–62.
9. Cunningham NJ. "Study of the Structure, Composition, and Stability of Y-Ti-O nm-Scale Features" [PhD Thesis]. University of California, Santa Barbara, 2012.
10. Miller MK, Russell KF, Pareige P, Starink MJ, et al. "Low temperature copper solubilities in Fe-Cu-Ni", 1998;250:49–54.
11. Perez M, Perrard F, Massardier V, Kleber X, et al. "Low-temperature solubility of copper in iron: experimental study using thermoelectric power, small angle X-ray scattering and tomographic atom probe", *Philos. Mag.* 2005;85(20):2197–2210.

Chapter 5 Neutron Irradiations

5.1 Introduction

This chapter focuses on results from high ϕt test reactor and surveillance irradiations. First, APT results for six steels from two irradiation conditions, G1 and ATR1, are presented. The G1 condition, with $\phi t_e \approx 3.0x10^{19}$ n/cm^2, is very consistent with previous studies at low to medium ϕt, where Cu has a dominant effect of the formation of precipitates and the corresponding hardening. On the other hand, precipitates from ATR1 condition, at very high $\phi t_e \approx 2.1x10^{20}$ n/cm^2, are heavily dominated by the Mn, Ni and Si. In this condition, contrary to the current embrittlement prediction models, Cu has little effect on the total volume fractions or hardening. It should be noted that the highest ϕt that will be seen at an 80 year extended life is $\approx 1x10^{20}$ n/cm^2, so these two conditions span from well before to well after the predicted end of life. While the ATR1 results are beyond the maximum ϕt that will experienced by RPVs at 80 years of operation, the main purpose of the condition was to generate significant quantities of MNSP that could be readily characterized and modeled.

Next, the role of Ni at very high ϕt_e is examined in further detail, including the effect of reducing or removing Ni on the formation of precipitates. Following this, results from a low ϕ surveillance program are presented and compared to a similar alloy from the very high ϕt_e ATR1 condition. Finally, the chapter concludes with a brief discussion on the relationship between the precipitates and hardening, though this is a much larger focus of Chapter 8.

5.2 Measured Compositions and Compositional Variation

APT was carried out on 6 steels in three irradiation conditions, G1, TU and ATR1. Note that the TU results are not presented in detail here, but can be found in appendix A.3. The full details for these two conditions can be found in section 3.2.1. The average APT bulk solute compositions, in at.%, are given in Table 5.1 and Table 5.2 for the medium (G1) and very high (ATR1) ϕt_e conditions, respectively. The nominal bulk chemistries are given in parenthesis. Observed differences between the measured total and nominal values are largely expected. For example, the alloys that nominally contain ≈ 0.34% Cu have a lower average total APT content of ≈ 0.25%. This value is consistent with previous observations of lower residual amounts in solution due to coarse scale pre-precipitation during tempering and stress relief heat treatments, when the total Cu is beyond the solubility limit [1–4]. Likewise the Mn contents are lower than the nominal value since this element is partially sequestered in coarse $Mn_{0.6}Fe_{2.4}C$ and MnS precipitates. The quantitative differences between the nominal and measured bulk compositions are shown in Table 5.1 and Table 5.2.

These overall composition averages do not reflect the tip-to-tip variations in individual alloys, which are significant in some cases. For example, the standard error for the bulk Mn measurements of a given alloy is as large as 0.20%. While seemingly an esoteric detail, it is show below that the effects of the tip-to-tip composition variations in a given alloy are directly reflected in the precipitates, and are also consistent with observed alloy-to-alloy trends. A corollary is that it is important to use the actual local compositions in analyzing the APT precipitate data.

Table 5.1. Bulk APT and nominal (in parentheses) compositions in at.% for the medium ϕt_e condition (G1).

Alloy	Cu	+/-	Ni	+/-	Mn	+/-	Si	+/-
LC	0.21 (0.36)	0.02	0.91 (0.81)	0.10	0.97 (1.46)	0.20	0.53 (0.46)	0.06
LD	0.21 (0.33)	0.01	1.00 (1.16)	0.01	1.08 (1.37)	0.10	0.52 (0.45)	0.03
LG	0.01 (0.01)	0.00	0.86 (0.69)	0.05	1.09 (1.36)	0.09	0.49 (0.43)	0.02
LH	0.08 (0.09)	0.00	0.72 (0.69)	0.01	0.97 (1.38)	0.03	0.45 (0.47)	0.01
LI	0.15 (0.17)	0.01	0.72 (0.69)	0.01	1.21 (1.36)	0.03	0.43 (0.46)	0.01
CM6	0.00 (0.02)	0.01	1.34 (1.57)	0.10	1.09 (1.50)	0.20	0.33 (0.33)	0.06

**Note that these steels also contain Mo, C, P, and other trace impurities*

Table 5.2. Bulk APT and nominal (in parentheses) compositions in at.% for the very high ϕt_e condition (ATR1).

Alloy	Cu	+/-	Ni	+/-	Mn	+/-	Si	+/-
LC	0.28 (0.36)	0.01	0.80 (0.81)	0.03	1.16 (1.46)	0.01	0.43 (0.46)	0.02
LD	0.25 (0.33)	0.02	1.18 (1.16)	0.05	1.08 (1.37)	0.08	0.54 (0.45)	0.02
LG	0.00 (0.01)	0.01	0.71 (0.69)	0.01	0.87 (1.36)	0.08	0.43 (0.43)	0.01
LH	0.08 (0.09)	0.01	0.73 (0.69)	0.02	1.19 (1.38)	0.06	0.42 (0.47)	0.01
LI	0.15 (0.17)	0.01	0.70 (0.69)	0.01	0.97 (1.36)	0.10	0.42 (0.46)	0.01
CM6	0.00 (0.02)	0.01	1.69 (1.57)	0.04	1.42 (1.50)	0.03	0.39 (0.33)	0.01

**Note that these steels also contain Mo, C, P, and other trace impurities*

5.3 Medium ϕt_e G1 Condition

Figure 5.1 shows atom maps for the highest Ni content, Cu-free steel (CM6) and the high Ni-Cu content steel (LD) in the medium ϕt_e condition. The precipitates are numerous and well defined in the Cu-bearing steel, but are not as easy to observe in the Cu-free alloy; however, they are readily characterized by the cluster search algorithm.

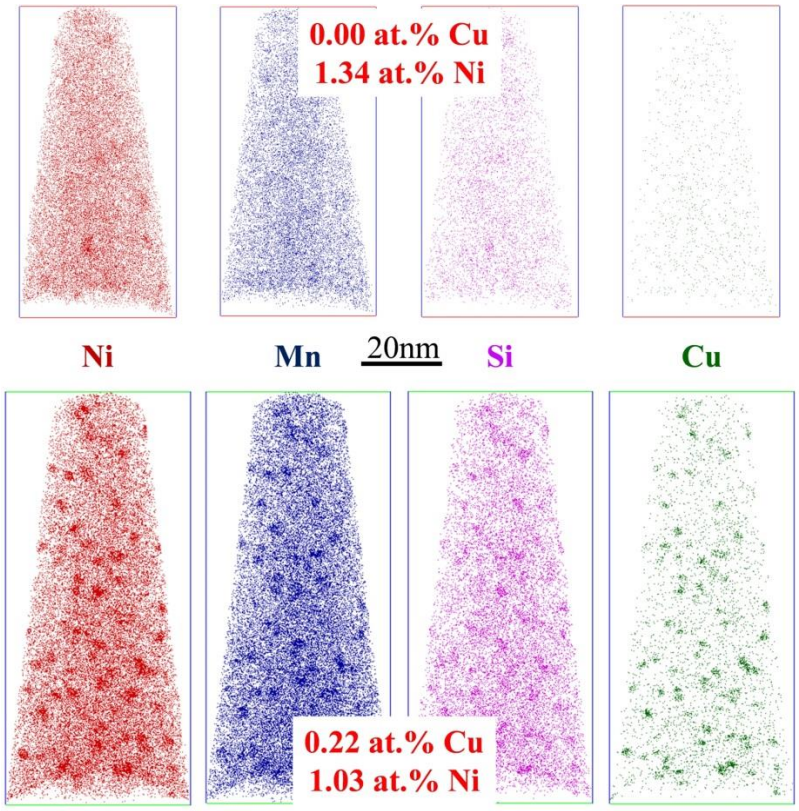

Figure 5.1. Atom Maps for the highest Ni, Cu free (top) and high Ni-Cu (bottom) alloys irradiated to medium ϕt_e.

Table 5.3 and Table 5.4 summarize the corresponding APT precipitate measurements and matrix compositions, respectively. The left portion of Table 5.3 gives the Cu-Mn-Ni-Si compositions of the precipitates. The nominal precipitate Fe content is also shown to the right of the precipitate compositions. While it is thought that the Fe is largely an APT artifact, it is included for those who might seek an alternative analysis. The right portion of Table 5.3 gives the average radius (<r>), number density (N) and mole fraction (f_v) of the MNSP, as well as the standard error uncertainties in the measurements.

Table 5.3. Precipitate compositions and <r>, N and f_v at medium ϕt_e (G1).

Alloy	Precipitate Relative Compositions (at.%)								Fe*	<r> (nm), N (1E23 m^{-3}), f_v (%)					
	Cu	+/-	Ni	+/-	Mn	+/-	Si	+/-		<r>	+/-	N	+/-	f	+/-
LC	25.7	1.4	35.1	5.0	23.6	7.2	15.7	3.8	60.8	1.15	0.10	9.2	1.4	0.58	0.08
LD	22.2	0.7	37.8	0.5	24.6	1.2	15.5	0.7	58.6	1.13	0.02	11.5	0.7	0.68	0.04
LG	0.5	0.1	46.8	2.3	25.5	3.6	27.2	1.9	53.3	0.72	0.04	5.3	1.5	0.08	0.02
LH	14.8	0.9	39.8	2.5	25.1	1.8	20.3	0.1	58.7	0.92	0.05	4.9	0.5	0.16	0.01
LI	24.2	1.0	34.2	0.5	27.4	0.8	14.2	0.4	57.2	1.10	0.03	6.9	0.6	0.37	0.04
CM6	0.1	0.1	58.9	5.0	25.6	7.2	15.5	3.8	49.6	0.70	0.10	4.6	3.0	0.07	0.04

** Nominal Fe assumed to be an artifact, but provided for alternative interpretations.*

Table 5.4. Matrix compositions at medium ϕt_e (G1).

Alloy	Cu	+/-	Ni	+/-	Mn	+/-	Si	+/-
LC	0.06	0.01	0.70	0.08	0.84	0.18	0.43	0.06
LD	0.06	0.00	0.74	0.02	0.91	0.08	0.41	0.03
LG	0.01	0.00	0.81	0.04	1.07	0.09	0.46	0.02
LH	0.06	0.01	0.66	0.01	0.93	0.03	0.41	0.01
LI	0.06	0.00	0.59	0.00	1.11	0.02	0.37	0.01
CM6	0.00	0.01	1.27	0.08	1.05	0.18	0.31	0.06

The bar chart in Figure 5.2a summarizes the precipitate f_v and corresponding compositions. It will later be show that the f_v directly scales with the individual tip solute contents. Thus Figure 5.2a shows the mole fraction for individual tips with bulk compositions close to the average values of the alloy. The trends for Ni content in Cu-free steels, Cu content at medium Ni content, and Cu content at both the higher and the highest Ni content, are individually highlighted in the three sections. The corresponding <r> and N are plotted in Figure 5.2b.

The major observed trends are as follows:

- The highest Ni content, Cu-free steel has only a slightly larger f_v than the Cu-free, medium Ni content alloy (Fig. 3a left). The Cu-Mn-Ni-Si mole fraction of the precipitates, hence the

total f_v, increase with increasing Cu content in the medium Ni content steels (Fig. 3a center). The mole fraction of Cu in the precipitates increases from ≈ 0, in the Cu-free steel, to 0.15% in the highest Cu content steel. The average residual matrix Cu content is 0.06% in the Cu-bearing steels, indicating incomplete phase separation for this highly insoluble element (Table 5.4).

- The increase in f_v with higher Ni content in the 0.21% Cu steels is due to higher contents of Ni, Mn and Si in the precipitates (Fig. 3a center and right). These results clearly demonstrate the thermodynamically driven synergisms between these elements, and the very important role played by Ni. The corresponding effect of increasing Ni content on f_v in the Cu-free and high Cu content steels is minimal in this case (Fig. 3a right) because f_v is so strongly dependent on Cu.

- Both N and <r> increase with Cu content (Fig. 3b). N also increases with Ni content, except in the Cu-free steels. It should be noted that at these small f_v and <r>, the uncertainties in N are larger.

- The relative Mn-Ni-Si compositions are generally similar in the medium and high Ni content steels (LG, LH, LI, LC, LD) with fractional averages and standard deviations of: 0.31±0.04 Mn, 0.47±0.01 Ni and 0.22±0.03 Si. The precipitate Ni fraction is higher and the Si is lower in the highest Ni content, Cu-free steel (CM6) averaging 0.26 Mn, 0.59 Ni and 0.15 Si.

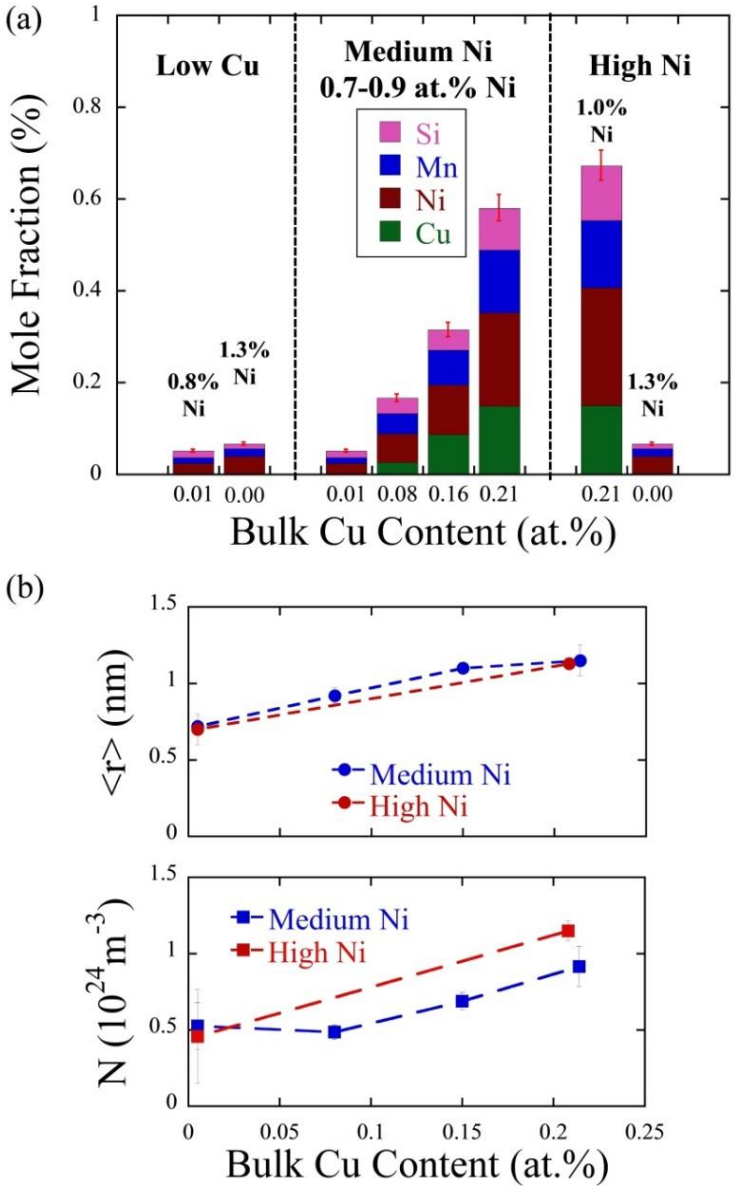

Figure 5.2. (a) The precipitate f_v for the individual constituent elements in a single run of all 6 alloys; and, (b) <r> and N plotted as a function of Cu. Note that in some cases, the error bars were smaller than the size of the symbols.

The most important observation for the medium ϕt_e condition is that Cu and Ni play a combined role in mediating f_v, although Cu seems to have a stronger influence over the range

of Ni compositions studied here. While the features in the Cu-bearing steels contain more than 75% Mn-Ni-Si, the total f_v of these elements roughly scales with the alloy Cu content. This can be seen in Figure 5.3, which plots the Mn-Ni-Si f_v, i.e. ignores the Cu portion of the total f_v, as a function of a) Cu and b) Ni. Each point represents the bulk Cu or Ni along with the measured MNSP f_v for a given atom probe tip. Thus, higher Cu content clearly leads to larger amounts of Mn, Ni and Si coming out of solution.

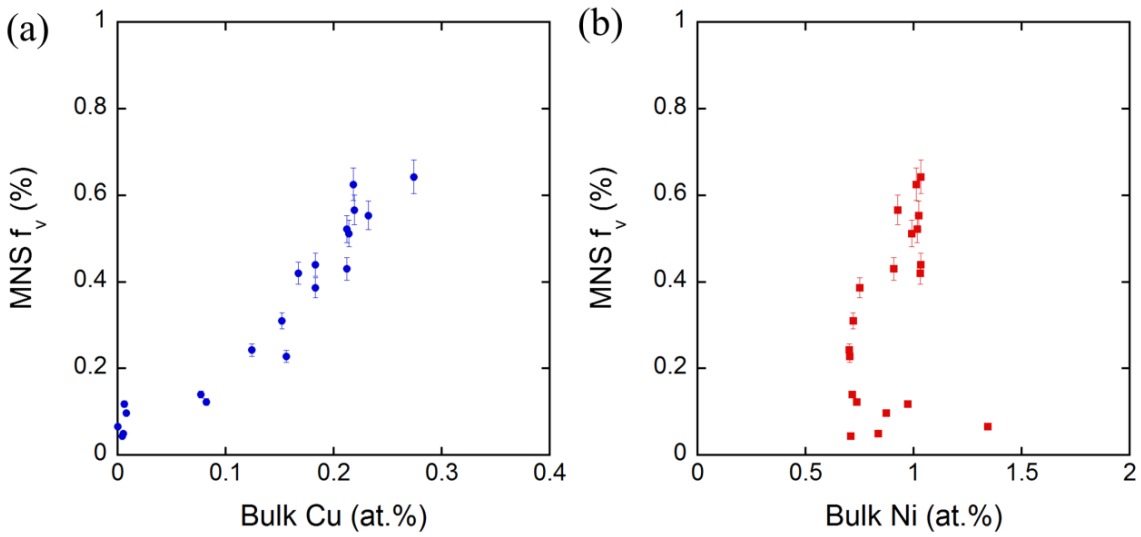

Figure 5.3. MNSP f_v as a function of a) bulk Cu and b) bulk Ni.

The most plausible hypothesis for explaining these observations is that in the Cu-free steels, the clusters are still predominantly matrix features. However, the presence of Cu catalyzes the formation of MNSP. The Cu is highly supersaturated, thus precipitates quickly, while simultaneously being enriched in the other solutes. In the presence of Cu, the difficult nucleation step for nearly pure Mn-Ni-Si phases is largely avoided by co-precipitation, and these solutes subsequently flow to the Cu-catalyzed precipitates starting at relatively low ϕt.

5.4 Very High ϕt_e ATR1 Condition

Atom maps, for the same alloys as Figure 5.1, but from the very high ϕt_e condition (ATR1) are shown in Figure 5.4. They clearly demonstrate the large changes that occur when going from medium to very high ϕt_e. It should again be stressed that in this case, the $\phi t_e \approx 2.1 \times 10^{20}$ n/cm^2 is over twice that any RPV is expected to experience even at an 80 year extended life. The average precipitate parameters are summarized in Table 5.5. These large changes are not surprising, since the ϕt_e increased by a factor of ≈ 7 between the medium and very high ϕt_e conditions. The major observations can be summarized as follows:

- There is a large increase in f_v between the medium and very high ϕt_e conditions. The histograms in Figure 5.5a, again for individual tips with bulk compositions close to the average values, show both the total f_v and precipitate composition for each alloy. These results demonstrate that the effect of Cu is not nearly as significant at very high versus medium ϕt_e, and that Ni plays a much stronger role than in the former case. At very high ϕt_e, the MNSP no longer need Cu to form. The precipitate f_v more than doubles in the Cu-free steels with increasing bulk Ni from ≈ 0.7% to 1.6% (Fig. 5a left). In contrast, at medium Ni contents, increasing the bulk Cu only slightly increases f_v (Fig. 5a center); this increase is almost entirely caused by the higher amount of co-precipitate Cu itself. Notably, the highest ≈ 1.6% Ni, Cu-free steel (CM6) has a larger f_v than in the high 1.2% Ni, 0.25% Cu (LD) alloy (Fig. 5a right).

- Figure 5.5c shows that <r> modestly increases with Cu in both medium and higher Ni content steels. In contrast, the corresponding N decreases with Cu. In the case of the high Ni-

Cu content steel (LD), the very high ϕt_e N is lower than for the medium ϕt_e condition, perhaps suggesting that the precipitates have begun to coarsen.

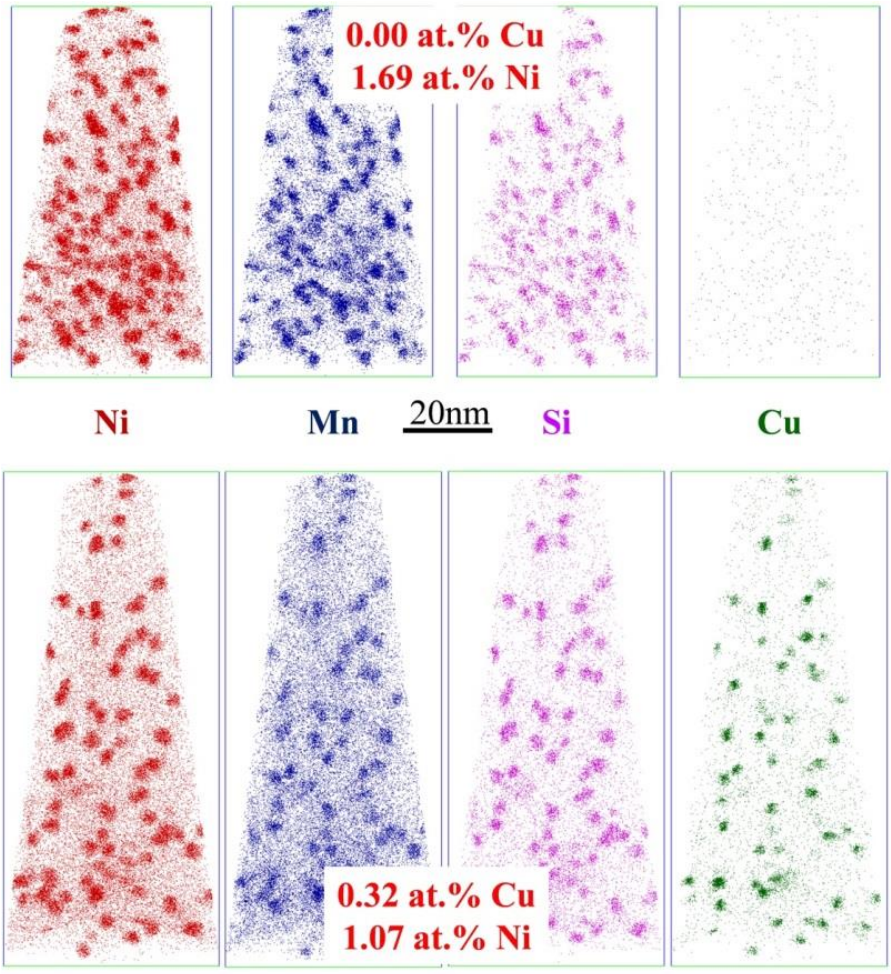

Figure 5.4. Atom Maps for the highest Ni, Cu free (top) and high Ni-Cu (bottom) alloys irradiated to very high ϕt_e.

- Table 5.5 shows that at the very high ϕt_e, the precipitates in the nominally Cu-free steel contain < 0.01 of this element. In the medium Ni content steels, the precipitate Cu composition increases (LH, LI, LC) with this element up to ≈ 15% (LC).

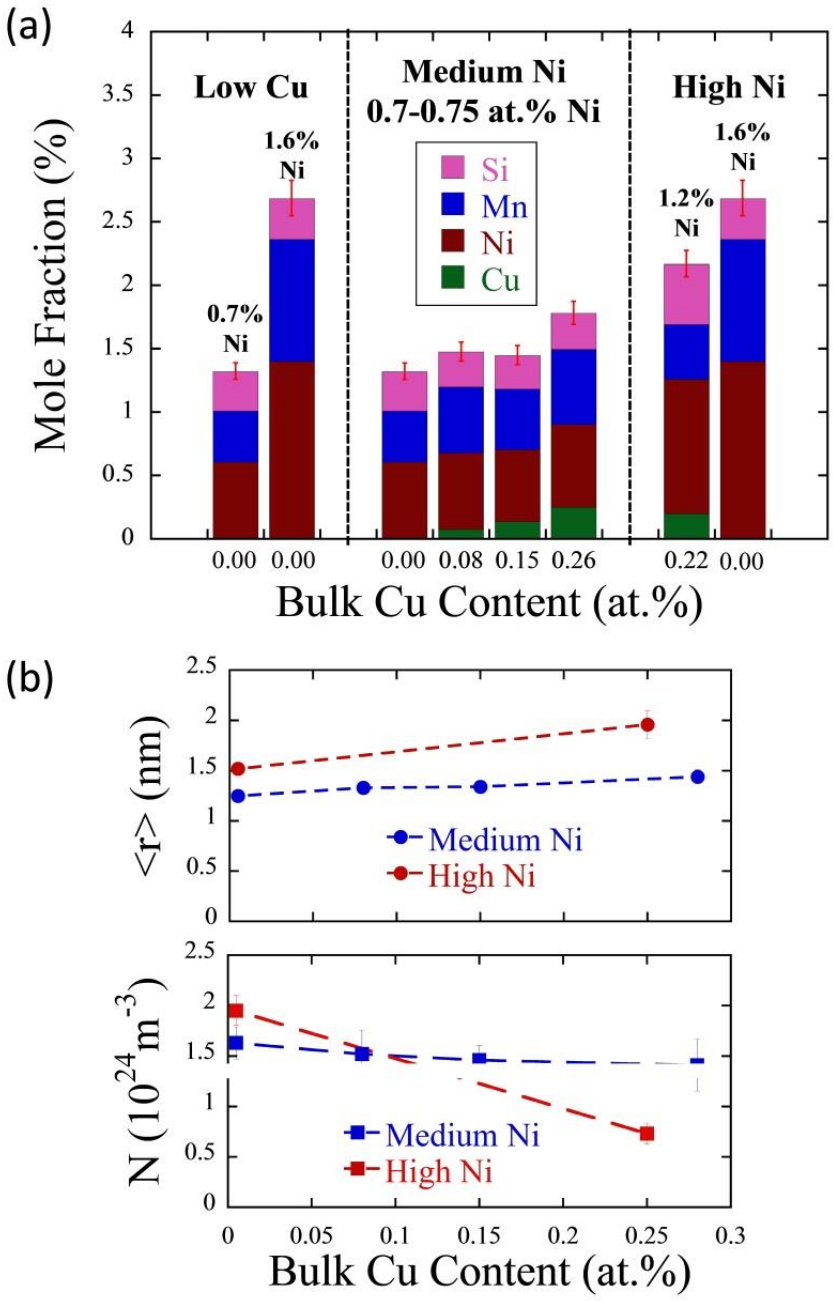

Figure 5.5. The Cu dependence of: (a) f_v showing the constituent elements for individual runs of each alloy and (b) <r> and N at very high ϕt_e. Note that in some cases, the error bars were smaller than the size of the symbols.

Table 5.5. Precipitate compositions and <r>, N and f_v at very high ϕt_e (ATR1).

Alloy	Precipitate Relative Compositions (at.%)								Fe*	<r> (nm), N ($10^{23}m^{-3}$), f_v (%)					
	Cu	+/-	Ni	+/-	Mn	+/-	Si	+/-		<r>	+/-	N	+/-	f	+/-
LC	14.8	2.5	37.4	1.8	31.9	1.2	15.9	1.4	62.0	1.44	0.07	14.1	2.6	1.81	0.19
LD	10.3	2.4	46.9	3.6	22.5	2.5	20.3	1.8	55.4	1.96	0.14	7.3	1.0	2.11	0.23
LG	0.2	0.1	46.1	1.5	31.2	2.8	22.5	1.6	63.5	1.25	0.04	16.3	1.6	1.33	0.03
LH	5.0	0.2	40.7	1.5	35.6	2.4	18.6	1.1	64.9	1.33	0.05	15.2	2.4	1.48	0.03
LI	9.5	0.5	39.7	2.5	31.9	4.2	18.9	1.9	62.7	1.34	0.06	14.6	1.4	1.46	0.04
CM6	0.1	0.0	52.5	1.2	35.5	1.9	11.9	0.5	58.9	1.52	0.06	19.54	1.5	2.82	0.14

** Nominal Fe assumed to be an artifact, but provided for alternative interpretations.*

Table 5.6. Matrix compositions at very high ϕt_e (ATR1).

Alloy	Cu	+/-	Ni	+/-	Mn	+/-	Si	+/-
LC	0.02	0.01	0.11	0.01	0.47	0.02	0.10	0.01
LD	0.03	0.01	0.18	0.01	0.57	0.07	0.08	0.01
LG	0.00	0.00	0.08	0.01	0.37	0.06	0.10	0.01
LH	0.02	0.01	0.11	0.01	0.57	0.04	0.11	0.01
LI	0.02	0.01	0.11	0.01	0.41	0.05	0.11	0.01
CM6	0.00	0.00	0.17	0.01	0.32	0.01	0.04	0.01

Figure 5.6 shows the relative precipitate Mn-Ni-Si compositions do not change much between medium and very high ϕt_e. For example, the average fractional compositional difference for the medium Ni content steels (LG, LH, LI, LC) is 0.02 Mn, -0.01 Ni and -0.01 Si in going from medium to very high ϕt_e. Further, the Mn-Ni-Si precipitate compositions are generally similar in the medium Ni content steels at very high ϕt_e (LG, LH, LI, LC) with fractional averages and standard deviations of: 0.35±0.03 Mn, 0.44±0.02 Ni and 0.20±0.02 Si. The precipitate Mn fraction is lower and Ni is higher in the high Ni-Cu content steel (LD) at 0.25 Mn, 0.52 Ni, and 0.23 Si. The corresponding composition of the highest Ni content,

Cu-free steel (CM6) is 0.36 Mn, 0.52 Ni and 0.12 Si. Thus the precipitate compositions clearly reflect changes in the bulk alloy Ni and Si chemistry.

- Cu approaches full depletion at very high ϕt_e, at a matrix level of ≈ 0.03%, while there is still a modest fraction of the other elements left in solution.

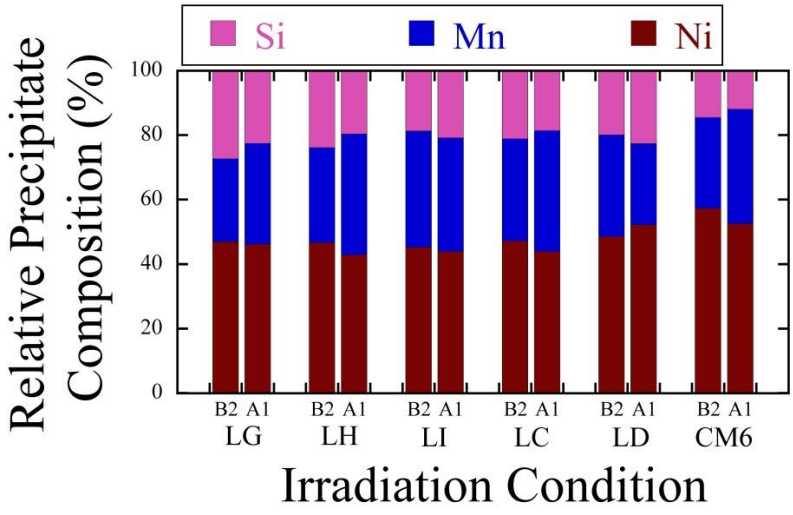

Figure 5.6. The average precipitate Mn-Ni-Si compositions at medium and very high ϕt_e.

- Figure 5.7 illustrates the evolution of the morphology of precipitates with increasing ϕt_e in the high Ni-Cu content (LD) steel. Figure 5.7a shows a cross section of a precipitate at medium ϕt_e, where there appears to be a Mn-Ni-Si shell surrounding a Cu-rich core, consistent with previous experimental results and Lattice Monte Carlo simulations [5–8]. Figure 5.7b shows a precipitate at very high ϕt_e, where there is a Cu-rich core-shell structure, similar to that at medium ϕt_e, but this feature is associated with a nearly "pure" Mn-Ni-Si co-precipitate appendage. Such appendages have also been seen in irradiated surveillance steels [9].

In summary, the evolution between medium and very high ϕt_e is dominated by the continued flow of Mn-Ni-Si to the precipitates. In Cu-free steels it is likely that the precipitates evolve from matrix feature solute-defect clusters initially formed in displacement cascades. At higher supersaturated Cu contents, Cu precipitates form and become rapidly enriched in Mn, Ni and Si. While initially the Mn, Ni and Si form a shell around the Cu-rich core, an almost pure Mn-Ni-Si co-precipitate appendage continues to grow on the CRP at higher ϕt_e.

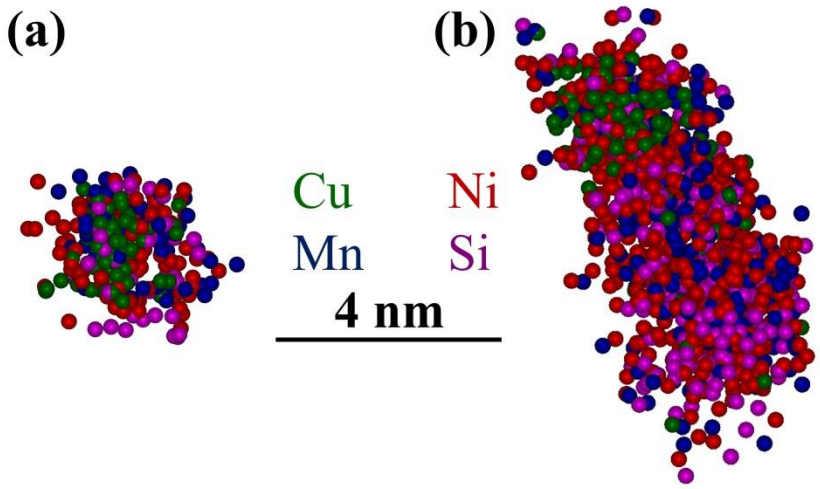

Figure 5.7. APT maps of typical precipitates in the high Ni-Cu content steel (LD): (a) at medium ϕt_e, and (b) at very high ϕt_e.

5.5 APT Precipitate Compositions vs Mn-Ni-Si Intermetallic Phases

As Figure 5.6 demonstrated, the Mn-Ni-Si compositions of the precipitates in Cu-free steels are similar to those in the co-precipitates formed in Cu-bearing steels at very high ϕt_e. These compositions can be compared to known intermetallic phases in the corresponding Mn-Ni-Si ternary and Mn-Ni-Si-Fe quaternary systems. As described in detail in [10], recent

Calphad-Thermocalc computational modeling studies carried out at the University of Wisconsin (UW), in collaboration with UCSB, have shown there are a variety of equilibrium Mn-Ni-Si intermetallic phases in the Fe-Mn-Ni-Si quaternary system at low RPV operating temperatures. Briefly, this model was based on thermodynamic parameters from a commercial database, which predicts varying fractions of Γ_2 ($Mn(Ni_xSi_{1-x})_2$, T6) and G ($Mn_6Ni_{16}Si_7$, T3) phases, depending on the alloy Mn-Ni-Si composition. In this case, the bulk composition of the alloy was determined from the average APT values measured in this study.

Figure 5.8 shows the APT Mn-Ni-Si precipitate compositions, from the very high ϕt_e ATR1 condition, (filled symbols) plotted on the Mn-Ni-Si ternary phase diagram for both the medium (circles) and high (squares) Ni content steels compared to the predicted average compositions for the CALPHAD model. The model predicts 100% Γ_2 (T6) (open cyan square) for the highest Ni content, Cu-free (CM6) steel, which is very consistent with the APT data (filled cyan square). The model predicts ≈ 73% G (T3) and ≈ 27% Γ_2 (T6) phases (open red square) for the high Ni-Cu content (LD) steel, again very close to the measured value (filled red square). The medium Ni content alloys cluster around the Si-rich end of the Γ_2 phase field (filled circles), shown by the heavy green line at ≈ constant Mn, while the commercial database predicts the presence of either G or Γ_2 phases (open circles).

The precipitates in the Cu-free, medium Ni content steel (LG, filled blue circle) have slightly less Mn and higher Ni than the other three medium Ni content steels that contain various amounts of Cu. This might be interpreted to suggest that there is some effect of Cu

on the dominantly Mn-Ni-Si phases. However, these differences are actually highly consistent with variations in the bulk alloy Ni contents, that trade off with Mn in the precipitates, at approximately constant Si. For example, the medium Ni content alloy with the greatest fraction of Mn in the precipitates (LH), which is furthest to the right of the Γ_2 line in the Mn-Ni-Si ternary (filled green circle), has a bulk Mn/Ni of 1.6. On the other hand, the alloy furthest to the left of the Γ_2 line (LG, filled blue circle) has much less bulk Mn, with a bulk Mn/Ni of 1.2.

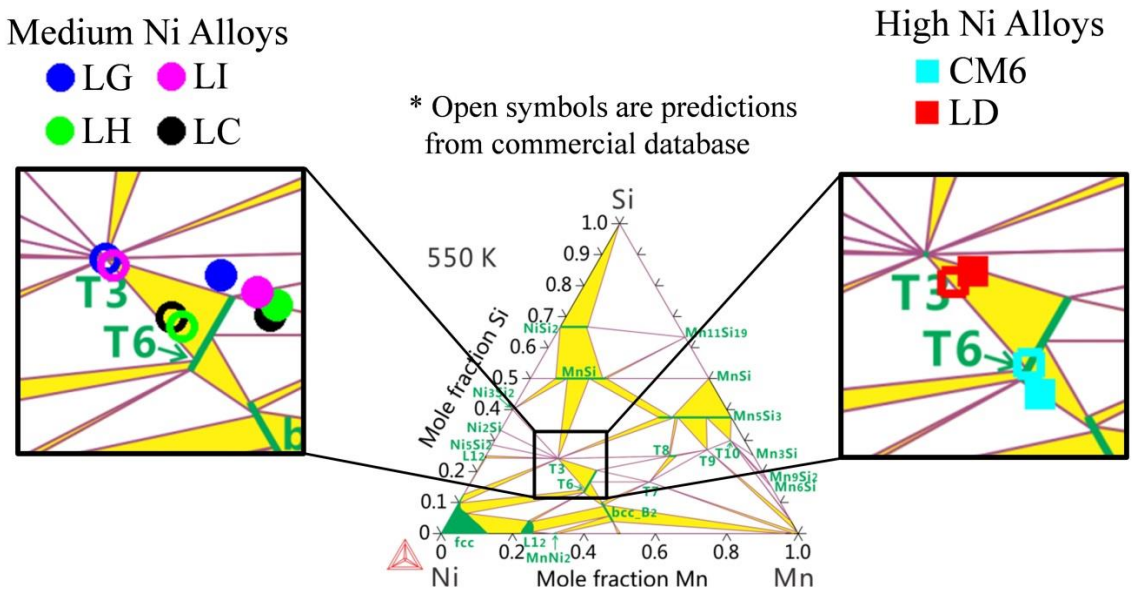

Figure 5.8. A Gibbs triangle showing APT Mn-Ni-Si precipitate compositions (filled symbols) at very high ϕt_e compared to UW CALPHAD predictions for a commercial database (open symbols) [10]. Note that the T3 and T6 phases are referred to in the text as G and Γ2, respectively.

While the relatively good agreement between Thermocalc average composition predictions and the APT measurements is encouraging, there are also important differences that should be noted. In particular, the commercial database predicts the presence of multiple

near-stoichiometric phases in some alloys. In contrast, the APT measurements show that there is a unimodal distribution of MNSP precipitate compositions that decreases in extent with increasing precipitate size, converging to a relatively narrow range of Mn-Ni-Si at the largest r_p, seen in Figure 5.9. The corresponding average compositions also appear to vary somewhat with r_p. The variation and spread in compositions with r_p is an example of the additional insight available from APT measurements, though the large spread at small sizes is predominantly caused by counting statistics due to the low efficiency of the LEAP.

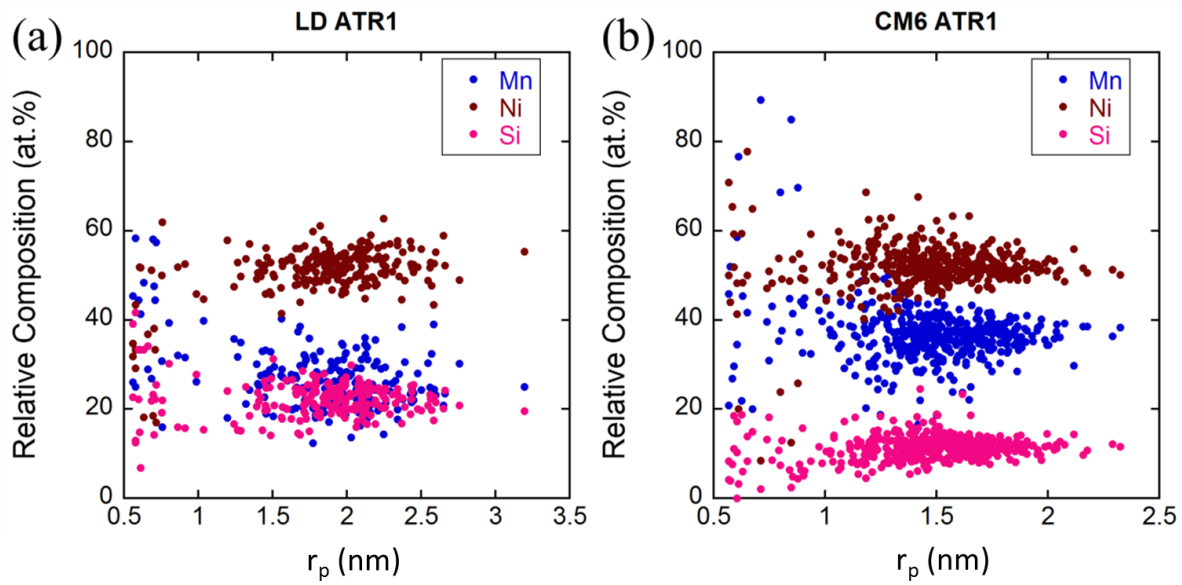

Figure 5.9. Precipitate relative MNS composition for the high Cu-Ni steel (LD) and Cu-free, highest Ni content steel (CM6) form the very high ϕt_e condition.

5.6 Precipitate Structure

The very close agreement between equilibrium thermodynamic predictions and APT precipitate compositions and f_v present a very strong case that the precipitates are in fact intermetallic phases. While not within the scope of this thesis, it should be noted that

Sprouster et. al. at Brookhaven National Laboratory (BNL), in collaboration with UCSB, used X-ray diffraction measurements at the National Synchrotron Light Source II to determine the crystal structure of the precipitates from the ATR1 condition [11]. XRD patterns for LD before and after irradiation are shown in Figure 5.10, from [11].

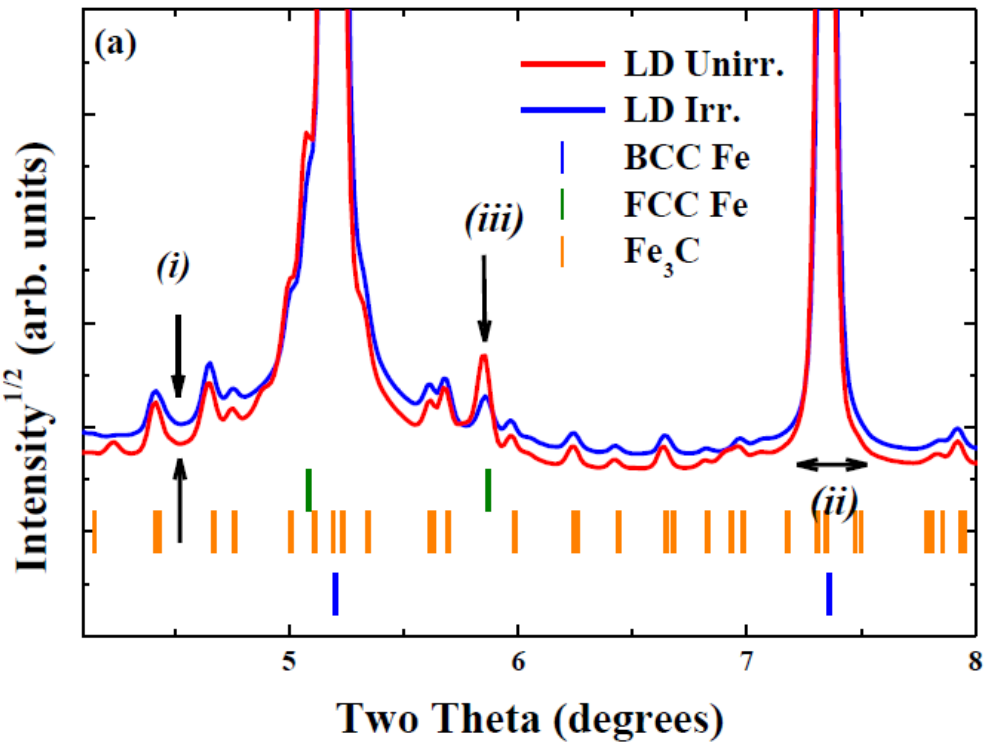

Figure 5.10. XRD pattern for LD in the baseline and ATR1 irradiated conditions showing an increase in the structured scattering background following irradiation, from [11].

The G phase, referred to as the T3 phase in Figure 5.8, is a complex intermetallic phase with the $Mg_6Cu_{16}Si_7$-type structure and the stoichiometric composition of $Mn_6Ni_{16}Si_7$. It belongs to the space group Fm-3m and has a lattice constant of 1.1158 nm [12, 13]. The Γ2 phase, referred to as the T6 phase in Figure 5.8, has a finite phase field with a composition of

$Mn(Ni_xSi_{1-x})_2$ [10]. It has the Cu_2Mg structure and belongs to the Fd-3m space group with a lattice parameter of 0.6687 nm [12].

The peaks from the Mn-Ni-Si phases, which are significantly broadened due to the nm-scale of the precipitates, are thought to be the cause of the increase in the background of the irradiated samples. Thus, the Rietveld refinement incorporated either the G ($Mn_6Ni_{16}Si_7$) or Γ_2 ($Mn(Ni_xSi_{1-x})_2$) phases and used a fixed size for the Mn-Ni-Si precipitates, but allowed the f_v and lattice parameter to vary. Interestingly, when incorporating the G phase into the refinement, the best fit f_v and lattice parameter were very consistent with the APT results and the theoretical lattice parameter for all alloys except CM6. On the other hand, CM6 returned non-physical parameters when refined with the G phase, but resulted in f_v and lattice parameters consistent with APT and theory when fit with the Γ_2 phase [11].

Table 5.7. Summary of experimental and modeling predictions from the ATR1 irradiated condition.

Alloy	Nominal Composition (at.%)		Likely Phase		
	Bulk Cu	Bulk Ni	APT Composition	Thermocalc Prediction	XRD Structure
CM6	0.02	1.57	Stoichiometric Γ_2	Γ_2	Γ_2
LD	0.33	1.16	Stoichiometric G	G	G
LC	0.36	0.81	Si rich end of Γ_2	G	G
LI	0.17	0.69	Si rich end of Γ_2	Γ_2	G
LH	0.09	0.69	Si rich end of Γ_2	G	G
LG	0.00	0.69	Si rich end of Γ_2	Γ_2	G

A summary of APT, XRD and CALPHAD predictions based on the Thermocalc database is shown in Table 5.7. Two alloys, CM6 and LD, have very consistent agreement among both experimental techniques and the equilibrium predictions. The medium Ni alloys

all show precipitate compositions near the Si-rich end of the Γ_2 phase, though XRD shows the precipitates to have the G phase structure. The models predict either the G or Γ_2 phases for these 4 alloys. The reason for this variation in predicted phase for alloys with nominally the same Ni, Mn and Si is because the models were calibrated using the measured APT compositions, which showed wider variations in Ni and Mn for the alloys. It is unclear why APT shows compositions closer to one phase, while XRD shows the structure of another, but the likely reason is the very small nature of the precipitates. With such high surface area compared to the total volume for the nm-scale precipitates, any interfacial chemistry changes, possibly driven by the surface energy between the MNS phase and Fe matrix, would have a large result on the average precipitate composition. Unfortunately, accurately determining whether the precipitate has, for example, Mn enrichment at the interface is not possible due to resolution limits of APT. In addition, the phase diagram shown in Figure 5.8 has not been experimentally verified, because reaching equilibrium at such low temperatures is not feasible due to the low kinetics. Thus, it may be that the phase field for the G phase is much larger than predicted and does not require exact stoichiometry. Last, the role of radiation induced segregation should not be ruled out.

5.7 Role of Ni at Very High ϕt_e

As was shown in Figure 5.3, at medium ϕ_e Cu is the dominant variable dictating both the total and MNSP f_v. Alternatively, at very high ϕt_e condition, large f_v of MNSP form even in steels that contain no Cu. Figure 5.11 shows the MNSP f_v, again with the Cu mole fraction being subtracted from the total f_v as in Figure 5.3 for the medium ϕt_e condition, as a function

of a) Cu and b) Ni. The medium Ni steels, labelled as blue circles in Figure 5.11a, all have ≈ the same MNSP f_v, even with bulk Cu contents varying from 0 to 0.35%. This is because the very high ϕt_e is well beyond the range where Cu is needed to catalyze Mn-Ni-Si precipitation. Indeed, the small increase in the Mn-Ni-Si f_v with increasing Cu is largely due to the fact that slightly higher Ni contents happen to accompany the increase of Cu in this case. In contrast to the effect of Cu, higher Ni contents cause a significant increase in Mn-Ni-Si f_v in the higher Ni content alloys (LD and CM6) seen in the green in Figure 5.11a. The role of Ni can be seen much more clearly in Figure 5.11b, where there is a strong correlation between the bulk Ni content of the alloys and the MNS f_v. This is drastically different at medium ϕt_e, seen in Figure 5.3b, where there is little correlation between the bulk Ni and MNS f_v.

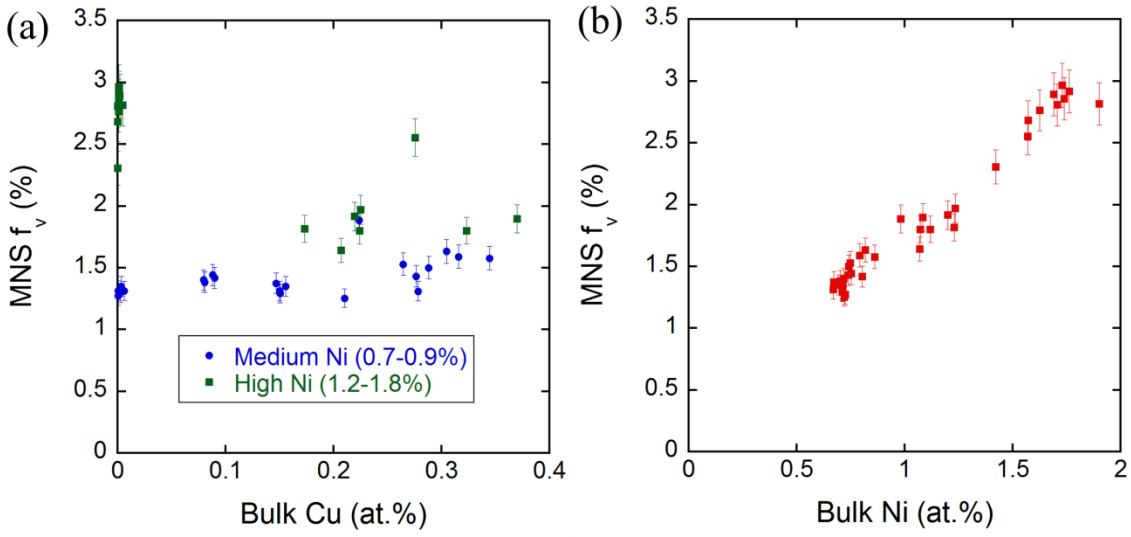

Figure 5.11. MNS f_v from the very high ϕt_e condition as a function of a) Cu and b) Ni.

As noted previously, the total APT local chemistries vary from tip to tip, allowing characterization of the effects of both smaller single-alloy and larger alloy-to-alloy changes

in composition. Figure 5.12 shows the precipitate individual solute f_v as a function of local composition for Cu (a), Ni (b), Mn (c), and Si (d). The plots of f_v versus bulk solute for Cu and Ni form a tight band in both cases, with least square fit slopes of 0.95 and 0.89, combined with thresholds of ≈ 0.01% Cu and ≈ 0.05% Ni, respectively (Fig. 10 a and b). In the case of Mn, all the alloys fall into one tight band, except for the highest Ni content, Cu-free (CM6) steel (Fig. 10c). The least square fit slope for the 0.8-1.2% Ni steels is 0.36 with an intercept of Mn ≈ -0.32%. The corresponding least squares fit Mn slope for the highest Ni content, Cu-free alloy is 0.80 with an intercept of Mn ≈ 0.17%. There are also two bands for the effect of Si on f. The medium Ni content steels with varying Cu content (LG, LH, LI, LC) fall along a line with a least square fit slope of 0.80 and a threshold of Si ≈ 0.07%, while the least square fit slope is 0.63 with an intercept of Si ≈ -0.14%, for the highest Ni content, Cu-free and high Ni-Cu content steels (CM6 and LD). Note the high Ni content fits are less reliable in the cases of Mn and Si since they are for only 1 and 2 alloys, respectively.

The very systematic behavior in precipitate f_v as a function of alloy composition will be used to develop physically based chemistry factors for advanced ΔT embrittlement models. The most significant observation is that the precipitation behavior is consistent with two Mn-Ni-Si intermetallic phases at ≈ 550K that are found in Thermocalc evaluations. Further at very high ϕt_e, Ni has a dominant role in precipitation, compared to Mn and Si, in terms of both the strength of the effect itself, and the wider range of Ni content in the steels studied here. These results are also very consistent with previous observations on the effect of Ni and Mn on both the precipitates and hardening and also help clarify the role of Si [3, 5–

7, 14–23]. However, since developing robust physically based chemistry factor will require evaluation of a wider range of alloy compositions and irradiation conditions; this will not be discussed further.

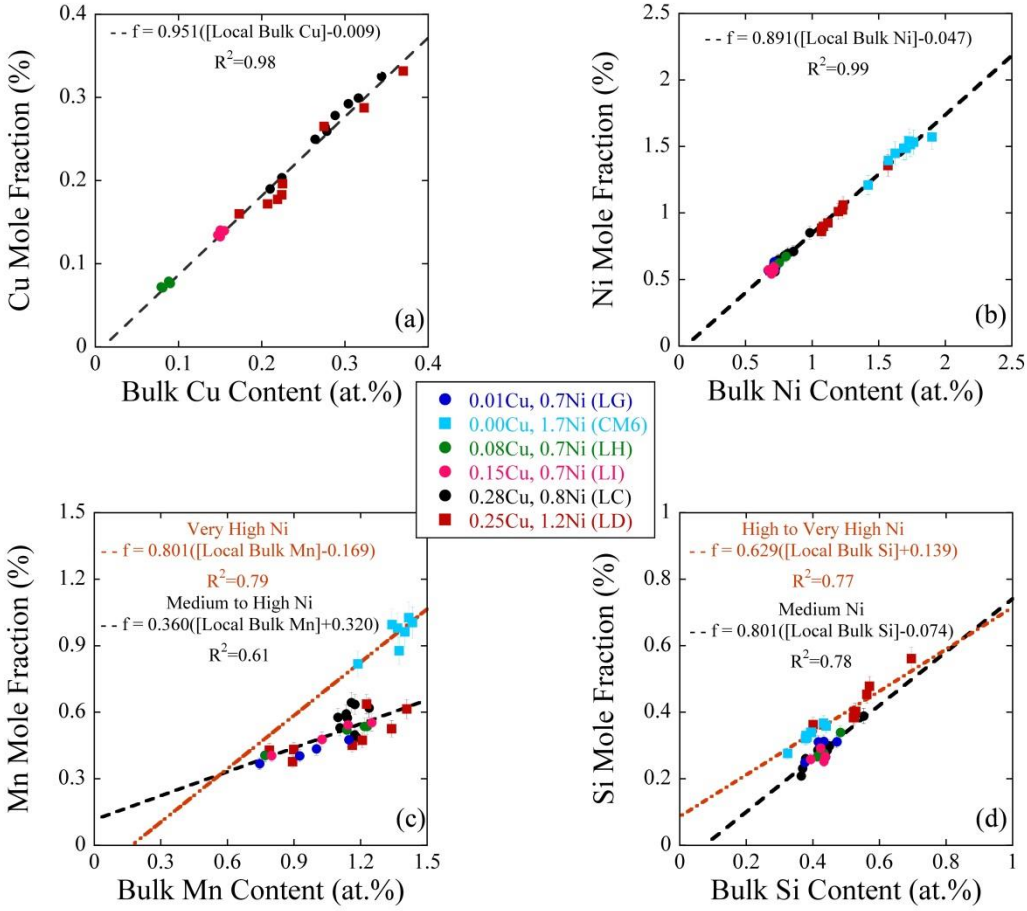

Figure 5.12. The precipitate f_v for individual elements as a function of their corresponding bulk solute compositions.

5.8 Effect of low Ni

The strong effect of Ni at very high ϕt_e was clearly demonstrated in section 5.6. Two high Cu (0.4%) alloys with 0.00% and 0.18% Ni were also included in the very high ϕt_e

ATR1 irradiation and allow for the study of Cu, Mn and Si precipitation when the Ni is significantly reduced or even removed.

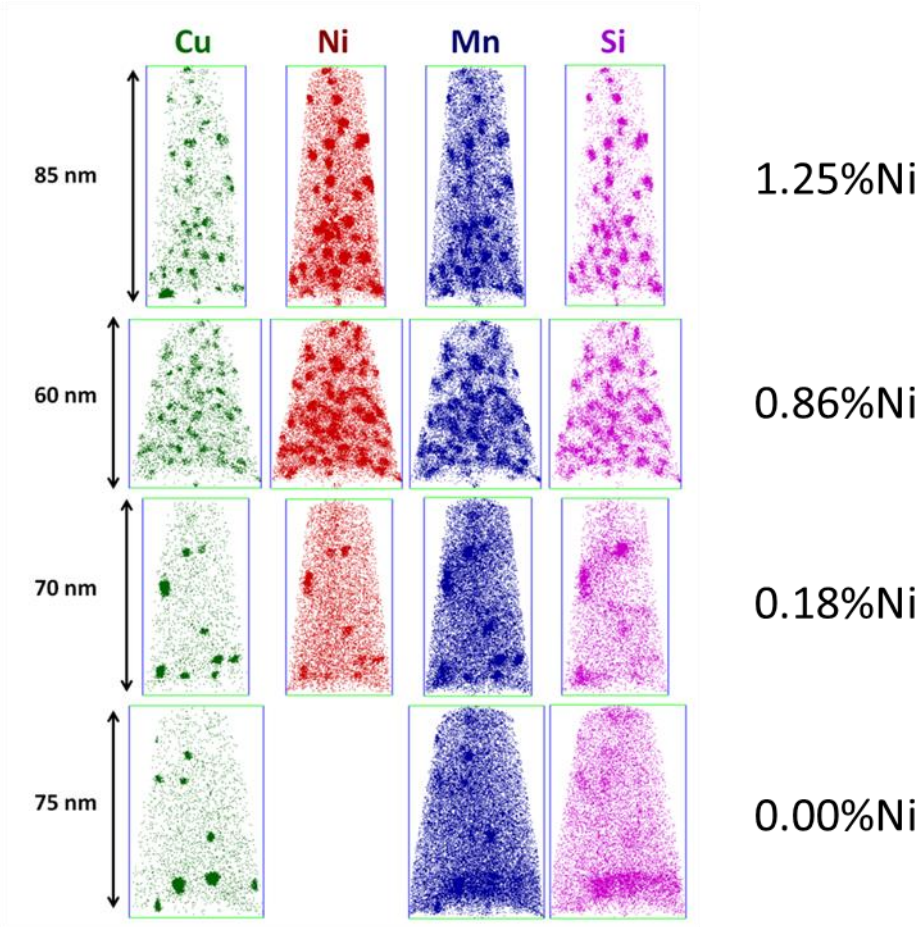

Figure 5.13. Atom maps from the 4 high Cu steels with a) 1.25% Ni, b) 0.86% Ni, c) 0.18% Ni, and d) 0.00% Ni.

Atom maps from the 4 high Cu (0.3-0.4%) steels with varying Ni contents from 0.00% to 1.25% can be seen in Figure 5.13. Note that results from the top two samples, LD and LC, were discussed in significant detail in sections 5.4 - 5.6. The atom maps demonstrate a number of differences at low vs high Ni. The Mn and in particular Si are much more diffuse around the Cu clusters in the lower Ni steels and the precipitate N is significantly

reduced. This reduction in number density, coupled with a constant amount of precipitated Cu in all cases, results in larger precipitates in the low Ni steels, as seen quantitatively in Figure 5.14. The reason for the increase in <d> and reduction in N when going from 0.8 to 1.2% Ni is likely due to the earlier coarsening that is occurring in the highest Ni steel. A reduction in precipitate number density with decreases in bulk Ni content has been reported previously for thermally aged steels [24]. Mn and Ni have been shown to reduce the Fe-Cu interfacial interface energy by forming a shell around the Cu-rich core [5, 18, 25, 26]. The nucleation step for Cu-rich precipitates is likely more difficult at lower Ni contents, resulting in a reduced number density.

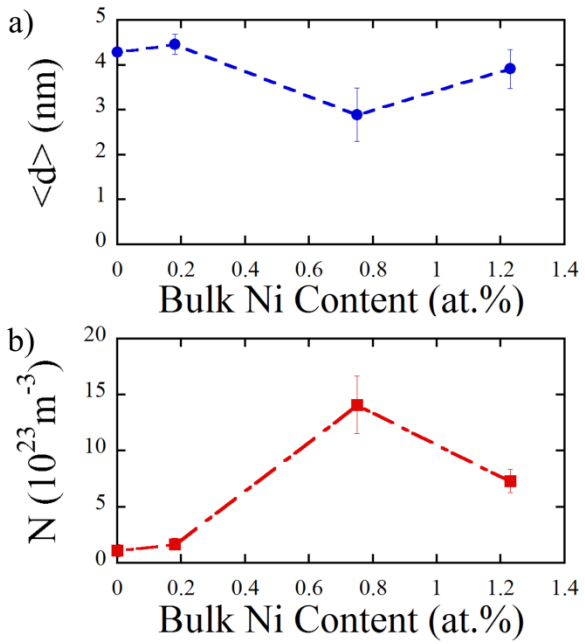

Figure 5.14. Average precipitate size and number density as a function of Ni for the 4 high Cu steels.

Figure 5.15 shows the total f_v for the 4 high Cu steels. The differences in Cu mole fraction are caused by differences in bulk Cu of the measured APT tips. The more important

point is that the Mn and Si which have precipitated are significantly reduced at lower Ni contents.

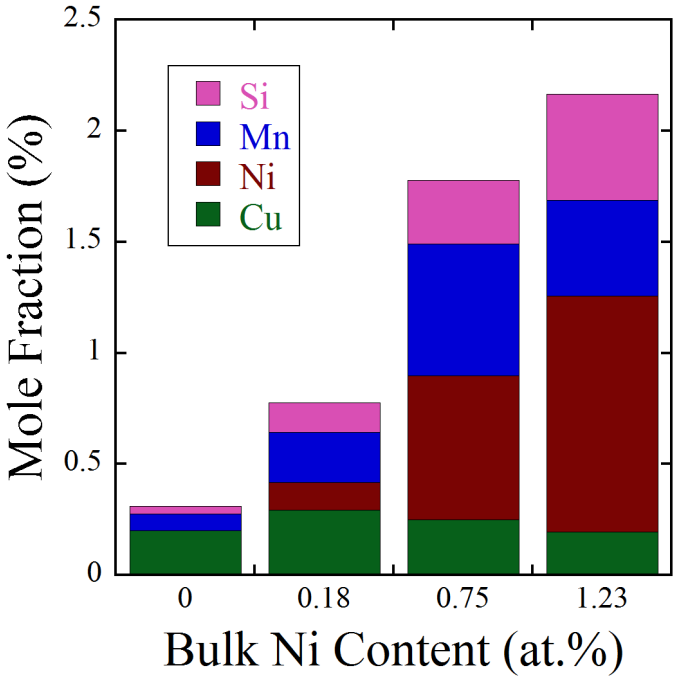

Figure 5.15. Precipitate f_v vs bulk Ni for steels all containing 0.3-0.4% nominal Cu.

As results from the two higher Ni steels have already been discussed, the two lower Ni steels will now be examined in more detail. First, as shown in Figure 5.15, the precipitates in the two lower Ni steels are dominated by Cu. The precipitates are ≈ 65% and ≈ 40% Cu in the Ni-free and 0.18% Ni steel, respectively. The balance of the precipitates is made up of Mn, Ni and Si, with Mn making up ≈ 2-3x that of the Si. Precipitates from the Ni free steel can be seen in more detail in Figure 5.16. One example is given of precipitates likely on a dislocation and one example of a precipitate not on a dislocation are shown in a) and b), respectively. While APT cannot detect dislocations themselves, they can observe them if the

dislocations are enriched in solutes. In the case of Figure 5.16a, Mn and Si can be seen to be enriched along a line, with two large Cu precipitates also on the same line.

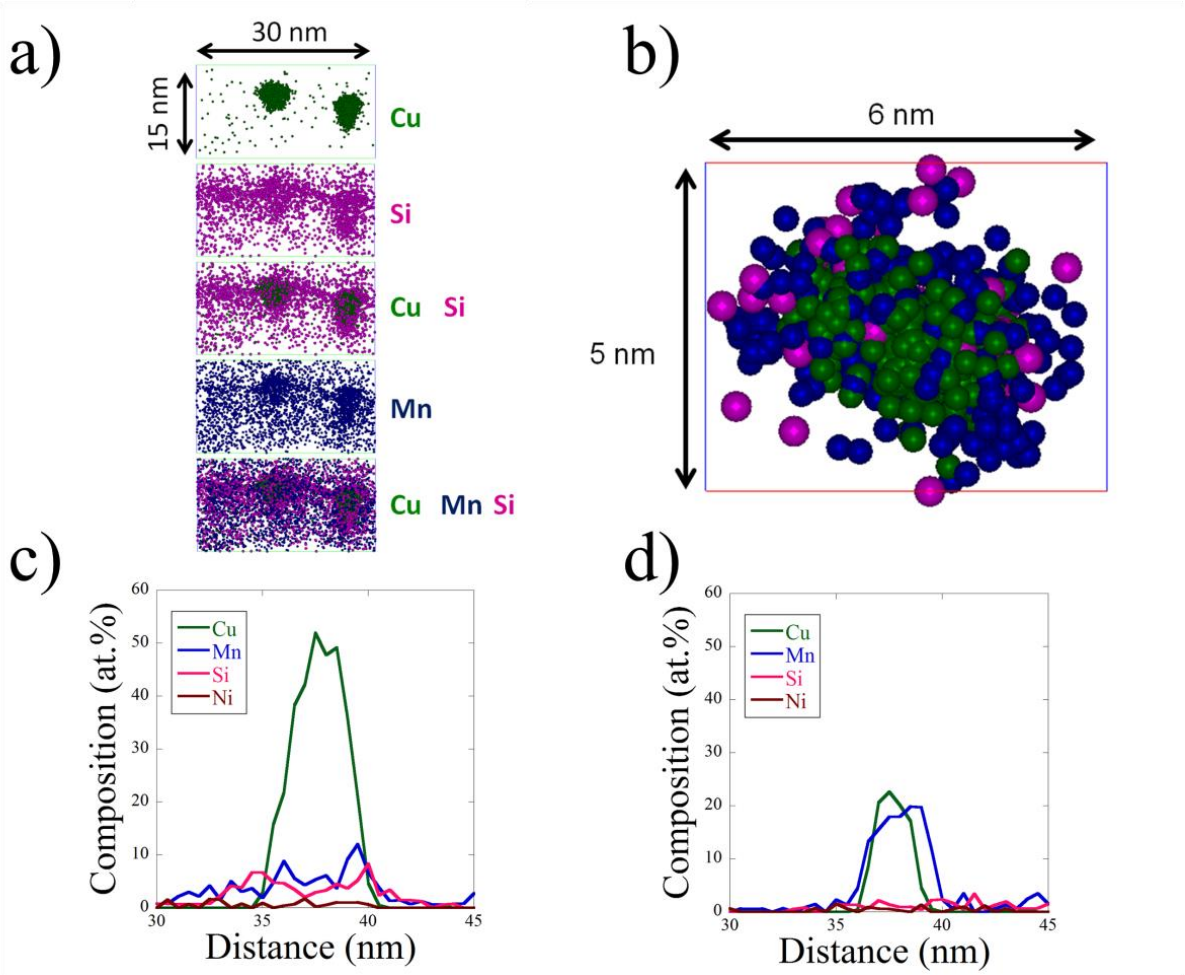

Figure 5.16. Blown up pictures of precipitates from the Ni steel (LA) showing a) precipitates and Si enrichment along a dislocation and b) a precipitate in the matrix.

A line compositional profile through one of the precipitates in Figure 5.16a is seen in Figure 5.16c. In this case, Si is enriched up to ≈ 7% with peaks on both sides of the precipitate, forming what appears to be a shell. On the other hand, the line compositional profile through the precipitate in Figure 5.16b, shown in Figure 5.16d, shows very little Si

enrichment to the Cu-rich cluster. Thus, Si only appears to associate with the Cu-rich precipitates if they nucleate along dislocations, where Si would likely segregate with or without a precipitate present. For precipitates not on dislocations, there is very little Si enrichment when Ni is not present. In either case, Mn segregates to the Cu-rich clusters and in some case, as seen in Figure 5.16b and d, can exist in equal amounts as the Cu.

The 0.18% Ni steel shows very similar trends to the 0.00%Ni steel. Two precipitates, and corresponding line compositional profiles through them, from the 0.18% Ni steel are shown in Figure 5.17. Figure 5.17a and Figure 5.17c show a smaller precipitate and the corresponding line compositional profile showing very little Ni enrichment. In this case, there is again significant Mn enrichment that appears to form a shell, but also shows significant enrichment through the core of the precipitate. The Ni composition peaks at ≈ 6% with even less Si. A separate, much larger precipitate, seen in Figure 5.17b contains a Cu-rich portion and a Mn-Ni-Si rich portion, similar to that found in Figure 5.7. In this case, the Ni is approximately equal to the Mn in the Mn-Ni-Si portion of the precipitate, even though it is present in a very dilute amount of 0.18% vs 1.4% for Mn. In addition, the Si is significantly enriched in the Mn-Ni-Si portion, representing 27% of the Mn, Ni and Si, with the Ni and Mn being approximately equivalent. In the Cu-rich portion of the precipitate, the Mn is much more enriched compared to the Ni and Si.

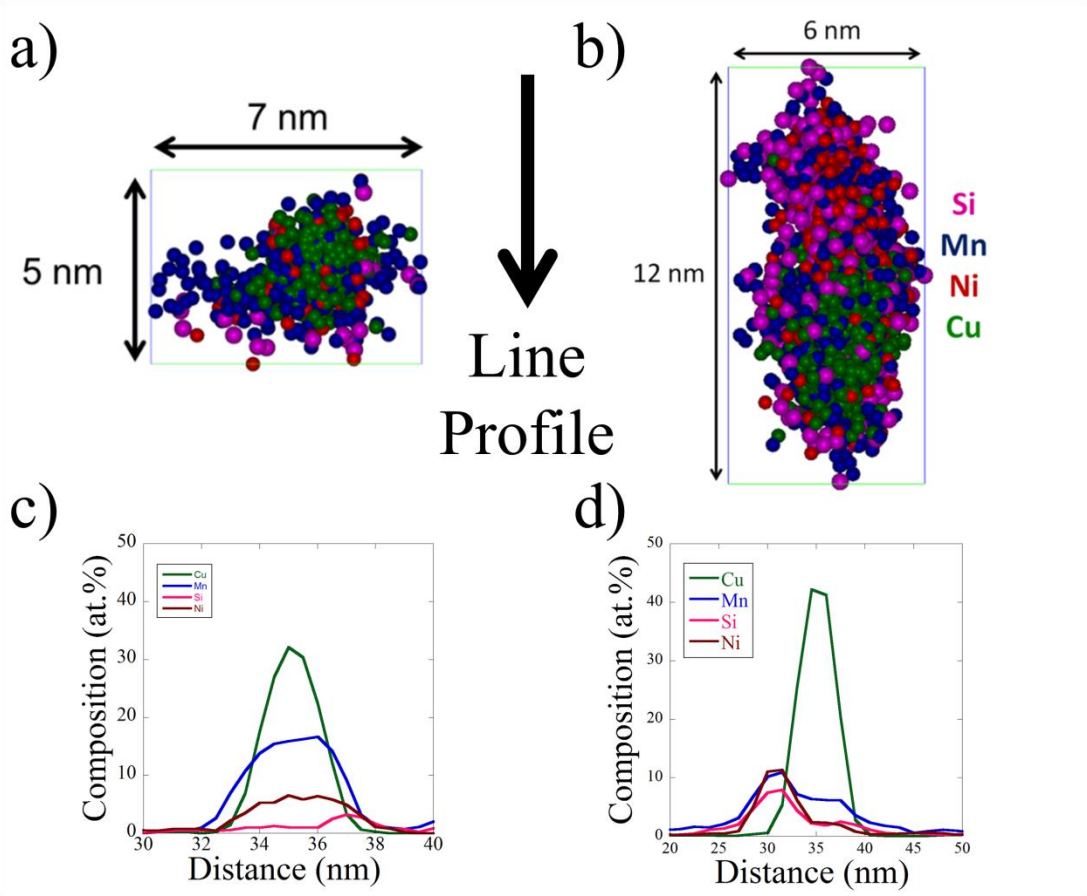

Figure 5.17. Line profiles through precipitates in the 0.18% Ni steel (LB) showing a small precipitate with little Ni and b) a larger precipitate with a Mn-Ni-Si appendage.

While the precipitates in the Ni free steel are likely just Cu precipitates that have been enriched in Mn and Si, the 0.18% Ni steel clearly contains some precipitates with a Mn-Ni-Si appendage. Interestingly, comparing the relative Mn-Ni-Si in just the MNS appendage to the results from the medium Ni (0.7-0.8%) steels presented in section 5.5, shows very similar results, as seen in Table 5.8, though the Ni is less enriched and Si more enriched in LB than in the medium Ni steels (LC, LG, LH, LI)..

Table 5.8. Relative Mn-Ni-Si in the precipitates for the various steels at very high ϕt_e.

Steel	Measured APT Bulk Ni	Mn	+/-	Ni	+/-	Si	+/-
LB (MNS Appendage)	0.18	35.5	*	37.0	*	27.4	*
LC	0.80	37.5	1.8	43.9	1.2	18.6	1.1
LG	0.71	31.3	2.9	46.2	1.5	22.5	1.6
LH	0.73	37.5	2.4	42.9	1.4	19.6	1.1
LI	0.70	35.3	4.4	43.9	2.5	20.9	1.9

*Note that the uncertainty cannot be measured for the LB appendage because only1 was measured.

One final interesting point to note in the lower Ni steels is the presence of a high density of dislocation loops, which are enriched in Mn, Ni and Si and also appear to act as nucleation sites for Cu precipitates. An example run of the 0.18% Ni steel with a high loop density, along with a higher magnification image of one of the loops are seen in Figure 5.18 and Figure 5.19, respectively. It should be noted that 4 loops were observed in this small run, while 1 loop was observed in every ≈ 5-10 runs for the medium and high Ni steels. Unfortunately, only several APT samples were taken from these two alloys, which makes it difficult to determine whether they actually have a higher loop density or whether the APT randomly sampled a small region containing more loops. Post irradiation annealing results, discussed in Chapter 6, show that the hardening features in the low Ni steels are much more stable than the higher Ni steels at annealing temperatures of 400-450°C. Whether or not the loop density is in fact higher, the reason behind the higher density, and the high temperature stability of the loops are ongoing investigations and will not be discussed further.

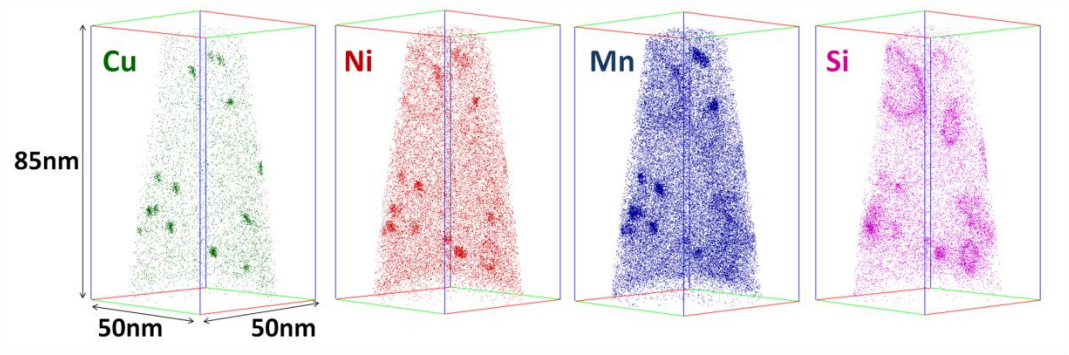

Figure 5.18. Atom maps from the high Cu, 0.18% Ni steel with a high density of dislocation loops.

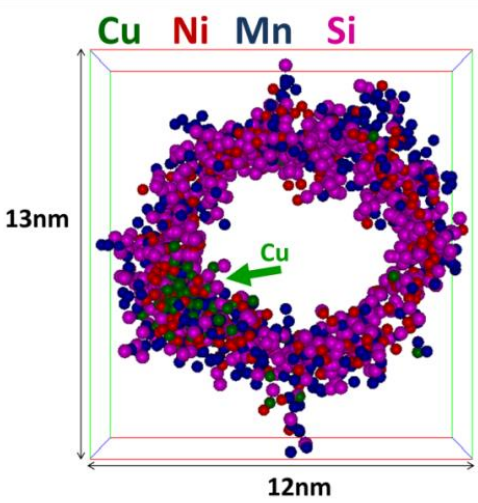

Figure 5.19. Magnified view of a dislocation loop from the tip seen in Figure 5.18 showing Mn, Ni and Si enrichment along the entirety of the loop along with a Cu-rich precipitate.

5.9 Results from Surveillance Program Irradiation

In addition to the high flux test reactor irradiations, material from a surveillance irradiation was also examined. This material, from the Ringhals reactor in Sweden, was provided by Oak Ridge National Lab and was irradiated at a flux of 1.5×10^{11} n/cm^2-s to a ϕt of 6.1×10^{19} n/cm^2. The flux in this case was > 3 orders of magnitude lower than the test

reactor irradiations. The measured bulk APT composition of the low-Cu steel is given in Table 5.9.

Table 5.9. Measured APT bulk composition for the Ringhals surveillance specimen.

Specimen	Cu	+/-	Ni	+/-	Mn	+/-	Si	+/-
Ringhals	0.03	0.01	1.43	0.08	1.12	0.18	0.26	0.06

Atom maps from one of the Ringhals steel can be seen in Figure 5.20. Even though this steel is low in Cu, containing ≈ 0.03%, Cu can still be seen in some of the clusters. The Mn, Ni and Si is clearly clustered and P is also seen to be enriched in some of the clusters. In addition, two dislocations can be seen that are enriched in Ni, Mn, Si and P.

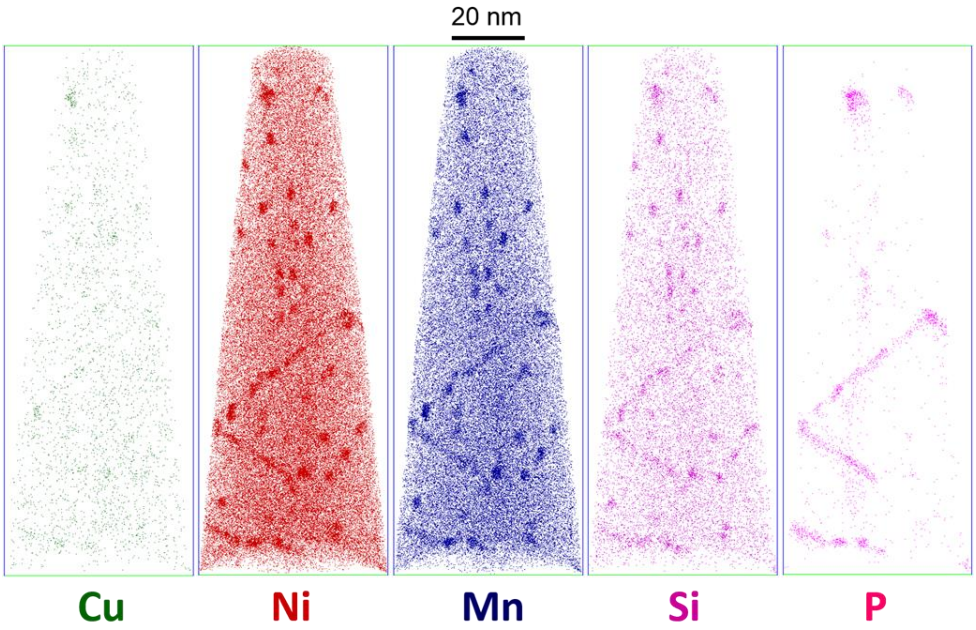

Figure 5.20. Atom maps from the Ringhals surveillance irradiated specimen.

The most comparable UCSB steel is CM6, which nominally contains 0.02%Cu and 1.74%Ni. Figure 5.21 shows the measured f_v for the Ringhals steel, (blue circle) and various

conditions of CM6 (all other points) as a function of ϕt_e. The different colors and shapes represent conditions with different ϕ, showing a ϕ range from 0.1×10^{12} n/cm^2-s (Ringhals) to 230×10^{12} n/cm^2-s (ATR1). In addition, the relative precipitate compositions for the Ringhals and CM6 ATR1 conditions are shown in Table 5.10.

Table 5.10. Relative amount of Mn, Ni and Si in the clusters for the Ringhals N180 condition and the CM6 ATR1 condition.

Steel	Condition	Mn	Ni	Si
Ringhals	N180	32.9	55.2	11.9
CM6	ATR1	35.5	52.6	11.9

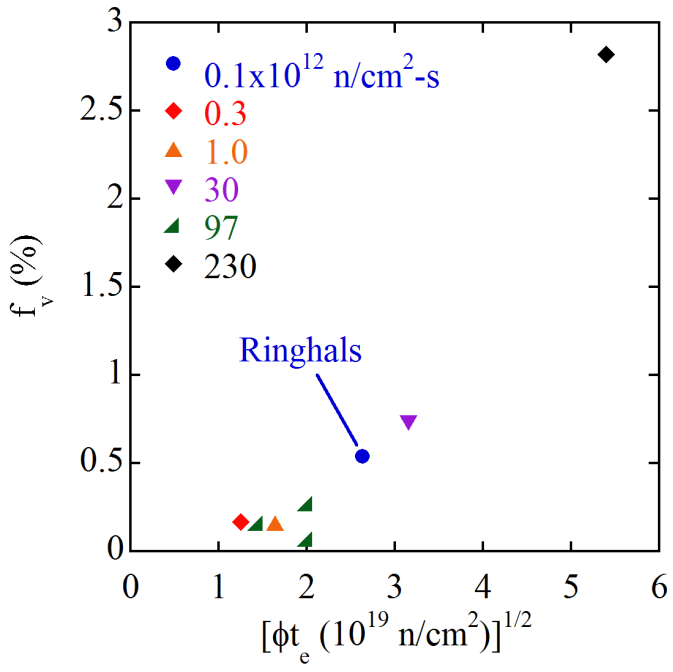

Figure 5.21. f_v as a function of ϕt_e for Ringhals N180 (blue circle) and various conditions of CM6 (all others).

The very consistent precipitate compositions and f_v between the Ringhals and CM6 precipitates, again with ϕ differences between the Ringhals and ATR1 condition of 4 orders

of magnitude, offer further evidence that the precipitates in these irradiated steels are thermodynamic phases and are not significantly altered at high ϕ.

5.10 Hardening

Relating the precipitates to hardening will be discussed rigorously in Chapter 8, but will be briefly addressed here to show the enormous amount of hardening present in the very high ϕt_e test reactor irradiated steels. The Russell-Brown model relates changes in yield stress ($\Delta\sigma_y$) to the precipitate radius (r) and volume fraction (f_v) of precipitates using the following relation, $\Delta\sigma_y \propto \sqrt{f_v}/r$ [27]. While a more rigorous correlation uses a size dependent strength parameter, $\alpha(r)$, the determination of α will be presented in Chapter 8. $\Delta\sigma_y$ vs $\sqrt{f_v}/r$ is plotted in Figure 5.22 for the 6 UCSB steels with Ni contents > 0.7% presented in this chapter (LC, LD, LG, LH, LI, CM6). Included with the ATR1 and TU data are data from previous UCSB irradiations including data from BR2, which includes the G1 condition, and the IVAR program. Note that the IVAR and some of the BR2 microstructure and hardening data were taken by past staff and students of the UCSB MRPG group. The correlation between the precipitates and hardening is very clear and makes a compelling case that the hardening is primarily caused by the precipitates. In addition, the ATR1 irradiation shows enormous hardening of up to almost 700 MPa. The typical relation for converting $\Delta\sigma_y$ to ΔT is given by [28]

$$\Delta T(°C) \approx 0.68\Delta\sigma_y(MPa) \quad (5.1)$$

Using this relation results in a ΔT of ≈ 460°C for the Cu-free, highest Ni steel (CM6) in the ATR1 condition. It should again be stressed that the ATR1 condition, even when

adjusted for ϕ, has a ϕt_e well above any which would be experienced by an in-service vessel at 80 years. These data is presented not to suggest actual vessels will experience such a large $\Delta\sigma_y$ and ΔT, but to show the importance of including these phases in embrittlement prediction models for extended life.

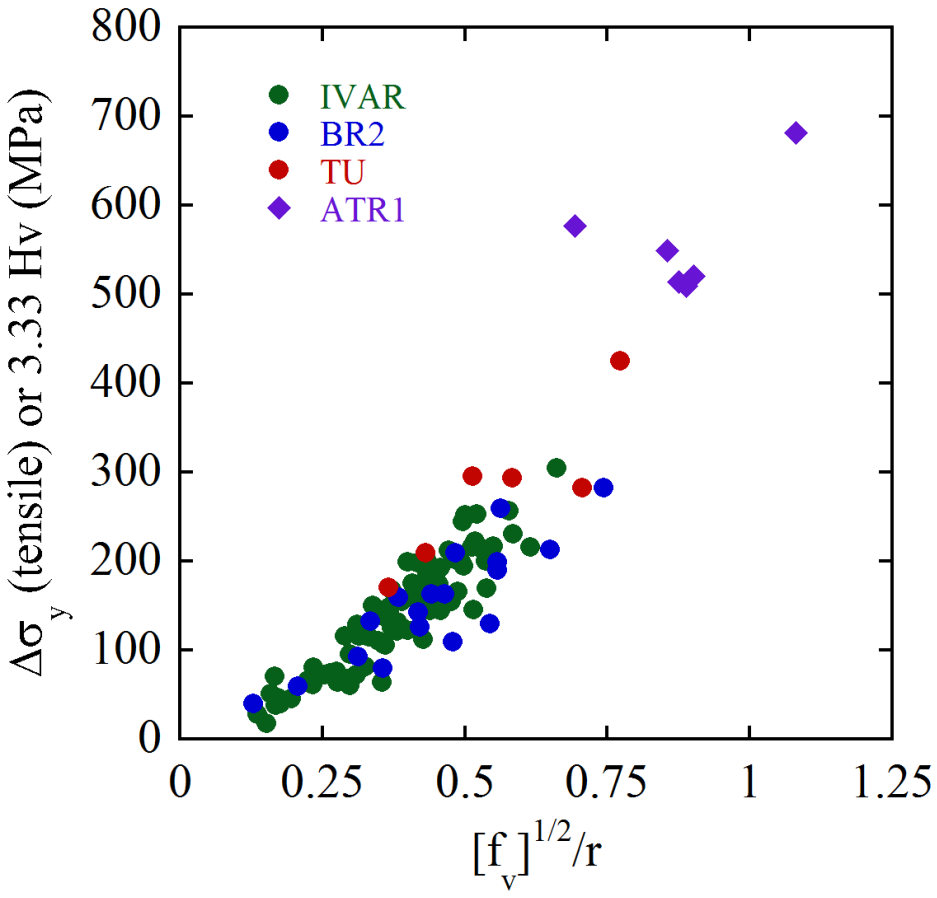

Figure 5.22. Yield stress increase after irradiation vs $\sqrt{f_v}/r$ for steels in a number of different irradiation conditions.

5.11 Summary, Conclusions and Future Work

Large mole fractions of Mn-Ni-Si dominated LBP precipitates form in both Cu-free and Cu-bearing RPV steels at very high ϕt_e. Consistent with longstanding predictions:

- In Cu-free steels the MNSP likely evolve from defect-solute cluster matrix feature precursors that constitute only a small $f_v \approx 0.1\%$ at medium ϕt_e, but subsequently grow to much larger mole fractions at very high ϕt_e.

- Cu catalyzes the initial formation of MNSP. This is especially the case of rapidly forming precipitates at the high supersaturations of Cu. Thus at the high flux-high ϕt condition in this study, Cu and Ni are the primary compositional variables leading to large mole fractions of MNSP.

- However, since the precipitates are dominated by Mn-Ni-Si, Cu has a much weaker effect at very high ϕt_e, while Ni has the major influence on the f.

- The relative amounts of Mn, Ni and Si are very consistent with known intermetallic phases. The precipitates in the high Ni-Cu content (LD) steel are close to G phase ($Mn_6Ni_{16}Si_7$), while they are close to the Γ_2 phase ($Mn(Ni_xSi_{1-x})_2$) in the highest Ni content, Cu-free (CM6) steel. Thermocalc predictions for these two steels are very consistent with the experimentally found compositions. The precipitate compositions in the other medium Ni content alloys were in reasonably good agreement with the Si-rich end of the Γ_2 phase field although the Thermocalc predictions vary somewhat from these compositions in this case.

- Cu-rich precipitates still formed in the Ni-free and low Ni steels, though at a much lower number density than the medium and high Ni steels. In addition, while Mn was found to

enrich the Cu-rich precipitates in all cases, the Si was only associated with them if they were nucleated along a dislocation. An addition of only 0.18% Ni resulted in a Mn-Ni-Si appendage forming on one of the Cu-rich precipitates.

- A low Cu surveillance steel irradiated to a fluence of $6.1x10^{19}$ n/cm2 contained large f_v of MNSP with compositions very similar to those found in the Cu-free, high Ni steel (CM6) in the ATR1 condition. Thus, ϕ does not appear to significantly alter the character of MNSPs.

- The increase in precipitate mole fractions leads to correspondingly large increases in hardness; hence, also leads to severe embrittlement.

5.12 References

1. Eason ED, Odette GR, Nanstad RK and Yamamoto T. "A physically based correlation of irradiation-induced transition temperature shifts for RPV steels," Oak Ridge National Lab, 2007; ORNL/TM-2006/530.
2. Eason ED, Odette GR, Nanstad RK and Yamamoto T. "A physically-based correlation of irradiation-induced transition temperature shifts for RPV steels", *J. Nucl. Mater.* 2013;433:240–254.
3. Odette GR and Lucas GE. "Recent Progress in Understanding Reactor Pressure Vessel Steel Embrittlement", *Radiat. Eff. Defects Solids* 1998;144(1-4):189–231.
4. Odette GR and Lucas GE. "Recent Advances in Predicting Embrittlement of Reactor Pressure Vessel Steels", In: *Proceedings of the 2nd International Symposium on Environmental Degradation of Materials for Nuclear Power Systems-Water Reactors*, ANS; 1986. p. 295.
5. Liu CL, Odette GR, Wirth BD and Lucas GE. "A lattice Monte Carlo simulation of nanophase compositions and structures in irradiated pressure vessel Fe-Cu-Ni-Mn-Si steels", *Mater. Sci. Eng. A* 1997;238(1):202–209.
6. Miller MK and Russell KF. "Embrittlement of RPV steels: An atom probe tomography perspective", *J. Nucl. Mater.* 2007;371(1-3):145–160.
7. Miller MK, Russell KF, Sokolov MA and Nanstad RK. "APT characterization of irradiated high nickel RPV steels", *J. Nucl. Mater.* 2007;361:248–261.
8. Wirth BD, Odette GR, Pavinich W, Lucas GE, et al. "Small Angle Neutron Scattering

Study of Linde 80 RPV Welds", In: *18th ASTM International Symposium on the effects of radiation on materials*, ASTM STP-1325; 1999. p. 102.

9. Miller MK, Powers KA, Nanstad RK and Efsing P. "Atom probe tomography characterizations of high nickel, low copper surveillance RPV welds irradiated to high fluences", *J. Nucl. Mater.* 2013;437(1-3):107–115.

10. Xiong W, Ke H, Wells PB, Barnard L, et al. "Thermodynamic models of low temperature Mn-Ni-Si precipitation in reactor pressure vessel steels", *MRS Commun.* 2014;4(3):101–105.

11. Sprouster DJ, Sinsheimer J, Dooryhee E, Ghose SK, et al. "Structural Characterization of Nanoscale Intermetallic Precipitates in Highly Neutron Irradiated Reactor Pressure Vessel Steels", *Scr. Mater.* 2016;113:18–22.

12. Gupta KP. "The Mn-Ni-Si (Manganese-Nickel-Silicon) System", *J. Phase Equiilibria Diffus.* 2006;27(5):529–534.

13. Hu B, Xu H, Liu S, Du Y, et al. "CALPHAD : Computer Coupling of Phase Diagrams and Thermochemistry Experimental investigation and thermodynamic modeling of the Mn – Ni – Si system", *CALPHAD Comput. Coupling Phase Diagrams Thermochem.* 2011;35(3):346–354.

14. Odette GR. "Radiation Induced Microstructural Evolution in Reactor Pressure Vessel Steels", *Mater. Res. Soc. Symp. Proc.* 1995;373:137–148.

15. Odette GR and Wirth BD. "A computational microscopy study of nanostructural evolution in irradiated pressure vessel steels", *J. Nucl. Mater.* 1997;251:157–171.

16. Odette GR. "Modeling of Irradiation Embrittlement in Pressure Vessel Steels", In: *Irradiation Effects on Pressure Vessel Steels*, IAEA IRRWG-LMNPP-98-3; 1998. p. 438.

17. Mader E. "Kinetics of irradiation embrittlement and the post-irradiation annealing of nuclear reactor pressure vessel steels" [PhD Thesis]. University of California, Santa Barbara, 1995.

18. Odette GR, Liu CL and Wirth BD. "On the Composition and Structure of Nanoprecipitates in Irradiated Pressure Vessel Steels", *Mater. Res. Soc. Symp. Proc.* 1997;439:457–469.

19. Hyde JM, Ellis D, English CA and Williams TJ. "Microstructural Evolution in High Nickel Submerged Arc Welds", In: *20th ASTM International Symposium on effects of radiation on nuclear materials*, ASTM STP 1405; 2001. p. 262.

20. Hyde JM, Sha G, Marquis E a., Morley a., et al. "A comparison of the structure of solute clusters formed during thermal ageing and irradiation", *Ultramicroscopy* 2011;111(6):664–671.

21. Styman PD, Hyde JM, Wilford KB and Smith GDW. "Quantitative methods for the

APT analysis of thermally aged RPV steels", *Ultramicroscopy* 2013;132:258–264.

22. Carter RG, Soneda N, Dohi K, Hyde JM, et al. "Microstructural characterization of irradiation-induced Cu-enriched clusters in reactor pressure vessel steels", *J. Nucl. Mater.* 2001;298(3):211–224.

23. Buswell JT, Phythian WJ, McElroy RJ, Dumbill S, et al. "Irradiation-induced microstructural changes, and hardening mechanisms, in model PWR reactor pressure vessel steels", *J. Nucl. Mater.* 1995;225:196–214.

24. Osamura K, Okuda H, Asano K, Furusaka M, et al. "SANS Study of Phase Decomposition in Fe-Cu Ally with Ni and Mn Addition", *ISIJ Int.* 1994;34(4):346–354.

25. Zhang C and Enomoto M. "Study of the influence of alloying elements on Cu precipitation in steel by non-classical nucleation theory", *Acta Mater.* 2006;54(16):4183–4191.

26. Wirth BD. "On the Character of the Nano-Scale Features in Reactor Pressure Vessel Steels" [PhD Thesis]. University of California, Santa Barbara, 1998.

27. Russell KC and Brown L. "A dispersion strengthening model based on differing elastic moduli applied to the iron-copper system", *Acta Metall.* 1972;20(7):969–974.

28. Odette GR and He MY. "Cleavage toughness master curve model", *J. Nucl. Mater.* 2000;283-287:120–127.

Chapter 6 Post Irradiation Annealing

6.1 Introduction

Although the existence of MNSPs is not in question, there are a number of unresolved issues regarding their detailed character and formation mechanisms. For example, though the results in the previous chapter provide a compelling argument that the Mn-Ni-Si clusters are intermetallic phases which are driven to form by thermodynamics, there is substantial debate in the literature regarding whether they truly are phases or are solute clusters induced by the high density of defects created under irradiation. In addition, the presence of other hardening features at doses relevant to RPV life extension must be investigated to better inform embrittlement prediction models. This chapter focuses on two separate post irradiation annealing (PIA) experiments of the steels from the ATR1 condition designed to offer insight into both issues.

The first section contains results from a series of 1 week anneals at steadily increasing temperature, using microhardness to measure the recovery after each anneal. These isochronal anneals help to determine the hardening contributions from the various features formed under irradiation. Brief microstructure results from APT are presented along with the microhardness data to investigate the cause of the hardening recovery.

The next section presents APT data from two low-Cu steels with a wide variation in Ni content following annealing for various times at 425°C. These isothermal anneals are

designed to clarify the formation mechanism of the precipitates by measuring dissolution or coarsening of the precipitates at the two different solute contents. For example, if the precipitates are induced by radiation, they should not be stable under annealing and should dissolve at all solute contents. Due to sluggish kinetics at annealing temperatures below ≈ 450°C, multiple measurements were taken to separate kinetic from thermodynamic effects. Cluster dynamics and CALPHAD modeling results are also presented to help rationalize the precipitate dissolution/coarsening.

6.2 Isochronal Annealing

Isochronal annealing helps to determine the balance and character of the different hardening features for various irradiation-alloy conditions, since the features have different recovery signatures. In this experiment, the 8 model steels irradiated in the ATR1 experiment were annealed at temperatures from 350-450°C in 25° increments. The microstructures of these steels in the as irradiated condition were presented in sections 5.4 and 5.8. A final recovery anneal was performed at 550°C, and the hardness after this anneal was used for the unirradiated, baseline hardness. Vickers hardness measurements were taken from the samples following each anneal and converted to yield strength to determine the increase in yield strength ($\Delta\sigma_y$) over the unirradiated condition, using $\Delta\sigma_y = \sigma_{y,ann} - \sigma_{y,BL}$, where $\sigma_{y,ann}$ is the yield strength for the specific irradiated and annealed condition and $\sigma_{y,BL}$ is the yield strength of the steel prior to irradiation. The $\Delta\sigma_y$ is reduced after each anneal as the hardening features which formed under irradiation dissolve. The main two goals of this experiment were to 1) investigate the presence of other hardening features, and 2) compare the recovery among the

different steels to determine the effects of compositional variations on the formation of hardening features.

6.2.1 Hardening Recovery

Figure 6.1 shows the $\Delta\sigma_y$ for a) low Ni (0.00-0.18%) steels with high Cu (0.4%), b) medium Ni (0.74-0.86%) steels with varying Cu contents (0.01-0.41%) and c) high Ni (1.25 and 1.68%) steels with high (0.38%) and no Cu, respectively. The initial as-irradiated hardening in the low Ni steels, $\Delta\sigma_y \approx 300$ MPa, is significantly less than the medium and high Ni steels, $\Delta\sigma_y \approx 550$-750 MPa. Section 5.7 demonstrated the strong relationship between the bulk Ni content and the total precipitate f_v. Thus, the lower hardening in the low Ni steels is to be expected because there is less precipitation. Though the low Ni steels have much less initial hardening, their hardening features are very stable up to 450°C with the two steels still retaining ≈ 250 MPa of hardening following the 450°C anneals. Note that the low Ni steels have not undergone further annealing, but this is planned for future work. In contrast, the medium and high Ni steels retain less than 100 MPa of hardening following the 450°C anneal. This may be further evidence that dislocation loops are present in significant higher quantities in the lower Ni steels. An alternative explanation is that the Cu precipitates, which are much smaller in the higher Ni steels, are below the critical radius at higher temperatures and thus dissolve instead of coarsen at higher T_{ann}. This dissolution at higher Ni would recover significant hardening, but the slow coarsening at high Ni would not.

The medium Ni steels show very consistent hardness recovery at all temperatures even though they have a large variation in Cu content from 0.01-0.41%. The Cu content

appears to play no or very little role in the stability of the hardening features. This suggests that the precipitates, including the Cu fully dissolve, likely because they are so small and below the critical radius at this increased temperature. There is substantial recovery at 400°C and below, with almost 250 MPa of recovery in all 4 medium Ni steels.

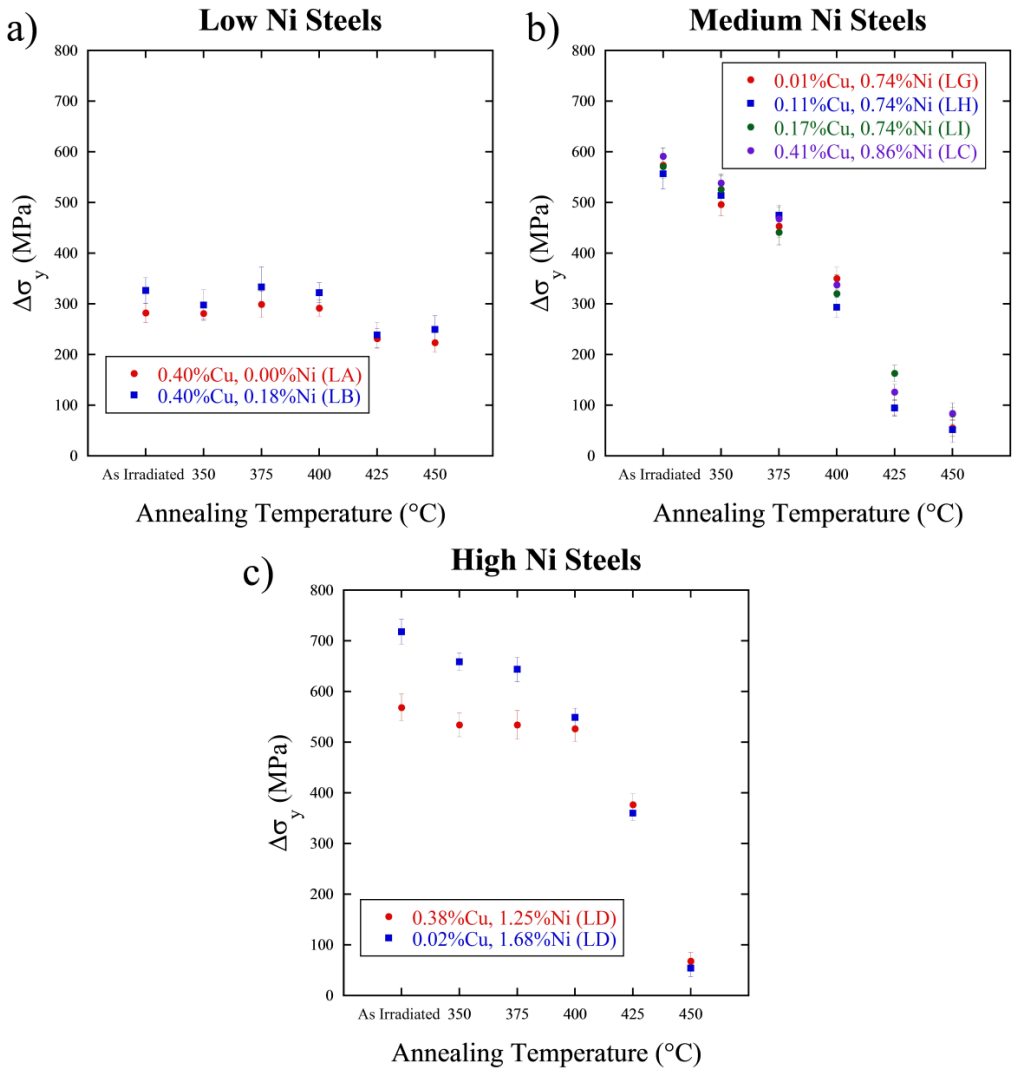

Figure 6.1. Isochronal 1 week annealing results for the ATR1 irradiated a) Low Ni (0-0.2%), b) medium Ni (0.7-0.8%), and c) high Ni (1.2-1.7%) steels.

On the other hand, the two higher Ni steels show a different trend. The high-Cu/Ni steel LD shows almost no recovery following the 350°C, 375°C and 400°C anneals, while the low-Cu, highest-Ni steel (CM6) shows about 150 MPa of recovery. In addition, the residual hardening in the higher Ni steels is over double that of the medium Ni steels following the 425°C anneals. Following annealing at 450°C, almost all of the hardening is recovered in all of the medium and high Ni steels.

6.2.2 Low Temperature Precipitate Stability

To investigate the cause of the hardening recovery at lower temperatures, the microstructure of two steels (LD and LG) was measured with APT following a 375°C, 1 week anneal. Figure 6.2 shows atom maps from the high Cu/Ni steel (LD) in the as irradiated (top) and 375°C, 1 week annealed condition (bottom). Qualitatively, no changes can be observed following annealing for LD or LG (not shown). The <r>, N and f_v for both steels are given in Table 6.1.

There are no significant changes in the average measured precipitate parameters, thus it is not likely that precipitate dissolution is causing the recovery at 350-375°C, which was up to ≈ 100 MPa in the medium Ni steels. This is somewhat expected as the diffusion distance for Ni is expected to be ≈ 1 nm after a week at 375°C [1]. The most likely explanation is that dissolution of another hardening feature, such as matrix defects has occurred, though whether this matrix defect hardening was induced by the very high ϕ or whether it would also be seen at lower power reactor ϕ is unknown. While large dislocation loops may be stable at 375°C, which is why recovery was not observed in the low Ni steels, smaller defect clusters,

especially those of interstitial nature, may have enough mobility to dissolve. In any event, the dissolved feature is small enough that it is not able to be directly measured with any available characterization techniques.

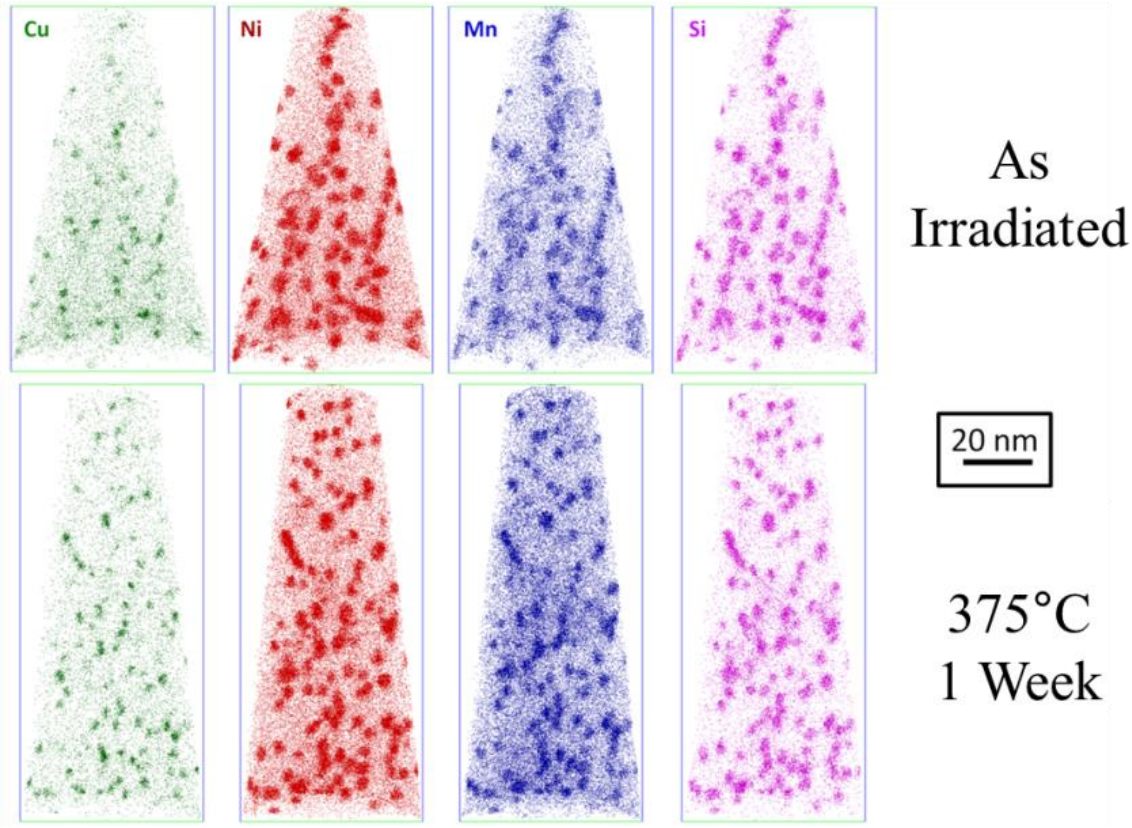

Figure 6.2. Atom maps of the ATR1 irradiated high Cu/Ni steel (LD) in the as irradiated (top) and 375°C – 1 week annealed condition.

Table 6.1. Precipitate <r> (nm), N (1023 m-3) and fv (%) for the ATR1 as irradiated and 375°C, 1 week annealed high Cu/Ni (LD) and Cu-free, low Ni steels.

Alloy	<r> (nm)				N (10^{23} m^{-3})				f_v (%)			
	AI	+/-	375°C	+/-	AI	+/-	375°C	+/-	AI	+/-	375°C	+/-
LD	1.96	0.14	1.88	0.09	7.3	1.0	7.9	0.9	2.11	0.23	2.08	0.06
LG	1.25	0.04	1.29	0.04	16.3	1.6	14.3	0.8	1.33	0.03	1.25	0.06

6.3 Isothermal Annealing

Because of the slow diffusion rates below ≈ 450°C, very long time (t_a) PIA is required to help distinguish RIS from RED effects, and to map MNSP phase boundaries for comparison to thermodynamic models. Thus, two Cu-free steels with nominal Ni contents of 0.69 at.% (LG) and 1.57 at.% (CM6) from the ATR1 condition were annealed for long times at 425°C. The Cu-free steels were selected to avoid the complications of Mn, Ni and Si enrichment around Cu clusters which will occur whether the MNS phases are stable or not. Atom probe tomography measurements were made at 1, 7, 17 and 29 weeks. Due to the limited amount of irradiated material, the PIA was performed on 1.5 mm punched discs, precluding direct microhardness measurements.

It must be emphasized that it is absolutely critical to compare the PIA data to predictions of models that properly account for thermodynamics and dissolution kinetics. Thermodynamic models, based on the Thermocalc enabled CALPHAD method, were used to guide the experimental design and to help analyze the annealing data [2]. The model predictions of the equilibrium f_v were presented in section 5.5 and compare favorably to the high ϕt_e ATR data [3]. The corresponding CALPHAD f_v for the two low Cu steels as a function of T_a are shown in Figure 6.3. CALPHAD predicts that only the Γ_2 phase ($Mn(Ni_xSi_{1-x})_2$) is stable in the high Ni (CM6) steel, while the G phase ($Mn_6Ni_{16}Si_7$) exists up to ≈ 390°C in the medium Ni (LG) steel; but at higher T_a, Γ_2 becomes more stable. Thus the f_v for the medium Ni steel is the sum of the Γ_2 and G phases at a given T_a. The XRD study of

the precipitates in the as irradiated condition found G phase precipitates in the medium Ni steel, while the high Ni steel contains the Γ_2 phase as predicted [4].

Figure 6.3 shows that the MNSPs in the medium Ni steel (LG) should completely dissolve above ≈ 415°C, while the Γ_2 phase in high Ni steel (CM6) are predicted to fully dissolves at ≈ 500°C. Again, because lower T_a results in lower solute diffusion rates, the isothermal annealing was carried out at an intermediate temperature of 425°C with the thermodynamic model predicting full dissolution in the medium Ni steel (LG) and the possibility of some MNSPs remaining in the high Ni steel (CM6). Note that the complete MNSP dissolution of the phase in the medium Ni steel also acts as a kinetic marker to help estimate the effective diffusion distances at various annealing times that approximately apply to both alloys.

Cluster dynamics (CD) modeling was also carried out to predict and interpret the MNSP dissolution and coarsening processes. Briefly, CD models the evolution of the MNSPs in discrete n-1, n and n+1 cluster sizes, where n is the number of atoms. Thus n ranges from 2 to n_{max} in a coupled set of n_{max}- 1 ordinary differential equations that incorporate n-dependent effective solute impingement and emission transition rate coefficients. The CD model for annealing used here assumes diffusion controlled kinetics, and requires only 4 key input parameters: a) the effective solute diffusion coefficient (D); b) the effective solute equilibrium solubility (X_e), as determined by the free energy difference between the dissolved and precipitated effective solute states or the equilibrium phase diagram; c) the

MNSP-Fe interface energy (γ); and, d) the as-irradiated MNSP size distribution, taken directly from the APT measurements [5].

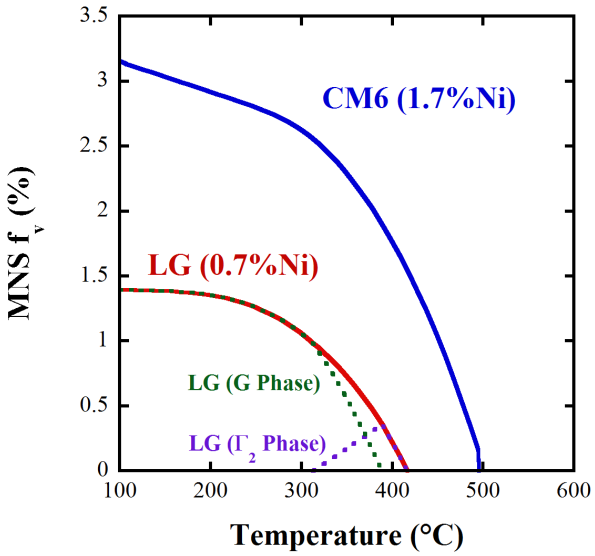

Figure 6.3. CALPHAD predictions of Mn-Ni-Si precipitate volume fraction as a function of annealing temperature for two Cu-free steels with varying Ni content.

The CD model was parameterized by fitting the MNSP evolution under irradiation. The D was taken from data in the literature, and the X_e derives from the CALPHAD thermodynamic model. This leaves only γ as a significant unknown fitting parameter; note, the fitted value of γ is consistent with first principles calculations. Full details for the model can be found elsewhere [5]. Thus the as-irradiated MNSP size distributions, bulk alloy composition and T_a fully mediate the MNSP evolution with t_a. It should be stressed that no further fitting of parameters was done in the CD modelling to better fit the annealed results.

6.3.1 Isothermal APT Results

Atom maps from the medium Ni steel (LG) in the AI and 425°C PIA conditions are shown in Figure 6.4. The clusters appear very diffuse following a one-week anneal with the Si appearing to be the most diffuse. The solutes in the medium Ni steel are essentially homogeneously dissolved after the seven week anneal as predicted in Figure 6.3, with only weak indications of a small amount of solute clustering. While not specifically measured, the solutes must be fully dissolved in the medium Ni (LG) steel after the 29 week anneal, given that the diffusion distances are about twice as large as those at seven weeks.

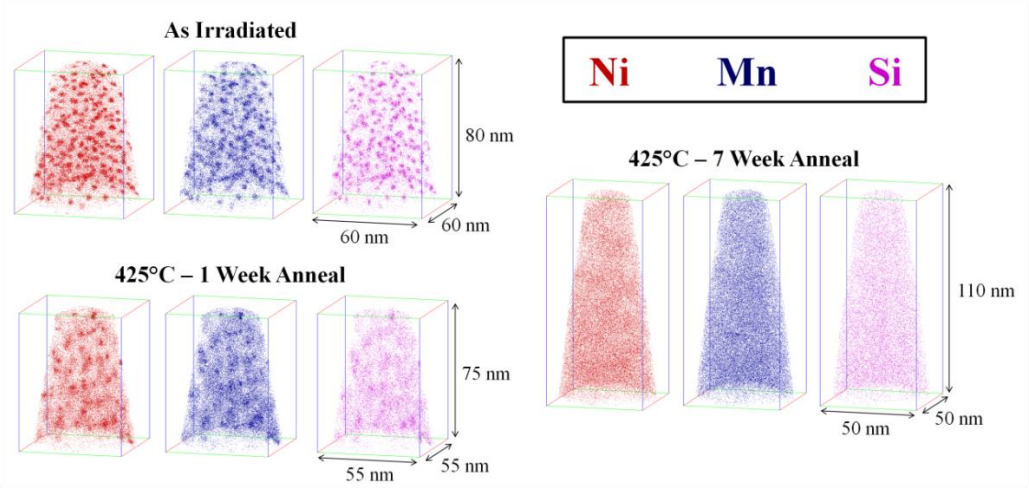

Figure 6.4. Atom maps for the Cu-free, medium Ni steel (LG) in the (a) AI condition, (b) 425°C - 1 week annealed condition, and (c) 425°C annealed - 7 week condition.

Atom maps for the low Cu, high Ni steel (CM6) in Figure 6.5 show much greater MNSP stability, with well-defined precipitates still remaining after PIA for 29 weeks. The <r>, N, and f_v are summarized in Figure 6.6. The lines in Figure 6.6 are the CD PIA predictions which will be discussed in section 6.3.2. Both N and f_v decrease rapidly with the increasing t_a. There is a corresponding increase in <r>, but this is primarily due to the

dissolution of the smallest MNSPs, rather than significant coarsening, manifested as growth of the largest MNSPs.

Table 6.2. Precipitate summary for the high Ni steel (CM6) from the AI and 425°C annealed conditions.

t_a (wk)	<d> (nm)	N (10^{24}/m^3)	f_v(%)	Mn/Ni/Si*
0	3.05	1.95	2.8	0.35/0.53/0.12
1	2.83	1.2	1.4	0.36/0.54/0.10
7	3.26	0.22	0.4	0.38/0.54/0.08
17	4.25	0.03	0.1	0.39/0.54/0.07
29	5.49	0.01	0.1	0.41/0.42/0.17

The average fractional precipitate compositions are also shown in Table 6.2. Note that while the standard IVAS reconstructions suggest that there is a significant amount of Fe in all of the MNSPs, this element is not included, since this is thought to be an APT artifact. The Fe is mainly due to trajectory aberrations that focus matrix atoms into the precipitate, also leading to non-physically high atom densities, typically by factors of 2-3 [6].

It is useful to compare the MNSP compositions to the closest known Mn-Ni-Si intermetallic phases as shown in Table 6.2. This comparison suggests that the Γ_2 phase is closest to the composition in the AI condition, but the MNSPs are somewhat poor in Si. Annealing for intermediate times lowers the Si further. However, at the longest t_a, the Mn fraction increases and Ni decreases, which may mark an incomplete transition between the Γ_2 and T_7 phases, e.g., $Mn(Ni_xSi_{1-x})_2$ partially transforming to Mn_3Ni_2Si or, as is discussed below, the potential formation of a Mn enriched shell around the clusters.

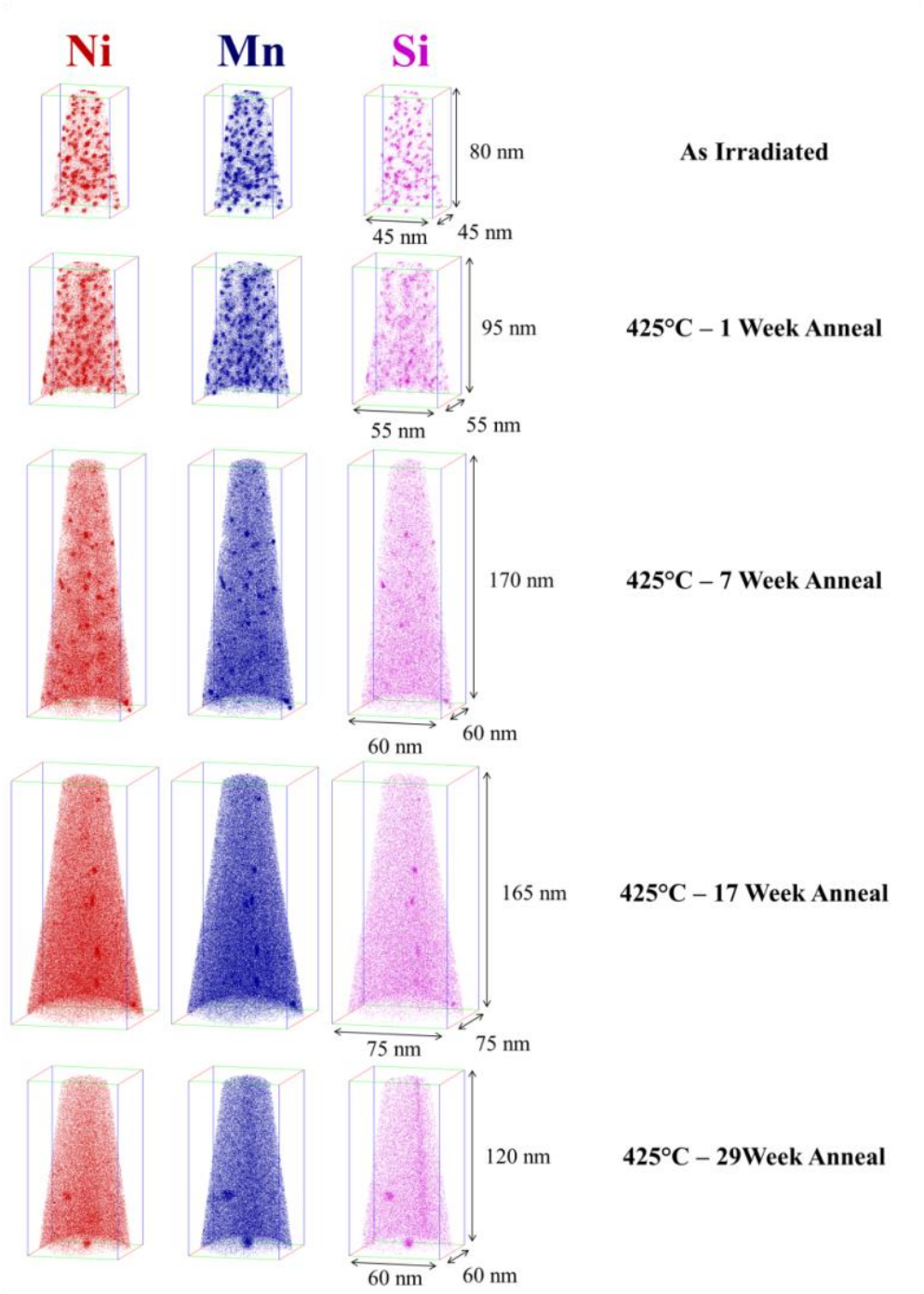

Figure 6.5. Atom maps for the low Cu, high Ni steel (CM6) in the (a) AI condition and 425°C annealed conditions at times of (b) 1 week, (c) 7 weeks, (d) 17 weeks and (e) 29 weeks.

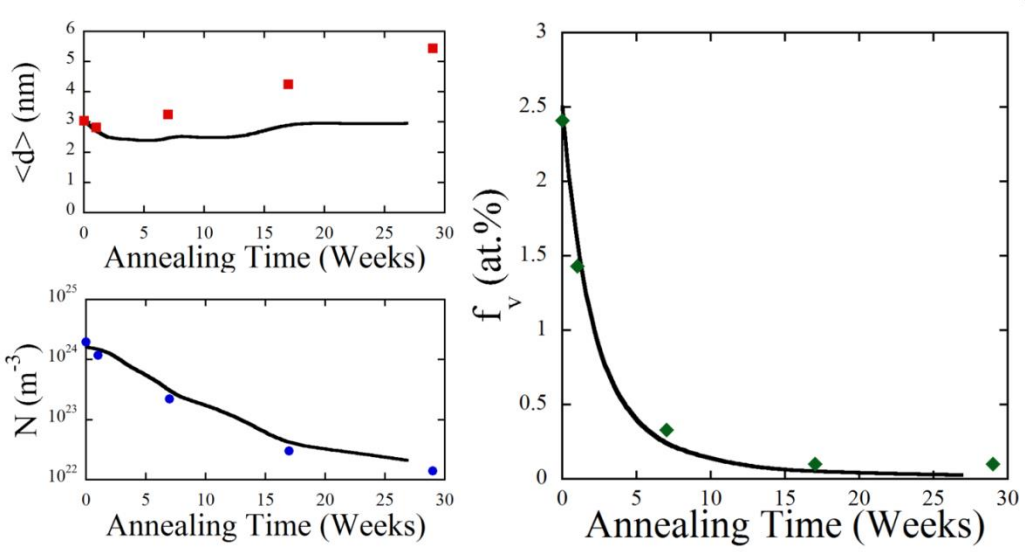

Figure 6.6. Precipitate <d> (nm), N (m-3) and fv (at.%) after annealing from APT (points) and CD predictions (lines) for the high Ni steel (CM6).

Figure 6.7 shows the corresponding MNSP radial composition profiles for both the AI and 29 week PIA conditions for the high Ni steel. Because the annealed sample only contained 2 precipitates, the composition profiles for the as-irradiated condition were calculated for only the 10 largest precipitates found in the given tip. Note it is difficult to draw specific conclusions from the results in Figure 6.7, due to very limited statistics, tip-to-tip inhomogeneity and a number of possible APT artifacts, though qualitative information can still be gleaned from these plots. First, the annealed MNSPs are significantly larger and have an approximately constant composition Mn and Si core, while the Ni appears to increase somewhat from the edge to center. Second, the as-irradiated MNSPs are more highly enriched in Ni than Mn over the entirety of the precipitate, but the annealed MNSPs are more enriched in Mn in the outer portion of the precipitate, with much more Ni in the core. Thus, when integrating over the entire precipitate, the Mn enriched shell, which represents a larger

volume than the Ni enriched core, results in the total Mn and Ni being ≈ equal, as seen in Table 6.2.

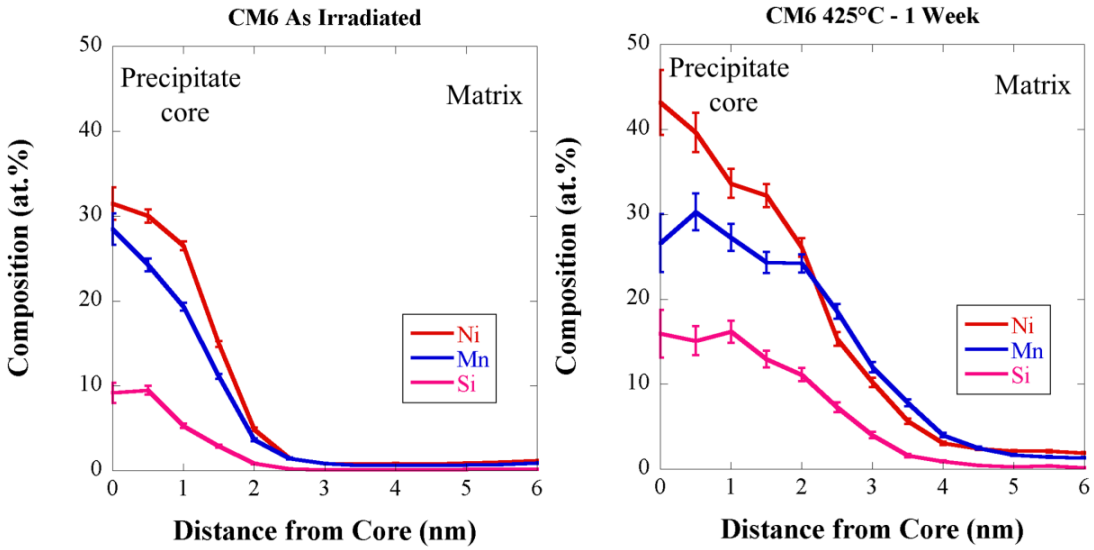

Figure 6.7. Radial composition profiles for the high Ni steel (CM6) from the a) AI and b) 425°C, 29 week annealed conditions.

Results presented in section 5.7 showed that tip-to-tip variability can be exploited to assess the effects of local compositional variations on precipitation [3]. For example, while MNSPs were still found in all the tips from the high Ni steel (CM6) in the AI, 1 week and 7 week t_a, they were only found in tips containing more than ≈ 1.6 at.%Ni and 1.4 at.%Mn (close to the nominal alloy composition) for longer t_a. Thus only tips that contained clusters were included in plots of size distributions and N.

Finally, it should be noted that C and Mo are co-segregated to the MNSPs following the 29 week anneal at solute concentrations of 3-5 at.% and 6-8 at%, respectively. Since these elements are depleted in the MNSPs in the AI condition, and unlikely constituents of

the intermetallic phase, it seems likely that this reflects the co-formation of Mo_2C type carbides.

6.3.2 Cluster Dynamics Modeling

As shown above, the CALPHAD model correctly predicts complete dissolution of MNSPs in the medium Ni steel (LG), which was indeed observed from 7 weeks of PIA. On the other hand, the high Ni steel (CM6) is predicted to have an equilibrium MNSP f_v of ≈ 1.4%, much greater than the measured f_v at 29 weeks of 0.11%. To investigate this difference, a cluster dynamics (CD) model was used to predict MNSP evolution in the high Ni steel (CM6) assuming a bulk composition of 1.63 at.%Ni and 1.38 at.%Mn, which was close to the local compositions found in the tips containing MNSPs at 17 and 29 weeks. It should be noted that this model is a work in progress and is still being fine-tuned. The other input to the PIA model was the AI MNSP size distribution. Note, the interfacial energy (γ) used in the model was fit to the MNSP evolution in a series of irradiated steels and was not altered to better fit the annealing data [5]. That is, the PIA model has no independently adjusted fit parameters. The predicted f_v as a function of t_a in Figure 6.6 is in very good agreement with the experimental results, except that it predicts complete dissolution by the 29 week anneal, while the experiment finds several large clusters that appear to be stable. Note that the model does not show the average precipitate size (<r>) go to zero over the time scale studied, but the model would likely show full dissolution at longer times.

The size distributions for all the t_a in Figure 6.8, show a decrease in the N for all precipitate sizes except for clusters those with r > 2.25 nm. Note that no clusters with r < 2.25

nm were found for the 29 week annealed condition. The largest MNSP in the AI condition was r = 2.3 nm, while the 3 precipitates found after the 29 week PIA all had r > 2.6 nm. While this may seem to be a small difference, the number of atoms in a cluster scales with r^3. The largest MNSP in the AI condition had ≈ 4500 Mn+Ni+Si atoms, while the 3 clusters found after the 29 week PIA contained 6500, 7200 and 8100 MNS atoms, respectively. Thus, not only are the clusters with r > 2.25 nm stable at this long annealing time, but they are growing, which seems to confirm the hypothesis that the MNSPs in irradiated RPVs are equilibrium phases.

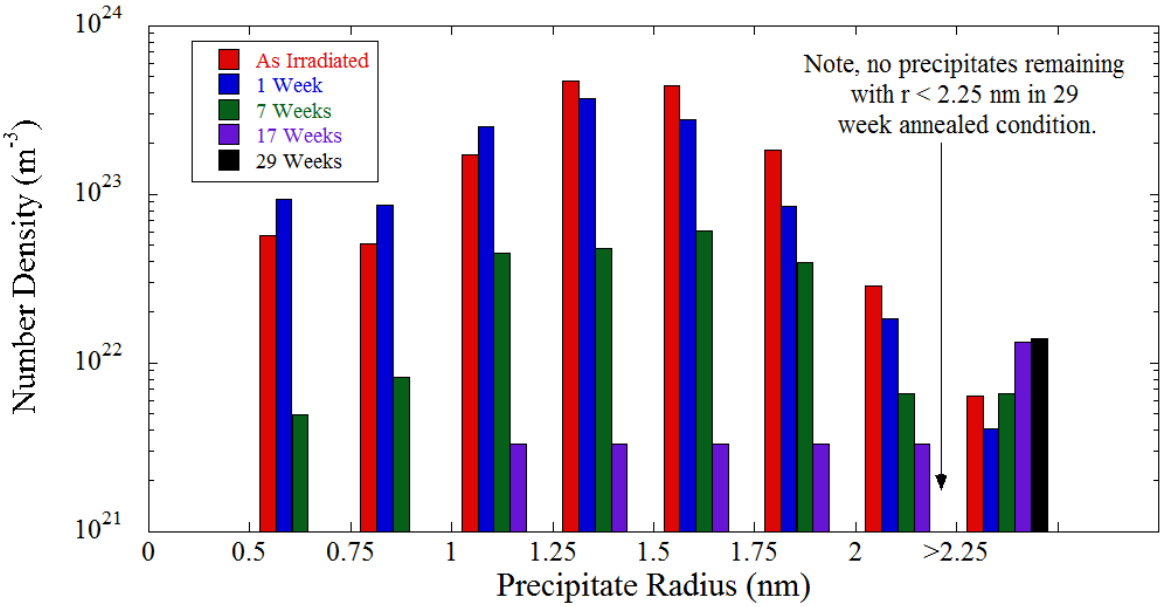

Figure 6.8. Size distribution of precipitates in the high Ni steel (CM6) for the AI and annealed conditions.

The CALPHAD model predicts that the stable phase at this temperature is the $Mn(Ni_xSi_{1-x})_2$ Γ_2 phase, with a composition of 33%Mn, 50%Ni and 17%Si. The MNSPs in the as-irradiated condition have compositions very close to Γ_2, with a slight deficit of Si. The

MNSPs in the 29 week PIA condition, which contained the largest precipitates, have an average composition of ≈ 41%Mn, 42%Ni and 17%Si. However, Figure 6.7b shows that the core composition of the MNSP is ≈ 33%Mn, 50%Ni and 17%Si, identical to the Γ_2 phase. The difference between the overall and core compositions is due to a higher ratio of Mn/Ni in the surrounding region. This may indicate a shell with a different composition or as noted previously a partial transition for the Γ_2 to the T_7 phase.

The full MNSP dissolution in the medium Ni steel (LG) at 7 weeks suggests that a 29-week t_a should be sufficient to dissolve the MNSPs in the high Ni steel (CM6) if they are not thermodynamically stable. The significant dissolution that is observed is consistent with the nano-scale size of the MNSPs, which are below the critical radius (r_c) in the initially solute depleted AI matrix. As the small MNSPs dissolve, the corresponding increase in the matrix solute concentration is sufficient to stabilize the larger precipitates. The fact that MNSPs with r > 2.3 nm are stable in a matrix only slightly solute depleted (≈ -0.11%) compared to the bulk alloy suggests that they are not induced by radiation, consistent with thermodynamic predictions. Indeed, the fact that the CD model predicts full dissolution of the MNSPs in the AI condition also suggests that either the CALPHAD thermodynamics volumetric free energy change (ΔG_v), or the fitted value of γ, or both, are slightly in error, where $r_c = 2\gamma/\Delta G_v$. Thus PIA can be used to fine tune both precipitation and annealing models. Annealing at lower temperatures is ongoing to further investigate the critical radius at different temperatures, however this is beyond the scope of the current paper.

6.4 Conclusions

A series of 1 week annealing treatments followed by microhardness measurements at steadily increasing temperature was performed on a series of steels from the ATR1 condition. While the two steels with very low Ni contents showed much less initial hardening than the medium and high Ni steels, their hardening features remained stable up to temperatures of 450°C. On the other hand, the medium and high Ni steels showed almost complete hardening recovery following the 450°C anneal. The large dislocation loops in the low Ni steels may be more stable at higher T_a than the MNSPs and thus are responsible for the higher retained hardening.

Though the medium and high Ni steels showed significant hardness recovery of up to 100 MPa following annealing at 375°C, APT could not detect a corresponding change in the precipitates. Thus, it is likely that another feature has recovered, likely the so called matrix defects that are very difficult to measure due to their very small size. Future work will focus on determining if this hardness recovery is also seen at lower flux and how to best incorporate the matrix features into embrittlement prediction models.

Long term isochronal annealing was used to investigate the formation mechanism of Mn-Ni-Si precipitates in neutron irradiated RPV steels. The annealing, conducted at 425°C for long times, resulted in complete dissolution of precipitates in medium Ni (0.74%) steel after only 7 weeks. Alternatively, some precipitates still remained at the longest annealing time of 29 weeks in the high Ni steel in tips that contained at least 1.6% Ni and 1.4% Mn, though there was a significant reduction in the precipitate number density. Contrary to the

equilibrium CALPHAD models, the volume fraction was reduced to 0.1%. This significant reduction in volume fraction and number density was rationalized from a cluster dynamics model, which predicts complete dissolution of all the nm-scale clusters at 425°C due to their small size, which was below the predicted critical radius.

The size distributions of precipitates in the various conditions show that the critical radius at 425°C and at the high Ni content is likely around 2.25 nm. The number density of clusters with radius greater than 2.25 nm does not decrease significantly in any of the PIA conditions, but all clusters below that size dissolve after long times. Lastly, the number of Mn-Ni-Si atoms per cluster in the three clusters found in the 29 week PIA sample is almost ≈ 50% higher than the largest cluster found in the AI condition. In summary, long term PIA of precipitates shows stable, growing precipitates that have compositions in the core of the precipitates very close to known intermetallic phases that are predicted to form by CALPHAD. Thus, the precipitates are likely actual phases, and not non-equilibrium solute clusters induced by radiation.

6.5 References

1. Hirano K, Cohen M and Averbach BL. "Diffusion of nickel into iron", *Acta Metall.* 1961;9(5):440–445.
2. Xiong W, Ke H, Wells PB, Barnard L, et al. "Thermodynamic models of low temperature Mn-Ni-Si precipitation in reactor pressure vessel steels", *MRS Commun.* 2014;4(3):101–105.
3. Wells PB, Yamamoto T, Miller B, Milot T, et al. "Evolution of manganese–nickel–silicon-dominated phases in highly irradiated reactor pressure vessel steels", *Acta Mater.* 2014;80:205–219.
4. Sprouster DJ, Sinsheimer J, Dooryhee E, Ghose SK, et al. "Structural Characterization of Nanoscale Intermetallic Precipitates in Highly Neutron Irradiated Reactor Pressure

Vessel Steels", *Scr. Mater.* 2016;113:18–22.

5. Ke H, Wells PB, Barnard L, Odette GR, et al. "Cluster dynamics modeling of Mn-Ni-Si precipitates in low-Cu reactor pressure vessel steels", In Prep.
6. Cunningham NJ. "Study of the Structure, Composition, and Stability of Y-Ti-O nm-Scale Features" [PhD Thesis]. University of California, Santa Barbara, 2012.

Chapter 7 Charged Particle Irradiations

7.1 Introduction

High flux material test reactors have been heavily utilized to study RPV embrittlement because they can reach high doses, measured in dpa, in only a fraction of the time it would take in a power reactor. Unfortunately, neutron irradiated material is inherently difficult and expensive to study due to neutron activation of the steels that results in radioactive specimens. Alternatively, heavy ion accelerators can irradiate material at even higher dose rates than neutrons and the resulting specimens are not radioactive. The short experiment times and ease in specimen testing mean that a large variable matrix can be studied with ion irradiations in a fraction of the time and cost of neutron irradiations.

While it should be stressed that ions cannot directly simulate neutrons, they can still offer insight into specific mechanisms relating to radiation damage and precipitation. The purpose of this chapter is to investigate how ion irradiations can best be used to investigate the mechanisms related to RPV embrittlement, with a specific focus on the precipitates. First, results from neutron and ion irradiations to the same dose will be presented to determine the similarities and differences between the precipitates in both cases. It will be shown that ion irradiations can create very similar microstructures to neutron irradiated material at similar doses. In fact, the precipitates in this study show much more similarities than differences. In

addition to comparing precipitate size, number density and volume fraction, the precipitate compositions in both conditions will be compared.

After the consistency between neutron and ion irradiations is established, results from a much higher temperature ion irradiation will be presented. As was shown in Chapter 6, post irradiation annealing can offer insight into the character and stability of the MNSPs as well as potentially measure their phase boundaries, but there are significant challenges associated with these experiments. For example, the potentially large critical radius at high T_a may result in precipitate dissolution even if the bulk phase is stable. Thus, creating a microstructure more amenable to these annealing experiments, i.e. generating a low density of large clusters, could help to more easily measure the phase boundaries. Thus, results from ion irradiations at 330°C and 400°C will be presented to show that the irradiations conditions for ion irradiations can indeed be modified to control the final microstructure. Post irradiation annealing on these precipitates to confirm the conclusions in Chapter 6 is ongoing, but has not yet been completed. In any event, this is a good example of how ion irradiations can be very informative without needing to directly simulate neutron irradiations.

7.2 Neutron vs Ion Irradiated Precipitates

Two steels, LD and LI, were irradiated to a dose of 0.2 dpa using neutrons in the BR2 reactor in Belgium (referred to as the G1 condition) and ions in the Dual Beam facility for Energy Science and Technology (DuET) at Kyoto University in Kyoto, Japan. The full details for these two irradiations can be found in section 3.2. The results from the G1 condition were presented in section 5.3, but will be analyzed in further detail here.

7.2.1 High Dose Results

Example atom maps from the four alloy/conditions are shown in Figure 7.1. Well defined Cu precipitates enriched in Mn, Ni and Si can be clearly seen in all four sets of atom maps and qualitatively very little differences can be observed between the neutron and ion irradiated conditions from a given alloy. These results are very consistent with previous thermal ageing and neutron irradiated studies of high Cu RPV steels showing a high number density of Cu-rich precipitates that are enriched in Mn, Ni and Si. Table 7.1 summarizes the average precipitate size, number density and volume fraction in the various alloy/conditions.

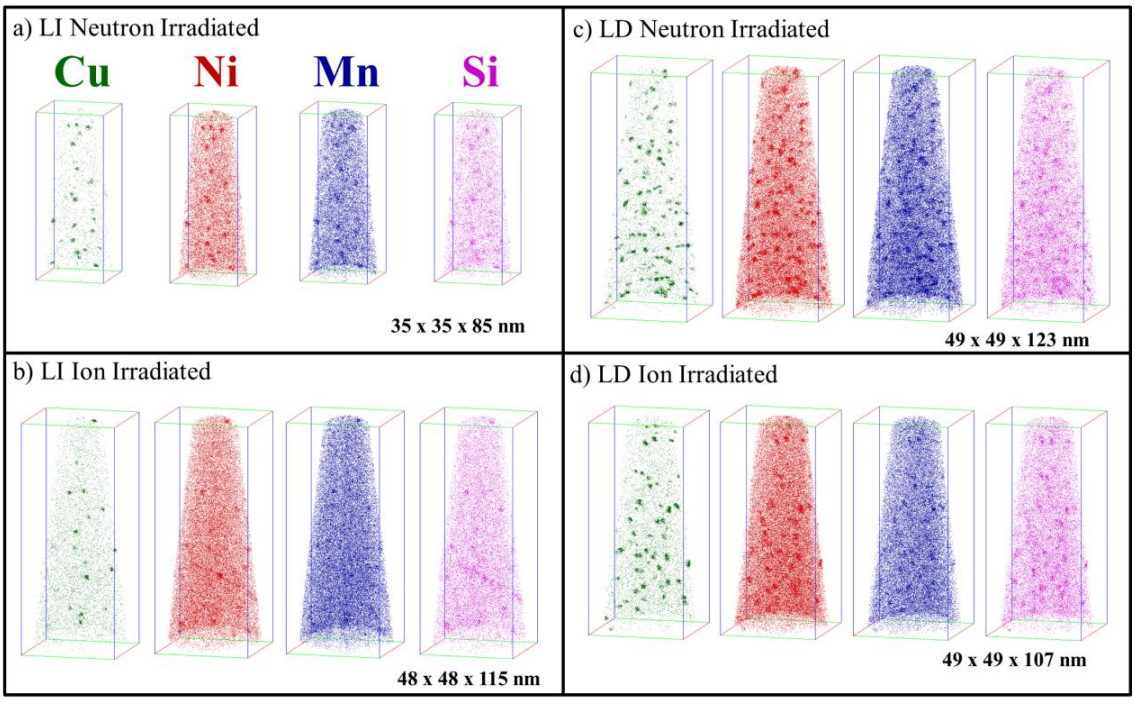

Figure 7.1. Atom maps from a) LI neutron irradiated, b) LI ion irradiated, c) LD neutron irradiated and d) LD ion irradiated. Note that the atom maps are all set at the same scale for comparison purposes.

Previous APT results of these steels showed that there are large inhomogeneities in solute contents over the very small length scales sampled with APT. These compositional variations can be exploited and treated as individual microalloys. Figure 7.2 shows the precipitate a) <d> and b) N and c) f_v as a function of bulk Cu content for the neutron (red) and ion (blue) irradiated material. Each point represents the <d> or N for a given APT tip. Thus, while nominally the steels had either 0.2 at.% Cu or 0.41 at.% Cu, the individual tips showed much variability from 0.1-0.3 at.%. There is a slight increase in precipitate size with increasing Cu content that can be seen in both irradiation conditions, but the <d> at a given Cu content is very consistent between the neutrons and ions. The N also shows large increase with increasing Cu, but the precipitates in the neutron irradiation are much more numerous than in the ion irradiation, being approximately twice as high at all Cu contents.

Table 7.1. Precipitate size (<d>), Number density (N), and mole fraction (f) and relative Mn, Ni and Si (at.%) for the four alloy/irradiation conditions.

Material	<d> (nm), N (10^{23}/m^3), f_v(%)							Relative Mn, Ni and Si in Precipitates (at.%)					
	Particle	<d>	+/-	N	+/-	f_v	+/-	Mn	+/-	Ni	+/-	Si	+/-
LD	Neutron	2.23	0.12	11.7	1.9	0.68	0.10	31.5	4.0	48.6	2.2	19.9	2.7
LD	Ion	2.28	0.07	7.5	1.2	0.46	0.06	25.6	1.2	51.1	0.6	23.3	1.1
LI	Neutron	2.19	0.11	6.9	1.1	0.37	0.08	36.1	1.6	45.2	1.6	18.7	0.8
LI	Ion	2.02	0.11	3.4	0.8	0.13	0.01	29.7	2.2	46.5	1.0	23.8	1.2

It should be noted that previous studies comparing neutron and ion irradiated precipitates showed the opposite of what is found in Figure 7.2 with precipitates in ion irradiated materials being much smaller and more numerous [1]. A very high density of small clusters in ion irradiations has also been reported by other groups, but these were not compared to results from neutron irradiations [2, 3]. It is unclear why previous studies found

a high density of small precipitates in ion irradiated material, while these results show a lower density of similarly sized precipitates, but this suggest much more focus should be not just on the differences between neutron and ion irradiations, but also on the differences between individual particle accelerators as well as how their parameters, such as ion energy and beam rastering vs a spread beam, affect precipitate morphology.

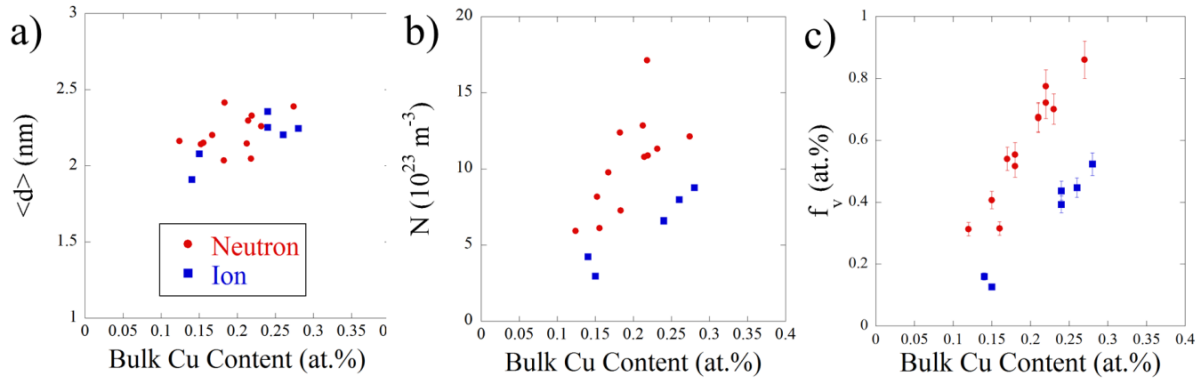

Figure 7.2. a) Precipitate <d>, b) N and c) f_v as a function of bulk Cu content for each individual tip.

As was shown in section 5.3 [4], there is a strong correlation between the precipitate f_v and bulk Cu content at this dose, which can be seen in Figure 7.2c. The ion irradiated condition consistently shows a lower precipitate mole fraction than the neutron irradiated samples. It has previously been shown that higher dose rate delays precipitation to a higher dose, due to the enhanced recombination of defects at higher dose rates [5–7]. Thus, the likely cause of the much lower mole fraction in the ion irradiations is the difference in dose rate. This is consistent with ion irradiation results by Dohi et al. that showed an approximately equal f_v between neutrons and ions when the dose of the ion irradiation was ≈ 100 times that of the neutron irradiation.

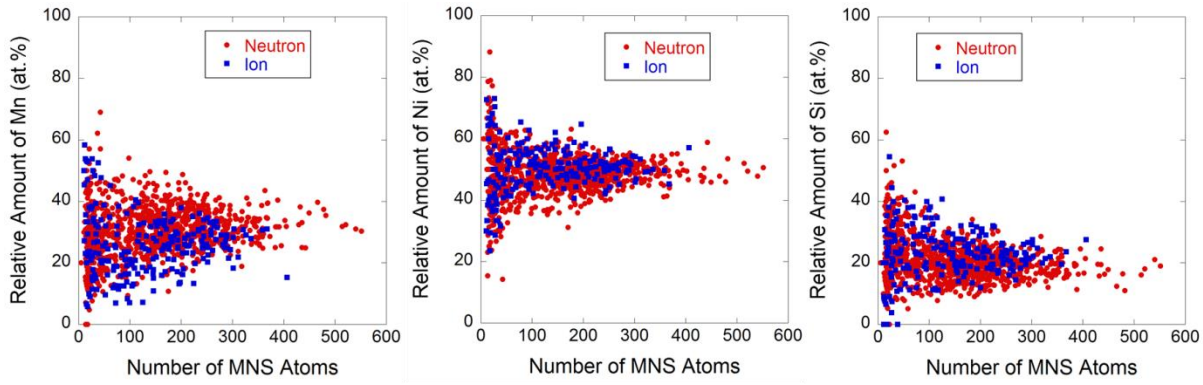

Figure 7.3. Relative amount of a) Mn, b) Ni, and c) Si in the clusters as a function of the number of Mn, Ni and Si atoms in the cluster.

The average precipitate compositions for each alloy/conditions are given in Table 7.1. For LD, the precipitates in both the neutron and ion irradiated conditions have compositions very close to the G Phase ($Mn_6Ni_{16}Si_7$), though the precipitates are slightly more enriched in Ni and Si while being slightly less enriched in Mn. This is shown in further detail in Figure 7.3 where the relative amount of Mn, Ni and Si in the precipitates is plotted vs the total number of Mn, Ni and Si atoms in the clusters for the LD alloy. Thus, it can be seen that the cause of the compositional variations is not driven by a size effect because at a constant number of MNS atoms, the precipitates have slightly different compositions between the two conditions. This is also true for the LI sample. It may be that at these very high ion irradiation dose rates, the effect of RIS is larger, resulting in precipitates that are less enriched in Mn with a tradeoff of being more enriched in Si.

7.3 High T_{irr} Ion Irradiations

While there are clearly some differences between the precipitates in neutron vs ion irradiated material, the overall consistency is encouraging. Thus, additional experiments were

performed using charged particle accelerators to test the hypothesis that the final microstructure can be fine-tuned by varying the irradiation conditions. For example, as was shown in the last chapter, PIA studies on neutron irradiated steels are complicated by the fact that 1) annealing must be done at $T_a > T_{irr}$ due to kinetics, and 2) Higher T_a results in a higher critical radius, meaning that the precipitates may dissolve even if the bulk phases may be stable. Thus, investigating the MNS phase boundaries in Fe at higher T may only be possible if the starting microstructure contains very large MNSPs. As nucleation rates are directly related to undercooling, or the difference between the actual temperature and the temperature of the phase boundary at a given solute content, then irradiating at temperatures near the phase boundary will result in a lower density of clusters. If the dose is high enough to reach saturation, then the precipitates will reach much larger sizes than at lower T_{irr}. Performing PIA studies on steels with variations in size distributions can also help to inform models as to the critical radius at a given matrix content and T_a.

The Cu free, high Ni steel (CM6) that underwent the long term isothermal annealing in section 6.3 was irradiated using Fe^{3+} ions at 330 and 400°C to a dpa of 2.2 and 2.5, respectively. The results from these two irradiation conditions will be compared to results from the very high dose ATR1 irradiation. The full irradiation conditions are found in Table 7.2.

Table 7.2. Irradiation conditions for investigating effect of T_{irr} on precipitate f_v and composition.

Particle	Dose (dpa)	Dose Rate (dpa/s)	T_{irr} (°C)
Neutron	1.7	$3.5x10^{-7}$	290
Fe^{3+}	2.2	$1x10^{-4}$	330
Fe^{3+}	2.5	$1x10^{-4}$	400

Atom maps from the three different irradiation temperatures are given in Figure 7.4. The average precipitate <r>, N, f_v and composition are given in Table 7.3. The precipitate <r> was approximately the same in both the 290°C neutron and 330°C ion conditions, but was significantly larger in the 400°C ion condition. In addition, the precipitates in both ion irradiated conditions were much less enriched in Mn that the neutron irradiated condition, with the relative amount of Mn decreasing with increasing T_{irr}. This can also be seen in the atom maps, where the Ni and Si is very densely clustered at all three temperatures, but the Mn is more diffuse in the two higher T_{irr} ion irradiation conditions. It should be noted that the results from the previous section showed that on average precipitates from the ion irradiated conditions were less enriched in Mn as well, thus it is unclear whether the difference between compositions is entirely caused by the temperature change, or partly caused by particle or dose rate differences as well.

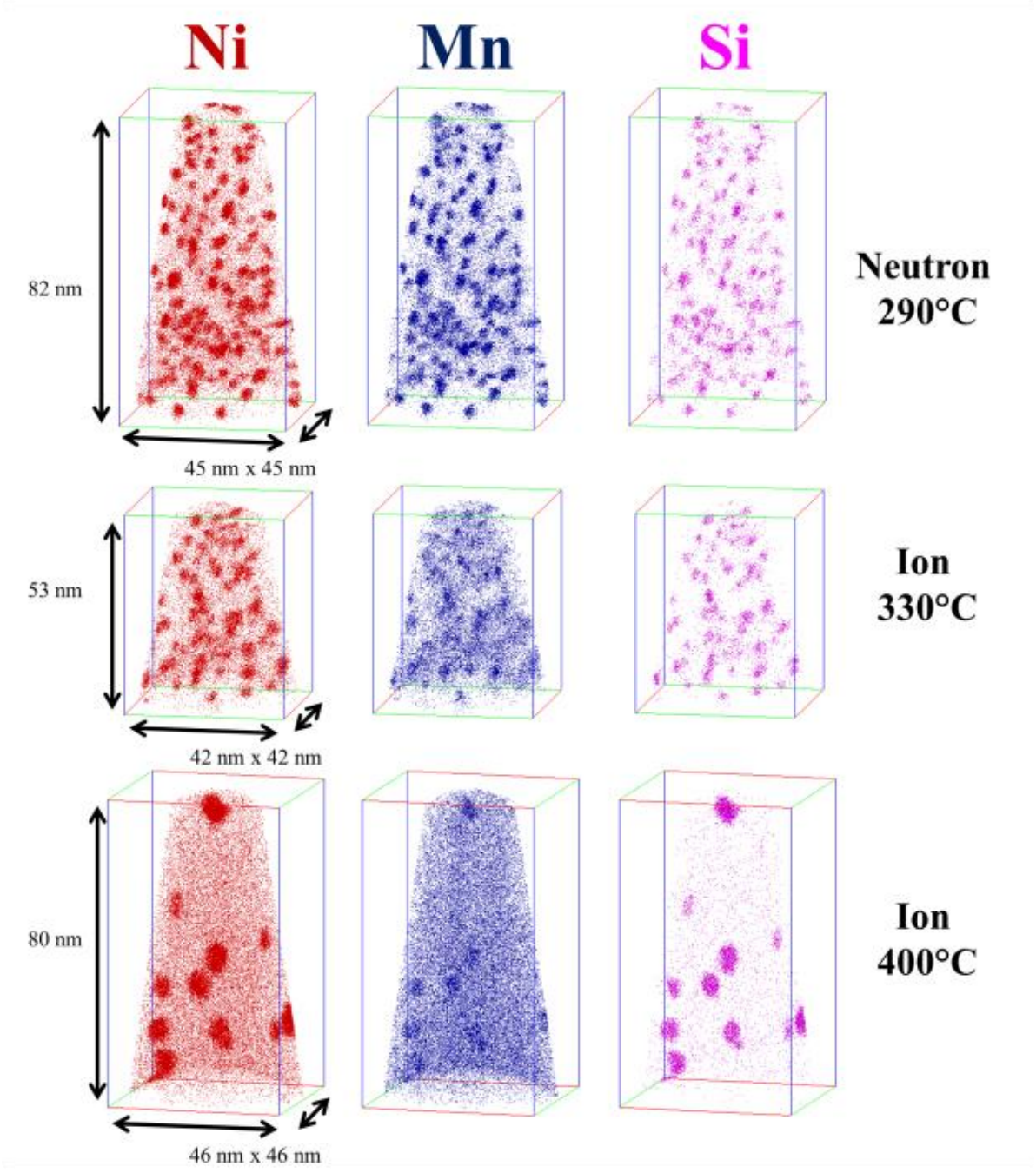

Figure 7.4. Atom maps from the Cu-free, high Ni steel (CM6) irradiated with neutrons at 290°C, ions at 330°C, and ions at 400°C.

Table 7.3. Precipitate <d>, N, f_v and relative composition.

Particle	Precipitate <r> (nm), N (10^{23} m^{-3}) and f_v (%)							Precipitate Relative Composition (at.%)					
	T_{irr} (°C)	<r>	+/-	N	+/-	f_v	+/-	Mn	+/-	Ni	+/-	Si	+/-
Neutron	290	1.53	0.06	19.5	1.5	2.82	0.14	35.5	1.8	52.6	1.3	11.9	0.6
Fe^{3+}	330	1.48	0.08	13.1	2.8	1.71	0.08	26.7	1.5	56.7	0.8	16.7	0.6
Fe^{3+}	400	2.67	0.24	2.6	1.5	1.79	0.39	16.5	3.4	63.9	2.3	19.6	1.6

The f_v in each condition are also particularly important because if the precipitate formation is driven by thermodynamics, then ion irradiations could be a tool to determine the phase boundaries at temperatures that are kinetically inaccessible without irradiation. While the f_v of the two ion irradiated conditions, shown in Table 7.3 are similar, this is largely caused by the fact that the sampled region from the 330°C condition happened to be much lower in solutes than the 400°C samples. Thus, the best way to determine the relative amount of precipitation is by plotting the f_v vs the total solute content, as seen in Figure 7.5, and by examining the matrix solute contents, shown in Table 7.4. The 330°C ion irradiated condition is shifted slightly below 290°C neutron irradiated condition for the total f_v vs bulk Mn + Ni + Si and an even larger shift is seen for the 400°C ion irradiated condition as seen in Figure 7.5a. Hence, the f_v at a given solute content is lower with increasing T_{irr}, which is to be expected.

Particularly interesting is that this trend is not consistent among with various solutes. For example, though the bulk Ni is less in the 330°C ion irradiated samples than the 290°C neutron irradiated samples, the Ni f_v vs bulk Ni seems to follow close to the same trend for both. The matrix Ni content at 330°C is 0.27 at.% vs 0.17 at.% at 290°C. The 400°C sample

shows much less Ni solubility, with a matrix content of 0.65 at.%. The Mn is the most affected by the variation in T_{irr}, with a matrix content of 0.32, 0.70, and 1.48 at.% at T_{irr} of 290, 330, and 400°C, respectively. The Si on the other hand, is almost totally unaffected by the T_{irr}, with a matrix solute content ranging from 0.03-0.06 at.%.

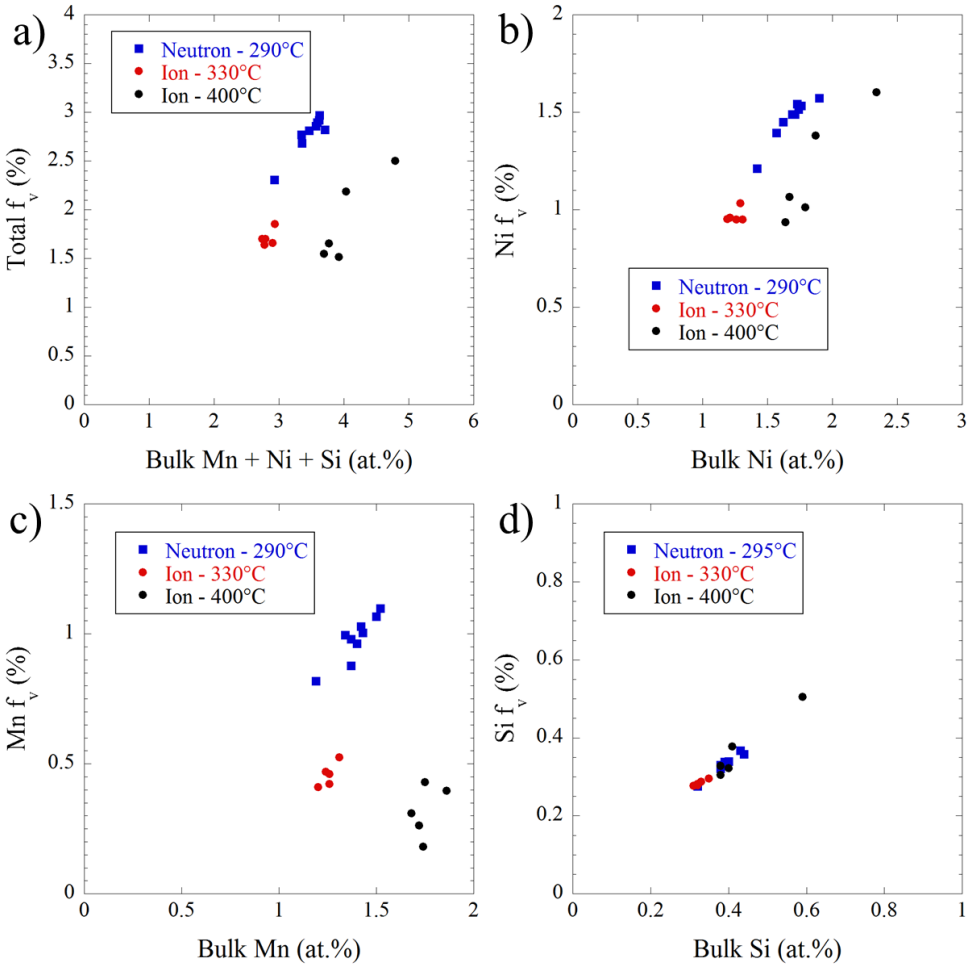

Figure 7.5. Volume fraction vs bulk solute content for a) Mn + Ni + Ni, b) Ni only, c) Mn only, and d) Si only.

Table 7.4. Matrix compositions for the 290°C neutron and 330°C and 400°C ion irradiations.

Particle	Matrix Composition (at.%)						
	T_{irr} (°C)	Mn	+/-	Ni	+/-	Si	+/-
Neutron	290	0.32	0.03	0.17	0.03	0.04	0.01
Fe^{3+}	330	0.70	0.07	0.27	0.08	0.03	0.01
Fe^{3+}	400	1.48	0.11	0.65	0.14	0.06	0.02

This inconsistency between the solute response at various T_{irr} results in a shift in precipitate compositions, as is seen in Figure 7.6. Higher T_{irr} results in more Ni and Si and less Mn in the precipitates. Again, this shift in composition was seen in the previous section when comparing neutrons to ions at a constant dose and T_{irr}, so the shift may be partly due to the difference in particles and/or dose rate, though the large shift from 330°C to 400°C under constant dose rate with ions shows that T_{irr} also plays a significant role in the final compositions.

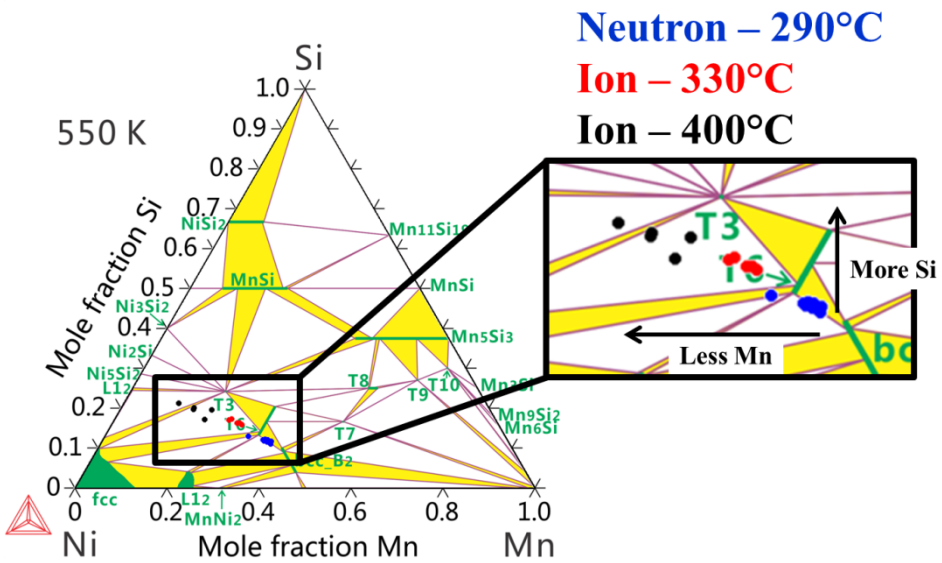

Figure 7.6. Relative amount of Mn, Ni and Si in the precipitates for the 290°C neutron irradiated condition and 330°C and 400°C ion irradiated conditions.

Ultimately, the experiment was designed to test the hypothesis that higher T_{irr} would result in a lower density of large clusters. This is qualitatively confirmed by looking at the atom maps in Figure 7.4, where the precipitates in the 400°C ion irradiated sample are much larger than at lower T_{irr}. Figure 7.7 shows the precipitate size distributions for the three T_{irr}. The distribution for the 330°C ion irradiated condition is slightly shifted to larger precipitates, but the 400°C condition contains significantly larger precipitates, with the small end of the distribution overlapping the large end of the lower T_{irr} conditions. The ion irradiated samples are currently undergoing annealing at 425°C to test the hypothesis that the larger clusters should remain stable, but the samples have not yet been investigated with APT.

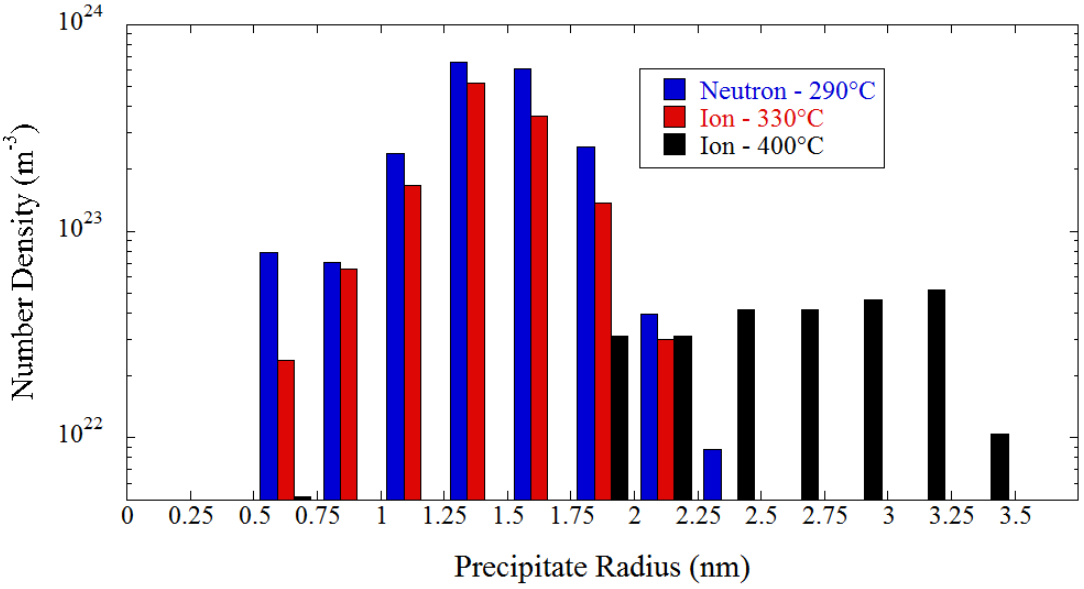

Figure 7.7. Precipitate size distribution for the 290°C neutron irradiated specimens and 330°C and 400°C ion irradiated specimens.

7.4 Conclusions

In summary, comparisons between precipitates in neutron and ion irradiated steels show more similarities than differences. While ion irradiations may never be able to directly simulate neutron irradiations in order to directly predict embrittlement at a given dose in power reactor relevant conditions, they can certainly provide useful insight into MNSPs. For example, they can be used to study various compositional variables, which is necessary for new alloy development. In addition, they can be very useful in PIA experiments, both from the perspective that the samples aren't radioactive and thus are easier to test, and that more desirable starting microstructures can be created prior to annealing.

Though the results are very encouraging, they also present a number of new questions. First, why do some ion accelerators result in a higher number density of small precipitates, as seen in literature, while the ion accelerator used in this study created a lower density of similarly sized precipitates to neutron irradiations? Why in general do ion irradiations result in precipitates that are Mn depleted and Ni/Si rich when compared to neutron irradiations? Why do the compositions of the precipitates shift at higher T_{irr}? Will the larger precipitates remain stable under annealing? These questions should be addressed with future work.

7.5 References

1. Dohi K, Nishida K, Nomoto A, Soneda N, et al. "Three Dimensional Atom Probe Observations of Reactor Pressure Vessel Model Alloys Irradiated by Neutrons and Heavy Ions", *J. Japan Inst. Met.* 2010;74(3):191–198.
2. Fujii K, Fukuya K and Hojo T. "Concomitant formation of different nature clusters

and hardening in reactor pressure vessel steels irradiated by heavy ions", *J. Nucl. Mater.* 2013;443(1-3):378–385.

3. Pareige P, Radiguet B and Barbu A. "Heterogeneous irradiation-induced copper precipitation in ferritic iron-copper model alloys", *J. Nucl. Mater.* 2006;352(1-3):75–79.
4. Wells PB, Yamamoto T, Miller B, Milot T, et al. "Evolution of manganese–nickel–silicon-dominated phases in highly irradiated reactor pressure vessel steels", *Acta Mater.* 2014;80:205–219.
5. Odette GR, Yamamoto T and Klingensmith D. "On the effect of dose rate on irradiation hardening of RPV steels", *Philos. Mag.* 2005;85(4-7):779–797.
6. Eason ED, Odette GR, Nanstad RK and Yamamoto T. "A physically based correlation of irradiation-induced transition temperature shifts for RPV steels," Oak Ridge National Lab, 2007; ORNL/TM-2006/530.
7. Odette GR. "Radiation Induced Microstructural Evolution in Reactor Pressure Vessel Steels", *Mater. Res. Soc. Symp. Proc.* 1995;373:137–148.

Chapter 8 Hardening Relationships

The data presented in the previous chapters demonstrates that reliable embrittlement prediction models of RPV ΔT at extended lifetimes must include the effects of MNSPs. While the creation of a new model will ultimately require the fitting of the large surveillance ΔT database, as well as possibly data from the UCSB ATR-2 experiment, the framework for a potential model is proposed here. First, it is shown that the measured hardening after irradiation can be directly correlated to the precipitate f_v. Next, because the previous chapters demonstrated that the MNSPs are intermetallic phases, whose formation is accelerated by radiation enhanced diffusion, a simple Avrami type model is used to predict $f_v(\phi t_e)$. The parameters in the Avrami model were determined through fitting the large f_v database generated by past students and staff at UCSB as well as the data presented in the preceding chapters.

Since $\Delta\sigma_y$ can be determined from f_v, the $f_v(\phi t_e)$ Avrami model is then converted to $\Delta\sigma_y(\phi t_e)$. The $\Delta\sigma_y$ predictions are then compared with actual measured mechanical property measurements to show very good agreement with the large UCSB test reactor database. To further evaluate the accuracy of this proposed model, the $\Delta\sigma_y$ predictions are compared with the first set of available tensile samples from the UCSB ATR-2 irradiation. The model again shows good agreement, which is of particular importance because no microstructure data from the ATR-2 experiment was used to determine the best fit parameters. Finally, a

conversion factor is used to translate $\Delta\sigma_y(\phi t_e)$ to $\Delta T(\phi t_e)$, which is used to compare the Avrami model with two current models used to predict RPV embrittlement. The residuals for the Avrami type model are shown to be on the same order as the models statistically fit to large mechanical property databases. While the final model will require fitting to actual mechanical property databases, the general framework proposed here shows great promise in predicting extended life ΔT.

8.1 Microstructure to Property Correlation

In order to create a physically informed model predicting $\Delta T(\phi t_e)$, a correlation must first be developed between the microstructure changes that occur under irradiation and the resultant mechanical property changes. The EONY model contains two microstructure features, matrix defects and Cu-rich precipitates. Though results from section 6.2 suggest that other features besides precipitates may be present in the samples from the ATR1 condition, a first order model will attempt to correlate only the precipitates with $\Delta\sigma_y$. The two low Ni alloys, which contained a high density of dislocation loops, will not be included in this analysis since the loops likely contribute to the overall hardening. Future work will focus on obtaining more reliable loop and precipitate measurements, though these alloys will not be discussed further here.

As was explained in section 2.5, the principle of superposition can be used to isolate the precipitate contribution to hardening, σ_{yp}, from the total hardening in an alloy. Here, the normalized MNSP hardening efficiency ($\sigma_{yp}/\sqrt{f_v}$) was determined through calibrating a modified Russell-Brown type model to a series of irradiated low Cu steels where both

microstructure and mechanical property data were available. In addition, the Cu-bearing steels from the ATR1 condition, which contain significant f_v of MNSPs were also included in the fit, shown in Figure 8.1. A peak hardening of ≈ 5700 MPa/√f_v occurs for <r> ≈ 1.2 nm. This shows fairly good agreement with a previous fit of hardening efficiency for CRPs [1], which found a peak hardening of ≈ 4800 MPa/√f_v. The comparison is even closer when considering that the model in that case subtracted off hardening for what were considered to be matrix features, which is the reason for the reduction of CRP hardening efficiency when compared to the fit here.

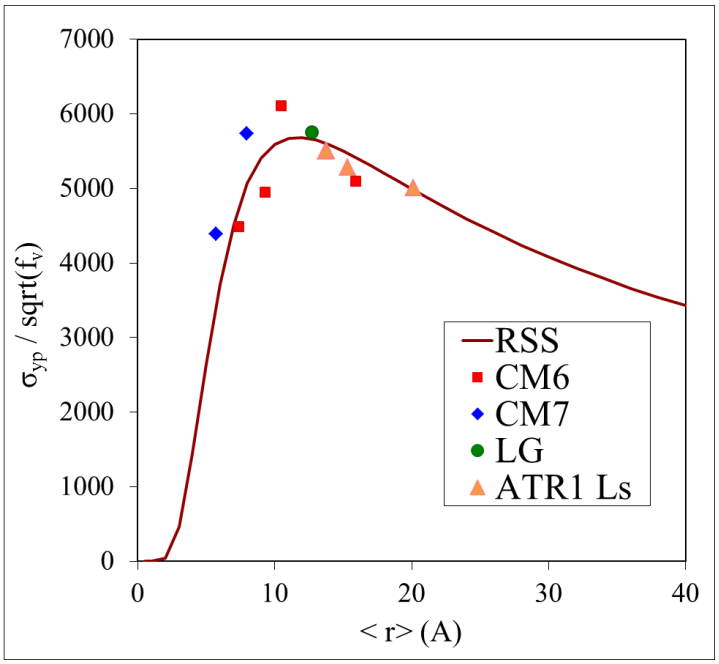

Figure 8.1. Modified Russell-Brown fit to determine the precipitate hardening efficiency.

The large microstructure and mechanical property database generated by past students and staff at UCSB (IVAR and BR2), as well as the data presented in the previous chapters (ATR1 and BR2), can be used to test the accuracy of this model. The full set of data is shown

in appendix A.7, along with the $\sigma_{yp}/\sqrt{f_v}$ used for each condition, where precipitate <r> and f_v was measured using either APT or SANS. The hardening efficiency ($\sigma_{yp}/\sqrt{f_v}$) was determined for the measured <r> and then multiplied by $\sqrt{f_v}$ to determine σ_{yp}. Superposition was then used to combine σ_{yp} with the strength contributions of existing features (see eqn. 2.17) to predict $\Delta\sigma_y$ for a given alloy/condition. Mechanical property changes for a given condition were measured using either tensile tests to measure $\Delta\sigma_y$ (MPa) or hardness testing converted to $\Delta\sigma_y$ from the correlation $\Delta\sigma_y = 3.3*\Delta H$ [2].

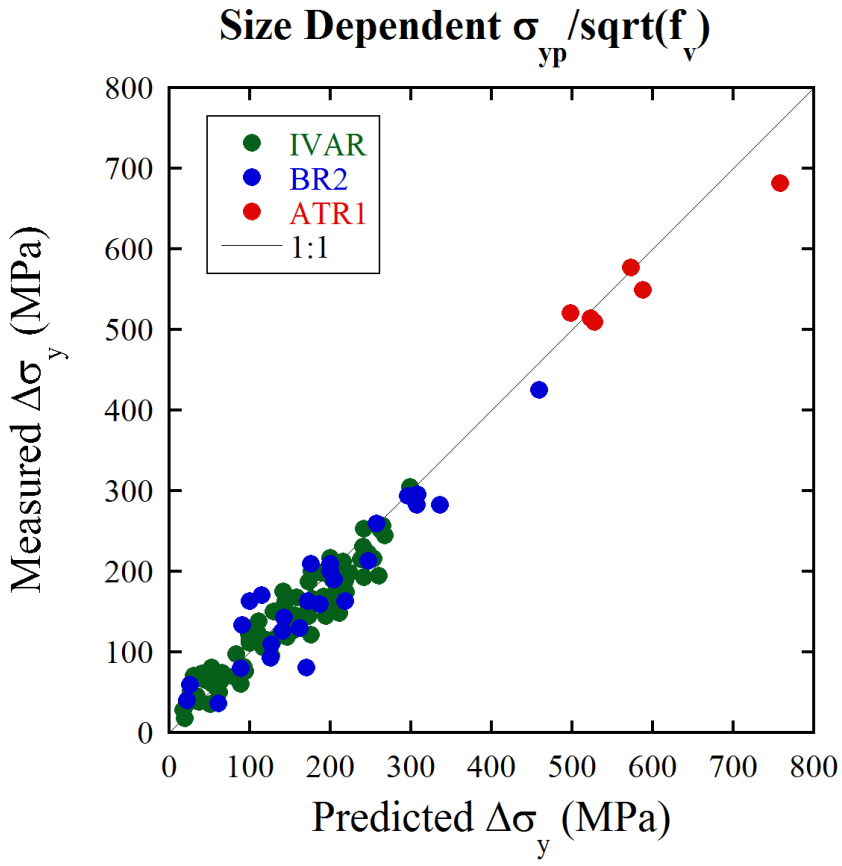

Figure 8.2. Measured vs predicted $\Delta\sigma_y$ where the predictions were made from a size dependent precipitate hardening efficiency.

Figure 8.2 shows that the agreement between the predicted and measured $\Delta\sigma_y$ is excellent. It should be noted that the calibration of the hardening efficiency, $\sigma_{yp}/\sqrt{f_v}$, was performed using only a handful of conditions, but it appears to be very accurate for all the alloy/conditions studied. Thus, while the results from section 6.2 showed hardening recovery under annealing, but no precipitate changes, which might suggest the existence of another hardening feature, it may be that undetectable precipitate changes occurred which are responsible for the recovery. In any event, since the total $\Delta\sigma_y$ seems to be reliably predicted from the precipitate data, further analysis will assume they are the only hardening feature or at least that any other features present cause a negligible increase to the total hardening.

The motivation behind calibrating the precipitate hardening efficiency is ultimately to model $f_v(\phi t_e)$ and convert it to $\Delta\sigma_y(\phi t_e)$. As was shown in Figure 8.1, the precipitate hardening efficiency is affected by <r>. Unfortunately, accurately predicting $<r>(\phi t_e)$ is much more difficult than predicting $f_v(\phi t_e)$, especially when considering that the effect of ϕ on <r> is not well understood. The precipitates that form over the ϕt_e relative to reactor lifetimes have typically been shown to be on the order of $<r> \approx$ 1-2 nm, which have a relatively narrow $\sigma_{yp}/\sqrt{f_v}$ of ≈ 5300 MPa from Figure 8.1. Instead of using a size dependent $\sigma_{yp}/\sqrt{(f_v)}$, the prediction shown in Figure 8.3 uses a constant = 5300 MPa for $\sigma_{yp}/\sqrt{(f_v)}$. In this case, the overall agreement does not significantly change. Thus, if $f_v(\phi t_e)$ can be accurately predicted, then $\Delta\sigma_y(\phi t_e)$ should also be reasonably well predicted.

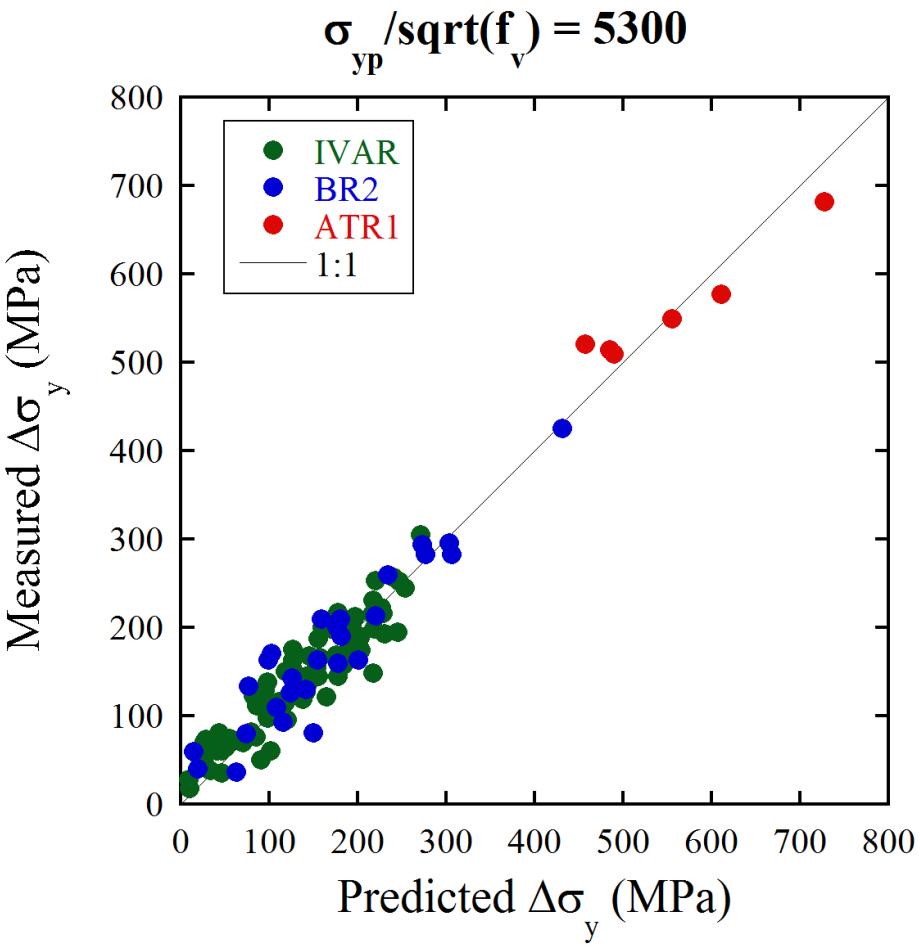

Figure 8.3. Measured vs predicted $\Delta\sigma_y$ where the predictions were made using $\sigma_{yp}/\sqrt{(f_v)} = 5300$ MPa.

8.2 Volume Fraction Prediction

8.2.1 Effective Fluence

As was explained in section 2.9, increasing ϕ delays precipitation to a higher ϕt. Thus, f_v predictions must be made for a specific reference flux, ϕ_r and compared to data either taken

at or scaled to the same ϕ_r. Here, an effective fluence, ϕt_e, is defined for each condition to compare data taken across a range of ϕ using

$$\phi t_e = \phi t \left(\frac{\phi_r}{\phi}\right)^p \tag{8.1}$$

where ϕ and ϕt are the actual flux and fluence for the condition, ϕ_r is a defined reference flux and p is a scaling parameter that varies with ϕ. Here, ϕ_r was selected to match that of the lowest ϕ IVAR condition, $\phi_r = 3x10^{11}$ n/cm^2-s. The best fit p was determined for the 6 core alloys (LC, LD, LG, LH, LI, CM6) and all showed p to vary between 0.25 and 0.3. Here p = 0.25 was used. Future work will focus on using the high ϕt, medium ϕ UCSB ATR-2 experiment to further refine p.

8.2.2 Avrami Model

Since $\Delta\sigma_y$ can be predicted from a given f_v, a model predicting $f_v(\phi t_e)$ must be developed to ultimately predict $\Delta\sigma_y(\phi t_e)$. Previous studies have shown that the precipitate f_v can be modelled with an Avrami equation [1, 3, 4], a type of which is given by

$$f(\phi t_e) = f_{max}\left\{1 - \exp\left[-\left(\frac{\phi t_e}{\phi t_0}\right)^\beta\right]\right\} \tag{8.2}$$

where f_{max} is the saturation f_v, ϕt_e is the effective fluence, ϕt_0 is the fluence requires to reach 63% of f_{max} and β is a parameter that depends on the rate controlling precipitation kinetic mechanisms [1, 3, 4]. For example, β = 3/2 corresponds to the case of diffusion controlled growth, where the growth of the precipitate is limited by the diffusion rate of atoms across the precipitate/matrix interface. $df/d\phi t_e$ is slow in the early stages of precipitates due to the difficult step of nucleation, increases during the growth stage and slows again at longer times

when most of the solute has been depleted from the matrix. In Cu-bearing alloys, the CRPs grow to saturation much before MNSPs, so in these cases, a two part Avrami model, CRP and MNSP, is used. Each portion of the model uses three parameters, f_{max}, β and ϕt_0. It is difficult to fit all three parameters simultaneously because they are interrelated. For example, the ϕt_0 is higher if f_{max} is increased. In addition, β doesn't necessarily need to be included in the fits because it is dictated by the physics relating to the nucleation and growth processes, as was described above. Thus, to simplify the fitting procedure, $f_{max,CRP}$, $f_{max,MNSP}$, β_{CRP} and β_{MNSP} were fixed and only $\phi t_{0,CRP}$ and $\phi t_{0,MNSP}$ were varied to find the best fit to the microstructural database for the 6 alloys.

The selection of $f_{max,CRP}$ for each alloy was determined based on each individual alloy's bulk Cu and Ni contents. In this case, $f_{max,CRP}$ was typically set to be ≈ 0.05-0.20% greater than the amount of Cu in solution. The CRP saturation was set above the available bulk Cu because the CRPs become enriched in Mn and Ni over time, something that would happen whether MNSPs form or not, so the total CRP f_v may be larger than the available Cu. $f_{max,MNSP}$ was selected so that the total f_v (CRP+MNSP) at saturation was ≈ that found in the ATR1 condition. While the assumption that the ATR1 condition has reached saturation has not been conclusively proven, it appears to be a relatively reasonable assumption for a number of reasons. First, the LD sample appears to have begun coarsening by this high ϕt_e, which would occur only after saturation has been reached. Second, the LG sample, which contained ~ 0.1% fv in the G1 condition, has ≈ the same MNSP f_v as all the other medium Ni alloys in the ATR1 condition. Since it contained a much smaller volume fraction than the

other alloys in the G1 condition, either the rate of precipitate formation was much faster in LG than in the other alloys, or more likely, it continued growing after the other alloys reached saturation.

Before performing the final fitting of ϕt_0, β_{CRP} and β_{MNSP} were varied to qualitatively observe the best fit values and compare these with the expected theoretical values in each case. CRPs nucleate as BCC crystals before transforming to FCC at a larger size. Because the small CRPs have the same crystal structure as the Fe matrix, the interface movement is controlled by the diffusion of atoms across the interface. Thus, it is expected that in the case of CRPs, $\beta = 3/2$, corresponding to diffusion controlled 3D growth. In actuality, the best fit β for CRPs has previously been shown to be slightly different than the theoretical value with $\beta_{CRP} = 1.1$ [1]. Here, the best fit was found to be $\beta_{CRP} = 1$. For MNSPs, the best fit β was determined to be $\beta_{MNSP} = 2.5$. This corresponds to diffusion controlled growth of precipitates with a constant nucleation rate.

Thus, the only fit parameters were ϕt_0 for both portions, CRP and MSNP. These were least square fit to determine the best fit ϕt_0 by minimizing the error between the predicted and measured total f_v. An example of the two feature Avrami fit is shown in Figure 8.4. The final fits for all alloys can be seen in Figure 8.5.

Overall, the two feature Avrami model appears to capture the total measured f_v very well, as can be seen from Figure 8.6 which plots the measured vs Avrami predicted f_v for all alloy/conditions. The best fit parameters for the various Avrami models are shown in Table 5.7. The first thing to note is that the MNSP ϕt_0 is ≈ 5-30 times higher than that for the CRPs.

This very slow evolution is MNSPs is the reason they were first called "Late Blooming Phases" over 20 years ago [5]. The MNSP ϕt_0 is slightly higher for the medium Ni steels, but there doesn't appear to be a significant trend among the medium Ni steels with varying Cu. While a systematic trend would be expected based on the chemistry of the alloys, with higher Cu and Ni contents accelerating the formation of MNSPs, it should be stressed that there are very few high ϕt data points where significant quantities of MNSPs were observed. Thus, the limited data is expected to result in some uncertainty in the fitted ϕt_0.

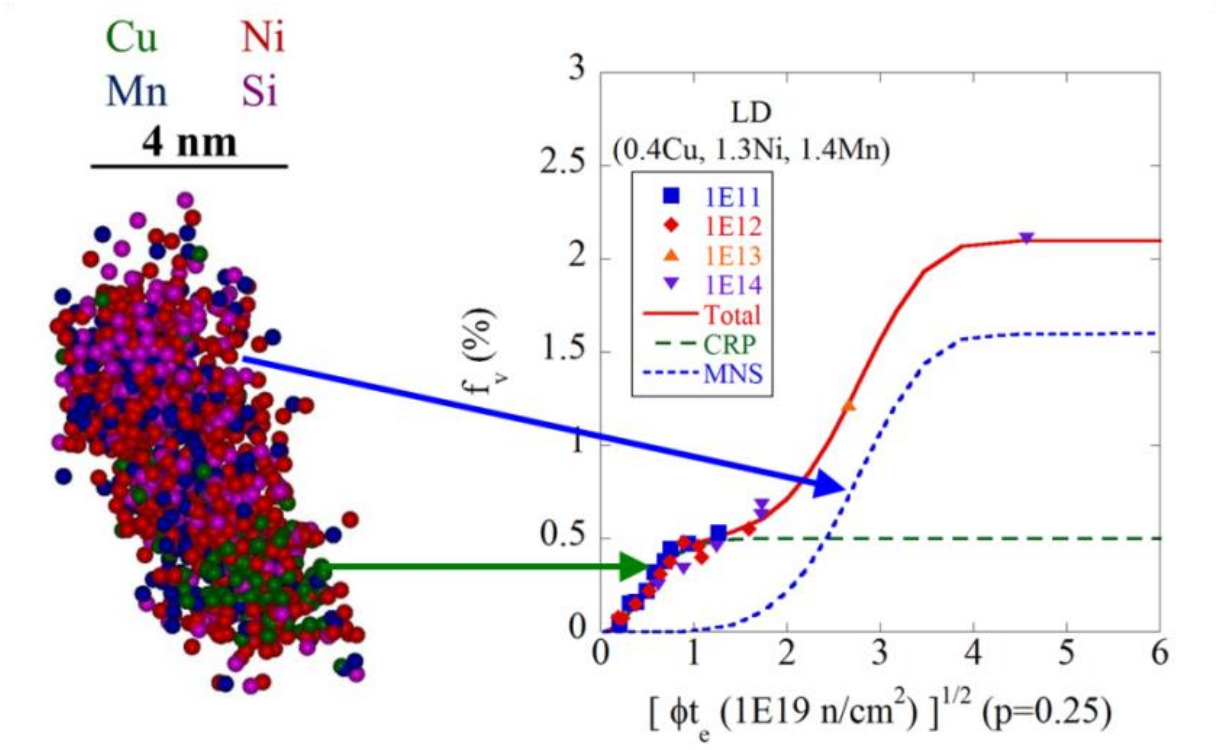

Figure 8.4. Illustration of a two part Avrami fit for high Cu steels, where the total fv is the sum of the CRP f_v and MNS f_v.

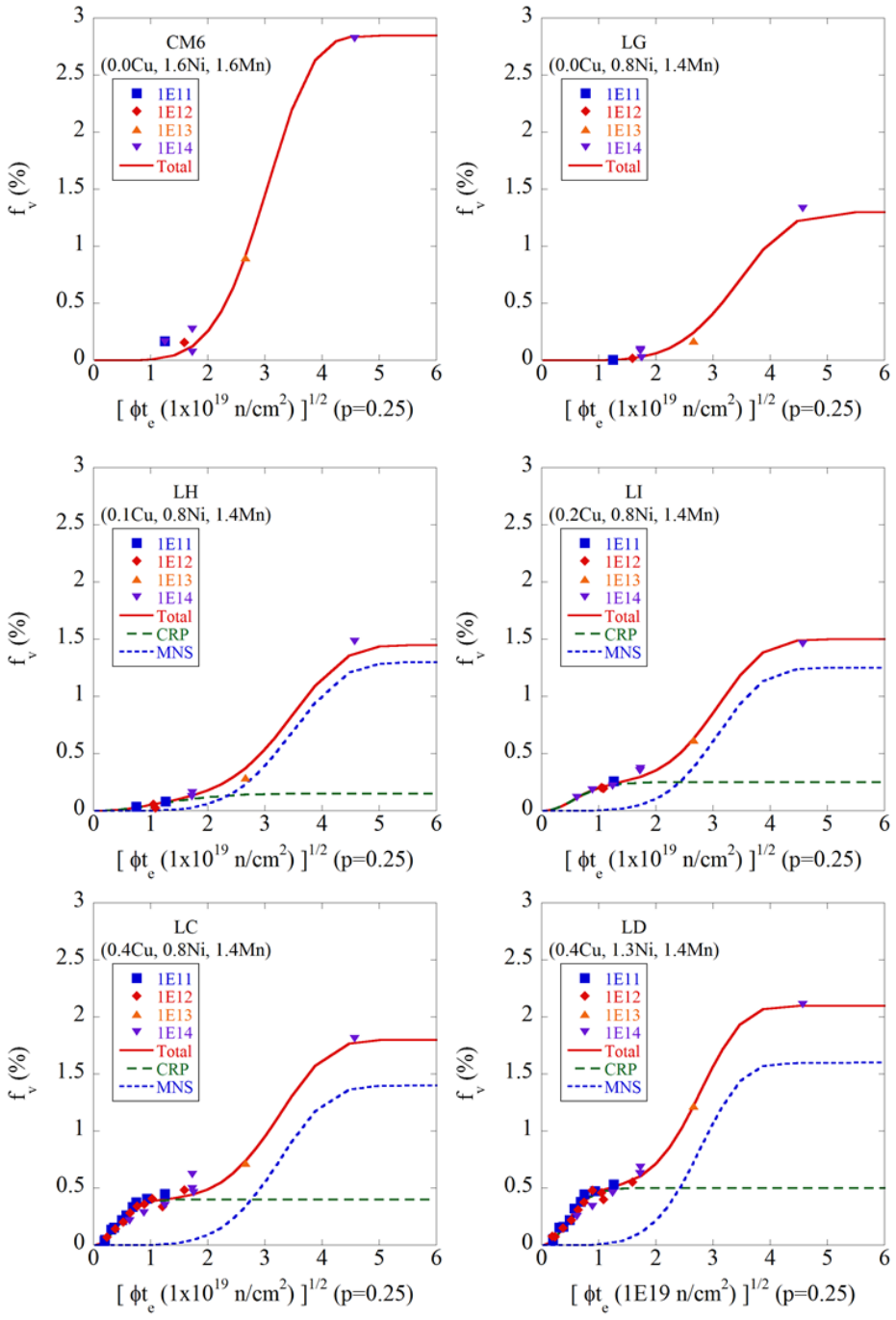

Figure 8.5. Avrami f_v fits for the 6 core alloys with conditions at different ϕ labeled in different colors. Note the units of ϕ are in n/cm^2-s.

Finally, no large conclusions should be drawn from the absolute values of ϕt_0, as they are largely affected by the choice of the p exponent when performing the ϕ correction. For example, varying p from 0.2 to 0.3 results in a shift of $\phi t_{0,MNSP}$ in LG from $17.2x10^{19}$ n/cm2 to $10.0x10^{19}$ n/cm^2. This large shift is likely due to the fact that there is essentially no microstructure data available for the low ϕ conditions because MNSPs aren't seen until higher ϕt. Again, the ATR-2 experiment, which contains a large number of high ϕt conditions over a range of medium ϕt, will be very valuable in refining the best fit $\phi t_{0,MNSP}$.

Table 8.1. Summary of best fit Avrami parameters for CRPs and MNSPs with p=0.25.

Alloy	CRP Parameters			MNSP Parameters		
	β	f_{max} (%)	ϕt_0 ($1x10^{19}$ n/cm^2)	β	f_{max} (%)	ϕt_0 ($1x10^{19}$ n/cm^2)
CM6	-	-	-	2.5	2.85	10.2
LC	1	0.4	0.3	2.5	1.40	11.8
LD	1	0.5	0.4	2.5	1.60	8.6
LG	-	-	-	2.5	1.30	13.2
LH	1	0.15	2.4	2.5	1.30	13.5
LI	1	0.25	0.6	2.5	1.25	10.6

Table 8.2. Summary of best fit Avrami parameters for CRPs and MNSPs.

Alloy	CRP ϕt_0 ($1x10^{19}$ n/cm^2)			MNSP ϕt_0 ($1x10^{19}$ n/cm^2)		
	P=0.20	P=0.25	P=0.30	P=0.20	P=0.25	P=0.30
CM6	-	-	-	12.8	10.2	10.0
LC	0.3	0.3	0.3	14.9	11.8	9.2
LD	0.4	0.4	0.4	10.8	8.6	7.0
LG	-	-	-	17.2	13.2	10.0
LH	2.8	2.4	2.1	17.9	13.5	10.1
LI	0.8	0.6	0.5	13.1	10.6	8.6

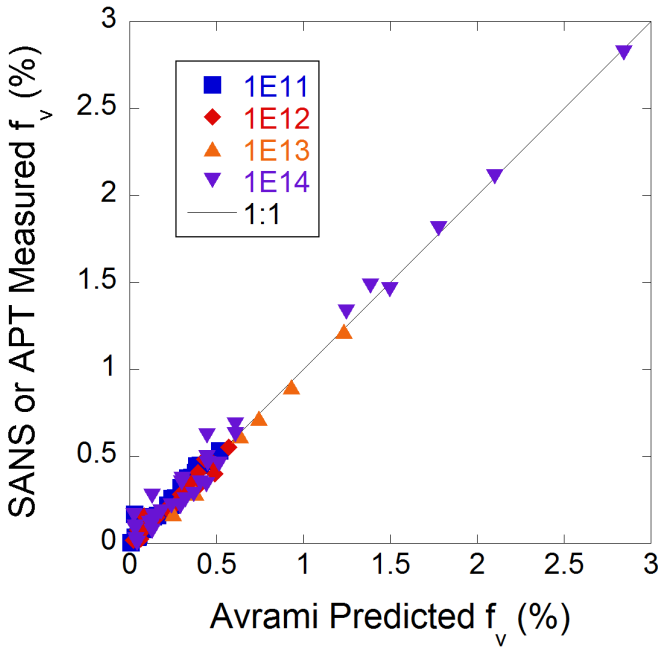

Figure 8.6. Measured vs predicted f_v from the Avrami model fits.

8.3 Predicting Mechanical Properties from Microstructure

The $f_v(\phi t_e)$ Avrami model can be converted to $\Delta\sigma_y(\phi t_e)$ simply by using the correlation established in section 8.1, which found $\Delta\sigma_{yp} = 5300\sqrt{f_v}$. Then, using the principle of superposition, found in eqn. 2.17, $\Delta\sigma_y$ can be determined. This $\Delta\sigma_y(\phi t_e)$ is compared with actual mechanical property measurements for the large UCSB test reactor database, as is seen in Figure 8.7. There appears to be an under prediction at low fluence for most every alloy, though the overall magnitude of this under prediction is fairly small. Figure 8.8 shows the measured vs predicted $\Delta\sigma_y$ to more clearly view the accuracy of the model. Figure 8.9 shows the same data as in Figure 8.8, but at a different scale to better see the under prediction at lower $\Delta\sigma_y$.

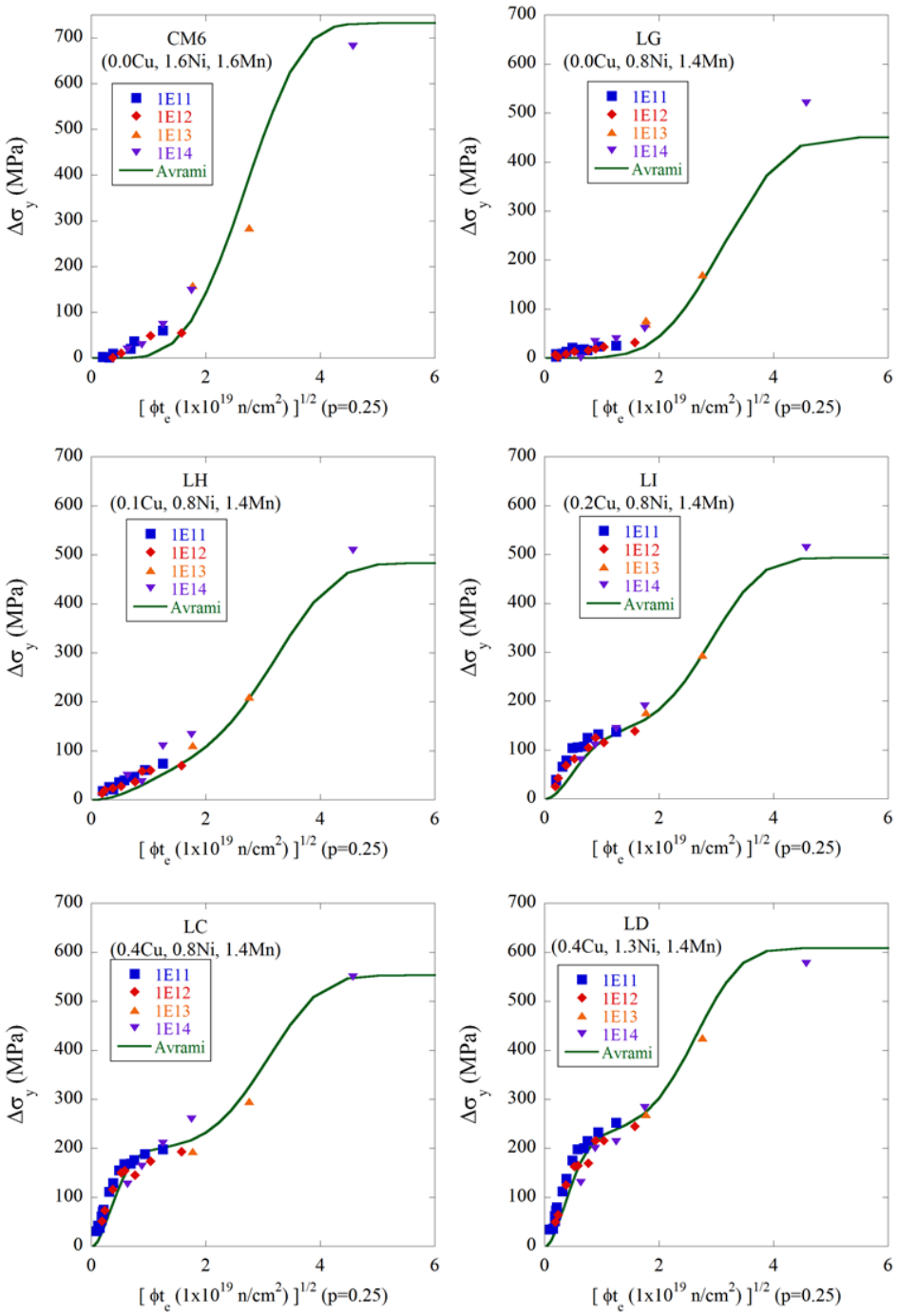

Figure 8.7. Avrami $\Delta\sigma_y(\phi t_e)$ model compared to the UCSB test reactor database with conditions at different ϕ labeled in different colors. Note the units of ϕ are in n/cm^2-s.

This under prediction is largely caused by the lower Cu steels, which have measurable hardening at low ϕt_e, but not much predicted hardening due to the slowly nucleating MNSPs. This further suggests that the MNSPs evolve from matrix features, which have long been hypothesized to cause the hardening seen in low Cu alloys at low fluence. Future model development will focus on accounting for this low fluence hardening, but the focus here is on accurately predicting extended life embrittlement so this will not be discussed further. In any event, the low ϕt_e hardening is only under predicted by ≈ 25 MPa and the model shows very good agreement at higher ϕt_e.

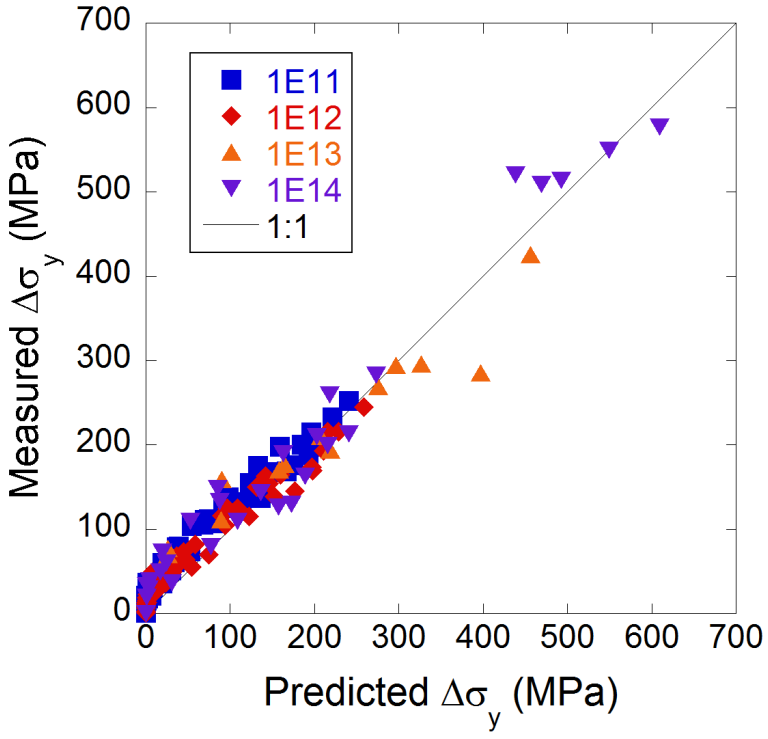

Figure 8.8. Measured vs Predicted $\Delta\sigma_y$ where the predictions are from the $\Delta\sigma_y(\phi t_e)$ Avrami model.

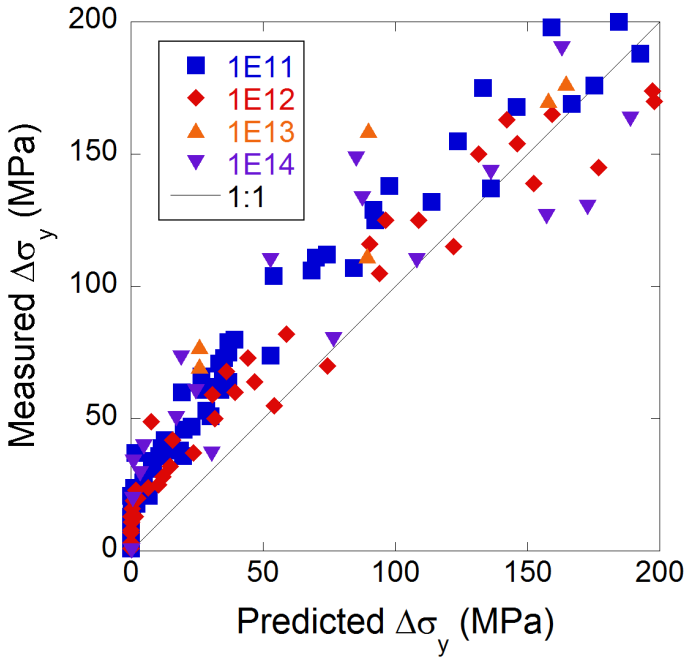

Figure 8.9. Higher magnification view of Figure 8.8 to more clearly seen the predictions at lower $\Delta\sigma_y$.

8.4 ATR2 Irradiation

The large scale UCSB ATR2 irradiation is designed to investigate RPV embrittlement at extended life fluences. The first batch of tensile specimens from this irradiation were recently received and tested at UCSB. The irradiation condition for the core 6 alloys is shown below. The ϕt_e is calculated using p = 0.25 and $\phi_r = 3x10^{11}$ n/cm^2-s.

Table 8.3. UCSB ATR-2 irradiation condition.

Condition	Neutron ϕ* (n/cm2/s)	Neutron ϕt* (n/cm2)	Neutron ϕt_e* (n/cm2)	Dose Rate (dpa/s)	Dose (dpa)	Tirr (°C)
ATR2	3.6E+12	1.2E+20	6.5E+19	5.4E-09	0.18	290

*For neutron energies > 1 MeV

Two examples of unirradiated and irradiated σ-ε curves for the Cu-free, high Ni steel (CM6) and high Cu/Ni steel (LD) are given in Figure 8.10 and Figure 8.11, respectively. The curves for all 6 core alloys are given in appendix A.8.

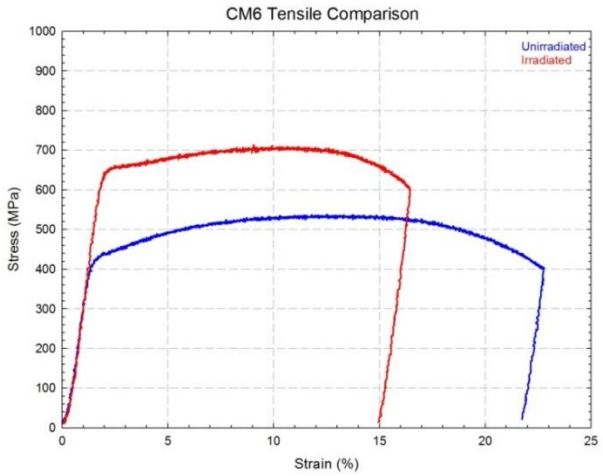

Figure 8.10. Unirradiated (blue) and irradiated (red) σ-ε curves for the Cu-free, high Ni steel (CM6) in the ATR-2 condition.

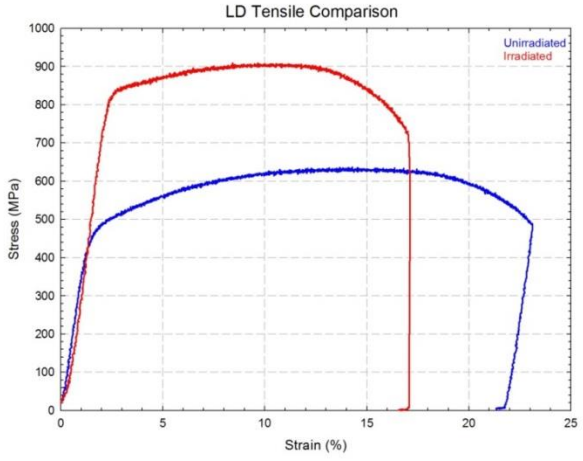

Figure 8.11. Unirradiated (blue) and irradiated (red) σ-ε curves for the high Cu/Ni steel (LD) in the ATR-2 condition.

Significant hardening has clearly occurred in both steels. The $\Delta\sigma_y(\phi t_e)$ model was used to predict the $\Delta\sigma_y$ for the steels in the ATR-2 condition, with the measured vs predicted $\Delta\sigma_y$ data shown in Figure 8.12. The actual prediction numbers were made using p = 0.25, but the uncertainty in the prediction was determined by also making predictions at p = 0.2 and 0.3 to determine the sensitivity of the prediction to varying p. Only one alloy, CM6, was > 50 MPa from the predicted Δσy. This is not surprising considering that data on < 10 conditions was available for the f_v fit. The overall consistency is very encouraging, again considering that the ATR-2 property predictions were made from microstructure fits of a database that didn't include ATR-2 data.

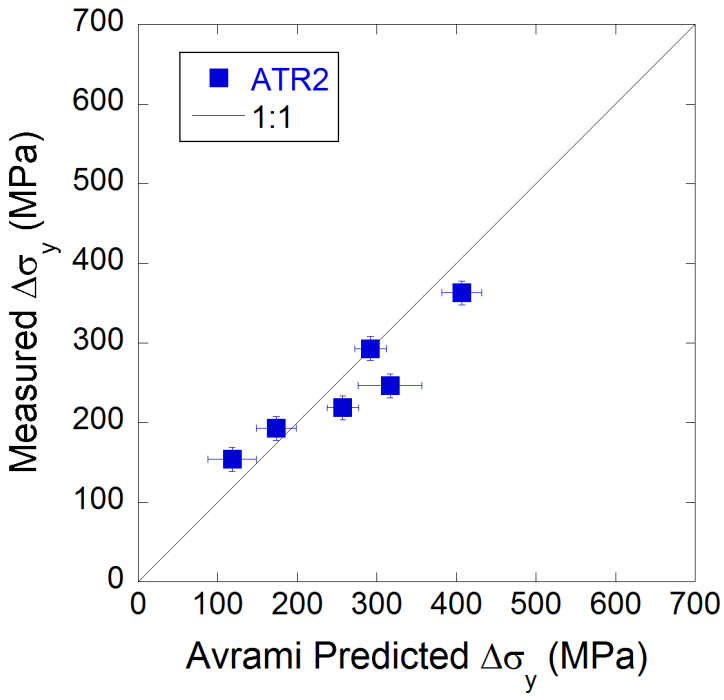

Figure 8.12. Measured vs predicted $\Delta\sigma_y$ for the ATR2 condition, where the predicted $\Delta\sigma_y$ come from the $\Delta\sigma_y(\phi t_e)$ Avrami model.

8.5 Comparisons to regulatory models

In order to compare the Avrami model with models used by the NRC (EONY) and ASTM (PE900), the $\Delta\sigma_y(\phi t_e)$ Avrami model must first be converted to $\Delta T(\phi t_e)$. This is done using a simple scaling relationship that has been established as $\Delta T=0.68\Delta\sigma_y$ [6]. The two models which will be compared to the Avrami model are the Eason-Odette-Nanstad-Yamamoto (EONY) model and the PE900 model. EONY is currently used by the NRC for failure analysis related to pressurized thermal shock. While it was statistically fit to the large surveillance ΔT database, it was motivated and structured based on an understanding of the physics leading to RPV embrittlement. On the other hand, PE900, which was recently accepted as a standard by the ASTM, is purely a statistical model that was fit to the surveillance database. As has previously been explained, EONY does not contain a term for MNSPs and because of this, significantly under predicts high ϕt_e ΔT. The PE900 model included recent surveillance data from the Ringhals reactor, which contains MNSPs at high fluence, and large corresponding ΔT. Thus, while PE900 does not explicitly treat MNSPs, it does predict significant ΔT at high ϕt_e for high Ni steels.

Figure 8.13 shows ΔT predictions for the three models compared to the UCSB test reactor database for the high Ni, Cu-free steel (CM6) and high Cu/Ni steel (LD). These EONY and PE900 plots were made using the ASTM E10 Embrittlement Database Plotter prepared by M. Erickson-Kirk [7]. The EONY model (blue lines) under predicts the high ϕt_e data for both alloys. On the other hand, while the PE900 model significantly under predicts LD at higher ϕt_e, it is reasonably accurate for the highest ϕt_e CM6 data points, though it

largely over predicts at lower ϕt_e. The reason for the high accuracy of the PE900 model for CM6 is that it was directly fit to a high ϕt_e condition from the Ringhals reactor, which showed large f_v of MNSPs. Note, APT data of this condition was shown in section 5.9. In addition, the Ringhals RPV and CM6 have a very similar composition, which means the PE900 also fairly accurately predicts CM6 at high fluence as well.

To better evaluate the accuracy of all three models, the residuals (predicted - measured ΔT) as a function of ϕt_e are shown in Figure 8.13. The left portion of the figure shows the residuals for the entire database and the right figure excludes the highest ϕte data points to better see the lower ϕt_e residuals. The Avrami model slightly under predicts at low ϕt_e, which was also shown in Figure 8.9, but is within ≈ 60°C to all data points at higher ϕt_e, while the two other models largely under predict by > 50°C. The PE900 over predicts in a few high ϕt cases, again for the CM6 steel.

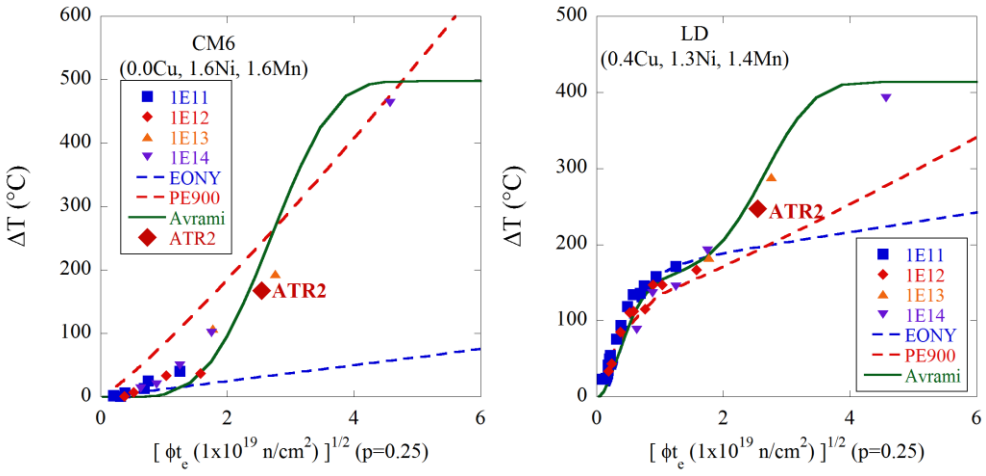

Figure 8.13. ΔT data for the high Ni, Cu-free steel (CM6-left) and high Cu/Ni steel (LD-right) compared to the three prediction models: Avrami (green), EONY (blue), PE900 (red). Note the different color data points correspond to different ϕ, with units in n/cm^2-s.

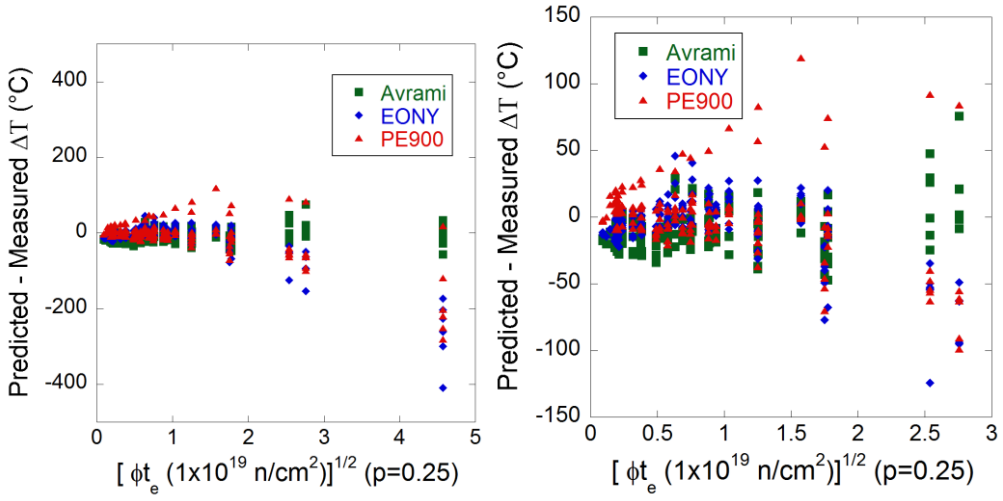

Figure 8.14. Predicted - measured ΔT vs ϕt_e for the three models: Avrami (green), EONY (blue), PE900 (red). Note that both figures show the same data, but the figure on the right is zoomed in on the lower ϕt_e data to better see the residuals.

The goodness of fit for each model was evaluated by determining the bias, or mean residual, as well as the root mean square difference for the residuals using the following equations

$$Bias = \frac{\sum_{i=1}^{n} r_i}{n} \tag{8.3}$$

$$RMSD = \sqrt{\frac{\sum_{i=1}^{n} (r_i)^2}{n}} \tag{8.4}$$

where r_i is the residual, or predicted – measured ΔT, for the i'th data point and n is the total number of data points. Essentially, the bias measures whether a given model on average over or under predicts and the RMSD measures the overall accuracy of the model. The bias and RMSD for all three models are shown in Table 8.4. These values were calculated for all data points and also for all data except the ATR1 condition, since this is the only condition past

the highest expected extended life ϕt_e. The PE900 shows the smallest Bias both when including and excluding the ATR1 data. On closer inspection, the reason for the low bias is because it under predicts most all data, except CM6, which it significantly over predicts. This results in the PE900 model having the largest RMSD when excluding the ATR1 data. The EONY model has the largest RMDS when including the ATR1 data because it significantly under predicts this condition. Finally, the Avrami model has a slightly larger bias than the PE900 data, but the smallest RMSD. The bias occurs especially at low fluence, where the Avrami model largely under predicts.

Table 8.4. Bias and RMSD for the three models for all data, and for all data except ATR1.

Model	All Data		Excluding ATR1	
	Bias (MPa)	RMSD (MPa)	Bias (MPa)	RMSD (MPa)
Avrami	-10.3	20.0	-10.1	19.5
EONY	-18.1	58.5	-9.1	28.3
PE900	-7.0	48.0	-0.8	29.9

8.6 Avrami Prediction for Surveillance Data

Recent high ϕt_e surveillance data from a low Cu, high Ni weld also has shown large f_v of MNSPs and larger than expected ΔT, as has been published by other groups [8] and shown in section 5.9. For further examination of the accuracy of the EONY model, data from these two reactors, Ringhals 3 and Ringhals 4, are plotted along with CM6 in Figure 8.15. The compositions for the three alloys are given in Table 8.5. The data are all plotted using the effective fluence scaling parameters established in section 8.2.1, with $\phi_r = 3x10^{11}$ n/cm^2-s and $p = 0.25$. Note that the Ringhals 3 ΔT at a given ϕt_e are higher than the Ringhals 4 ΔT. This is

likely because Ringhals 3 has a slightly higher Cu content, which accelerates MNSP formation. Furthermore, while the CM6 model does slightly over predict near the expected end of life ϕt_e of 10^{20} n/cm^2, or 3.3 on this scale, the data falls right in line with the UCSB test reactor database. This is especially important because it confirms that the ϕ correction used to compare the high ϕ test reactor data with the much lower ϕ surveillance data on the ϕt_e scale appears to be relatively accurate. Overall, the model shows remarkable agreement and while it slightly over predicts the highest ϕt_e data, it slightly under predicts the medium ϕt_e data.

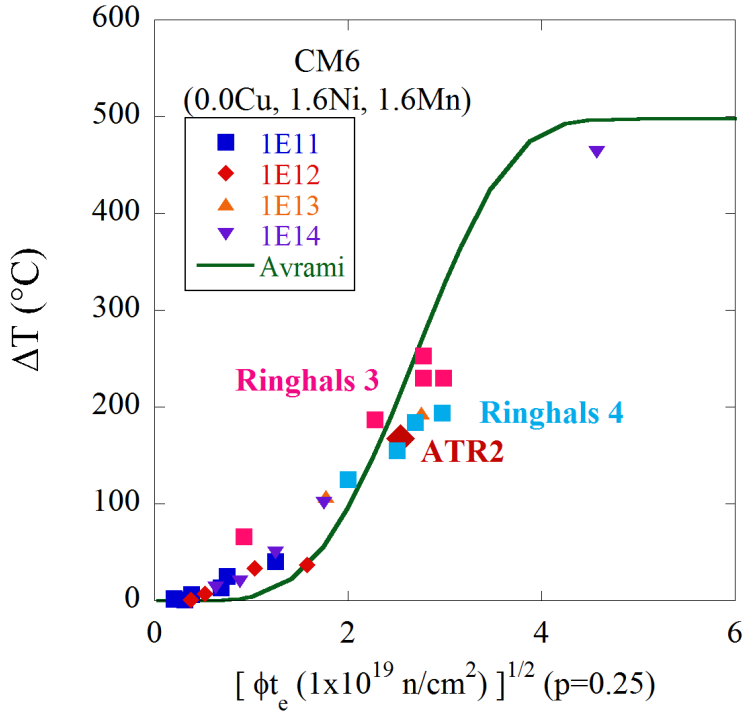

Figure 8.15. Avrami model prediction compared with CM6 data from UCSB test reactor database and data from the Ringhals surveillance program.

Table 8.5. Composition (wt.%) for the low Cu, high Ni steels shown in Figure 8.15.

Alloy	Alloy Composition (wt.%)					
	Cu	Ni	Mn	Si	P	C
CM6	0.02	1.68	1.67	0.15	0.003	0.13
Ringhals 3	0.08	1.58	1.46	0.21	0.009	0.052
Ringhals 4	0.05	1.66	1.35	0.14	0.001	0.068

8.7 Summary and Conclusions

Using framework that has previously been presented by Odette [1, 5], a preliminary model for $\Delta T(\phi t_e)$ was proposed here. First, a general correlation between the precipitate f_v and observed $\Delta\sigma_y$ was established. Second, a simple Avrami model was presented that consists of two parts, one for CRPs and one for MNSPs. The Avrami parameters were determined through a combination of the data presented in previous chapters, the physics behind the precipitation process, and a fit of the UCSB test reactor microstructural database. Following this, the $f_v(\phi t_e)$ Avrami model was converted to $\Delta\sigma_y(\phi t_e)$ using the correlation established in section 8.1. This model was shown to be fairly accurate in predicting the $\Delta\sigma_y$ from the ATR-2 condition, which was not used in the microstructure fitting. Finally, the $\Delta\sigma_y(\phi t_e)$ model was converted to $\Delta T(\phi t_e)$ to show that the residuals for the Avrami model compare favorably with models statistically fit to large ΔT databases, especially at high ϕt_e, where the other two models largely under predict ΔT.

This information is not presented to suggest that this simple Avrami model can more accurately predict ΔT than the two other models, especially because it has yet to be applied to the large surveillance ΔT database. It should also be stressed that if the EONY and PE900

models were fit using the mechanical property data shown here, they would have much smaller residuals. The main point here is that the Avrami model was fit to a *microstructure* database and converted to $\Delta\sigma_y$ using very simplified relations. The fact that the ΔT residuals are even close to the statistically fit models demonstrates the great promise in the framework presented here. Furthermore, it seems to confirm the general findings in the previous chapters that the MNSPs are intermetallic phases that can accurately be modelled using a simple phase transformation model and that the precipitates are the dominant hardening feature. In addition, the fact that the model also can predict data from a surveillance program at high ϕt_e gives even more confirmation to the general principles outlined in the previous chapters, especially the effective fluence scaling and Avrami model. Future work will focus on refining the Avrami fit parameters, and especially in determining $\phi t_{o,MNSP}$ for various alloys, with an ultimate goal of creating a model that can determine $\phi t_{o,MNSP}$ as a function of alloy chemistry, namely Cu and Ni.

8.8 References

1. Eason ED, Odette GR, Nanstad RK and Yamamoto T. "A physically based correlation of irradiation-induced transition temperature shifts for RPV steels," Oak Ridge National Lab, 2007; ORNL/TM-2006/530.
2. He MY, Odette GR, Yamamoto T and Klingensmith D. "A universal relationship between indentation hardness and flow stress", *J. Nucl. Mater.* 2007;367-370 A(SPEC. ISS.):556–560.
3. Odette GR, Yamamoto T and Klingensmith D. "On the effect of dose rate on irradiation hardening of RPV steels", *Philos. Mag.* 2005;85(4-7):779–797.
4. Porter DA, Easterling KE and Sherif MY. "Phase Transformations in Metals and Alloys" Third Edit. CRC Press, 2009.
5. Odette GR. "Radiation Induced Microstructural Evolution in Reactor Pressure Vessel

Steels", *Mater. Res. Soc. Symp. Proc.* 1995;373:137–148.

6. Odette GR and He MY. "Cleavage toughness master curve model", *J. Nucl. Mater.* 2000;283-287:120–127.
7. ASTM E10 Embrittlement Database Plotter, compiled by M. Erickson Kirk, 2014.
8. Miller MK, Powers KA, Nanstad RK and Efsing P. "Atom probe tomography characterizations of high nickel, low copper surveillance RPV welds irradiated to high fluences", *J. Nucl. Mater.* 2013;437(1-3):107–115.

Chapter 9 Conclusions and Future Work

The goal of this work was to improve the understanding of RPV embrittlement at extended life fluences, primarily by focusing on the details and consequences of Mn-Ni-Si precipitates. The major conclusions are summarized below.

9.1 Nature of Precipitates

Consistent with predictions by Odette over 20 years ago [1], the steels from the very high ϕt_e ATR1 condition, with $\phi t_e \approx 2.9 \times 10^{20}$ n/cm^2, contain significant f_v of Mn, Ni and Si enriched precipitates in all the steels that were studied, including those nominally free in Cu. APT studies show that the precipitates have compositions very near to known intermetallic Mn-Ni-Si phases. Four of the studied alloys have the same nominal bulk Ni content of ≈ 0.8 at.%, but have nominal Cu variations from 0.01-0.4 wt.%. Even with this large variation in Cu level, the total MNSP f_v and composition were approximately consistent in all steels at very high ϕt_e. Thus, it appears that Cu precipitates act only as a nucleation site for the formation of MNSPs and does not alter the saturation f_v.

Equilibrium thermodynamic modeling, performed by the University of Wisconsin, Madison, and XRD measurements, made by Brookhaven National Lab, in collaboration with UCSB, present a compelling case that the precipitates are intermetallic phases. The thermodynamic models predict very similar compositions and f_v to what is found in the very

high ϕt_e ATR1 condition, which may have reached full saturation. XRD confirms that the precipitates have the expected crystal structure of the intermetallic Mn-Ni-Si phases.

Finally, while the formation mechanism of the precipitates has been highly debated in the literature, long term annealing at 425°C of a Cu free, high Ni steel shows MNSP stability at long times. Though most precipitates dissolve, a cluster dynamics rationalizes this dissolution by showing that the high $T_a = 425°$, which is much higher than $T_{irr} = 290°C$ where the precipitates formed, along with the solute depleted matrix, results in a large precipitate critical radius, driving dissolution of the nanoclusters even though, according to the model, the bulk phases should be stable. The apparent coarsening of the few remaining precipitates at long times further suggests the thermodynamic stability of the phases. Thus, the most reasonable conclusion from the overall body of work is that the MNSPs which form under irradiation are intermetallic phases whose formation is enhanced by radiation.

9.2 Role of Ion Irradiations

Though charged particle irradiations cannot directly simulate the microstructure and mechanical property changes that occur under neutron irradiation, they can play an important role in better understanding RPV embrittlement. The precipitates in two different steels irradiated with both neutron and Fe^{3+} ions have fairly consistent sizes and compositions. The higher f_v seen in the neutron irradiation is likely caused by the higher dose rate in the ion irradiated condition, which has previously been shown to delay a given f_v to higher doses. While the compositions of the ion irradiated MNSPs is shifted to a higher Ni and Si region of the MNS phase diagram, the overall consistency between both conditions is very

encouraging and suggests that CPI may be a very useful tool to study the susceptibility of a given steel to irradiation embrittlement.

Ion irradiations were also carried out at temperatures of 330°C and 400°C. These high temperatures were selected to test the hypothesis that the final irradiated microstructure of an RPV steel may be controlled by varying the conditions of the ion irradiation. In this case, the high temperature was selected to generate a lower density of large MNSPs, which, it is hypothesized, will show more thermal stability than the smaller precipitates from the ATR1 condition. Ion irradiations at 400°C showed a lower number density of much larger precipitates than the ion or neutron irradiations at 330°C and 290°C, respectively. The precipitate composition also shifted with increasing temperature, becoming more and more Mn deficient. PIA on this steel with very large MNSPs is currently ongoing.

9.3 Hardening Models

The large $\Delta\sigma_y$ in the irradiated steels is directly correlated to the MNSP size and f_v. An Avrami model was fit to the large UCSB test reactor microstructure database, which includes data presented here, to determine the MNSP $f_v(\phi t_e)$. The corresponding $\Delta\sigma_y$ and ΔT were then calculated from this f_v using established correlations. The Avrami model, along with two other models used to predict ΔT for RPVs, were then compared to the UCSB test reactor mechanical property database. The bias and root mean square differences were calculated for all three models. The Avrami model shows a slightly higher bias than the PE900 model, which is largely because the PE900 mostly over predicts the UCSB database, but for one alloy largely over predicts which results in a bias ≈ 0°C. The RSMD is lowest for

the Avrami model, especially when including the highest ϕt_e ATR1 data. The Avrami model also accurately predicts data from both the UCSB ATR-2 irradiation and the Ringhals Surveillance program, neither of which was used in the fitting of the microstructural Avrami model. While future work will focus on further refining this model, the general framework shows great promise.

9.4 References

1. Odette GR. "Radiation Induced Microstructural Evolution in Reactor Pressure Vessel Steels", *Mater. Res. Soc. Symp. Proc.* 1995;373:137–148.

Appendix A

A.1 Previous UCSB Irradiation Conditions

Condition	Reactor	Neutron Flux* (n/cm2/s)	Neutron Fluence* (n/cm2)	Dose Rate (dpa/s)	Dose (dpa)	T_{irr} (°C)
T1	Ford	7.8E+11	7.00E+17	1.17E-09	0.001	290
T2	Ford	7.8E+11	1.80E+18	1.17E-09	0.003	290
T3	Ford	7.8E+11	3.40E+18	1.17E-09	0.005	290
T4	Ford	9.7E+11	7.50E+18	1.46E-09	0.011	290
T5	Ford	7.8E+11	1.36E+19	1.17E-09	0.020	290
T6	Ford	1.0E+12	3.42E+19	1.50E-09	0.051	290
T11	Ford	2.6E+11	4.00E+17	3.89E-10	0.001	290
T12	Ford	3.2E+11	1.00E+18	4.77E-10	0.002	290
T13	Ford	3.1E+11	2.40E+18	4.70E-10	0.004	290
T14	Ford	3.2E+11	4.80E+18	4.77E-10	0.007	290
T15	Ford	2.6E+11	8.50E+18	3.95E-10	0.013	290
T16	Ford	3.0E+11	1.57E+19	4.50E-10	0.024	290
T21	Ford	1.0E+11	3.00E+17	1.50E-10	0.000	290
T22	Ford	1.0E+11	1.10E+18	1.53E-10	0.002	290
T23	Ford	8.4E+10	2.40E+18	1.26E-10	0.004	290
T24	Ford	8.4E+10	4.00E+18	1.26E-10	0.006	290
G1	BR2	1.00E+14	1.334E+20	1.50E-07	0.200	300
G2	BR2	1.00E+14	6.67E+19	1.50E-07	0.100	300
G3	BR2	1.00E+14	1.6675E+19	1.50E-07	0.025	300
G4	BR2	1.00E+14	3.335E+19	1.50E-07	0.050	300
G5	BR2	3.00E+12	1.6675E+19	4.50E-09	0.025	300

A.2 APT Data – ATR1

		Bulk (at.%)				Precipitate (%)				Precipitate f_v (%)						
Run	Alloy	Cu	Ni	Mn	Si	Cu	Ni	Mn	Si	Cu	Ni	Mn	Si	<d>	N_v	f_v (%)
1965	LC	0.22	0.98	1.16	0.55	9.8	40.8	30.8	18.6	0.20	0.85	0.64	0.39	2.91	1.66E+24	2.09
1967	LC	0.26	0.75	1.13	0.41	14.1	36.5	33.3	16.1	0.25	0.65	0.59	0.29	3.38	9.10E+23	1.78
1968	LC	0.21	0.72	1.18	0.36	13.2	38.7	33.7	14.4	0.19	0.56	0.49	0.21	3.02	1.09E+24	1.45
1987	LC	0.34	0.86	1.14	0.44	17.1	37.4	30.2	15.3	0.33	0.71	0.57	0.29	3.13	1.20E+24	1.90
2164	LC	0.30	0.82	1.17	0.45	15.2	36.3	33.0	15.5	0.29	0.70	0.64	0.30	3.09	1.29E+24	1.93
2165	LC	0.28	0.74	1.11	0.38	15.6	37.8	31.2	15.3	0.26	0.64	0.53	0.26	3.25	9.57E+23	1.70
2166	LC	0.32	0.79	1.24	0.42	15.8	35.9	32.8	15.4	0.30	0.68	0.62	0.29	3.02	1.31E+24	1.89
2236	LC	0.29	0.74	1.10	0.44	15.7	35.8	32.4	16.1	0.28	0.64	0.58	0.29	3.06	1.27E+24	1.78
2237	LC	0.28	0.71	1.17	0.37	16.5	37.0	31.7	14.7	0.26	0.58	0.50	0.23	2.96	1.18E+24	1.57
1391	LD	0.28	1.57	1.23	0.70	9.4	48.1	22.6	19.9	0.27	1.36	0.64	0.56	4.54	6.38E+23	2.82
1392	LD	0.17	1.23	0.79	0.40	8.1	51.8	21.7	18.4	0.16	1.02	0.43	0.36	4.29	5.47E+23	1.98
2482	LD	0.22	1.23	0.90	0.57	9.1	48.9	19.9	22.1	0.20	1.06	0.43	0.48	4.28	5.81E+23	2.17
2483	LD	0.22	1.20	1.16	0.56	8.5	48.3	21.5	21.7	0.18	1.01	0.45	0.45	3.76	8.60E+23	2.09
2486	LD	0.22	1.12	1.21	0.53	9.2	46.6	23.9	20.3	0.18	0.93	0.47	0.40	3.71	8.29E+23	1.98
2487	LD	0.37	1.08	1.41	0.52	14.9	40.3	27.6	17.2	0.33	0.90	0.61	0.38	3.75	9.14E+23	2.23
2489	LD	0.21	1.07	0.89	0.52	9.5	47.5	20.8	22.2	0.17	0.86	0.38	0.40	3.64	7.42E+23	1.81
2491	LD	0.32	1.07	1.34	0.52	13.8	42.4	25.2	18.7	0.29	0.89	0.53	0.39	3.84	7.57E+23	2.09
1789	LG	0.00	0.72	1.00	0.38	0.4	46.0	34.1	19.5	0.00	0.59	0.44	0.25	2.41	1.75E+24	1.28
1790	LG	0.00	0.71	0.93	0.47	0.2	45.6	30.6	23.6	0.00	0.60	0.40	0.31	2.43	1.77E+24	1.32
1795	LG	0.00	0.71	0.77	0.42	0.2	46.8	30.0	23.0	0.00	0.63	0.41	0.31	2.56	1.53E+24	1.35
1796	LG	0.01	0.67	1.15	0.44	0.3	43.3	36.2	20.2	0.00	0.57	0.48	0.27	2.69	1.30E+24	1.32
1800	LG	0.00	0.71	0.74	0.43	0.2	47.4	28.4	24.1	0.00	0.62	0.37	0.31	2.48	1.60E+24	1.30
1780	LH	0.09	0.80	0.77	0.48	5.1	45.1	27.1	22.7	0.08	0.67	0.41	0.34	2.33	2.24E+24	1.50
1785	LH	0.08	0.72	1.14	0.43	4.9	41.0	35.3	18.8	0.07	0.60	0.52	0.28	2.72	1.43E+24	1.47
1786	LH	0.08	0.70	1.23	0.41	4.9	39.9	36.9	18.3	0.07	0.58	0.54	0.27	2.78	1.30E+24	1.46
1788	LH	0.09	0.75	1.22	0.42	5.2	41.2	35.2	18.4	0.08	0.63	0.54	0.28	2.74	1.42E+24	1.52
1971	LI	0.16	0.69	1.25	0.43	9.4	36.5	37.2	17.0	0.14	0.54	0.55	0.25	2.88	1.25E+24	1.49
1973	LI	0.15	0.71	1.03	0.44	9.2	39.3	33.1	18.5	0.13	0.57	0.48	0.27	2.72	1.41E+24	1.44
1974	LI	0.15	0.71	0.80	0.42	9.8	41.6	28.2	20.4	0.14	0.60	0.40	0.29	2.65	1.49E+24	1.43
1980	LI	0.15	0.67	1.14	0.39	8.9	38.0	36.0	17.1	0.13	0.57	0.54	0.26	2.92	1.19E+24	1.51
2179	CM6	0.00	1.62	1.34	0.38	0.1	52.4	35.9	11.6	0.00	1.45	0.99	0.32	3.20	1.72E+24	2.77
2180	CM6	0.00	1.76	1.42	0.44	0.1	52.5	35.2	12.3	0.00	1.53	1.03	0.36	2.96	2.13E+24	2.92
2185	CM6	0.00	1.90	1.37	0.43	0.1	55.7	31.1	13.0	0.00	1.57	0.88	0.37	3.07	1.91E+24	2.82
2186	CM6	0.00	1.42	1.19	0.32	0.1	52.5	35.5	12.0	0.00	1.21	0.82	0.28	3.20	1.53E+24	2.31
2493	CM6	0.00	1.74	1.43	0.39	0.0	53.0	35.1	11.8	0.00	1.51	1.00	0.34	3.25	1.70E+24	2.86
2495	CM6	0.00	1.71	1.37	0.40	0.1	53.0	34.9	12.1	0.00	1.49	0.98	0.34	3.26	1.66E+24	2.81
2496	CM6	0.00	1.73	1.52	0.38	0.1	51.9	36.9	11.1	0.00	1.54	1.10	0.33	3.30	1.61E+24	2.97
2497	CM6	0.00	1.57	1.40	0.38	0.1	52.0	35.9	12.1	0.00	1.39	0.96	0.32	3.14	1.70E+24	2.68
2498	CM6	0.00	1.69	1.50	0.40	0.1	51.4	36.8	11.7	0.00	1.49	1.07	0.34	3.15	1.79E+24	2.89
3002	JRQ	0.16	1.06	1.13	0.57	5.6	47.2	20.7	24.7	0.09	0.78	0.34	0.41	3.79	5.98E+23	1.65

A.3 APT Data – TU Condition

		Bulk (at.%)				Precipitate (%)				Precipitate f_v (%)						
Run	Alloy	**Cu**	**Ni**	**Mn**	**Si**	**Cu**	**Ni**	**Mn**	**Si**	**Cu**	**Ni**	**Mn**	**Si**	**<d>**	**N_v**	**f_v**
5505	LC	0.24	0.70	1.13	0.40	28.8	31.9	23.6	15.7	0.20	0.22	0.16	0.11	3.46	3.39E+23	0.68
5617	LC	0.24	0.80	1.19	0.43	24.4	34.9	24.4	16.4	0.19	0.27	0.19	0.13	3.29	4.13E+23	0.78
5618	LC	0.18	0.77	0.84	0.38	23.4	37.4	20.1	19.0	0.14	0.22	0.12	0.11	2.92	3.89E+23	0.58
5803	LC	0.18	0.75	1.20	0.41	21.9	36.0	24.7	17.4	0.13	0.22	0.15	0.10	3.31	3.42E+23	0.60
5806	LC	0.30	0.74	1.17	0.43	29.1	32.3	23.1	15.6	0.24	0.27	0.19	0.13	3.37	4.15E+23	0.83
5859	LD	0.38	1.19	0.95	0.56	25.1	38.7	18.1	18.1	0.32	0.50	0.23	0.23	2.79	1.13E+24	1.28
5860	LD	0.39	1.23	1.00	0.56	25.1	38.6	18.7	17.6	0.34	0.52	0.25	0.24	3.02	1.02E+24	1.35
5877	LD	0.24	1.18	1.38	0.54	15.3	41.1	26.7	16.9	0.19	0.50	0.33	0.21	2.80	1.03E+24	1.23
5880	LD	0.22	1.18	0.89	0.56	15.6	44.2	18.6	21.6	0.17	0.48	0.20	0.23	2.84	9.15E+23	1.08
5500	LG	0.01	0.76	1.23	0.45	1.1	44.3	24.8	29.9	0.00	0.09	0.05	0.06	2.21	2.83E+23	0.21
5805	LG	0.01	0.72	1.15	0.44	0.3	46.0	22.9	30.8	0.00	0.07	0.04	0.05	2.19	2.38E+23	0.16
5593	LG	0.01	0.73	1.29	0.44	0.1	44.5	25.8	29.6	0.00	0.08	0.05	0.05	2.54	2.20E+23	0.18
5869	LH	0.07	0.66	1.09	0.44	5.3	41.7	26.0	27.0	0.02	0.12	0.08	0.08	2.69	2.69E+23	0.29
5870	LH	0.09	0.76	1.30	0.50	3.4	37.1	34.5	25.0	0.02	0.22	0.21	0.15	1.79	1.57E+24	0.60
5871	LH	0.09	0.74	0.67	0.42	11.6	43.7	15.1	29.6	0.02	0.09	0.03	0.06	2.64	2.12E+23	0.20
5881	LH	0.08	0.71	1.23	0.43	7.3	40.9	27.4	24.5	0.02	0.09	0.06	0.05	2.54	2.40E+23	0.22
5624	LI	0.18	0.83	1.44	0.45	16.4	36.4	31.9	15.4	0.12	0.26	0.23	0.11	2.65	7.19E+23	0.72
5809	LI	0.17	0.81	0.66	0.42	20.2	41.2	15.2	23.5	0.11	0.22	0.08	0.12	2.78	4.49E+23	0.53
5858	LI	0.17	0.84	1.41	0.48	14.2	35.3	32.4	18.1	0.10	0.26	0.24	0.13	2.48	8.41E+23	0.73
5873	LI	0.21	0.92	0.75	0.49	22.0	41.9	12.7	23.4	0.13	0.25	0.08	0.14	2.64	5.96E+23	0.60
5501	CM6	0.00	1.74	1.22	0.38	0.1	56.1	27.0	16.8	0.00	0.58	0.28	0.17	2.26	1.56E+24	1.03
5591	CM6	0.00	1.50	1.20	0.32	0.1	54.7	27.6	17.6	0.00	0.28	0.14	0.09	2.49	6.34E+23	0.51
5592	CM6	0.00	1.62	1.27	0.35	0.2	55.2	27.4	17.2	0.00	0.39	0.19	0.12	2.47	8.65E+23	0.71
5623	CM6	0.00	1.75	0.98	0.37	0.1	58.9	22.3	18.7	0.00	0.49	0.19	0.16	2.39	1.16E+24	0.84
5804	CM6	0.00	1.67	1.02	0.35	0.1	58.1	22.9	18.9	0.00	0.47	0.19	0.15	2.40	1.03E+24	0.81

A.4 APT Data – G1 Condition

		Bulk (at.%)				Precipitate (%)				Precipitate f_v (%)						
Run	Alloy	Cu	Ni	Mn	Si	Cu	Ni	Mn	Si	Cu	Ni	Mn	Si	<d>	N_v	f_v (%)
5390	LC	0.21	0.91	0.97	0.53	25.7	35.1	23.6	15.7	0.15	0.20	0.14	0.09	2.30	9.16E+23	0.58
4116	LD	0.21	1.01	0.93	0.59	22.3	38.2	21.8	17.7	0.15	0.26	0.15	0.12	2.15	1.29E+24	0.67
4117	LD	0.18	1.03	0.93	0.59	20.5	39.1	21.1	19.2	0.11	0.22	0.12	0.11	2.03	1.24E+24	0.55
4118	LD	0.17	1.03	0.83	0.34	22.1	40.6	23.8	13.5	0.12	0.22	0.13	0.07	2.20	9.76E+23	0.54
4119	LD	0.21	0.99	0.85	0.52	24.1	37.8	21.3	16.8	0.16	0.25	0.14	0.11	2.30	1.08E+24	0.68
4128	LD	0.22	1.01	1.58	0.57	19.1	36.1	31.2	13.5	0.15	0.28	0.24	0.10	2.05	1.71E+24	0.77
4135	LD	0.27	1.03	0.99	0.53	25.2	36.5	23.1	15.2	0.22	0.31	0.20	0.13	2.39	1.21E+24	0.86
5224	LD	0.23	1.02	1.34	0.58	21.0	37.8	26.6	14.7	0.15	0.27	0.19	0.10	2.26	1.13E+24	0.70
5233	LD	0.22	0.93	1.42	0.55	21.4	36.3	28.7	13.7	0.15	0.26	0.21	0.10	2.33	1.09E+24	0.72
4036	LG	0.00	0.71	1.15	0.41	0.3	39.8	33.6	26.3	0.00	0.02	0.02	0.01	1.26	4.25E+23	0.04
5201	LG	0.01	0.83	1.15	0.47	0.5	45.9	25.0	28.6	0.00	0.02	0.01	0.01	1.53	2.72E+23	0.05
5225	LG	0.01	0.87	1.24	0.52	0.7	43.5	33.9	21.9	0.00	0.04	0.03	0.02	1.25	9.59E+23	0.10
5226	LG	0.01	0.97	0.83	0.52	0.4	51.2	18.7	29.8	0.00	0.06	0.02	0.04	1.48	6.95E+23	0.12
4041	LH	0.08	0.72	0.95	0.46	15.5	37.8	26.4	20.3	0.03	0.06	0.04	0.03	1.91	4.49E+23	0.17
4042	LH	0.08	0.74	1.00	0.44	13.6	43.3	22.8	20.3	0.02	0.06	0.03	0.03	1.73	5.43E+23	0.14
4945	LI	0.12	0.70	1.18	0.44	22.3	34.9	28.0	14.8	0.07	0.11	0.09	0.05	2.16	5.93E+23	0.31
4947	LI	0.16	0.70	1.14	0.44	27.5	34.3	24.1	14.0	0.09	0.11	0.08	0.04	2.15	6.11E+23	0.31
4966	LI	0.15	0.72	1.25	0.40	23.7	33.3	28.5	14.4	0.10	0.14	0.12	0.06	2.14	8.17E+23	0.41
4967	LI	0.18	0.75	1.28	0.44	25.1	34.9	27.0	13.0	0.13	0.18	0.14	0.07	2.42	7.28E+23	0.52
4054	CM6	0.00	1.34	1.09	0.33	0.1	58.9	25.6	15.5	0.00	0.04	0.02	0.01	1.40	4.58E+23	0.07

A.5 APT Data – DuET Condition

		Bulk (at.%)				Precipitate (%)				Precipitate f_v (%)						
Run	Alloy	**Cu**	**Ni**	**Mn**	**Si**	**Cu**	**Ni**	**Mn**	**Si**	**Cu**	**Ni**	**Mn**	**Si**	**<d>**	**N_v**	**f_v (%)**
3940	LD	0.28	1.07	1.32	0.53	28.4	36.6	18.8	16.2	0.15	0.19	0.10	0.08	2.25	8.78E+23	0.52
4709	LD	0.24	1.05	1.26	0.53	28.5	37.4	17.6	16.5	0.11	0.15	0.07	0.06	2.25	6.64E+23	0.39
4710	LD	0.24	1.05	1.05	0.55	31.0	35.0	18.1	16.0	0.14	0.15	0.08	0.07	2.36	6.59E+23	0.44
4711	LD	0.26	1.07	0.99	0.58	31.9	34.7	15.6	17.7	0.14	0.16	0.07	0.08	2.20	7.99E+23	0.45
3961	LI	0.15	0.71	1.27	0.44	24.1	34.9	23.5	17.5	0.03	0.04	0.03	0.02	2.08	2.96E+23	0.13
3962	LI	0.14	0.69	1.11	0.45	19.2	38.3	22.4	20.1	0.03	0.06	0.03	0.03	1.91	4.24E+23	0.15

A.6 APT Data – HIT Condition

T_{irr} = 330°C

		Bulk (at.%)				Precipitate (%)				Precipitate f_v (%)						
Run	Alloy	Cu	Ni	Mn	Si	Cu	Ni	Mn	Si	Cu	Ni	Mn	Si	<d>	N_v	f_v (%)
6131	CM6	0.00	1.19	1.24	0.31	0.1	56.0	27.6	16.3	0.00	0.95	0.47	0.28	2.99	1.25E+24	1.70
6138	CM6	0.00	1.26	1.20	0.32	0.0	57.8	25.0	17.1	0.00	0.95	0.41	0.28	2.88	1.28E+24	1.64
6232	CM6	0.00	1.21	1.26	0.32	0.0	56.5	27.1	16.4	0.00	0.96	0.46	0.28	2.97	1.24E+24	1.70
6258	CM6	0.00	1.29	1.31	0.35	0.1	55.7	28.3	15.9	0.00	1.03	0.52	0.29	2.73	1.78E+24	1.85
6280	CM6	0.00	1.31	1.26	0.33	0.1	57.2	25.4	17.3	0.00	0.95	0.42	0.29	3.12	1.08E+24	1.66

T_{irr} = 400°C

		Bulk (at.%)				Precipitate (%)				Precipitate f_v (%)						
Run	Alloy	Cu	Ni	Mn	Si	Cu	Ni	Mn	Si	Cu	Ni	Mn	Si	<d>	N_v	f_v (%)
6129	CM6	0.00	2.34	1.86	0.59	0.0	64.0	15.8	20.1	0.00	1.60	0.40	0.50	4.38	6.13E+23	2.50
6132	CM6	0.00	1.79	1.74	0.40	0.0	66.7	12.0	21.3	0.00	1.01	0.18	0.32	5.81	1.72E+23	1.52
6211	CM6	0.00	1.87	1.75	0.41	0.0	63.1	19.6	17.3	0.00	1.38	0.43	0.38	5.26	3.12E+23	2.19
6212	CM6	0.00	1.67	1.72	0.38	0.0	64.3	15.9	19.8	0.00	1.06	0.26	0.33	5.49	1.94E+23	1.65
6259	CM6	0.00	1.64	1.68	0.38	0.0	60.4	20.0	19.6	0.00	0.94	0.31	0.30	5.07	2.11E+23	1.55

A.7 UCSB Microstructural Database Used in Fitting Avrami Model

Alloy	Condition	Technique	<r> (nm)	f(%)	$\sigma_{vp}/\sqrt{f_v}$ (Mpa/$\sqrt{f_v}$)
LC	A5	SANS	1.09	0.03	5657
LC	T1	SANS	0.85	0.07	5245
LC	T2	SANS	1.20	0.14	5681
LC	T3	SANS	1.32	0.20	5633
LC	T4	SANS	1.33	0.34	5628
LC	T5	SANS	1.41	0.41	5580
LC	T6	SANS	1.53	0.49	5479
LC	G1	SANS	1.25	0.50	5664
LC	G2	SANS	1.22	0.35	5675
LC	G3	SANS	1.10	0.21	5666
LC	G4	SANS	1.21	0.28	5679
LC	G5	SANS	1.52	0.34	5488
LC	G1	SANS	1.25	0.50	5664
LC	G2	SANS	1.22	0.35	5675
LC	G3	SANS	1.10	0.21	5666
LC	G4	SANS	1.21	0.28	5679
LC	G5	SANS	1.52	0.34	5488
LC	T7	SANS	1.12	0.28	5671
LC	T8	SANS	1.33	0.39	5631
LC	T9	SANS	1.35	0.25	5615
LC	T10	SANS	1.44	0.34	5551
LC	T11	SANS	0.96	0.05	5519
LC	T12	SANS	1.06	0.14	5637
LC	T13	SANS	1.20	0.22	5681
LC	T14	SANS	1.34	0.34	5620
LC	T15	SANS	1.42	0.41	5572
LC	T16	SANS	1.61	0.45	5401
LC	T17	SANS	1.14	0.31	5674
LC	T18	SANS	1.24	0.52	5666
LC	T19	SANS	1.53	0.27	5472
LC	T20	SANS	1.82	0.45	5183
LC	T21	SANS	1.16	0.04	5675
LC	T22	SANS	1.26	0.15	5661
LC	T23	SANS	1.37	0.26	5601
LC	T24	SANS	1.37	0.38	5603
LC	T25	SANS	1.23	0.29	5670

Alloy	Condition	Technique	<r> (nm)	f(%)	$\sigma_{yp}/\sqrt{f_v}$ (Mpa/$\sqrt{f_v}$)
LC	T26	SANS	1.27	0.38	5656
LC	T27	SANS	1.52	0.25	5483
LC	T28	SANS	1.46	0.31	5537
LC	T30	SANS	0.91	0.03	5412
LC	K2	SANS	1.30	0.28	5648
LC	Piggy	SANS	1.38	0.36	5599
LC	TU	APT	1.64	0.72	5364
LC	ATR1	APT	1.44	1.81	5551
LD	T1	SANS	0.77	0.07	4893
LD	T2	SANS	0.99	0.15	5573
LD	T3	SANS	1.09	0.22	5664
LD	T4	SANS	1.14	0.38	5674
LD	T5	SANS	1.32	0.46	5633
LD	T6	SANS	1.50	0.55	5505
LD	G1	SANS	1.07	0.63	5640
LD	G2	SANS	1.04	0.46	5619
LD	G3	SANS	0.93	0.25	5449
LD	G4	SANS	1.04	0.34	5622
LD	G5	SANS	1.36	0.40	5607
LD	G1	SANS	1.07	0.63	5640
LD	G2	SANS	1.04	0.46	5619
LD	G3	SANS	0.93	0.25	5449
LD	G4	SANS	1.04	0.34	5622
LD	G5	SANS	1.36	0.40	5607
LD	T7	SANS	1.11	0.29	5669
LD	T8	SANS	1.29	0.46	5649
LD	T9	SANS	1.17	0.29	5677
LD	T10	SANS	1.53	0.38	5472
LD	T11	SANS	0.83	0.05	5178
LD	T12	SANS	0.92	0.16	5443
LD	T13	SANS	1.15	0.22	5675
LD	T14	SANS	1.15	0.38	5675
LD	T15	SANS	1.33	0.48	5628
LD	T16	SANS	1.46	0.53	5535
LD	T17	SANS	1.07	0.35	5644
LD	T18	SANS	1.18	0.61	5679
LD	T19	SANS	1.44	0.29	5551
LD	T20	SANS	1.46	0.53	5534

Alloy	Condition	Technique	<r> (nm)	f(%)	$\sigma_{yp}/\sqrt{f_v}$ (Mpa/$\sqrt{f_v}$)
LD	T21	SANS	0.79	0.04	5008
LD	T22	SANS	1.12	0.16	5671
LD	T23	SANS	1.14	0.32	5674
LD	T24	SANS	1.27	0.45	5659
LD	T25	SANS	1.06	0.34	5636
LD	T26	SANS	1.14	0.45	5674
LD	T27	SANS	1.45	0.26	5540
LD	T28	SANS	1.43	0.36	5563
LD	K2	SANS	1.24	0.31	5668
LD	Piggy	SANS	1.13	0.48	5672
LD	T16	SANS	1.44	0.54	5555
LD	TU	APT	1.43	1.22	5563
LD	ATR1	APT	1.96	2.11	5035
LG	G1	SANS	0.68	0.02	4361
LG	G2	SANS	0.52	0.10	2856
LG	TU	APT	1.12	0.17	5672
LG	ATR1	APT	1.25	1.33	5664
LH	T3	SANS	0.81	0.01	5084
LH	T5	SANS	0.81	0.06	5094
LH	T6	SANS	1.20	0.11	5680
LH	G1	SANS	1.04	0.12	5618
LH	G5	SANS	1.24	0.03	5667
LH	G1	SANS	1.04	0.12	5618
LH	G5	SANS	1.24	0.03	5667
LH	T8	SANS	1.07	0.06	5646
LH	T14	SANS	0.95	0.03	5488
LH	T15	SANS	1.11	0.07	5670
LH	T16	SANS	1.08	0.08	5656
LH	T18	SANS	0.90	0.13	5405
LH	T19	SANS	0.75	0.01	4812
LH	T20	SANS	1.27	0.05	5656
LH	T23	SANS	0.91	0.03	5425
LH	T24	SANS	1.12	0.04	5671
LH	T26	SANS	1.00	0.05	5584
LH	TU	APT	1.25	0.29	5663
LH	ATR1	APT	1.33	1.48	5628
LI	T2	SANS	0.94	0.08	5477
LI	T3	SANS	1.09	0.13	5657

Alloy	Condition	Technique	<r> (nm)	f(%)	$\sigma_{yp}/\sqrt{f_v}$ (Mpa/$\sqrt{f_v}$)
LI	T5	SANS	1.36	0.20	5612
LI	G1	SANS	1.06	0.35	5638
LI	G2	SANS	1.12	0.22	5671
LI	G3	SANS	0.95	0.11	5493
LI	G4	SANS	0.89	0.18	5366
LI	G5	SANS	1.41	0.20	5574
LI	G1	SANS	1.06	0.35	5638
LI	G2	SANS	1.12	0.22	5671
LI	G3	SANS	0.95	0.11	5493
LI	G4	SANS	0.89	0.18	5366
LI	G5	SANS	1.41	0.20	5574
LI	T8	SANS	1.30	0.23	5646
LI	T10	SANS	1.49	0.19	5510
LI	T14	SANS	1.19	0.18	5680
LI	T15	SANS	1.29	0.24	5651
LI	T16	SANS	1.41	0.26	5578
LI	T17	SANS	0.93	0.23	5466
LI	T18	SANS	1.25	0.30	5664
LI	T19	SANS	1.33	0.14	5626
LI	T20	SANS	1.52	0.21	5486
LI	T23	SANS	1.15	0.17	5675
LI	T24	SANS	1.25	0.22	5663
LI	K2	SANS	1.16	0.16	5676
LI	G1	APT	1.13	0.29	5672
LI	TU	APT	1.35	0.62	5617
LI	ATR1	APT	1.34	1.46	5622
CM6	T6	SANS	0.55	0.16	3125
CM6	G1	SANS	0.93	0.27	5454
CM6	G2	SANS	0.66	0.16	4206
CM6	T8	SANS	0.44	0.15	1948
CM6	T16	SANS	0.56	0.17	3287
CM6	T18	SANS	0.74	0.41	4724
CM6	T20	SANS	0.55	0.07	3169
CM6	TU	APT	0.73	1.21	5677
CM6	ATR1	APT	1.52	2.82	5483

A.8 ATR2 Tensile Curves

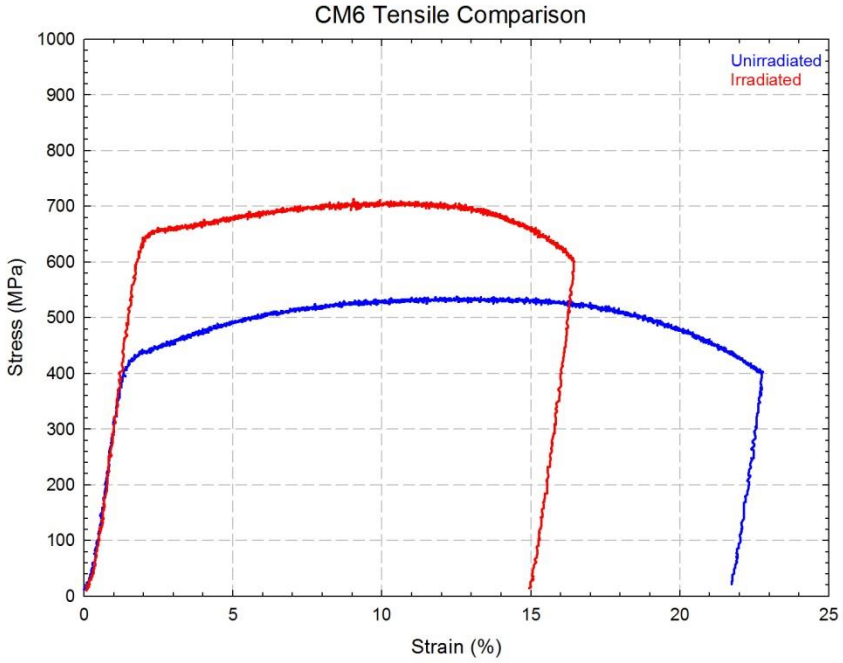

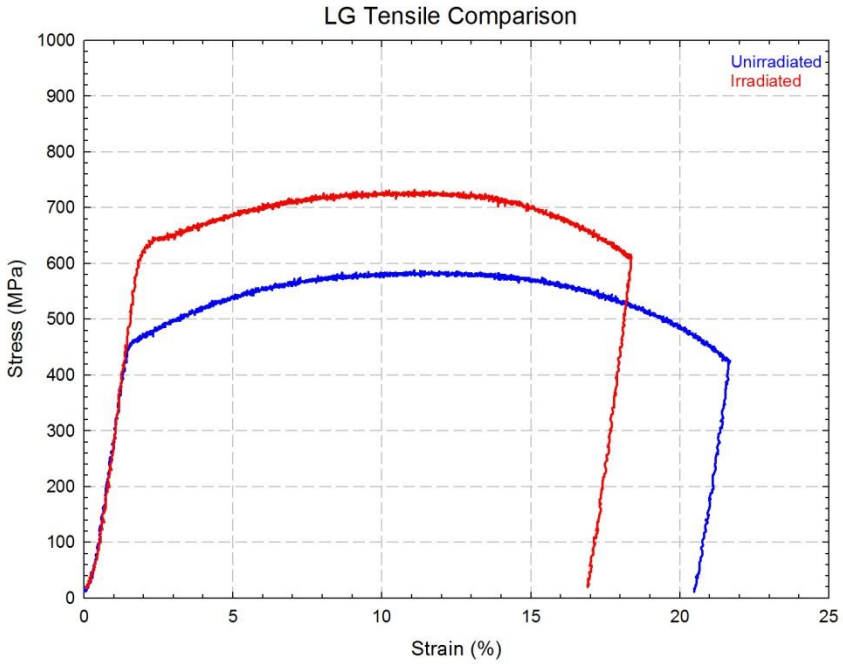

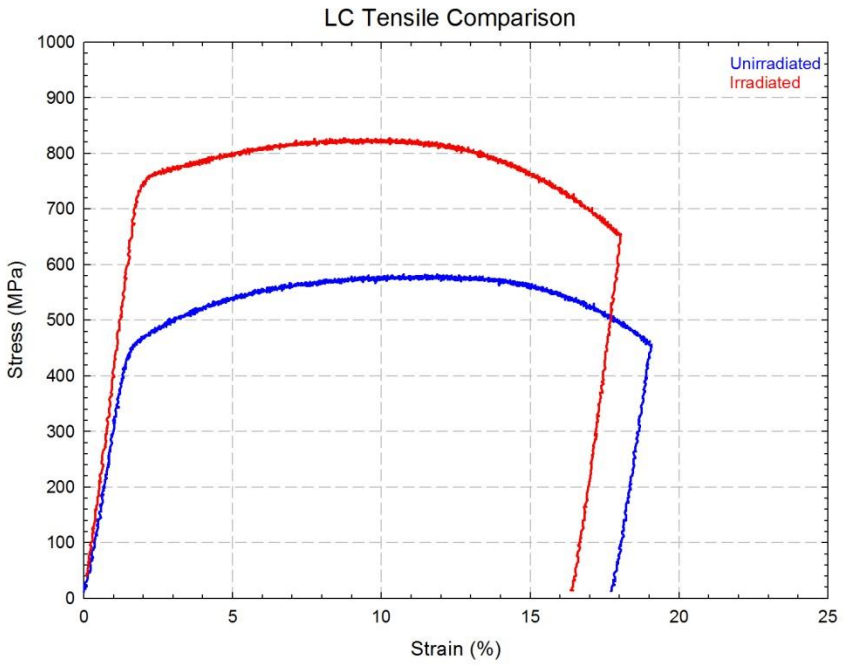
LC Tensile Comparison
Unirradiated
Irradiated
Stress (MPa)
Strain (%)
0
100
200
300
400
500
600
700
800
900
1000
0
5
10
15
20
25

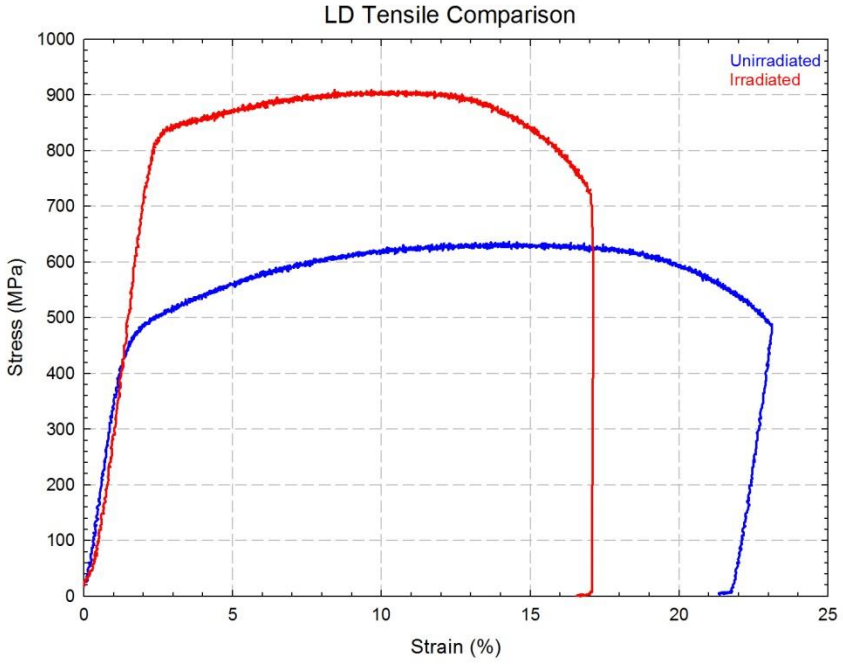
LD Tensile Comparison
Unirradiated
Irradiated
Stress (MPa)
Strain (%)
0
100
200
300
400
500
600
700
800
900
1000
0
5
10
15
20
25

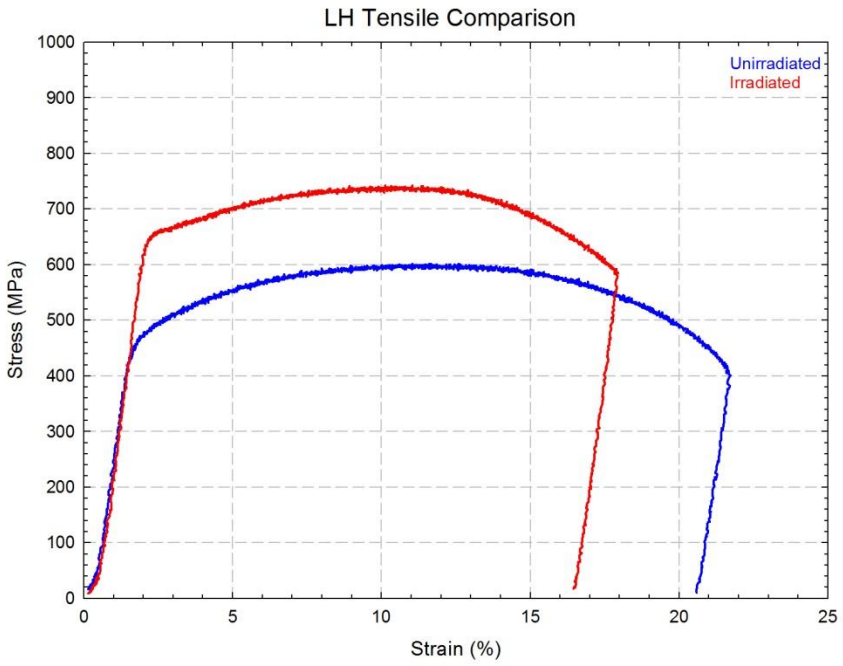
LH Tensile Comparison
Unirradiated
Irradiated
Stress (MPa)
Strain (%)
0
100
200
300
400
500
600
700
800
900
1000
0
5
10
15
20
25

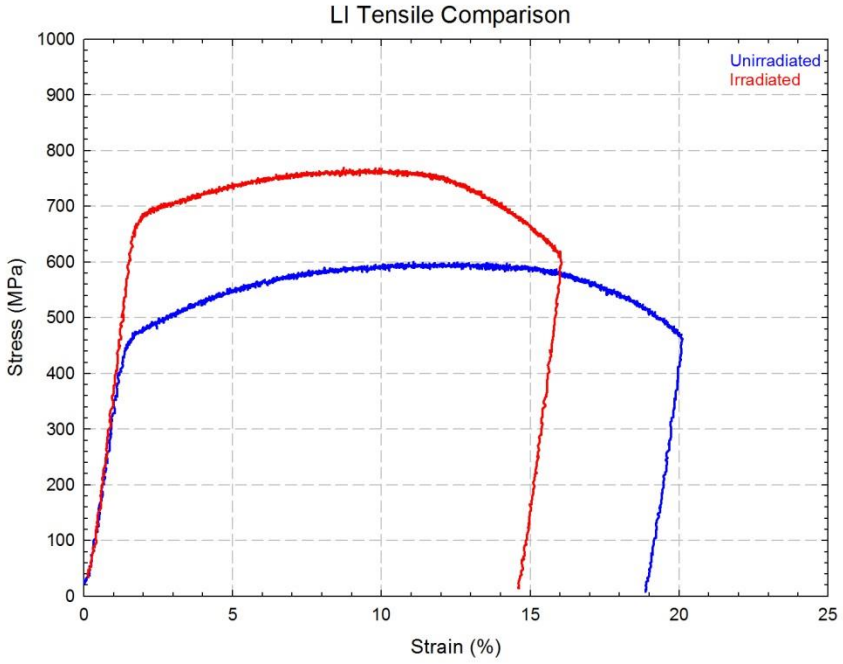
LI Tensile Comparison
Unirradiated
Irradiated
Stress (MPa)
Strain (%)
0
100
200
300
400
500
600
700
800
900
1000
0
5
10
15
20
25